1 August 2008 | $10

Science

CHINA'S ENVIRONMENTAL CHALLENGES

AAAS

Volume 321, Issue 5889

COVER

Heavy pollution blankets Tiananmen Square, Beijing, on 27 December 2007. Chinese authorities are taking drastic measures to improve the city's air quality for the Olympics. Bad air is just one of many environmental challenges China is facing. See the special News Focus section beginning on page 628.

Image: Feng Li/Getty Images

DEPARTMENTS

EDITORIAL

NEWS OF THE WEEK

NEWS FOCUS

China's Environmental Challenges

LETTERS

BOOKS *ET AL.*

POLICY FORUM

PERSPECTIVES

642

CONTENTS continued >>

Science

SCIENCE EXPRESS

www.sciencexpress.org

DEVELOPMENTAL BIOLOGY

Induced Pluripotent Stem Cells Generated from Patients with ALS Can Be Differentiated into Motor Neurons

J. T. Dimos et al.

Skin cells from elderly individuals with a mutation that causes amyotrophic lateral sclerosis (ALS) were used to derive stem cells that could then be differentiated.

10.1126/science.1158799

PALEOCLIMATE

Regional Synthesis of Mediterranean Atmospheric Circulation During the Last Glacial Maximum

J. Kuhlemann et al.

A three-dimensional reconstruction of atmospheric temperatures in the Mediterranean during glacial times is analogous to one of winter during the Little Ice Age.

10.1126/science.1157638

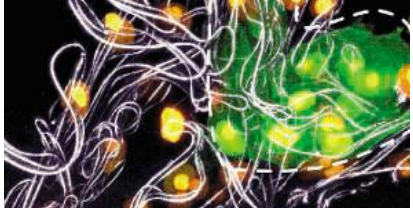

DEVELOPMENTAL BIOLOGY

Dual Origin of Tissue-Specific Progenitor Cells in *Drosophila* Tracheal Remodeling

M. Weaver and M. A. Krasnow

When fruit flies metamorphose from larvae, a new trachea forms both from undifferentiated cells of the imaginal disc and differentiated cells that re-enter the cell cycle.

10.1126/science.1158712

CHEMISTRY

In Situ Formation of an Oxygen-Evolving Catalyst in Neutral Water Containing Phosphate and Co^{2+}

M. W. Kanan and D. G. Nocera

A catalyst that precipitates in situ when cobalt ions are reduced in a phosphate buffer efficiently forms oxygen from water needed for electrochemical applications.

>> News story p. 620; Science *Podcast*

10.1126/science.1162018

TECHNICAL COMMENT ABSTRACTS

NEUROSCIENCE

Comment on "Magnetic Resonance Spectroscopy Identifies Neural Progenitor Cells in the Live Human Brain" 640

J. C. Hoch, M. W. Maciejewski, M. R. Gryk

full text at www.sciencemag.org/cgi/content/full/321/5889/640b

Comment on "Magnetic Resonance Spectroscopy Identifies Neural Progenitor Cells in the Live Human Brain"

S. D. Friedman

full text at www.sciencemag.org/cgi/content/full/321/5889/640c

Comment on "Magnetic Resonance Spectroscopy Identifies Neural Progenitor Cells in the Live Human Brain"

J. F. A. Jansen, J. D. Gearhart, J. W. M. Bulte

full text at www.sciencemag.org/cgi/content/full/321/5889/640d

Response to Comments on "Magnetic Resonance Spectroscopy Identifies Neural Progenitor Cells in the Live Human Brain"

P. M. Djurić et al.

full text at www.sciencemag.org/cgi/content/full/321/5889/640e

REVIEW

PALEONTOLOGY

Hopping Hotspots: Global Shifts in Marine Biodiversity 654

W. Renema et al.

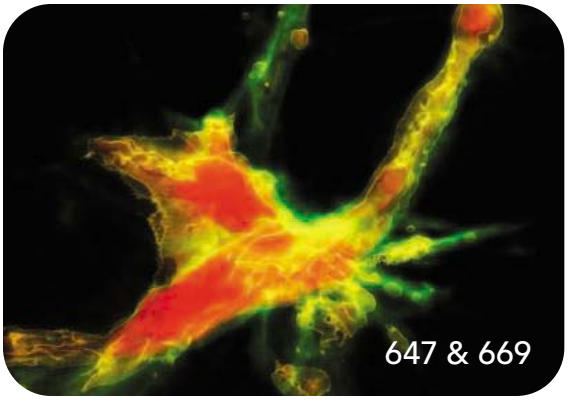

BREVIA

BIOCHEMISTRY

Evidence of Global Chlorophyll d 658

Y. Kashiyama et al.

A survey of chlorophyll d, used by a cyanobacterium for harvesting infrared light, implies that this microbe inhabits a much wider range than previously thought.

RESEARCH ARTICLES

BIOCHEMISTRY

Crystal Structure of the Termination Module of a Nonribosomal Peptide Synthetase 659

A. Tanovic, S. A. Samel, L.-O. Essen, M. A. Marahiel

A large enzyme complex assembles peptide natural products without ribosomal participation by successive catalytic steps at the end of a flexible, substrate-loaded arm.

CELL BIOLOGY

Essential Cytoplasmic Translocation of a Cytokine Receptor–Assembled Signaling Complex 663

A. Matsuzawa et al.

Degradation of one member of a protein complex that forms when a cytokine receptor is activated causes the complex to move to the cytoplasm, triggering the downstream pathway.

>> Perspective p. 648

REPORTS

ASTRONOMY

Protostar Formation in the Early Universe 669

N. Yoshida, K. Omukai, L. Hernquist

A model traces the coalescence of small variations in gas density after the Big Bang into protostars, showing that the first stars would be large enough to make heavy elements.

>> Perspective p. 647

CONTENTS continued **>>**

REPORTS *CONTINUED...*

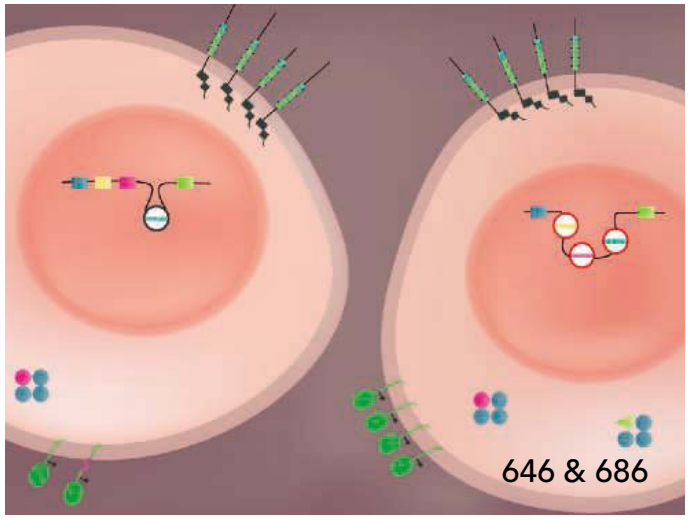

AAAS
ADVANCING SCIENCE, SERVING SOCIETY

SCIENCE (ISSN 0036-8075) is published weekly on Friday, except the last week in December, by the American Association for the Advancement of Science, 1200 New York Avenue, NW, Washington, DC 20005. Periodicals Mail postage (publication No. 484460) paid at Washington, DC, and additional mailing offices. Domestic individual membership and subscription (51 issues): $142 ($74 allocated to subscription). Domestic institutional subscription (51 issues): $710; Foreign postage extra: Mexico, Caribbean (surface mail) $55; other countries (air assist delivery) $85. First class, airmail, student, and emeritus rates on request. Canadian rates with GST available upon request, GST #1254 88122. Publications Mail Agreement Number 1069624. SCIENCE is printed on 30 percent post-consumer recycled paper. **Printed in the U.S.A.**

Change of address: Allow 4 weeks, giving old and new addresses and 8-digit account number. **Postmaster:** Send change of address to AAAS, P.O. Box 96178, Washington, DC 20090–6178. **Single-copy sales:** $10.00 current issue, $15.00 back issue prepaid includes surface postage; bulk rates on request. **Authorization to photocopy** material for internal or personal use under circumstances not falling within the fair use provisions of the Copyright Act is granted by AAAS to libraries and other users registered with the Copyright Clearance Center (CCC) Transactional Reporting Service, provided that $18.00 per article is paid directly to CCC, 222 Rosewood Drive, Danvers, MA 01923. The identification code for *Science* is 0036-8075. *Science* is indexed in the *Reader's Guide to Periodical Literature* and in several specialized indexes.

Printed on 30% post-consumer recycled paper.

CONTENTS continued **>>**

Legally drunk.

SCIENCE**NOW**

www.sciencenow.org

HIGHLIGHTS FROM OUR DAILY NEWS COVERAGE

Now That's a Party Animal
Researchers discover a wild tree shrew that lives on alcoholic nectar.

Take a Deep Breath—and Thank Mount Everest
Plate tectonics gave rise to atmospheric oxygen.

To Sleep, Perchance to Forget
Aging may impair the consolidation of memories during sleep.

Anesthetics increase postoperative pain.

SCIENCE **SIGNALING**

www.sciencesignaling.org

THE SIGNAL TRANSDUCTION KNOWLEDGE ENVIRONMENT

PODCAST
N. R. Gough and A. M. VanHook
Some anesthetics activate TRPA1 channels to trigger pain and nerve-mediated inflammation.

PRESENTATION: A Static Network Analysis Tool for Pharmacological Analysis of Signal Transduction Pathways
B. B. Samal and L. E. Eiden
Simulate knocking out one or more components from a pathway to find alternate connections between a stimulus and a target response.

A career in keeping athletics clean.

SCIENCE **CAREERS**

www.sciencecareers.org/career_development

FREE CAREER RESOURCES FOR SCIENTISTS

Taken for Granted: The Fat Lady Sings
B. L. Benderly
Organizers claim success in unionizing postdocs on University of California campuses.

A Scientist in the Service of Clean Sports
E. Pain
Chemist Osquel Barroso matches his scientific and sporting interests at the World Anti-Doping Agency.
>> News story p. 627

Careers in Research Support
S. Gaidos
Institutions recognize the advantages of hiring science Ph.D.'s as research administrators.

August 2008 Funding News
J. Fernández
Learn about the latest in research funding, scholarships, fellowships, and internships.

SCIENCE**PODCAST**

www.sciencemag.org/multimedia/podcast

FREE WEEKLY SHOW

Download the 1 August *Science* Podcast to hear about a water-splitting catalyst for energy storage applications, the molecular basis of pain, China's environmental challenges, and more.

Separate individual or institutional subscriptions to these products may be required for full-text access.

EDITED BY STELLA HURTLEY

How Fast Is Fast? >>

Ice core records have shown that substantial changes can happen very rapidly. Even with the high temporal resolution that some ice cores provide, it has been difficult to determine exactly how rapidly most shifts occurred, due largely to the amount of interannual variability displayed by most climate indicators and the difficulty of synchronizing the time scales of different records. **Steffensen *et al.*** (p. 680, published online 19 June; see the Perspective by **Flückiger**) employed sophisticated analytical methods to measure multiple climate proxies in a single, high-resolution ice core from Greenland. Measuring several parameters in the same ice obviated problems that arise from trying to intercalibrate data from different sites, and high-resolution measurements tracked changes at subannual time scales. Some attributes of climate were observed to change in as little as a single year during two abrupt warmings within the last deglaciation.

Spotlight on Biodiversity Hotspots

Certain regions of the globe harbor particularly high numbers of species of organisms. These regions have become known as biodiversity hotspots. However, the history of hotspots is not well charted. **Renema *et al.*** (p. 654) review global shifts in marine biodiversity hotspots. By combining evidence from the paleontological and molecular evolutionary literature, they identify multiple Cenozoic hotspots that were mobile and responded to global tectonic events. The authors suggest a mechanistic basis for this mobility and for the formation of modern faunas and explain the dynamic nature of biodiversity.

Nonribosomal Peptide Synthetase Structure

Nonribosomal peptide synthetases (NRPS) are multimodular megaenzymes that catalyze the biosynthesis of complex peptides, including medically important compounds, such as the antibiotic vancomycin. Each module comprises at least an adenylation domain, a peptidyl carrier protein domain, and a condensation domain. Although structures of all the essential domains are available, how they are organized to achieve peptide elongation has remained unclear. Now **Tanovic *et al.*** (p. 659, published online 26 June) have determined the structure of a complete termination module. The organization of the domains suggests how the catalytic steps are coordinated within the NRPS module, which may facilitate efforts to engineer chimeric NRPS proteins to allow biosynthesis of new peptides.

Shaking Out Gold Structures

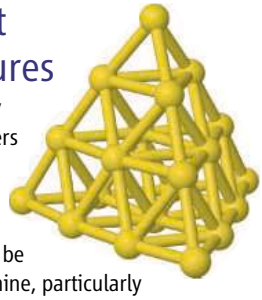

Oxidative catalysis by nanoscale gold clusters is exquisitely sensitive to cluster size and geometry, but these parameters can be challenging to determine, particularly in a heterogeneous sample. **Gruene *et al.*** (p. 674) take advantage of the structural purity attainable by mass selection in the gas phase to explore the geometries of three neutral clusters: Au_7, Au_{19}, and Au_{20}. By measuring vibrational spectra in the far-infrared and comparing them with calculated absorptions of model compounds analyzed by density functional theory, the authors assign a planar structure to the smallest cluster, and a tetrahedral geometry to Au_{20}, which is truncated by loss of a vertex atom in Au_{19}.

Signaling in Time and Place

Proteins that participate in biological regulatory mechanisms are often assembled into large complexes, within which various signaling molecules interact to propagate a biochemical signal. **Matsuzawa *et al.*** (p. 663, published online 17 July; see the Perspective by **Eliopoulos**) characterize such a complex of proteins assembled at the activated receptor CD40 (a member of the tumor necrosis factor receptor family) on the cell surface. The complex formed at the cell surface within a few minutes after binding of ligand to the receptor, but after 30 minutes had moved to the cytoplasm. Surprisingly, activation of mitogen-activated protein kinases (MAPKs) JNK and p38 and of the MAPK kinase MEKK1 was only detected once the complex left the receptor and moved into the cytosol. Degradation of the adaptor protein TRAF3 was required to initiate release of the complex from CD40. Other receptors may also use such a mechanism to specify the time and place at which signaling proteins are activated in response to receptor stimulation.

A Star Is Born

Observations of early stars in the universe suggest that even earlier stars that formed after the Big Bang were massive enough to produce some heavy elements. **Yoshida *et al.*** (p. 669; see the Perspective by **Bromm**) now describe computer simulations that begin after the Big Bang and extend to the time of the formation of an early star. The results suggest that a tiny protostar much smaller than the density variations in dust produced by the Big Bang could provide the nucleus for a protostar smaller than the Sun but that can grow to a massive star.

CREDITS (TOP TO BOTTOM): NGRIP PICTURE ARCHIVE; GRUENE *ET AL.*

Polymer Electrodes for Oxygen Reduction

A number of important electrochemical devices, including fuel cells and various air batteries, rely on the fast rate of oxygen reduction over platinum electrodes. The cost and scarcity of Pt has long driven a search for alternatives, which often include Pt as an alloy component or suffer in terms of rate. Conducting polymers could provide an alternative if they could be stabilized as a high-surface-area material. **Winther-Jensen *et al.*** (p. 671; see the News story by **Service**) have grown poly(3,4-ethylenedioxythiophene) (PEDOT) through vapor-phase polymerization onto a Goretex membrane. They report oxygen reduction rates in gas phase and aqueous solution comparable to that of high-area Pt electrodes. Unlike Pt, the PEDOT electrodes are not slowed down by the presence of CO, which can be a contaminant in some applications.

Human Immunity—Naturally

Animal models continue to influence our understanding of immunity to infection, but how accurately do they predict how our own immune systems respond to different pathogens? **Von Bernuth *et al.*** (p. 691) continue a series of studies in which they use rare human immune deficiencies to help unpick the roles played by distinct innate immune pathways. The study focuses on MyD88, a signaling adaptor that is crucial in mice for protection against a wide range of pathogens by connecting key Toll-like receptor (TLR) and interleukin-1 (IL-1) pathways to the activation of immune response genes. In contrast to findings in mice, deficiency of the same protein in the human patients caused susceptibility to only a handful of pyogenic bacteria, despite leaving the subjects with broad deficits in their TLR and IL-1 responses.

Preliminary Purge

B lymphocytes express somatically rearranged immunoglobulin receptors on their surface containing the same heavy and light chains as the antibodies the cells will produce later. However, only the heavy chain is expressed during early developmental transitions, meaning that a surrogate light chain (SLC) is needed to help the heavy chains arrive at the cell surface to generate a pre-B cell receptor. This strategy "pre-selects" B cells that have successfully completed heavy chain rearrangement before committing them to light chain production. **Keenan *et al.*** (p. 696, published online 19 June) provide evidence for a further role of the SLC in weeding out potentially harmful self-reactive B cells. Mice deficient in the SLC showed elevated levels of circulating autoantibodies, resulting directly from the escape of autoreactive cells at the early stages of B cell development.

The Pain Specialists

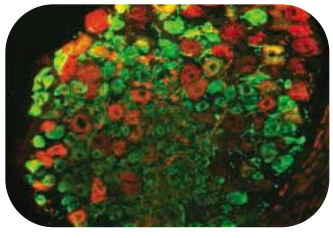

In pain research it has been assumed that most nociceptive neurons are polymodal, responding to different damaging stimuli by means of a repertoire of cell surface receptors specialized for the detection of particular types of insult. Attempts to ascribe pain modalities and behavior to individual sensory neuron receptors have been problematic, probably because of the existence of multiple damage-sensing molecules. Now, however, by genetically ablating subsets of nociceptors, followed by behavioral and electrophysiological assays, **Abrahamsen *et al.*** (p. 702) have found that sensory neurons expressing a specific type of sodium channel ($Na_v1.8$) have a modality-specific function in pain transmission. $Na_v1.8$-expressing sensory neurons are essential for cold, mechanical, and inflammatory pain behavior. Strikingly, neuropathic and heat pain behavior do not require $Na_v1.8$-expressing neurons.

Pluripotent Reprogramming

Adult mouse and human fibroblasts can be reprogrammed to a pluripotent state after the viral integration of four transcription factors. However, questions remain as to the origin of the pluripotent cells, whether specific genomic integration sites are needed, and how tumorigenicity might be reduced. **Aoi *et al.*** (p. 699, published online 14 February) now reprogram adult mouse hepatocytes and stomach epithelial cells to a pluripotent state, termed iPS cells. These cells show great similarity to embryonic stem cells, are of a differentiated cell origin, do not require a specific viral integration site, and are not tumorigenic to at least 30 weeks. This work provides insight for understanding the mechanism of iPS reprogramming and moves another step toward using these cells to study disease in culture and the hoped-for application in human therapy.

CREDIT: ABRAHAMSEN *ET AL.*

Bojie Fu is a professor at the State Key Laboratory of Urban and Regional Ecology, Research Center for Eco-Environmental Sciences, Chinese Academy of Sciences (CAS), and Director-General of the Bureau of Science and Technology for Resource and Environment, CAS. E-mail: bfu@rcees.ac.cn

Blue Skies for China

WITH THE OLYMPIC GAMES OPENING NEXT WEEK, THE SPOTLIGHT HAS BEEN ON CHINA'S FINAL push to reduce atmospheric pollution by limiting automobile use in Beijing, expanding public transportation, and temporarily shutting down some industries. One can now see a blue sky, a testament to the country's effort to clean house before the guests arrive. The important question is whether these intentions will be maintained, and even amplified, after the games are finished.

The mismatch between China's limited natural resources and the demands of a huge population (1.3 billion) has resulted in major environmental pollution, directly affecting public health and fueling social conflicts. Environmental deterioration has been considered one of the important sources of social unrest in Chinese society. In 2005, there were 51,000 conflicts among local residents and polluters over degradation incidents, including contaminated water, dust, and landslides. Furthermore, the environmental degradation caused by a fast-growing economy is itself causing economic losses. Over the past 20 years, the total cost from environmental pollution and ecological deterioration is estimated to have been 7 to 20% of the annual gross domestic product (GDP). In a global context, China will affect, and be affected by, the outside world both economically and environmentally. Effective and innovative strategies, therefore, must be established and implemented not only to facilitate sustainable development in China but to contribute to the sustainable future of the world.

The major environmental challenges include water contamination, air pollution, and land degradation. Last year, 40% of urban wastewater was discharged into neighborhood water bodies without treatment. In 2007, water quality at half of the 197 monitored rivers of China was rated as heavily polluted with ammonium nitrate, permanganate, and petroleum. In more than 60% of China's large lakes, minerals and organic compounds are so concentrated that there is overproliferation of plant life (especially algae), which has reduced dissolved oxygen and thus depleted the lakes of other organisms, including fish.

Air and land quality are no better. Of the 287 large cities monitored in 2007, only 60.5% had air quality that met the Ministry of Environmental Protection of China standard (comparable to the National Ambient Air Quality Standards of the United States). Land degradation resulting from overexploitation of land resources takes the forms of soil erosion, desertification, and habitat fragmentation. For example, excess erosion from wind and water has deteriorated about 37.1% of China's total land mass.

The most difficult mission will be to find effective ways to regulate the behaviors and relationships of the various stakeholders—different levels of government, the industrial sectors, and the public—who often have different and sometimes conflicting objectives and expectations. For example, China's government has made great efforts to mitigate lake eutrophication. However, these efforts have been undermined by local governments' pursuit of economic growth through industrial development that is not sensitive to environmental issues. Capacity-building is needed in basic scientific research, technological innovation, policy and institutional design, and environmental legislation and enforcement. For instance, market-based incentives for pollution control and efficient resource use, such as those in the United States for vehicle pollution control, are needed. The Chinese environmental management authorities still depend largely on a government command-and-control approach because the market-based mechanism is immature and weak. More financial support from the government is needed to enhance environmental monitoring and management. Although this support has continually increased since the 1980s, the current rate is still below 1.5% of GDP annually. China also needs to develop cost-effective pollution-control (such as wastewater treatment) and resource-recycling technologies, because the current processes are either too costly or not profitable to operate.

For decades, rapid economic growth and the improvement of human living status for the world's biggest population have been accomplished at the expense of environmental integrity. Now, human welfare, rather than living status, should be a priority in developing a strategy for a sustainable China. Hopefully, the world's attention, so focused on conditions in Beijing right now, will continue to focus on China's environmental issues beyond next week. **– Bojie Fu**

10.1126/science.1162213

EDITED BY GILBERT CHIN AND JAKE YESTON

CHEMISTRY

Building pHotoswitches

Some compounds exhibit significant changes in inherent acidity upon electronic excitation. However, the excited states in these photoacids tend to be too short-lived for practical use in tuning bimolecular reactivity. Two research teams have extended the scope of phototunable reactivity by building molecules in which light absorption at different wavelengths switches the structure reversibly between two stable isomers of differing acidities. Lemieux *et al.* prepared a boronate derivative in which the boron is initially conjugated in a planar ring with six π electrons from oxygen and olefin groups, and so has comparatively low Lewis acidity. Ultraviolet (UV) irradiation links two thiophene rings pendant to the olefin, disrupting the conjugation geometry and thereby raising the Lewis acidity to increase the pyridine binding constant from undetectable to ~7000. Blue light cleaves the thiophene linkage and restores the inert geometry. At the opposite end of the pH scale, Peters *et al.* relied on sterics rather than electronics to tune the basicity of a piperidine derivative. A pendant azobenzene group blocks the basic piperidine nitrogen with a bulky aryl or *tert*-butyl substituent in the trans geometry, but rotates this blocking group out of the way upon UV-induced isomerization to the cis geometry. — JSY

Angew. Chem. Int. Ed. **47**, 5034; 10.1002/anie.200802050 (2008).

CLIMATE SCIENCE

Dry and Getting Drier

Global warming is expected to have a substantial impact on the amount and pattern of rainfall worldwide. Although projections indicate that

the overall effect should be an increase in precipitation, at a regional scale there will be areas that receive less rainfall; many such areas are already arid and particularly vulnerable to further drying. One of these regions is northwestern Africa, which recently suffered a severe drought from 1999 to 2002. In order to establish a context for understanding drought frequency and severity in the region, Touchan *et al.* constructed a 547-year summer drought record by measuring and analyzing ring widths of cedar and pine trees across Algeria and Tunisia. They found that the multiyear drought of 1999 to 2002 was the longest in their entire record and that 2002 was the single driest year, a troubling set of statistics if the data do indeed reflect ongoing anthropogenic climate change. Climate models are unable to identify the physical causes of drought in this region, however, so a mechanistic understanding of rainfall dynamics there remains elusive. — HJS

Geophys. Res. Lett. **35**, L13705 (2008).

PSYCHOLOGY

A Numbers Game

Low-tech inexpensive means for enhancing childhood proficiency in mathematics would be of broad utility, and if applied early on and as unobtrusively as possible, might well yield long-lasting benefits. Siegler and Mu find that Chinese kindergartners (5 to 6 years old) score higher than U.S. children of the same age on two tests: the addition of single-digit numbers and the placement of numbers on a number line. The former result is not unexpected as it fits with previous reports of extensive parental involvement in explicit numerical instruction (such as counting) in China. The latter outcome, however, reveals a precocious and implicitly acquired transition from a logarithmic to a linear representation of magnitude, which occurs at elementary school age in the United States and does not appear to occur at all in the absence of formal education (see Dehaene *et al.*, Reports, 30 May, p. 1217). Ramani and Siegler show that the number-line skills of preschoolers from low-income households can be improved by playing simple board games designed to instill multimodal instantiation of numerical concepts. A follow-up analysis revealed that mathematical proficiency in this cohort correlated with commercial board games played outside of preschool, but not with video gaming. — GJC

Psychol. Sci. **19**, 633 (2008); *Child Dev.* **79**, 375 (2008).

MATERIALS SCIENCE

Naturally Sticky

A key property of good composites is a strong adhesion of the reinforcing material to the matrix. Pommet *et al.* sought to optimize this feature while advancing the environmentally friendly goal of deriving plastics from renewable sources. They took beds of sisal or hemp fibers and used them as substrates for the bacterium *Acetobacter xylinum*. During fermentation, a thin film of bacterial cellulose was deposited onto the fibers; to improve coverage, fibers were treated with acetone to remove any waxy coatings. Pullout tests showed greater interfacial shear strength, a measure of adhesion, for both fiber types when they were embedded in a matrix of polymeric cellulose acetate butyrate. For a composite of sisal fibers and poly(lactic

acid), Juntaro *et al.* showed that the tensile strength and Young's modulus improved by about 50% in the direction of the fiber orientation. In the transverse direction, the Young's modulus was greater than that of the pure matrix polymer, but the strength decreased significantly, possibly because of adhesive failure or internal failure of the fibers themselves. Because the cellulose coating technique should work with any natural fiber that has a sufficiently hydrophobic surface, it may be possible to improve further the properties of a biologically sourced and potentially biodegradable polymer composite. — MSL

Biomacromolecules **9**, 1643 (2008); *Adv. Mater.* **20**, 10.1002/adma.200703176 (2008).

ANIMAL BEHAVIOR

Turning Turtles

The peregrinations of the remaining leatherback turtles in the eastern Pacific are governed by an urge to go south regardless of currents and temperature. Concerned by the plummeting populations afflicted by human predation of eggs and by fisheries-mediated mortalities, Shillinger *et al.* attached satellite tracking tags to 46 female leatherbacks that nested on Costa Rican beaches between 2004 and 2007. After laying their eggs, the turtles headed south, parallel to the Cocos Ridge. By swimming at speeds sometimes exceeding 60 km per day, they were able to win through the strong oceanic currents that ply the waters between Central America and the Galápagos. Once released from this web, the turtles slowed down and dispersed in the South Pacific Gyre. During February and April when the females set out to sea, their route is highly predictable and hence makes a multinational conservation strategy practical. — CA

PLoS Biol. **6**, e171 (2008).

DEVELOPMENT

Pore Differentiation

Developmental signals are relayed inside cells via nucleocytoplasmic transport in which information and macromolecules are exchanged between the cytoplasm and nucleus via the nuclear pore complex (NPC), which in mice is composed of about 30 different proteins. Thus far, mutational analyses of several nucleoporins have produced embryonic lethality. Lupu *et al.* find that mouse embryos express the conserved nucleoporin Nup133 in a cell-type– and stage-specific pattern, suggesting that it may not function as a general structural component of the NPC but could instead be a modulator of NPC activity. When *Nup133* was disrupted, nuclear pore complexes assembled normally, but mouse gastrulation was defective. Specifically, neural progenitors formed, but cells maintained the features of an earlier pluripotent state and differentiated inefficiently. — BAP

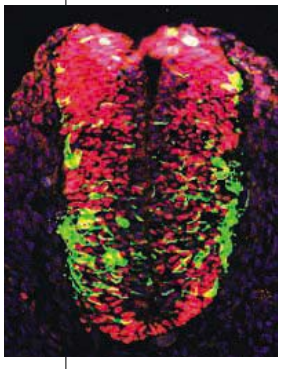

Differentiated cells (green) within a tube of neural progenitors (red).

CREDIT: LUPU *ET AL.*, *DEV. CELL* **14**, 831 (2008)

Dev. Cell **14**, 831 (2008).

Science Signaling
AAAS

<< Facilitating Multicellularity

Tyrosine kinase signaling plays an integral role in intercellular communication in multicellular animals (metazoans). There are three essential molecular components: protein tyrosine kinases (PTKs), protein tyrosine phosphatases (PTPs), and SH2 domains (phosphotyrosine-binding modules). Once thought to be limited to metazoans, these components have been identified in choanoflagellates (such as the recently sequenced *Monosiga brevicollis*), their closest unicellular relatives. Manning *et al.* and Pincus *et al.* have surveyed the *Monosiga* genome for genes encoding PTKs, PTPs, and SH2 domains and report a large number, most of which have no metazoan orthologs. For example, only eight of the PTKs identified by Manning *et al.* have metazoan orthologs, indicating that the expansion of the PTP-, PTK- and SH2-containing protein families occurred after the ancestral lineage had split. Both lineages have evolved similar functionality through domain shuffling. For example, receptor tyrosine kinases with cysteine-rich motifs appear in both lineages. Fungi and slime molds, eukaryotes lying outside the metazoan-choanoflagellate lineage, have PTPs and SH2-containing proteins but not PTKs, and Pincus *et al.* point out that having only these two components could be advantageous because some serine/threonine kinases, which fungi and slime molds have in abundance, do perform tyrosine phosphorylation inefficiently. — AMV

Proc. Natl. Acad. Sci. U.S.A. **105**, 9674; 9680 (2008).

www.sciencemag.org

Science

1200 New York Avenue, NW
Washington, DC 20005
Editorial: 202-326-6550, FAX 202-289-7562
News: 202-326-6581, FAX 202-371-9227
Bateman House, 82-88 Hills Road
Cambridge, UK CB2 1LQ
+44 (0) 1223 326500, FAX +44 (0) 1223 326501

Subscription Services For change of address, missing issues, new orders and renewals, and payment questions: 866-434-AAAS (2227) or 202-326-6417, FAX 202-842-1065. Mailing addresses: AAAS, P.O. Box 96178, Washington, DC 20090-6178 or AAAS Member Services, 1200 New York Avenue, NW, Washington, DC 20005

Institutional Site Licenses please call 202-326-6755 for any questions or information

Reprints: Author Inquiries 800-635-7181
Commercial Inquiries 803-359-4578

Permissions 202-326-7074, FAX 202-682-0816

Member Benefits AAAS/Barnes&Noble.com bookstore www.aaas.org/bn; AAAS Online Store http://www.apisource.com/aaas/ code MKB6; AAAS Travels: Betchart Expeditions 800-252-4910; Apple Store www.apple/eppstore/aaas; Bank of America MasterCard 1-800-833-6262 priority code FAA3YU; Cold Spring Harbor Laboratory Press Publications www.cshlpress.com/affiliates/aaas.htm; GEICO Auto Insurance www.geico.com/landingpage/go51.htm?logo=17624; Hertz 800-654-2200 CDP#343457; Office Depot https://bsd.officedepot.com/portalLogin.do; Seabury & Smith Life Insurance 800-424-9883; Subaru VIP Program 202-326-6417; VIP Moving Services http://www.vipmayflower.com/domestic/index.html; Other Benefits: AAAS Member Services 202-326-6417 or www.aaasmember.org.

science_editors@aaas.org	(for general editorial queries)
science_letters@aaas.org	(for queries about letters)
science_reviews@aaas.org	(for returning manuscript reviews)
science_bookrevs@aaas.org	(for book review queries)

Published by the American Association for the Advancement of Science (AAAS), *Science* serves its readers as a forum for the presentation and discussion of important issues related to the advancement of science, including the presentation of minority or conflicting points of view, rather than by publishing only material on which a consensus has been reached. Accordingly, all articles published in *Science*—including editorials, news and comment, and book reviews—are signed and reflect the individual views of the authors and not official points of view adopted by AAAS or the institutions with which the authors are affiliated.

AAAS was founded in 1848 and incorporated in 1874. Its mission is to advance science, engineering, and innovation throughout the world for the benefit of all people. The goals of the association are to: enhance communication among scientists, engineers, and the public; promote and defend the integrity of science and its use; strengthen support for the science and technology enterprise; provide a voice for science on societal issues; promote the responsible use of science in public policy; strengthen and diversify the science and technology workforce; foster education in science and technology for everyone; increase public engagement with science and technology; and advance international cooperation in science.

Information for Authors
See pages 634 and 635 of the 1 February 2008 issue or access www.sciencemag.org/about/authors

Let the Games Begin

Just in time for the start of the Beijing Summer Games, German researchers announced last month that they had located traces of one of ancient Olympia's most famous racecourses. The hippodrome, where chariot races took place, was the largest structure in the ancient Greek sports complex. Described in several ancient texts, the course was also the site of Roman Emperor Nero's quest for Olympic laurels in 67 C.E. (He won them despite falling out of his chariot.)

Archaeologists began excavating the site more than a century ago but found no sign of the racecourse and assumed that flooding from the nearby Alfeiós River had washed it away. A recent reinterpretation of a medieval text prompted sports historian Norbert Müller of the University of Mainz and colleagues to look again. Using geomagnetic mapping and georadar, the team found evidence of long, parallel ditches, walls, and earthworks along a 1.2-kilometer stretch about 2 meters below the current surface. The proportions and location—south of the

already excavated stadium—match those of the ancient texts. The find is not a huge surprise given the texts' descriptions, says Paul Christesen, a classicist at Dartmouth College. But further digging should prove interesting, he says, because few hippodromes from the period have been excavated.

Follow the Bouncing Ion

If you're looking for some action, forget about the latest Hollywood blockbuster and check out a stimulated neuron. Ions stream into and out of the cell, membrane channels open and slam shut, impulses speed along the axon, neurotransmitters spill into the synapse. Nervous-system newbies can watch these events unfold at Neurons, an animated primer from neuroanatomist Patricia Stewart of the University of Toronto in Canada and colleagues.

The eight chapters detail the structure and workings of the excitable cells. Readers can follow along, step by step, as neurons load up on sodium ions in preparation for firing, depolarize, and then release neurotransmitters. One sequence, for example, illustrates how cocaine leads to prolonged activation of brain neurons and euphoria. Like a monkey wrench in a machine, the cocaine molecule jams the pump that normally removes the neurotransmitter dopamine from synapses. As a result, neurons keep firing.

>>icarus.med.utoronto.ca/neurons/index.swf

CREDITS (TOP TO BOTTOM): IMAGE COURTESY OF VIRGIN GALACTIC/START CREATIVE LTD.; NORBERT MÜLLER/UNIVERSITY OF MAINZ; GETTY IMAGES

TICKET TO RIDE

Virgin Galactic and its competitors hope to send commercial passengers to the edge of space for several minutes of zero gravity when their new suborbital airlines start operations. NASA is considering sending scientists, too. The space agency has asked researchers to design experiments that could be conducted aboard the commercial ships to make what NASA calls "astronomical, solar, planetary, and Earth observations at wavelengths and special observing geometries not accessible from the ground."

Astronomer Daniel Durda helped develop the idea while working with NASA's science directorate. Durda, now at Southwest Research Institute in Boulder, Colorado, has observed asteroids from F-18s, obtaining data that weather often obscures from observatories on the ground. Suborbital flights could offer other scientists similar opportunities, he says.

"We're looking for creative new thinking," says NASA's Kelly Snook. Virgin is aiming for commercial flights in 2009 and has booked more than 200 tickets at $200,000 each for the 5-minute excursions. Each flight, which will hold six passengers, will reach 100 kilometers in altitude. Other companies developing suborbital aircraft, including Amazon founder Jeff Bezos's Blue Origin, would also be eligible for the program.

Which Chicken Came First?

Last year, scientists reported that the first chickens in the New World might have come from Polynesia. Now, a new DNA analysis contradicts that notion, instead linking the bird to its European kin. The result bolsters claims that chickens first arrived in South America with Spaniards in the 15th century.

The study, published online 28 July in the *Proceedings of the National Academy of Sciences*, refutes findings in an earlier *PNAS* paper, in which Alice Storey of the University of Auckland in New Zealand and colleagues analyzed chicken mitochondrial DNA (mtDNA) from a bone recovered from an archaeological dig in Chile. Radiocarbon analysis of the bone dated the bird to just before the Spanish arrived, and some mtDNA sequences seemed to match those in Polynesian chickens. But those sequences are also common to European chickens, says a team led by Jaime Gongora of the University of Sydney in Australia. The new analysis of mtDNA of 41 modern Chilean chickens found no trace of a uniquely Polynesian sequence. And wear and tear on the bone from the marine climate could have affected carbon-dating results, the researchers report.

Smithsonian Institution archaeologist Bruce Smith, who was not involved in either study, says the new results demonstrate the importance of replicating studies. "This shows that science works," he says.

EDITED BY YUDHIJIT BHATTACHARJEE

Celebrities

SWINGING WITH MATH. In a television ad for the Mickelson ExxonMobil Teachers Academy, the world's second-ranked golfer tees off as equations dance in the foreground. Last week, Phil Mickelson told Congress why the link between math and his game isn't that far-fetched.

"I use statistics to maximize my practice," explained Mickelson, who, with his wife, Amy, stole the show from the rest of an eight-member panel testifying before the House Education and Labor Committee on industry-backed efforts to improve science and math education. "I do a drill with 3-foot putts. And I can make 100% of them. But at 4 feet, it's 88%, at 5 feet 78%, and at 6 feet, it's only 65%. So while I may not be wasting my time trying to add 20 yards to my drives, what I really need to do is hit my chip shots within 3 feet of the hole. That's the best way to lower my score."

Mickelson donates his time, money, and name to the academy, which in the past 3 years has trained 1400 teachers from grades three to five in 1-week summer sessions. "A lot of the teachers don't know who he is," admits Truman Bell, who manages the teachers' academies for the foundation. "But once they meet Phil and Amy, they realize how sincere they are about improving science and math education."

MOVERS

HOT SEAT. Stewart Prager says his new job is "an adventure at a time [in life] when it's great to have an adventure." The 59-year-old plasma physicist is leaving the University of Wisconsin, Madison, this fall after 31 years to become director of the Princeton Plasma Physics Laboratory (PPPL), a Department of Energy (DOE) facility that Princeton University has managed since 1951.

The lab is still coping with DOE's decision in May to pull the plug on one of two major fusion physics projects: the incomplete and over budget National Compact Stellarator Experiment. Prager hopes to help the facility recover from that setback by focusing on the ongoing National Spherical Tokamak Experiment—another fusion project—and pursuing a variety of experiments of different sizes not just in fusion but in plasma physics more broadly.

Prager currently leads Wisconsin's fusion physics experiment, the Madison Symmetric Torus, and his work ranges from the science of fusion reactors to astrophysics. Prager's "broad scientific vision" should benefit PPPL, says Richard Hazeltine of the University of Texas, Austin. However, Hazeltine says, Prager will have to fix some "morale issues" at the lab: "There is a cadre of engineers at PPPL who have come up with a series of wonderful ideas, and none of them has been built." Prager says the best way to improve morale is to keep producing ideas for great experiments large and small.

Robert Strain has been named the new director of NASA's Goddard Space Flight Center in Greenbelt, Maryland. Strain has led the space department at the Johns Hopkins University Applied Physics Lab in Laurel, Maryland, since 2006 and has worked as a manager for the defense and space industries for more than 25 years. He succeeds Edward Weiler, who was appointed associate administrator for NASA's Science Mission Directorate in May.

IN THE COURTS

NO SIMPLE ANSWER. A biologist is suing a California community college for improperly firing her based on a student's complaint about how she answered a question on the heritability of homosexuality. In the 16 July lawsuit filed in a California district court, June Sheldon claims that San José City College (SJCC) violated her academic freedom and asks to be reinstated as an adjunct faculty member.

Sheldon was released from her position in February after the university said its investigation upheld a complaint filed by a student about comments Sheldon made during a 2007 summer course she taught on human heredity. According to the complaint, Sheldon cited a German researcher's work showing that pregnant mice under stress were more likely to have gay male offspring and, the student alleges, stated that "there are hardly any gay men in the Middle East because the women are treated very nicely." When asked what causes homosexuality in women, the complaint said, "Professor Sheldon promptly replied that there aren't any real lesbians."

Sheldon's attorney, David Hacker of the Alliance Defense Fund in Folsom, California, told *Science* that Sheldon denies making the two latter statements, though she acknowledges that she did note work by the German researcher, Gunter Dörner. "She is contesting what the student claimed in the complaint," says Hacker. Neither Sheldon nor SJCC is commenting on the lawsuit.

Got a tip for this page? E-mail people@aaas.org

Two Cultures >>

A collection of new paintings by New York City–based artist **Jonathan Feldschuh** provides an abstract impression of subatomic particles being smashed together inside the Large Hadron Collider, the 27-km-long CERN accelerator that is expected to go online later this summer. Feldschuh has an undergraduate degree in physics. The works depict splatterings on detectors and other instruments inside the accelerator, as if paint had collided with its surface and left a mark. This painting is part of an exhibit at the Galerie Vernon and Vernon Projekt in Prague and can also be viewed at www.jonathanfeldschuh.com.

CREDITS (TOP TO BOTTOM): JOHN HARRINGTON; PPPL; JONATHAN FELDSCHUH

Q&A with Argentina's science minister
622

Science and the Olympics
624

CHEMISTRY

New Catalyst Marks Major Step in The March Toward Hydrogen Fuel

Climate change concerns, high gas prices, and a good deal of international friction would fade if scientists could learn a trick every houseplant knows: how to absorb sunlight and store its energy in chemical bonds. What's needed are catalysts capable of taking electricity and using it to split water to generate hydrogen gas, a clean fuel. Unfortunately, the catalysts discovered so far work under harsh chemical conditions, and the best ones are made from platinum, a rare and expensive metal.

No more. This week, researchers at the Massachusetts Institute of Technology (MIT) in Cambridge led by chemist Daniel Nocera report online in *Science* a new water-splitting catalyst that works under environmentally friendly conditions (www.sciencemag.org/cgi/content/abstract/1162018). More important, it's made from cobalt and phosphorus, fairly cheap and abundant elements. The new catalyst needs improvements before it can solve the world's energy problems, but several outside researchers say it's a crucial development.

"This is a great result," says John Turner, an electrochemist and water-splitting expert at the National Renewable Energy Laboratory in Golden, Colorado. Thomas Moore, a chemist at Arizona State University in Tempe, goes further. "It's a big-to-giant step" in the direction of powering industrial societies with renewable fuels, he says. "I'd say it's a breakthrough." Meanwhile, on pages 671 and 676, other groups report related advances—a cheap plastic fuel cell catalyst that converts hydrogen to electricity, and a solid oxide fuel cell catalyst that operates at lower temperatures—that affect another vital component of any future solar hydrogen system.

English chemists first used electricity to split water more than 200 years ago. The reaction requires two separate catalytic steps. The first, the positively charged electrode, or anode, swipes electrons from hydrogen atoms in water molecules. The result is that protons (hydrogen atoms minus their electrons) break away from their oxygen atoms. The anode catalyst then grabs two oxygen atoms and welds them together to make O_2. Meanwhile, the free protons drift through the solution to the negatively charged electrode, or cathode, where they hook up with electrons to make molecular hydrogen (H_2).

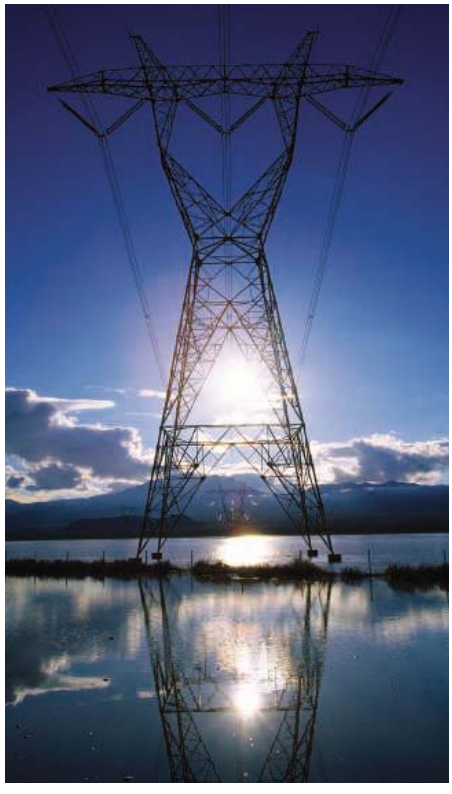

Water power. Cobalt-phosphorus catalyst opens the way to using sunlight to extract hydrogen from water.

The hard part is finding catalysts that can orchestrate this dance of electrons and protons. The anode, which links oxygens together, has been a particularly difficult challenge. Platinum works but is too expensive and rare to be viable on an industrial scale. "If we are going to use solar energy in a direct conversion process, we need to cover large areas," Turner says. "That makes a low-cost catalyst a must." Other metals and metal oxides can do the job but not at a neutral pH—another key to keeping costs down. In 2004, Nocera's team reported in the *Journal of the American Chemical Society* a cobalt-based catalyst that did the reverse reaction, catalyzing the production of water from O_2, protons, and electrons. "That told us cobalt could manage multielectron and proton-coupled reactions," Nocera says.

Unfortunately, cobalt is useless as a standalone water-splitting anode because it dissolves in water. Nocera and his Ph.D. student Matthew Kanan knew they couldn't get over this hurdle. So they went around it instead. For their anode, they started with a stable electrode material known as indium tin oxide (ITO). They then placed their anode in a beaker of water, which they spiked with cobalt (Co^{2+}) and potassium phosphate. When they flipped on the current, this created a positive charge in the ITO. Kanan and Nocera believe this initially pulls electrons from the Co^{2+}, turning it first to Co^{3+}, which pairs up with negatively charged phosphate ions and precipitates out of solution, forming a film of rocklike cobalt phosphate atop the ITO. Another electron is yanked from the Co^{3+} in the film to make Co^{4+}, although the mechanism has not yet been nailed down. The film forms the critical water-splitting catalyst. As it does so, it swipes electrons from hydrogen atoms in water and then grabs hold of lone oxygen atoms and welds them together. In the process, the Co^{4+} returns to Co^{2+} and again dissolves into the water, and the cycle is repeated.

The catalyst isn't perfect. It still requires excess electricity to start the water-splitting reaction, energy that isn't recovered and stored in the fuel. And for now, the catalyst can accept only low levels of electrical current. Nocera says he's hopeful that both problems can be solved, and because the catalysts are so easy to make, he expects progress will be swift. Further work is also needed to reduce the cost of cathodes and to link the electrodes to solar cells to provide clean electricity. A final big push will be to see if the catalyst or others like it can operate in seawater. If so, future societies could use sunlight to generate hydrogen from seawater and then pipe it to large banks of fuel cells on shore that could convert it into electricity and fresh water, thereby using the sun and oceans to fill two of the world's greatest needs.

–ROBERT F. SERVICE

CREDIT: JOSEPH SOHM/VISIONS OF AMERICA/CORBIS

China's environmental challenges
628

RISK ASSESSMENT

Regulators Seek to Redefine 'Working Life'

Figuring out if millions of American workers are at risk from on-the-job exposure to hazardous chemicals has long been a thorny scientific problem. Last week, it became a prickly political issue too. Two senior Democrats in Congress demanded that the Bush Administration kill a proposal to change how the Department of Labor conducts the risk assessments that underpin worker safety regulations. Senator Edward Kennedy (D–MA) and Representative George Miller (D–CA), who lead Congress's labor committees, charged that a leaked draft of the proposal shows that the Administration is rushing to "slip through a rule that may have profound negative impacts on worker safety" before leaving office in January.

Labor Department officials reject the charge, saying that the changes they're proposing—including one that could reduce a worker's estimated exposure to dangerous substances—are designed to make risk assessments more "consistent, reliable, and transparent." And they say that if the new guidelines move forward, there will be plenty of time to hash out scientific issues.

Critics are skeptical. "There certainly could be an interesting and worthwhile debate about the technical assumptions that go into risk assessment, but you don't do that by shoving new guidelines out at the last minute," says David Michaels, an epidemiologist and worker safety advocate at George Washington University in Washington, D.C.

The Administration had not publicly released the proposal as *Science* went to press. But the draft leaked to *The Washington Post* calls for several changes in how two agencies, the Occupational Safety and Health Administration (OSHA) and the Mine Safety and Health Administration, approach risk assessments. One is bureaucratic: It would require the agencies to do more to notify the public—a move critics claim is designed to entangle new rules in red tape.

Another more controversial section calls for altering how regulators calculate a key risk measure called "working life." Currently, in most cases the agencies assume that a person works for 45 years (from age 20 to 65) and use that span to calculate potential total exposure to hazardous substances. From that, they estimate how many workers might get sick or die.

But that approach likely overstates risks, the draft says, because few workers stay in the same job for 45 years. To back that view, it includes statistics showing that less than 5% of American workers stay with the same employer for even 35 years. "Thus, the actual exposure of the overwhelming majority of workers will likely be substantially less" than current methods estimate, according to the proposal. Instead, it calls for basing assessments on studies of how long workers actually work each day, and how long they stay in the same industry.

That may not be a bad idea—but it's not good enough to dump the 45-year assumption, says Adam Finkel, a former OSHA regulator who now teaches at the University of Medicine and Dentistry of New Jersey in Piscataway. For one thing, regulators often don't have the time or money to collect such detailed information—if it actually exists, he says. And just because workers change jobs doesn't necessarily mean that their exposure risks go down, he adds. "Sandblasters who report a change of employer very often remain sandblasters, and are unlikely to become stockbrokers," he wrote in a 2002 paper in the journal *Human and Ecological Risk Assessment*. Finally, he says regulators will always need some yardstick for comparing risks. "The EPA [Environmental Protection Agency] uses 70 years," he notes, "and while you can argue whether 45 years is the right number, it's not a bad one if you want to err on the side of safety."

The proposal also fails to make transparent exactly what "cookbook" the government will follow in developing the assumptions that go into every risk assessment, says toxicologist Joseph Rodricks, head of health sciences at ENVIRON, an Arlington, Virginia–based consulting firm. "To do this correctly, you'd need to lay out all the science and then say how you are going to navigate the maze," he says. "This doesn't."

Even if the new risk rules are adopted, experts point out that they won't be the last word on worker safety regulations. Historically, they say OSHA has loosened the exposure limits suggested by risk assessments if the government decides industry can't afford to meet them or the technology doesn't exist. Finkel says "that's exactly what happened" in developing the only major new workplace rule written by the Bush Administration, which limits exposure to the carcinogen hexavalent chromium produced by welding, electroplating, and other industrial processes. "They looked at the risk assessment number," he says, "and then pretty much ignored it." **–DAVID MALAKOFF**

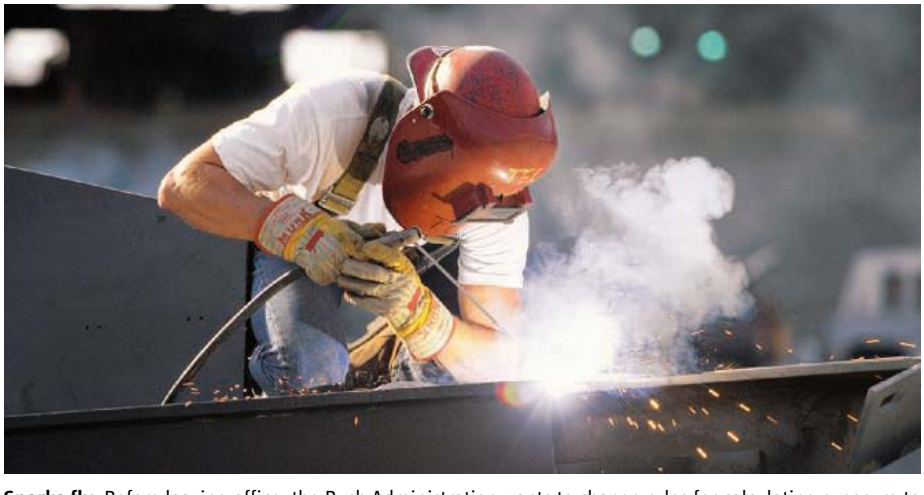

CREDIT: NATALIE FOBES/CORBIS

Sparks fly. Before leaving office, the Bush Administration wants to change rules for calculating exposure to chemicals in the workplace, a key factor in risk calculations that underlie health regulations.

David Malakoff is a science writer living in Alexandria, Virginia.

LINO BARAÑAO INTERVIEW

New Minister Raises Expectations For Science in Argentina

Last December, Argentina created a new ministry of science with an independent budget. The driving force behind this move—the new president, Cristina Fernández de Kirchner—then named cell biologist Lino Barañao, 54, the nation's first science minister. The elevation of science and the promotion of an active researcher are signs that life is looking up for researchers in Argentina 6 years after a devastating currency crash. During that crisis, grants went unpaid and talented researchers fled the country for jobs abroad. Now, a fellowship program designed to encourage young Argentine scientists to come home is celebrating its 400th recruit.

Expectations for science under Barañao are booming. "He's one of us. This is the first time we've had a real scientist reach such a position. We want him to succeed," says University of Buenos Aires (UBA) molecular biologist Alberto Kornblihtt.

Barañao, a faculty member at UBA, served simultaneously until last year as director of the country's main research grant-funding body, the Agencia Nacional de Promoción Científica y Tecnológica. (Another agency, CONICET, pays salaries and stipends.) As newly appointed science chief, Barañao has announced a plan to upgrade and build new research facilities—easing a severe space crunch, scientists say—and has pledged to increase science and technology spending from roughly 0.65% to 1% of gross domestic product for both basic and applied research by 2010. In addition, he supports corporate tax breaks for investing in research and development (R&D). Some researchers say they're hoping that CONICET under the new regime will raise scientists' salaries 20% to 30%. Barañao, though not giving details on possible salary changes, says he plans to target funds for fields with industrial promise, including biotechnology, nanotechnology, and computing.

Indeed, the country's scientific leaders, including Kornblihtt, have long argued that boosting basic science and getting companies in Argentina to invest in research would help build a more independent and stable economy. Barañao himself has worked with industry: He served as an adviser to an Argentine biotech company that created the country's first transgenic cattle in 2002 to make human growth hormone and other therapeutic proteins. That seemed daring at the time, he says, as many university scientists were afraid that an association with industry could hurt their careers.

Barañao shared his thoughts on Argentina's ambitions in a brief interview with *Science* last month.

–JOCELYN KAISER AND ELIOT MARSHALL

On Argentine attitudes

L.B.: We have a strong background in terms of basic science. We are the only Latin American country that has produced three Nobel Prize winners. … Usually, people associate science with a kind of cultural value. Now we have to show that this accumulation of knowledge can lead to an accumulation of wealth.

Luring scientists to industry

L.B.: [Most scientists are government employees.] The average amount they receive is up to $30,000 per year for equipment and supplies. [Under a new university-industry collaborative program], they can receive four times more; they can have more students. … When we opened a call for applicants 2 years ago, we were not very optimistic; we thought it would be difficult to have people from different institutions and different cultures working together. But we received 120 proposals. … So there has been a change in the way people think about this. They know they have to cooperate, … and they have to work with companies.

Targeted investment

L.B.: Technology-based enterprises in Argentina are very small; they do not have significant amounts of money. It is more like Italy than the United States. They see it as the government's role to put money in high-risk development. We have some multinational companies operating in Argentina, but they run most of their R&D out of headquarters. But what we are seeing now is that [multinationals] are considering outsourcing of R&D. Big pharma, for example, … is buying small companies or creating new platforms within the company to produce growth. … One example in Argentina is a company called Delta Biotech that developed a new method for vitamin D production based on funding from our agency. It has been growing at 400% a year, and now investments are coming from all over Europe. The oldest member of this company is 35 years old. That shows the potential for small companies to grow and be competitive.

Living up to expectations

L.B.: My son said to me, "For 4 years, you will be the best minister of science we have ever had." It's a big challenge. … I know the qualities and pitfalls of the scientific community. I'm confident that we will have some concrete results. We won't change everything right away, but to show that we have solved some particular problems, to develop a few successful companies, to have many students enrolled in interdisciplinary programs … will send a signal that changes are occurring.

CREDIT: GREG SCHALER

PALEONTOLOGY

Is Dinosaur 'Soft Tissue' Really Slime?

In 2005, researchers made headlines when they reported that they had found intact blood vessels from a 68-million-year-old *Tyrannosaurus rex*. The discovery raised hopes that paleontologists could get their hands on the flesh and blood of vanished animals. This week, however, other scientists challenged the results, arguing that the dinosaur flesh was in fact just coatings of young bacteria. But the original researchers stand by their results, calling the new argument weak. "There really isn't a lot new here," says Mary Schweitzer of North Carolina State University in Raleigh.

In 2003, a crew led by Jack Horner of the Museum of the Rockies in Bozeman, Montana, dug up an exquisitely preserved *T. rex* fossil. Schweitzer dissolved a fragment in weak acid. With the bone gone, transparent vessels were left behind (*Science*, 25 March 2005, p. 1852). Other fossils yielded branched tubes, spheres that resembled blood cells, and what appeared to be bone-forming cells known as osteocytes. Later, Schweitzer and colleagues isolated what they identified as collagen proteins from the *T. rex* and from a mastodon fossil. The sequence of amino acids in the mastodon collagen was closest to that of elephants; the *T. rex* collagen was most similar to that of birds, its closest living relatives.

These results inspired Thomas Kaye, a research associate at the Burke Museum of Natural History and Culture in Seattle, Washington, to look for soft tissue. He set out to use scanning electron microscopes to find it without having to dissolve the fossils first. "I thought, 'We'll just crack the bones open and take a look,' " he says.

The researchers selected a well-preserved turtle fossil and quickly found cell-like balls that turned out to be located in tubes. "We actually did a happy dance," he said.

But the happiness turned to suspicion when Kaye kept finding the spheres in other fossils, even in badly degraded ones. "It was clear they weren't blood cells," he says. He and his colleagues suspect that the balls are geological formations called framboids.

Schweitzer's tubes and osteocytes, they argue, are not blood vessels or cells but biofilms formed by bacteria that invaded the fossils after death. In a paper published Monday in the journal *PLoS ONE*, Kaye and colleagues report that carbon dating of one sample shows that the tubes are at most a few decades old and that their infrared spectra give a closer match to bacterial biofilms than to collagen. Troughs in the walls of the tubes resemble the track a microbe would make crawling through a biofilm, they note. "We think that's one of the smoking guns," Kaye says.

"This piece of work demonstrates just how careful we have to be when attempting to analyze fossil bones for traces of original molecules or biomarker molecules," says David Martill of the University of Portsmouth, U.K., a paleobiologist not involved in either study. Other researchers are less impressed. "There are a number of misinterpretations and lack of basic data in this paper," says Frances Westall, the director of the Centre de Biophysique Moléculaire–CNRS in Orléans, France.

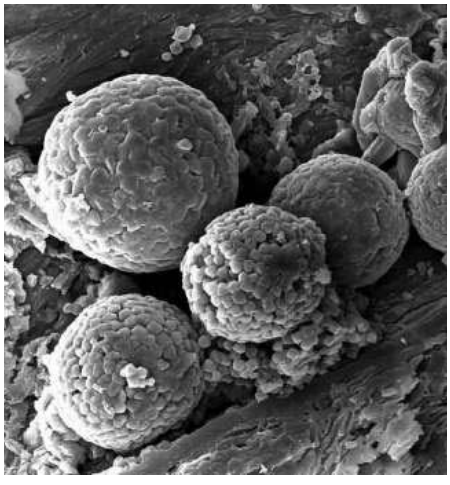

Cell-out? Researchers mistook "framboids" in dinosaur fossils for corpuscles, a new paper contends.

CREDIT: T. G. KAYE *ET AL.*, *PLOS* 3, 7 (JULY 2008)

Schweitzer says she welcomes skepticism but that Kaye and his team "only address aspects of our study that fit conveniently with their preconceived ideas." They did not explain how proteins from a bacterial biofilm could be similar to bird or elephant proteins, for example. "They pick and choose what to focus on," Schweitzer says, arguing that a rebuttal of her work must account for all of her evidence. She also doubts that bacteria could have formed the tubes.

Martill, however, thinks that the tubes might well be biofilms. He says his own experience shows how aggressively bacteria and fungi can invade fossils. Still, he considers Schweitzer's research "incredibly impressive" and believes that at least some of the dinosaur material is genuine collagen. "This is why we should not abandon hope," he says.

–CARL ZIMMER

Carl Zimmer is the author of *Microcosm: E. coli and the New Science of Life.*

Space Program Shakeup

The Italian Space Agency (ASI) has been thrown into turmoil by a wave of resignations and the appointment on 18 July of interim "commissioners" to its administrative council, says physicist Giovanni Bignami, ASI's president. He expects that the center-right government of Silvio Berlusconi may also dismiss him.

The resignation of six of seven administrative council members (Bignami being the eighth and chair) prompted the government to put Enrico Saggese, senior vice president for space operations of aerospace and defense company Finmeccanica, and University of Padua astronomer Piero Benvenuti in charge. As *Science* went to press, Bignami was still ASI's president but said the government may dismiss him after a Cabinet meeting on 8 August, if not before.

A spokesperson for Italy's education and research ministry said that the decision to appoint the commissioners was due entirely to "technical and administrative reasons."

–EDWIN CARTLIDGE

WikiPathways Debuts

The makers of GenMAPP, the popular online genetic data hub, have launched a site for sharing findings on metabolic pathways. Modeled after Wikipedia, WikiPathways (wikipathways.org) offers a way to integrate information on these complex networks, says creator and cell biologist Bruce Conklin of the University of California, San Francisco, who last week formally opened the project with colleagues at the University of Maastricht in the Netherlands. The site has more than 300 registered users and contains information on 500 metabolic pathways in seven species, including humans.

–RACHEL ZELKOWITZ

Warning on ITER

The "uncertain U.S. commitment to ITER," the key to fusion energy's future, is a matter of the "greatest concern," says a 29 July report from the National Academy of Sciences (NAS). Congress axed a proposed 2008 U.S. contribution of $149 million for the project, which begins construction this year. The NAS panel concluded that "fluctuations in the U.S. commitment to ITER will undoubtedly have a large negative impact." Stephen Dean of the Gaithersburg, Maryland–based advocacy group Fusion Power Associates grasped at a straw in the fact that "the academies think the project is important," which might sway Congress.

–DANIEL CLERY

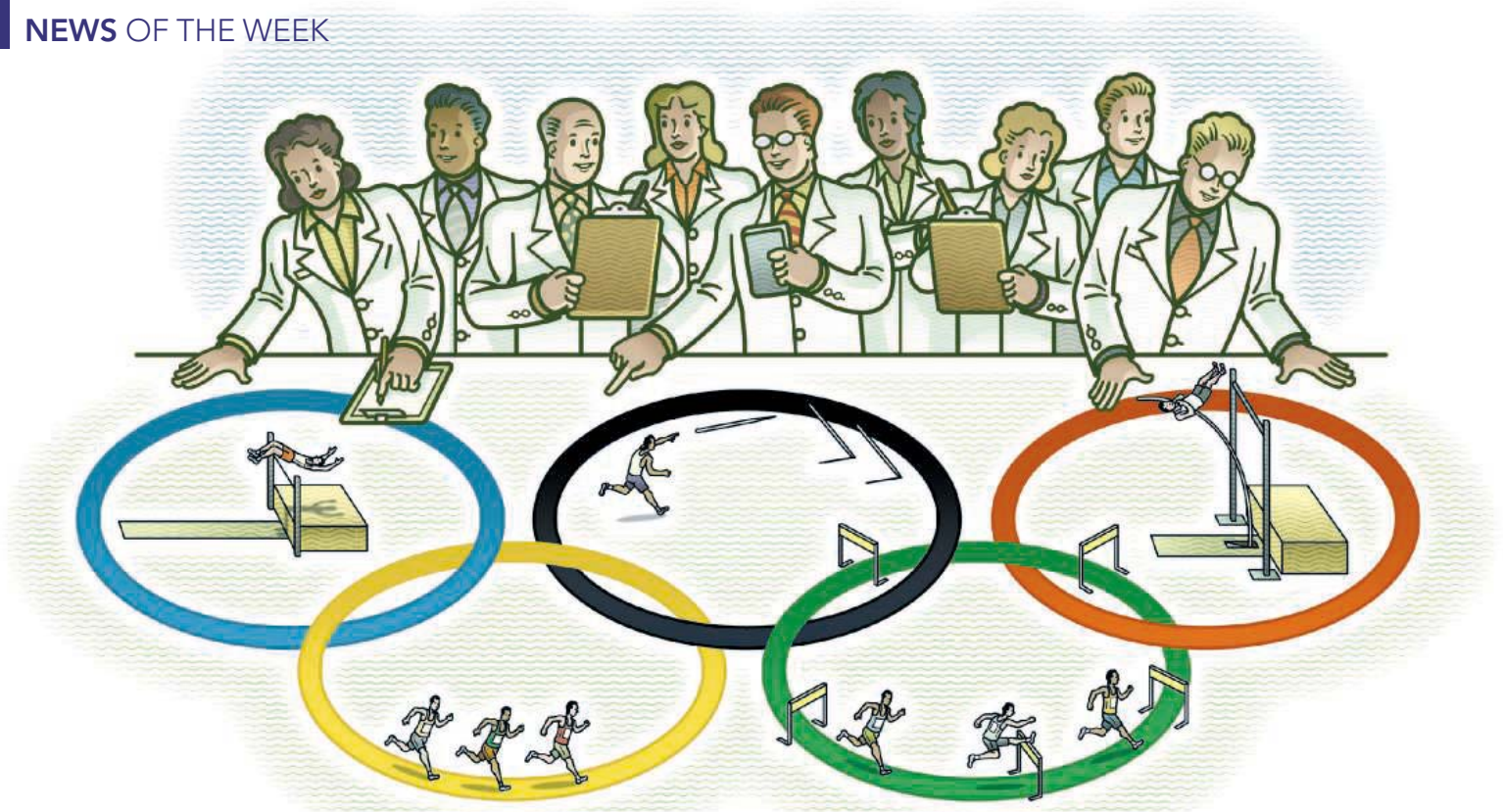

Science at the Olympics

Neuroimaging, high-tech materials, new asthma meds, detection-eluding drugs, thermoregulation—will all these make athletes stronger and faster at the 2008 Summer Games in Beijing? *Science* investigates

1 Will Beijing's Dirty Air Hurt Performance?

Will performance suffer if athletes hit a wall of hot, polluted air in Beijing? Probably, say experts, although there may be some surprising twists.

Among those chasing medals, perhaps the biggest fear is a pollution-induced asthma attack in someone who isn't normally asthmatic. On the other hand, some speculate that asthmatics—who take medicine as a precaution against pollution and other triggers—might actually have an advantage during a bad air day.

GASPING FOR AIR Former U.K. gold medalist Steve Ovett collapsed from asthma after an 800-meter race in the 1984 Los Angeles games. He finished fourth, spent 2 days in hospital, and blamed pollution.

Asthma is more common among elite athletes than in the general population, especially in endurance sports. Common symptoms—wheezing and shortness of breath—afflict perhaps up to 20% of elite athletes, because they spend so much time training outside. (Swimmers suffer from breathing air with chlorine.) Moreover, acute asthma attacks called exercise-induced bronchoconstriction (EIB) strike widely: up to 33% of swimmers, for example, even those without chronic asthma.

Precautions. A masked runner in an April 2008 long-distance race in Beijing.

The attacks happen because top athletes breathe in more than 150 liters of air per minute—through their mouths rather than their noses. "You can't pull out the pollen and the particulate matter, and they go directly into the lungs," says Timothy Craig of Pennsylvania State University College of Medicine in Hershey. By the time the air reaches the airways, it is also irritatingly dry. In response, the airway membranes inflame, muscles tighten, and mucus accumulates—all quickly constricting the passageways in the lungs and making it hard to breathe.

EIB is impossible to prevent entirely, but inhaled corticosteroids and β_2 agonists can help. The International Olympic Committee (IOC) allows these drugs, given medical proof of asthma. Using the drugs could potentially give medicated asthmatics an advantage over other athletes in terms of averting an attack, says Kenneth Rundell, a physiologist at Marywood University in Scranton, Pennsylvania. Recently, however, the U.S. Food and Drug Administration approved another asthma drug, montelukast sodium, for preventing EIB. Because it is not known to enhance performance, the

CREDITS: ILLUSTRATIONS BY PETER AND MARIA HOEY; FREDERIC J. BROWN/AFP/GETTY IMAGES

IOC hasn't banned it and any athlete can take it.

Aside from the risk of EIB, little is known about the subtler impact of pollution on athletic performance. One exception is a study of 15 college ice-hockey players who didn't have asthma. Rundell asked them to pedal an exercise bike as hard as they could for 6 minutes. Compared with breathing clean air, total power output fell roughly 5% when the athletes breathed soot particles in concentrations similar to air near a busy highway. Rundell thinks the power loss, reported in the January issue of the *Journal of Strength and Conditioning Research*, is due to inflammation driven by pollution. In another study, published in *Inhalation Toxicology* in 2005, Rundell showed that montelukast sodium guards against pollution-induced EIB: "Where the pollution is very high, one could probably benefit quite a bit."

National teams have prepared for Beijing by screening athletes for asthma to get IOC permission for restricted drugs. And to reduce the amount of time athletes spend breathing polluted air, some teams will arrive in Beijing just before an event. The USOC even designed carbon-filter masks that its athletes can wear.

The IOC, in turn, may reschedule endurance events if the air quality is bad. But IOC officials note that in test events conducted last August in Beijing, there were no complaints from national teams about the polluted air. A look back at the 1984 Olympics, in smoggy Los Angeles, suggests they may have a point: 67 asthmatic members of the U.S. team won a total of 41 medals.

Even so, Olympic officials have conceded that pollution may mean that fewer world records are broken in Beijing than in past Olympics. **–ERIK STOKSTAD**

WHAT'S AGE GOT TO DO WITH IT?
Medalists span the decades

11 Italy's Luigina Giavotti, 11, won silver in gymnastics in 1928.

13 Marjorie Gestring, 13, of the U.S. won gold in diving in 1936—the youngest gold medalist ever.

14 Hungarian swimmer Krisztina Egerszegi, 14, won gold in 1988.

15 U.S. runner Pearl Jones, 15, won gold in the 4 x 100-m relay in 1952.

33 U.S. swimmer Dara Torres, 33, won two gold and three bronze medals in 2000. Now 41, she is swimming in Beijing.

34 U.K. sprinter Kelly Holmes, 34, won gold in the 800- and 1500-m events in 2004.

46 Ethel Seymour, 46, won a bronze medal on Great Britain's gymnastics team in 1928.

59 Bill Northam of Australia, 59, won gold in yachting in 1964.

72 Swedish shooter Oscar Swahn, 72, won silver in the team double-shot running deer event in 1920.

2 Can Ice Vests Provide a Competitive Chill?

At the 2004 Athens games, 30 minutes before the women's marathon, Deena Kastor of the United States began her "warm-up." Instead of jogging in the 35°C heat, she donned an ice-filled vest, sat down, and waited for the start of the 42.2-kilometer run. More than 2 hours later, staying cool seemed to pay off. A kilometer from the finish, Kastor pulled into third place to secure a bronze medal. "The vest definitely helps performance because I am delaying the point in the race in which I overheat," says Kastor, who will race in Beijing.

The logic seems unimpeachable. As body temperature climbs to 40°C, strength and endurance evaporate. So cooling off before competition should enable an athlete to push harder and longer. Runners, rowers, cyclists, and others are already using ice vests. But how much does "precooling" help, and for which events? "It definitely lowers body temperature," says Iain Hunter, an exercise scientist at Brigham Young University (BYU) in Provo, Utah. "The question is, does it improve performance? And that's a lot less clear."

Since the 1970s, numerous studies have shown that precooling can dramatically affect some measures of athletic output. A 1995 study of 14 male runners found that if they were first chilled for 30 minutes in a chamber at 5°C, they could run on a treadmill at a certain level of exertion for an average of 26.4 minutes, a whopping 3.8 minutes longer than they averaged otherwise.

Olympic events are typically races over fixed distances, however, and the few studies of race times show much smaller improvements. In 2005, BYU's Hunter and colleagues studied 18 female cross-country runners, who had ingested encapsulated thermometers, as they participated in 4- and 5-kilometer races. Some wore ice vests for an hour before their race, and, on average, their core body temperatures were half a degree lower than those who did not, even at the ends of the races. But the researchers found only an insignificant difference of a few seconds in the two groups' average times.

Similarly, Kirk Cureton and colleagues at the University of Georgia, Athens, put nine male and eight female runners through simulated 5-kilometer races on treadmills. When the runners wore ice vests during a 38-minute warm-up of jogging and stretching, they finished the time trial 13 seconds faster on average than when they warmed up without them. That was a 57-meter lead over their warmer selves, and "even if it was 10 meters it would be important," Cureton says.

But Cureton and colleagues found that temperature differences vanished by race's end, suggesting that precooling is less valuable for long races like the marathon. It likely helps for races lasting between a minute and an hour, Cureton says. It definitely hurts in sprint events.

How it works is a mystery. When the skin is cool, less blood flows to it to carry away heat, leaving more to course through the muscles. Precooling may also change the input from the body's heat sensors to the brain, which regulates pacing, enabling the athlete to push harder, says Rob Duffield, an exercise physiologist at Charles Sturt University in Bathurst, Australia.

This much is certain: Using an ice vest won't make an athlete unbeatable. Paula Radcliffe of the United Kingdom, the world record holder for the women's marathon, wore one before the Athens race. She overheated and dropped out 6 kilometers from the finish. **–ADRIAN CHO**

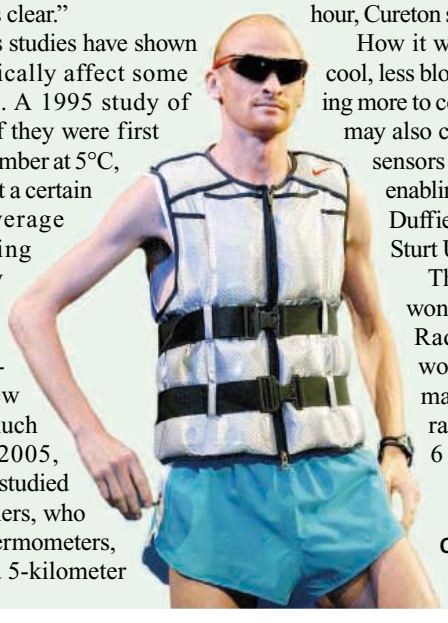

Chilled. Australian Olympic marathoner Lee Troop models an ice vest, 2004.

CREDIT: AP PHOTO/ROB GRIFFITH; SOURCES INCLUDE: OFFICIAL OLYMPICS WEB SITE, SPORTS REFERENCE, MENZIESERA.COM, GYMNASTICS ZONE

3 Do New Materials Make the Athlete?

NAKED TRUTH

Swimming goggles were first allowed in 1976.

Some of the first known spiked track shoes were invented by Joseph William Foster in the early 1890s.

Greek athletes usually competed nude. According to one ancient writer, Pausanias, a competitor deliberately lost his shorts so that he could run more freely during the race in 720 B.C.E., and clothing was then abolished. Other explanations abound.

In 1960, Ethiopian marathoner Abebe Bikila earned an Olympic gold medal without wearing any shoes. But bare feet on the Olympic track these days are passé, as athletes slip into ever more high-tech gear. Shoes, swimsuits, and clothing are getting lighter and stronger, adhering like glue to athletes' bodies and moving more fluidly through air and water.

In Beijing, U.S. track and field athletes will be wearing Nike shoes and clothing that incorporate threads made of Vectran, a superstrong liquid crystal polymer that withstands high temperatures. The result, according to Nike, is lighter, stiffer shoes to reduce friction and clothes that reduce drag by 7% compared with the Nike outfits worn at the 2004 games in Athens.

Sprinters will also benefit from even tighter compression garments. In theory, these improve performance because of proprioception, that unconscious ability that enables you to pinpoint your nose when your eyes are closed. Physiologist Russ Tucker of the University of Cape Town, South Africa, says that because runners need to contract muscles precisely—at the proper angle, velocity, and time—tight-fitting garments help the brain identify where in space the limb is poised so they know when to activate the muscle.

In the water, the Speedo LZR Racer suit, which debuted in March 2008, is all the buzz. Swimmers donning the suit have broken 46 world records so far. The suit includes polyurethane panels placed strategically around parts of the torso, abdomen, and lower back that experience high amounts of drag in the pool. It also incorporates a corset-like structure that keeps the body in a streamlined position. Raúl Arellano, a biomechanist at the University of Granada, Spain, says the LZR Racer suit could benefit older athletes like 41-year-old Dara Torres of the United States, especially in areas where fat tends to accumulate.

Some of the technologies needed to develop the suit "didn't really exist 10 years ago," says Jason Rance, head of Aqualab in Nottingham, U.K., the division of Speedo that designed the suit. Those include ultrasonic welding that eliminated the need for seams, and technology that allowed parts of the suit to be finely sanded and a water-repellent substance added to prevent water from leaking in.

But the suit has raised eyebrows. "Who's going to win the gold medal, the swimmer or the technician?" asks Huub Toussaint, a biomechanist at the Free University in Amsterdam, who worries that the suit gives swimmers an unfair edge, although the international body governing the sport approved it.

For all the hype surrounding space-age shoes and clothing, there's a flip side: Any boost to performance could just be psychological. South Africa's Tucker, who races for fun, says the compression garments make him feel powerful and secure. Such a superhero aura might give any competitor a mental edge. "It doesn't really matter if the advantages are physically real or not," he says, "as long as the athlete gets some benefit."

–ANDREA LU

4 Can Neuroscience Provide a Mental Edge?

For Olympic athletes, physical strength, speed, and stamina are a given. But when elite competitors go head to head, it can be the mind as much as the muscles that determines who wins. A collaboration between sports psychologists and cognitive neuroscientists is trying to figure out what gives successful athletes their mental edge.

Positive thinking. Canadian swimmer Brittany Reimer.

CREDIT: JERRY LAMPEN/REUTERS/CORBIS

One focus is why some athletes rebound better than others after a poor performance. Even at the Olympic level, it's not uncommon for an athlete to blow a race early in a meet and then blow the rest of the meet, says Hap Davis, the team psychologist for the Canadian national swim team. To investigate why—and what might be done about it—Davis teamed up with neuroscientists including Mario Liotti at Simon Fraser University in Burnaby, Canada, and Helen Mayberg at Emory University in Atlanta, Georgia.

The researchers used functional magnetic resonance imaging (fMRI) to monitor brain activity in 11 swimmers who'd failed to make the 2004 Canadian Olympic team and three who made the team but performed poorly. The researchers compared brain activity elicited by two video clips: one of the swimmer's own failed race and a control clip featuring a different swimmer. Watching their own poor performance sparked activity in emotional centers in the brain similar to that seen in some studies of depression, the researchers reported in June in *Brain Imaging and Behavior*. Perhaps more tellingly, the researchers found reduced activity in regions of the cerebral cortex essential for planning movements. Davis speculates that the negative emotions stirred up by reliving the defeat may affect subsequent performances by inhibiting the motor cortex.

Davis and neuroscientist Dae-Shik Kim at Boston University (BU) School of Medicine are now using diffusion tensor imaging to visualize the connections between emotion and motor-planning brain regions. Kim hypothesizes

5 Does Doping Work?

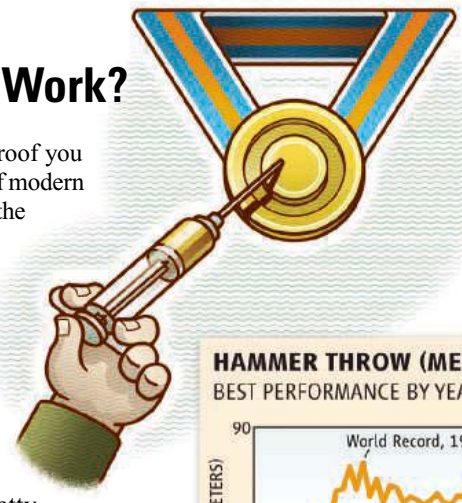

It depends on how much proof you want. By the tough standards of modern medicine, there's little hard evidence for the efficacy of dozens of compounds on the list of the World Anti-Doping Agency (WADA). They are rarely tested in placebo-controlled trials; for most, the evidence is what medical researchers would call "anecdotal."

Many substances on the list are probably useless, most researchers say, if not outright detrimental for athletic prowess. "The science behind it is pretty weak," concedes Swedish oncologist Arne Ljungqvist, a former Olympic high jumper who chairs WADA's Health, Medical & Research Committee.

Not that we don't know anything about what works. Decades ago, double-blind trials for amphetamines and other stimulants showed that they can enhance performance in short, explosive activities, such as sprinting. Anabolic steroids have been proved beyond any doubt to increase muscle mass and enhance performance among male athletes in sports that require strength, such as weightlifting and shot-putting; in women, they appear to work for endurance sports as well. History provides more circumstantial evidence: In many sports, the amazing rise in performances came to a halt after the crackdown on anabolic steroids began in earnest in the 1980s, and some records have not been broken since then.

But for many other compounds the evidence is thin, says Harm Kuipers, a physician and former speed-skating world champion who studies doping at Maastricht University in the Netherlands. One of the hottest substances of the moment, erythropoietin (EPO), has been tested for performance enhancement in only four double-blind trials, Kuipers says; they showed that it increased maximum oxygen uptake and performance, but apparently for short durations only.

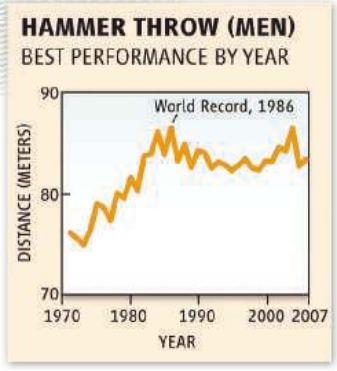

Data are lacking because rigorous trials are expensive, and there's little incentive to fund them. The drugs' target population, top athletes, usually can't be recruited into studies because it might ruin their careers. Also, the list of substances and combinations is endless; cyclists once used a cocktail of strychnine, cognac, and cocaine, for instance. And the risk of side effects can make ethics panels frown.

Still, some say WADA should promote more efficacy studies. The agency is currently spending millions of dollars to improve detection of human growth hormone, a banned substance that appears to be very popular and is very hard to detect. Yet, the "science on efficacy is really soft," says Donald Catlin, who until 2007 led a major antidoping lab at the University of California, Los Angeles. "I'd prefer to have true evidence before we go after it."

If WADA, created in 1999, had a more scientific attitude, it would drop many drugs from the list, which it inherited from the International Olympic Committee, says Kuipers, who sat on the panel for several years. Countless substances—such as beta-agonists, corticosteroids, and narcotics—are listed simply because athletes used them, or were rumored to use them, even though they are widely believed to be useless.

A spot on the list may actually encourage athletes to experiment with a substance, Kuipers says: "The doping list is a shopping list for some." Such experiments can be dangerous. In healthy people, for instance, an overdose of insulin—another listed substance that few believe does athletes any good—can lead to a fatal drop in blood sugar levels.

Ljungqvist takes the opposite view: Removing substances from the list would signal that it's okay to use them, he says. And WADA wants to protect athletes from any drug they don't need, if only to send a message to their young fans. Ljungqvist agrees that this means that practically anything can end up on WADA's list—and that athletes risk ending their careers by taking something that doesn't bring them one bit closer to a gold medal.

–MARTIN ENSERINK

Early player. British tennis Olympian Charlotte Sterry, 1908.

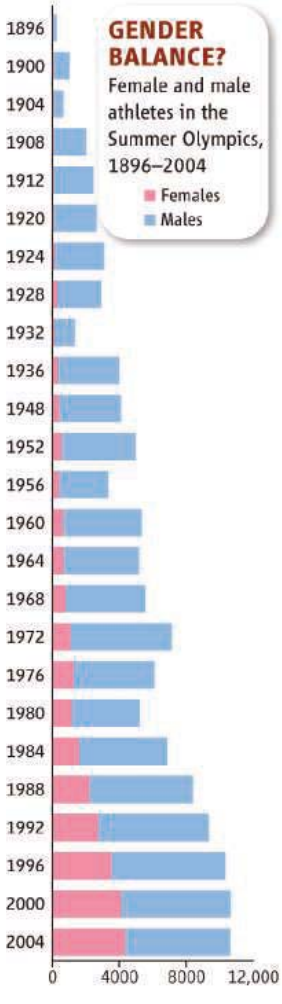

that these connections might differ in athletes who are better able to shake off a bad performance. So far his team has scanned about a dozen BU athletes. Meanwhile, Davis and collaborators have been looking for interventions that would perk up the motor cortex. Additional fMRI studies, as yet unpublished, suggest that positive imagery—imagining swimming a better race, for example—boosts motor cortex activity, even when athletes see a videotaped failure. Jumping exercises have a similar effect, Davis says.

The work has already changed the Canadian team's poolside strategy, he says: "We pick up on [any negativity] right away and intervene." Davis has the swimmers review a video of a bad performance within half an hour and think about how they would fix it. Anecdotally, it seems to be working, he says. "We're seeing more people turn it around."

The fMRI findings suggest that quick, positive intervention helps athletes bounce back, says Leonard Zaichkowsky, a sports psychologist at BU who collaborates with Davis and Kim. But coaches often take a different approach with athletes. "Typically what happens is they've got hard-assed coaches reaming them out for a bad performance," he says. "It's the opposite of what they should be doing."

–GREG MILLER

Three Gorges Dam: Into the Unknown

A marvel of engineering, the Three Gorges Dam will start operating at full capacity later this year. Already under way is an epic experiment on how a dam impacts the environment

YICHANG, CHINA—For millions of people along the Yangtze River, the turbid waters of Asia's longest river have long provided an abundance of fish, including one kind that locals are especially fond of: carp. But Yangtze fisheries are harvesting less than half the carp they were 5 years ago. Thanks in no small measure to the completion of the Three Gorges Dam, the world's biggest dam, the outlook for the prized fish is grim.

The Yangtze's four major carp species—bighead, black, grass, and silver—spawn when water levels rise during the summer monsoon rains. "They need this stimulation," says Liu Huanzhang, an ecologist at the Institute of Hydrobiology (IHB) of the Chinese Academy of Sciences (CAS) in Wuhan. Three Gorges reservoir, a 660-kilometer-long serpentine lake that began to fill in 2003, has subtly altered seasonal variations in water levels below the dam. Recent IHB surveys have found a sharp decline in carp eggs and larvae downstream. "It's a very bad sign," Liu says.

Online
sciencemag.org
Podcast interview with the author of this article.

Carp are not the only Yangtze species on the ropes. Fishers are hauling in anything with fins and gills that they can net or lay hooks on, including the tiniest of fish to feed aquaculture species such as catfish or mandarin fish, IHB has documented. The central government bans fishing on the Yangtze for 3 months each year, during spawning. But with vast stretches of the river in danger of being fished out, one of China's senior ecologists, IHB's Cao Wenxuan, last month made a bold public plea for a 10-year moratorium for the entire Yangtze.

Other troubles sapping the Yangtze's vitality include industrial effluents, raw sewage, and heavy boat traffic. But by greatly altering ecosystems on the Yangtze's middle reaches, the Three Gorges Dam, which operators plan to bring to full capacity by the end of the year, will complicate attempts to prevent a mighty river from becoming inhospitable to some aquatic life forms.

The Three Gorges Dam is one of several huge projects that are transforming China's environment. They include the recent completion of the world's highest railway across the Tibetan Plateau and a plan to divert billions of cubic meters of water each year from the Yangtze and other southern rivers to China's parched north (*Science*, 25 August 2006, p. 1034). But perhaps no endeavor has generated more debate on the economic and environmental tradeoffs of megaprojects than the $25 billion Three Gorges venture in Yichang.

The main justification is flood control. By regulating water flow, the dam is designed to prevent disastrous floods that have occurred every decade or so; the worst in the last century was a flood in 1931 that the government says killed 145,000 people and left 28 million homeless. (Unofficial tallies put the death toll at 3 million people or more.) Also on the plus side, the dam's hydropower station is expected to generate 84.7 billion kilowatt-hours per year of electricity, an amount equal to that produced by burning 50 million tons of coal. And Three Gorges has eased navigation as the rising waters have eliminated treacherous shoals upstream. For these and other reasons, the State Council Three Gorges Project Construction Committee (CTGPC) has hailed the dam as "greatly beneficial" to the environment. According to CTGPC vice director Li Yong'an, "the project has brought more ecological benefit than harm."

But to many critics, Three Gorges is a bête noire. Besides worsening the plight of fish, the dam has fragmented habitats in a

CREDIT: DU HUAJU/XINHUA PRESS/CORBIS

China's Environmental Challenges

China is waging a war on many fronts to stem environmental deterioration while sustaining rapid economic growth. This special report examines three prominent ventures: **1.** the world's largest dam, which is changing the ecology of a vast and fragile watershed (p. 628); **2.** plans to restore the Qinghai-Tibetan Plateau (p. 633); and **3.** Beijing's efforts to clean its notoriously foul air (p. 636).

Pulling out all the stops. Three Gorges is generating loads of electricity—and concern.

biodiversity hot spot, and it could erode inhabited islands in the Yangtze River delta. The impoundment of 39.3 billion cubic meters of water has destabilized slopes, heightening risk in a landslide-prone region, while the sheer weight of all that water has heaped strain on seismic faults. The rising waters have also uprooted more than 1 million people and submerged entire communities. Another 4 million of the 16 million people living in the reservoir area may have to be relocated in coming years, officials revealed last fall.

In China, public debate about the dam's dark side is muted. But for scientists, the myriad effects of Three Gorges are fair game. The government has sanctioned an ambitious program to monitor the Yangtze and the Three Gorges reservoir area, which at 58,000 square kilometers is bigger than Switzerland. "We're studying the changing landscape," says Wu Bingfang, whose team at CAS's Institute of Remote Sensing Applications (IRSA) in Beijing is using satellite imagery to follow how the dam impacts its surroundings. They also intend to estimate how much methane and other greenhouse gases the reservoir area emits as submerged vegetation rots.

"Now that the dam is a reality, I hope we can manage it well," says Niu Wenyuan, chief scientist of China's sustainable development strategy program and a counselor of the State Council. A wealth of data on the Yangtze's fragile condition has been posted to a CTGPC-run Web site, www.tgenviron.org. The findings are expected to guide priorities of a $7.3 billion monitoring and mitigation program over the next 12 years.

"Humanity deserves the opportunity to learn some lessons from this engineering exercise," says Chen Jiquan, a landscape ecologist at the University of Toledo in Ohio. In 2000, Chen led a 12-person delegation from the Society for Conservation Biology to China to assess Three Gorges. The group offered recommendations to a dozen bodies in China and at the United Nations but did not receive a single response. "It was a sad story," says Chen.

Well bred. A female jiangzhu and her two babies at IHB.

CREDIT: COURTESY OF WANG DING

Chinese scientists insist they are open to outside views and determined to confront the colossal project's mixed legacy. "Researchers want to tell the truth," says Wu.

A fading pulse

In the 1930s, engineers identified the picturesque Three Gorges region straddling Hubei and Sichuan provinces as an ideal spot for a dam to dwarf all others. The original idea was to tame the Yangtze's periodic floods, but planning sputtered until the early 1980s, when China's energy needs grew more intense. "They thought this large dam would solve a lot of problems," says Chen. Then-Premier Li Peng, a water engineer by training, pushed hard for Three Gorges, and in 1984 CAS began an environmental impact assessment. After weighing the pros and cons, the 8-year-long review gave Three Gorges the thumbs-up. Construction started in 2003—to the dismay of many scientists. "I felt there were serious problems. My opinion was to wait 20 or 30 years," says Niu.

In May 2006, some 26,000 workers completed a Great Wall for the Yangtze: a concrete

barrier 185 meters tall and 2.3 kilometers long. The reservoir had begun filling 3 years earlier and has risen from its original low water mark of 62 meters to the present 156 meters. By December, engineers expect to have finished installing the last five of 26 hydropower turbines.

For ships to move upstream, they must traverse five locks stacked like a staircase at the dam's northern end that raise craft more than 100 meters. Migratory fish don't have a chance. "There was serious debate about whether to build a passage for fish," says Liu. In the end, he says, authorities abandoned the idea because migratory fish can't pass the Gezhouba Dam spanning the Yangtze just 38 kilometers downstream, and it would have been "impossible" to build a big enough passage for the primary species that would have benefited from it, the Chinese sturgeon (*Acipenser sinensis*).

It turns out, however, that Chinese sturgeon may still have a future on the Yangtze. The ancient species spends much of its life at sea, migrating upriver to spawn. The original sturgeon spawning areas were hundreds of kilometers upstream of Three Gorges. The fish has been blocked from reaching those areas since Gezhouba Dam rose in 1981. But the sturgeon is now observed to spawn downstream of Gezhouba, and fishing for it is banned in China.

Although millions of lab-bred fingerlings have been released into the Yangtze in the past 2 decades, most young sturgeon captured in the Yangtze delta are wild, suggesting that the wild population is coping reasonably well, Liu says. Over the past 3 years, the Yangtze River Fisheries Research Institute in Jingzhou has released sturgeon into the Three Gorges reservoir to see if the fish can thrive exclusively in fresh water. Early results are discouraging, says the institute's Wei Qiwei, because the reservoir ecosystem is changing as the river slows and silt accumulates. "The lake now is not suitable for a benthic feeder," he says. Such upheavals threaten 40 other endemic fish

FEARS OVER WESTERN WATER CRISIS

ÜRÜMQI, CHINA—The Tarim River is the lifeblood of Xinjiang Province, providing more than half the irrigation water for this Alaska-sized region in western China. The largest inland river in Asia, the Tarim is also a green-fringed stockade keeping the vast Takla Makan Desert from advancing northward into rugged grasslands and fertile oases inhabited by the majority of the province's 20 million people. With Xinjiang's fortunes riding on the Tarim, officials watched with growing dismay last winter as the river's volume fell 28% below average and 300 kilometers of its 1321-kilometer-long course ran dry. After enjoying 2 decades of robust flow, water managers in May ordered strict rationing through September.

One group of researchers saw the crisis coming. Based on past flow rates and weather conditions anticipated for 2007–08, Chen Yaning and colleagues at the Chinese Academy of Sciences' Xinjiang Institute of Ecology and Geography in Ürümqi forecast a sharp drop in runoff feeding the Tarim. Their report in the 20 March issue of *Hydrological Processes* predicted that the river will bounce back this coming winter. But if their numbers are correct, another—and worse—crisis will happen in 2009–10, when the Tarim's inputs are predicted to be 12% less than the past year's poor flow. "Most farms will not be able to irrigate their crops," says Chen, who calls the looming threat "a big conflict between ecology and the economy."

The long-term prognosis is cloudier. On one hand, Xinjiang has been getting wetter over the past half-century, and models suggest that precipitation will continue to increase, says Ye Qian, a climate expert at the National Center for Atmospheric Research in Boulder, Colorado. But as the world warms, glaciers in the Tian Shan and Kunlun mountain ranges encircling the Tarim Basin are retreating, and the Tarim's fate is tied to its glacier-fed tributaries. "If the glaciers disappear, so will the source of the Tarim's water," says Liu Changming, a hydrologist at the Institute of Geographical and Natural Resources Research in Beijing. Rising temperatures will also increase freshwater loss through evaporation.

This is not the first water crisis to grip Xinjiang. In recent decades, the Tarim's nine historical tributaries have dried up one by one, leaving just three: the Aksu, the Yarkand, and the Hotan rivers. (Last winter, the Yarkand and Hotan stopped flowing altogether, only resuming in May with spring runoff.) Worried by the high evaporation rates as the Tarim neared its terminus, Chinese engineers in the early 1970s dammed the river to create the Daxihaizi Reservoir. The amputation dried up the Tarim's final 321 kilometers, turning villages downstream into ghost towns. In the meantime, the "green corridor"—a marshy vegetation belt extending 800 or so meters on either side of the Tarim—began to wilt as water diversion to Daxihaizi and smaller reservoirs drew down the water table. Since 2000, the central government has spent roughly $15 million shoring up this line of defense against the Takla Makan.

All signs indicate that provincial authorities must act fast to conserve water. Unbridled irrigation in the Tarim's upper reaches, Chen says, sucked the life from tributaries and caused rampant salinization that has ruined 1.1 million hectares of farmland, a quarter of Xinjiang's total. Water-saving steps could include switching from ditch irrigation to drip irrigation and moving away from water-intense crops.

The grand challenge is to find alternative water sources. Chen's group plans to team up with Wang Chi-Yuen of the University of California, Berkeley, to hunt for hidden aquifers. As a first step, they will chart features—such as limestone karst formations—likely to hold water. "There must be large aquifers in the mountains," Chen says. Xinjiang's future may depend on it.

–R.S.

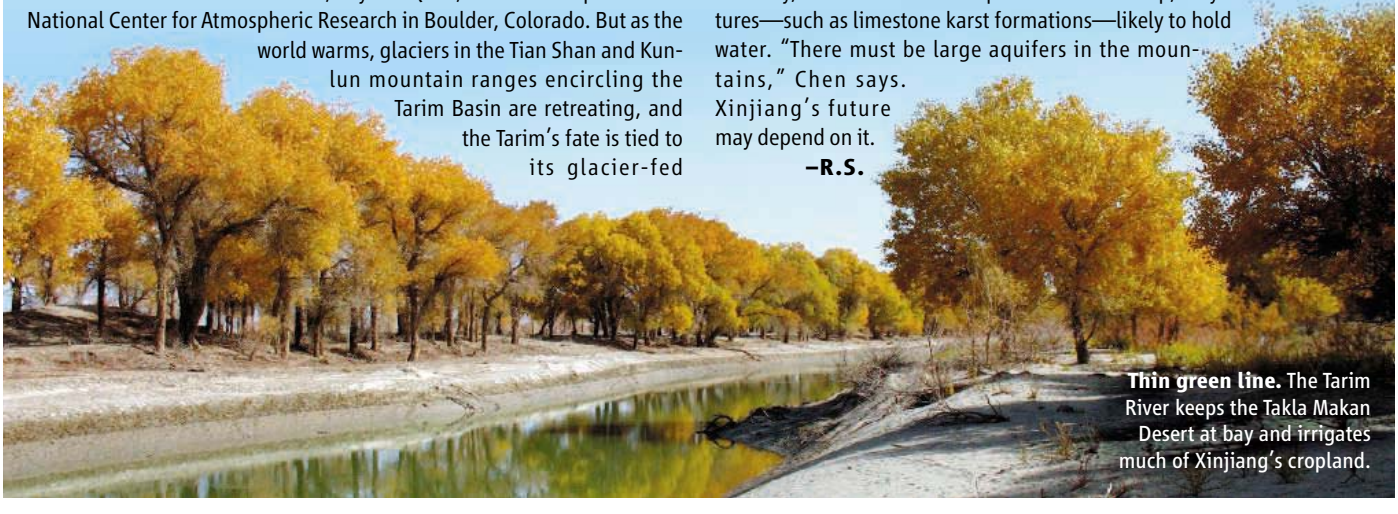

Thin green line. The Tarim River keeps the Takla Makan Desert at bay and irrigates much of Xinjiang's cropland.

CREDIT: CHEN YANING

species, IHB and other researchers say. "Species that cannot adapt to the reservoir will gradually disappear," says Liu.

Subtle changes to Yangtze hydrology have had unforeseen effects. "These changes hit the carp on several fronts," says Brian Murphy, a fisheries researcher at Virginia Polytechnic Institute and State University in Blacksburg. In April and May, Three Gorges Dam operators dump water from the reservoir to make room for summer monsoon rain surges. The modest spike in flow stimulates adult carp to leave floodplain lakes and start spawning runs before they have stored enough energy and before eggs have matured, says Murphy. The colder water they encounter on the river further retards egg maturation and suppresses hatching rates and development of fry. Dam operations in the fall reduce water flow, stimulating carp to migrate back to the floodplain earlier than normal, again reducing their chances to accumulate energy stores, Murphy says. Drift sampling at Jianli, 350 kilometers downriver from the dam, has revealed a precipitous fall from an estimated 2.5 billion eggs and larvae in 1997 to 100.5 million in 2005, Murphy, Xie Songguang of IHB, and others reported in *Fisheries* in July 2007.

It's unlikely that the carp can adapt to the new regime. "It seems that any such adaptation could only occur over many generations, and the severe nature of the present spawning reduction yields very few fish for selection to act upon," Murphy says.

For some declining species, it's hard to untangle the dam's impact from other ills. "I doubt that there are enough good 'before and after' data to determine which species have been most affected, nor would it be easy to separate declines due to pollution and overfishing from the dam's effects," says David Dudgeon, an aquatic ecologist at the University of Hong Kong.

A case in point is the Chinese paddlefish (*Psephurus gladius*), a monster known to reach 7 meters in length. Scientists haven't spotted one in years (*Science*, 22 June 2007, p. 1684), suggesting that the fate of this dying breed was sealed long before Three Gorges bisected the Yangtze. Fishers report occasional sightings upstream of the dam, so Wei says he has not given up on the possibility of 11th-hour heroics—artificial breeding—to prolong the species' survival if individuals can be captured.

Two high-profile victims of the Yangtze's many ills are mammals: the river dolphin, or baiji (*Lipotes vexillifer*), and the finless porpoise, or jiangzhu (*Neophocaena phocaenoides asiaorientalis*). A 2006 survey along 1700 kilometers of the Yangtze failed to spot a single baiji, suggesting that the cetacean is down to several dozen individuals and functionally extinct (*Science*, 22 December 2006, p. 1860). CTGPC has claimed that the baiji can be saved and has designated a reserve on the Xinluo stretch of the Yangtze. Experts say CTGPC's plan is either woefully out of date or wishful thinking.

There's still hope for the jiangzhu. Although the 2006 survey recorded fewer than 300 sightings, indicating a maximum population of 1800, IHB's Wang Ding and his colleagues are keeping the species on life support at IHB, where a jiangzhu was born in 2005—the first freshwater cetacean born in captivity in the world. Wang's group is also nurturing a small population in Tian-e-Zhou Reserve, an oxbow of the Yangtze about 250 kilometers east of Three Gorges. But the dam's long shadow may reach there as well. Because water released through the dam tends to carry little silt, the "sour" downstream flow eats away at banks and scours the bottom. Wang's group is monitoring whether erosion will deepen the Yangtze near Tian-e-Zhou. That could sever the connection between river and reserve and prevent water exchange that's critical to the jiangzhu.

To give the Yangtze's aquatic denizens a fair shot at survival, authorities will have to make serious progress in reducing the river's pollution. On an autumn 2000 cruise from Wuhan to Chongqing, a city of 9 million people at the reservoir area's western end, Chen's delegation observed scores of factories and small enterprises "discharging a lot of effluent directly into the river," Chen says. In Chongqing, officials showed off a sophisticated model of water flow—for determining how much waste they could get away with dumping in the Yangtze. "We were speechless," says Chen. "We didn't know if they were joking." It was no joke: That evening, Chen and colleagues saw "mountains of trash" near the Yangtze. "I hope they aren't dumping it anymore," he says.

Perhaps not, after pollution limits and enforcement tightened in 2002. Since then, CTGPC has spent nearly $5 billion on sewage treatment plants and garbage disposal centers. To supplement this effort, the State Environmental Protection Agency last February announced that it will spend $3.3 billion over the next 3 years on 460 projects to improve Yangtze water quality. Despite such measures, the amount of sewage and effluent dumped in the Yangtze in 2006 (the last year for which numbers are available) was nearly 30 billion tons, or more than 4.5 million tons for every kilometer of the river. Experts spar over whether the water is improving or actually getting worse. "People are always fighting, arguing over the data," says one CAS scientist.

By slowing the flow of the Yangtze and nearby tributaries, Three Gorges saps the rivers' ability to detoxify and flush out pollutants. Last week, environmental authorities revealed that they are battling a bloom of blue-green algae along a 25-kilometer stretch of the Xiangxi River—the first outbreak of its kind in the reservoir area. They blamed the bloom on a buildup of pollutants from upstream phosphor mines and chemical plants. In the absence of strict pollution controls, Chen and others fear that the reservoir could become a giant cesspool.

Urban Change in the Three Gorges Reservoir Area

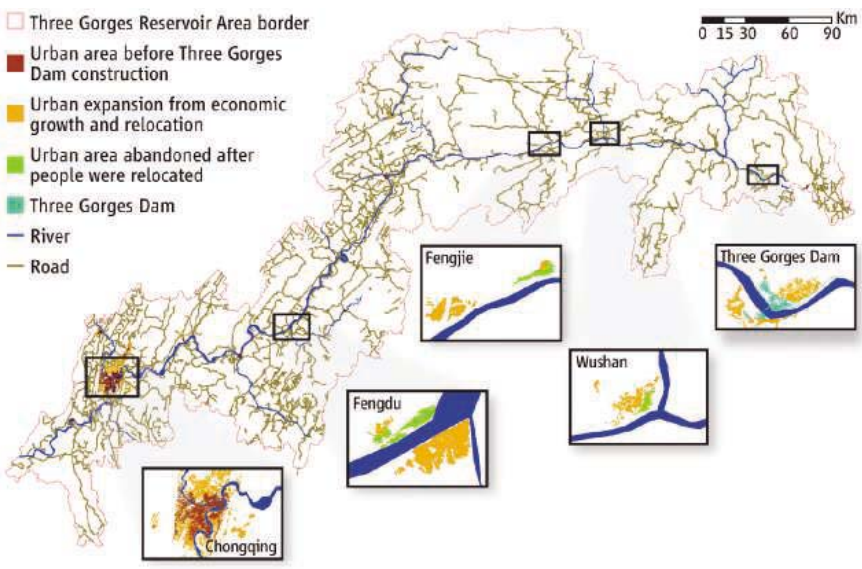

CREDIT: ZHOU YUEMIN/IRSA

A warped environment

In the rolling hills above Yichang, two graduate students unearth and examine the data recorder of a seismometer buried near a farmhouse. A team led by geophysicists Zhou Hua-wei of Texas Tech University in Lubbock and Xu Yixian of China University of Geosciences in Wuhan installed a network of 60 seismometers in the vicinity of Three Gorges Dam in mid-May, a few days after the devastating magnitude-7.9 Wenchuan earthquake centered 350 kilometers to the west. They are using recordings of thousands of aftershocks that rippled through the land here to map in detail the local geological structure and the strain placed on it by the reservoir.

The dam's location was carefully chosen in a section of crust called the Huangling core, an upwelling of granitic rock in a sea of unstable limestone. "This is called a weak seismic zone," says Zhou. "But I'm not so convinced." A key unknown is the deep structure of two fault systems skirting the edge of the Huangling core: one 20 kilometers to the west, and one less than 60 kilometers to the east. It's not clear, he says, whether stress propagates between the fault systems and whether the faults link up with each other deep below the surface, beneath the dam. Zhou expects to have preliminary results by the end of the year.

Although the risk of an earthquake powerful enough to bring down Three Gorges Dam is remote, the reservoir's impoundment has undeniably wrought massive changes on its surroundings. Currently, 632 square kilometers of terrain are under water. By the end of the year, engineers plan to begin raising the reservoir from 156 meters to its maximum capacity of 175 meters, which will submerge roughly 400 more square kilometers.

One immediate hazard is landslides. At a forum in Wuhan last fall, Huang Xuebin, chief of the Three Gorges' office of geological disaster prevention and control, said that landslides into the reservoir had produced towering waves that crashed into the shore, according to the official Xinhua News Agency. "Frequent geological disasters" threaten lives, Huang argued.

"We are concerned about what will happen when the reservoir level reaches 175 meters," says Qiao Jianping, a geophysicist at CAS's Institute of Mountain Hazards and Environment in Chengdu who has studied landslides in the Three Gorges area. The reservoir's rising waters have weakened slopes by saturating the soil. Qiao's team is developing a method to forecast slides a few days in advance by combining landslide hazard maps and rainfall data, as most slides are triggered by heavy rains. He expects to have a workable system in 2 or 3 years. In the meantime, the government has spent about $2 billion to stabilize landslide zones in the reservoir area by driving steel rods into the ground and building concrete retaining walls. "This work has enlarged the habitable areas along the river," Qiao says.

That's vital, considering that authorities in the past decade have relocated 1.2 million people to newly built towns and cities in the reservoir area. (Another 200,000 were moved to more distant locations.) Last fall, a Chongqing official told Xinhua that another 4 million people may have to be moved in the next 10 to 15 years.

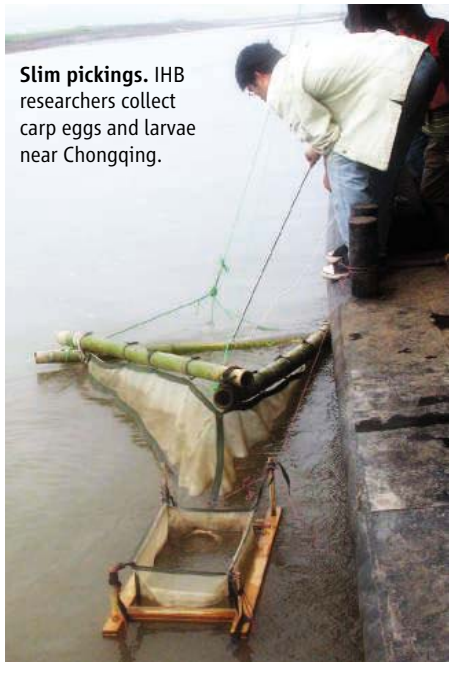

Slim pickings. IHB researchers collect carp eggs and larvae near Chongqing.

CREDIT: LIU HUANZHANG

The Chinese press has featured stories of resolute citizens starting life anew. To get a more systematic view on how people are coping, IRSA has hired a polling firm, Horizon Research Consultancy Group, to interview the displaced. "We want to find out how different generations are responding to the rapid changes," says Wu. The government has allotted $22 billion for resettlement and poverty alleviation in the reservoir area over the next 12 years.

People aren't the only creatures having to move out of harm's way. Scientists have mounted an operation to rescue two evergreen plants found only along the Yangtze's banks in the Three Gorges area. Much of the habitat of a shrub, *Myricaria laxiflora*, and that of a fern, *Adiantum reniforme* var. sinense, was lost when the reservoir's level rose to 156 meters. CTGPC funded a team led by Xie Zongqiang of CAS's Institute of Botany in Beijing to uproot more than 10,000 of the plants before the waters rose and replant them at four conservation centers.

One story only beginning to unfold is how ecosystems will respond to extensive habitat fragmentation after the reservoir's rising waters flooded valleys and turned several dozen hilltops into islands (*Science*, 23 May 2003, p. 1239). Xie and his colleagues are studying how communities of species are changing on several of the islands. They expect to see rapid biodiversity loss. "Such changes may test theories of island biogeography," says Xie. On the plus side, he says, the government has established several new nature reserves in the reservoir area.

A big wildcard is what will happen as silt builds up behind the dam—and as sedimentation is reduced downstream. In the second half of the 20th century, the Yangtze deposited about 40 million tons of sediment in its delta, forming the largest alluvial islands on Earth. Chongming Island, which started out as a sandbar 1400 years ago, now covers more than 1000 square kilometers and has a population of 650,000.

In 1979, authorities sought to consolidate these gains by planting on tidal mud flats *Spartina alterniflora*, a grass native to salt marshes in the southeastern United States. But the invader has spread rapidly and now threatens the Yangtze delta's ecological diversity, Chen and colleagues reported in the June *Journal of Plant Ecology*. Reduced sedimentation is expected to erode the alluvial islands, Chen says. At the same time, filling the Three Gorges reservoir and diverting water to other potential projects in the north will decrease the flow and allow more saltwater intrusion into the delta—spurring *Spartina*'s spread.

The biggest fear of all is a dam breach. "The dam's failure would result in one of the worst disasters in history," says Zhou. Some 75 million people live directly downstream of Three Gorges. One possible—albeit improbable—trigger could be an earthquake that's off the scale for the region. Another potential strain would be huge pulses of water from sustained heavy precipitation or sudden melting of glaciers that feed the Yangtze. "If any catastrophe happens," Chen says, "I'm not sure China—or any nation—could handle it."

A more likely scenario is that some decades from now, the Yangtze and the Three Gorges reservoir area will achieve an ecological equilibrium and the mammoth dam will become a monument to the profound transformation of the land around it.

–RICHARD STONE

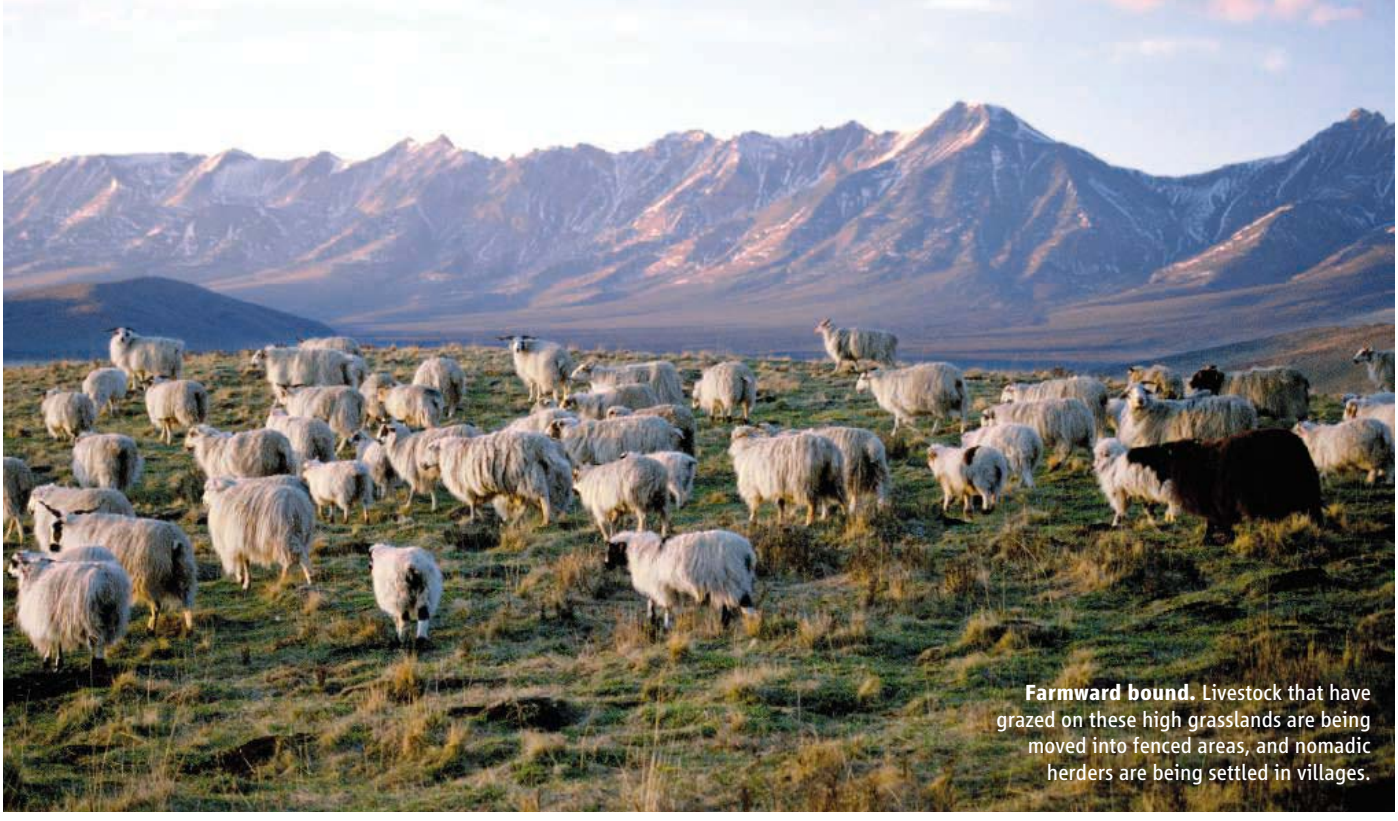

Farmward bound. Livestock that have grazed on these high grasslands are being moved into fenced areas, and nomadic herders are being settled in villages.

A Green Fervor Sweeps the Qinghai-Tibetan Plateau

In a controversial venture, officials plan to halt open grazing, eradicate rodents, restore "degraded" grasslands, improve wetlands, and plant many trees and shrubs

XINING, CHINA—No detail seems too small these days for officials working on environmental issues in western China's Qinghai Province. The chief of tree planting in the forestry bureau can attest to this. Leaving the telephone, he told a recent visitor that he had just had a surprising call: Qinghai's governor had noticed some unhealthy trees on her way to the airport. Her office wanted him to investigate.

Tending to sick trees is at one end of an array of government-led initiatives here that include some monumental undertakings as well. All have been deployed in the past decade in pursuit of a single goal. Government officials say that over several decades, human activities have left the grasslands of Qinghai in a "degraded" condition. Rivers and lakes are declining as well, according to this view, and environmental restoration is needed across the plateau, a fragile area that is the source of several major Asian rivers and is considered an ecological resource for eastern China. The central government has offered to share the costs, which helps to explain the enthusiasm for environmental reclamation in this province.

In May, Qinghai's governor announced the launch of the latest initiative, a 10-year plan to restore the region's crown jewel—Lake Qinghai, or Qinghai Hu—and surrounding lands. Embracing 30,000 square kilometers, the project includes a slew of tasks: to curtail grazing on grasslands, control rodents and insect pests that damage alpine meadows, protect wetlands, curb desertification, plant trees and shrubs, protect biodiversity, and construct small towns in which nomadic herders and their livestock would be settled in accord with "ecological migration."

Jewel in the crown. Lake Qinghai, affected by large agricultural projects in the past, is the focus of an environmental remediation program.

This sweeping program has been promised $227 million from the central government—about half the amount initially sought. It comes on the heels of a larger conservation effort begun in 2005 in the plateau's Sanjiangyuan region, the headwaters of the Yellow, Yangtze, and Lancang (Mekong) rivers. This plan covers 320,000 square kilometers and has been promised $1 billion in central government funds over 6 years.

Many welcome the government's green initiatives. Some also have reservations. Julia Klein, a global change researcher from Colorado State University in Fort Collins who is collaborating with Chinese researchers, gives a mixed review: "The protection of Lake Qinghai is an important endeavor," she says. "Some of the proposed actions, such as wetlands protection, are useful and practical objectives." However, she notes that other proposals, such as halting grazing, "may be ineffective or potentially harmful."

"Sanjiangyuan and Qinghai Hu are very good projects with huge investments," says Zhao Xinquan, director of the Northwest Institute of Plateau Biology of the Chinese Academy of Sciences (CAS) in Xining, "but they should be guided by science." A proposed scientific component of the Qinghai Hu project was dropped, and scientists say that so far they have had little input.

Better benchmarks

Both Chinese and U.S. scientists say more research is needed to understand the funda-

CREDITS (TOP TO BOTTOM): JULIA KLEIN/COLORADO STATE UNIVERSITY; LI XIAO-YAN/BEIJING NORMAL UNIVERSITY

Unlikely villains. Experts disagree on whether pikas (*inset*) deserve the blame for creating "black sands" areas within grasslands.

mental changes taking place in the area known as the Qinghai-Tibetan Plateau, sometimes called the "water tower of Asia." To begin with, there are no agreed-upon standards to measure environmental degradation, says Andrew Smith, a conservation biologist at Arizona State University in Tempe, who first visited Qinghai Hu in 1984. "Chinese officials characterize the plateau in broad terms," he says, "but it is huge—constituting 25% of the land area of China—and very diverse. One cannot say the entire plateau is degraded."

Cai Yanjun, a researcher at the CAS Institute of Earth Environment in Xi'an, agrees that clearer benchmarks are needed. But some exist: Grasslands are degraded, he notes, "if ground vegetative cover, biomass production, and quality of forage have decreased." A key issue, says Cai, is to determine if alterations are the result of global climate change or are caused by local human activities, such as overgrazing, that could be better regulated.

There's wide agreement that human activities over half a century can be blamed for some of the environmental damage around Qinghai Hu. Under Mao Zedong, grasslands along the shores of Lake Qinghai were plowed for crops. Mao's government also sited dozens of labor camps in Qinghai, to which a quarter of a million criminals and political prisoners were banished. Later, as commerce boomed in the 1980s, mineral prospectors and medicinal plant hunters gouged the area.

The pattern changed in 1999, when the Beijing government pushed for environmental improvement after a 1998 Yangtze River flood killed thousands of people. Many thought deforestation upstream in Sichuan and Qinghai contributed to the severity of the flood. The government launched the "grain to green" program to return farmlands not suitable for agriculture to forests or grasslands. In 2001, 12 military-owned farms around Qinghai Hu were returned to local civilian governments, and about 80% of tillage on shores developed in the 1950s has been returned to grass.

But critics worry that simple engineering solutions aren't adequate; they could lead to the same kind of brute-force, monolithic strategies that caused trouble in the first place. Many officials who advocate ecological improvement, Smith asserts, "do no science, utter proclamations, and spend ferociously to engage in activities that are totally unproven."

Fencing the plateau

Provincial officials often cite overgrazing as a major cause of land degradation on the Qinghai-Tibetan Plateau. According to the province's forestry bureau, grasslands around Qinghai Hu can support a maximum livestock equivalent of 3.65 million sheep, but the equivalent of 6 million sheep now graze there. The Qinghai Hu and Sanjiangyuan conservation plans calls for sealing off from grazing 854,700 hectares of grassland, resettling 881 households (4157 persons) away from the lake, and reducing livestock by the equivalent of 1 million sheep.

Resettlement has already been carried out in the Sanjiangyuan region on a larger scale, depopulating part of the plateau. Although the government provided $7000 to $12,000 per household to build houses and fences, herders have found it hard to live on this level of support, says Zhao. Smith is concerned about the social consequences; he claims that the low-status jobs and crime in resettlement villages have caused resentment.

The consequences of long-term overgrazing on the plateau are not clear, but removal of grazing entirely, as the Qinghai Hu conservation plan calls for, may be harmful, argues Klein. Since 1997, Klein has been simulating warming and grazing to observe the effects on grasslands in field experiments in Haibei county north of Qinghai Hu. She and her colleagues found that warming reduces plant biodiversity and alpine meadow biomass, but grazing helps to slow down the loss of species. When livestock are completely removed from rangeland, dried grass left over from the previous year stunts new growth, keeping grass yellow even at the height of the growing season. The Tibetan Plateau "is a system that has evolved with grazing; the removal of grazing from the system could have profound ecological consequences," says Klein.

Fencing off grasslands also may pose a threat to the critically endangered Przewalski's gazelle (*Procapra przewalskii*). This species, which is endemic to China, used to roam the dry western grasslands but is now found in small populations only in the vicinity of Lake Qinghai, according to the International Union for the Conservation of Nature, which in 1996 put Przewalski's gazelle on its Red List of Endangered Species. The last population survey conducted in 2003 counted about 600 gazelles, less than half the number of wild pandas.

Wang Dajun, a conservationist, and his grad students at Peking (Beijing) University have been conducting a new population survey since January 2008. Grad student Zhang Lu says that even though gazelles can jump over fences separating pastures, the barriers are dangerous to young or pregnant animals. Every year, there is news of a gazelle dying on a fence, says Zhang, and fences make it more difficult for gazelles to escape predators such as wolves.

Taking out a keystone

The Qinghai wolves' major food source—small native mammals including plateau pikas (*Ochotona curzoniae*), voles (*Microtus brandti*), and zokors (*Myospalax baileyi*)—have been blamed for causing grassland degradation as well and are targeted for eradication under the conservation plans. They are thought to compete for forage with livestock, and their burrows damage plant roots. Agriculture and animal husbandry

CREDITS: ANDREW SMITH/ARIZONA STATE UNIVERSITY, TEMPE

agencies lump them together as rodents.

For more than 4 decades, local government agencies have been trying to control plateau pika populations using various rodenticides, including Compound 1080 and Fussol; both have since been discontinued because of environmental contamination and collateral damage to predators. Now the primary chemicals are Gophacide and Zinophos and anticoagulants, according to Smith and J. Marc Foggin, founding director of Plateau Perspectives, an organization in the provincial capital Xining that supports conservation and sustainable development. (Foggin did research on mammals and birds in Qinghai as a grad student at Arizona State University in the 1990s.)

The pika eradication effort could have unintended consequences for other species, Foggin and Smith wrote in what is considered the definitive study in *Animal Conservation* in 1999. Pikas are a keystone species, providing many ecosystem functions to the Tibetan Plateau, they wrote. The animals are a major food source not just for wolves but for brown bears and most of the large predatory birds of the plateau, and many nesting bird species use pika burrows as shelters for breeding. Where pikas have been poisoned, bird populations are also low, they found. But Smith claims that "for all the money spent, there is little evidence to show [that poisoning is] effective." Adds Wang: "The main causes for grassland degradation are overgrazing and climate change; killing native wild animals will not solve the problem."

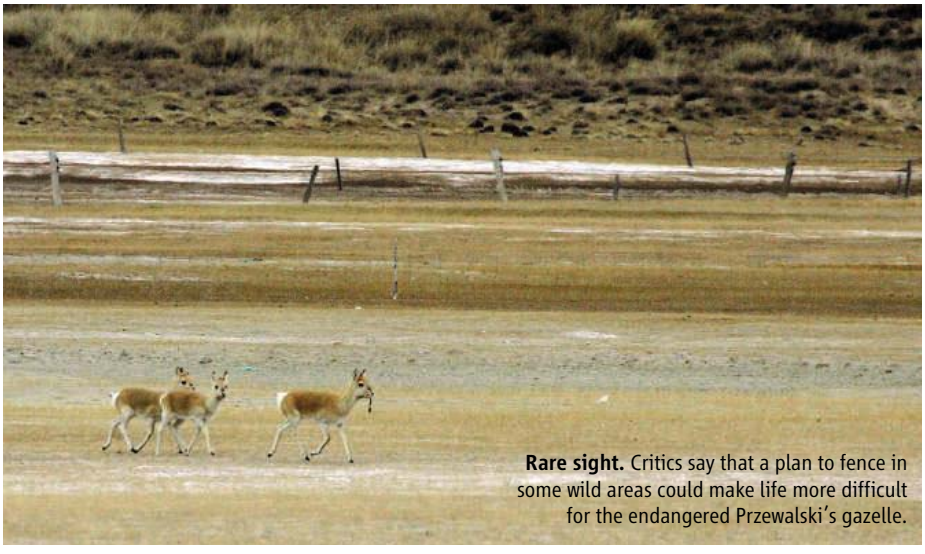

Rare sight. Critics say that a plan to fence in some wild areas could make life more difficult for the endangered Przewalski's gazelle.

CREDIT: WANG FANG/BEIJING UNIVERSITY

Water level rebounds

A fundamental—and critically important—rationale for remediation efforts in Qinghai is to protect the wetlands and prevent lakes from declining. A growing body of evidence, however, suggests that climate change is more important than human activity in changing water levels in Qinghai—and that water levels may be rebounding.

The earliest measurement of Lake Qinghai's water level was taken in 1908 by a Russian explorer. Since then and for almost the entire century afterward, the lake has been dropping. But that could be changing.

Using data from 1959 to 2000, Li Xiao-Yan and his colleagues at Beijing Normal University have studied water balances of Qinghai Hu. They found that the lake water level dropped at an average rate of 8 cm per year during this period, primarily from evaporation losses and reduced precipitation. They estimated that crop irrigation and livestock watering were less significant factors, amounting to only 1% of evaporation.

Li Shijie, a researcher at the CAS Nanjing Institute of Geography and Limnology, had observed high-altitude lakes decline for more than 2 decades. But in 2006, when he went back to Zigetang Co, a small saline lake fed primarily by surface discharges in northern Tibet, he "was very surprised" to find that its level had increased by 1.8 meters since 2002. Meteorological and hydrological data indicated that annual precipitation had increased since 2000 compared with the 1980s, at least over the southern part of the Qinghai-Tibetan Plateau. Some Chinese scientists had argued that climate warming would first make the plateau drier as land temperatures rose, but that later, as ocean temperatures caught up, heavier summer monsoons from the Indian Ocean would bring more rainfall to the plateau.

Li obtained data for four catchments near Qinghai Hu and applied the Soil and Water Assessment Tool developed by the U.S. Department of Agriculture to model the lake's water balances. Fitting past meteorology and hydrology to the model, he and his colleagues predicted that water levels in Qinghai Hu likely will fluctuate from 2006 to about 2010 and then rebound.

Remote sensing and weather data so far seem to bear out Li Shijie's modeling. According to Li Fengxia, director of the Qinghai Institute of Meteorological Science, the lake's surface area has fluctuated since 2005 and was 9.75 square kilometers larger in July 2005 than it was in July 2004. Several monitoring dates in July 2006 showed lake area increase as well. She attributes the trend to two factors: increased precipitation and increased snow melting feeding runoffs into the lake.

Although some say it's too early to tell whether this fluctuation is temporary or a turning point for lake water level, one thing is clear: The ecological issues affecting the Qinghai Hu basin are complex. "We are just beginning to understand how different drivers—such as climate change, large herbivore grazing, and small mammals—interact to affect the Tibetan Plateau grasslands and the water balance in this system," says Klein.

"The situation in the Qinghai Lake region illustrates how climate change can have some of its greatest impacts on subsistence-oriented communities who are tightly coupled to their natural resource base," says Klein. Although many problems require mitigation at a global scale, "local policies should enhance the herders' and the ecosystem's resilience and adaptation to these and future ecosystem changes. Herder relocation and its associated consequences will likely be counter to these goals."

Both Chinese and American scientists are planning more research in the area. The U.S. National Science Foundation recently approved a $1 million, 5-year project to study the social and ecological dimensions of pastoralism in Qinghai, says Smith, who is a co–principal investigator of the study, which involves researchers from several U.S. institutions.

The Chinese Ministry of Science and Technology wants to pick up the tab to support the scientific research left out of the Qinghai Hu conservation plan to help guide the engineering endeavor; the project's budget of $4.4 million is awaiting final approval by the finance ministry.

–HAO XIN

Bad air day. Beijing's smog is notorious.

Beijing's Marathon Run to Clean Foul Air Nears Finish Line

Drastic measures have brought down levels of some pollutants; a return to business as usual after the Olympics could be bad for health

BEIJING—Looking south from the roof of the Institute of Remote Sensing Applications (IRSA) in Beijing, the new Olympic Stadium known as the Bird's Nest shimmers on a hazy horizon. IRSA may not have a ringside seat for the competition that begins here next week, but it is on the frontlines of an Olympian struggle now reaching a climax: the grueling effort to clean Beijing's air.

Since 1 June, instruments perched atop IRSA—one of 14 stations in the Beijing region run by a team from six Chinese Academy of Sciences (CAS) institutes—have been monitoring gases and particulate matter around the clock. The stakes are high: In 2001, Beijing Olympics organizers vowed that concentrations of four of the worst pollutants—sulfur dioxide (SO_2), nitrogen dioxide (NO_2), carbon monoxide, and particulate matter less than 10 micrometers in diameter (PM_{10})—would meet World Health Organization (WHO) guidelines by 2008. Since then, the goalposts have shifted. In 2004, Beijing officials said that concentrations of PM_{10} would be reduced to levels comparable with other major cities in developing countries and that tropospheric ozone—a corrosive molecule that sunlight shears off from NO_2, volatile organic compounds, and other precursors—would meet China's air standard, which is more lenient than WHO's.

According to Beijing's Environmental Protection Bureau (EPB), last year SO_2 concentrations were 60.8% lower than in 1998, NO_2 was down 10.8%, and PM_{10} had declined 17.8%. "No doubt, there has been a great improvement in air quality," says Liu Wenqing, director of the Anhui Institute of Optics and Fine Mechanics and leader of the CAS monitoring team. But much of the gains were achieved between 1998 and 2001, when hundreds of noxious coal-fired plants were closed or fitted with scrubbers. Steven Q. Andrews, an environmental consultant in Washington, D.C., who has scrutinized Beijing's air-quality data, contends that gains in recent years are illusory. "Pollution levels have not decreased at all," he asserts.

The big question is whether aggressive measures over the past several months to further stem pollution, including shuttering hundreds of factories in Beijing and surrounding provinces, are having a substantial effect. The CAS team says so: As *Science* went to press, their data show dramatic reductions in SO_2 and NO_2 levels from this time last year—so much so that these two pollutants are now well under WHO limits. PM_{10} and ozone are still problems. An edict removing a million cars from Beijing's streets for the next 2 months should beat down these pollutants. CAS data show PM_{10} concentrations throughout Beijing at less than 150 micrograms per cubic meter ($\mu g/m^3$)—China's standard—but above WHO's limit of 50 $\mu g/m^3$. Ozone levels remain high. While most countries have tightened regulations in recent years, China raised its hourly ozone standard from 160 to 200 $\mu g/m^3$ in 2000; WHO's 8-hour average is 100 $\mu g/m^3$.

Eye on the birdie. Wang Yuesi at CAS's monitoring site near the Bird's Nest.

Indeed, air quality during the Olympics will be a matter of luck, says Kenneth Rahn Sr., an atmospheric chemist at the University of Rhode Island, Narragansett, who works with colleagues in China. A few times each summer, winds from the northwest flush out pollution—and everyone is pulling for such weather during the games. "The doomsday scenario," Rahn says, is a high-pressure system settling in and trapping pollutants.

Long, hard slog

The force majeure behind the miasma is rapid growth. Beijing's population has swelled from 11 million to 16 million in 7 years, and in that time the number of vehicles has doubled to 3.3 million. Some 1200 cars and trucks are being added to the streets each day. That's a huge burden, as vehicle emissions contribute as much as 70% of the city's air pollutants, says CAS team member Wang Yuesi of the Institute of Atmospheric Physics in Beijing.

Beijing is not the first Olympics host city beset by foul air. Nor will it be the most polluted: Imagine the air quality in London in 1948, Tokyo in 1964, or Mexico City in 1968. "Until the 1980s, Olympics organizers didn't pay much attention to the environment," says Liu. When they did wake up to pollution, they took aim at ozone. During the 1984 games in Los Angeles, the marathon course hugged the seaside to avoid downtown smog. High ozone levels also bedeviled Atlanta in 1996 and Athens in 2004.

But if there was a gold medal for bad air, Beijing would be hard to be beat. According to the World Bank, 16 of the 20 cities with the worst air pollution in the

CREDITS (TOP TO BOTTOM): GUANG NIU/GETTY IMAGES; R. STONE/*SCIENCE*

world are in China—including Beijing. Particularly alarming are PM_{10} levels, which last year in Beijing averaged 141 μg/m³—nearly three times the WHO standard. The Chinese Academy for Environmental Planning blamed air pollution for 411,000 premature deaths in China in 2003. "In Beijing, some days are really terrible for health and quality of life," says Guy Brasseur, director of the Earth and Sun Systems Laboratory at the National Center for Atmospheric Research in Boulder, Colorado.

Beijing is a prisoner of geography: Mountains to the west and north trap emissions, CAS researchers say. (Rahn says he is "unconvinced" that the mountains exert a trapping effect.) Air quality deteriorates in spring and summer, when temperatures and humidity soar and the prevailing winds pile on pollutants from industrialized regions to the south. "We think that other areas contribute 30% to 40% of Beijing's pollution," says Wang. In the warm months, the city often stews in acrid haze until rain or cleansing winds from Mongolia offer a brief reprieve. "In Beijing, air quality mostly depends on meteorology," says Liu. By early winter, air improves with more frequent Mongolian winds—although in the spring, these same winds can also usher in Beijing's infamous dust storms.

To cure Beijing of its ills, city officials, after winning the bid to host the 2008 games, promised to spend $12 billion on environmental cleanup to stage a "Green Olympics." Furnaces in tens of thousands of homes were converted from coal to gas and scores of coal-hungry factories were relocated to other provinces. That eased SO_2 levels considerably, as coal burning is the main source of that pollutant. But concentrations of nitrogen oxides and volatile organic compounds—precursors of ozone—rose from 2000 to 2005. The tide began to turn that year, when strict Euro IV emissions standards started to bite, says Wang, and since then levels of those pollutants have begun to taper off.

To consolidate these gains and tackle the big bugbear, PM_{10}, 19 industries around Beijing late last year were ordered to cut 2008 emissions by 30%. In March, new vehicle emissions standards came into effect that are expected to reduce PM_{10} emissions in Beijing in 2008 by 330 million tons, 27% less than last year. "In the past 5 years, the local government has done its best," says Liu. Rahn agrees. "I'm in their corner," he says. "They're doing all the right things."

But was their best good enough? Beijing EPB thinks so. Its Air Quality Index scales pollution levels from 0 to 500 on any given day; 100 or below is a "Blue Sky Day." Last year, Beijing had a record 246 Blue Sky Days (see table), and through the first half of 2008, precisely half of 2007's total—123 Blue Sky Days. But in the current issue of *Far Eastern Economic Review*, Andrews alleges that Blue Sky Days are a "misinformation campaign." Last year, he notes, Beijing reported 57 days when the index was between 96 and 100, and only 5 days between 101 and 105. Liu notes that EPB's equipment is not as advanced as CAS's and only measures air pollution at ground level at specific sites—not as pollutants mix over a large urban area. Nevertheless, Liu says his team's data largely vindicate EPB's.

Each of CAS's Beijing regional stations has a suite of instruments, including flux towers equipped with a scanning differential optical absorption spectrometer (DOAS), to measure pollutants in the air column. IRSA's rooftop is one of three "super" monitoring sites with additional instrumentation. CAS researchers also cruise Beijing's ring roads in a van equipped with DOAS and lidar. Data are being integrated with satellite imagery. Besides observing whether Beijing is living up to its clean-air vows, the team is probing questions such as how weather patterns influence regional pollution, and they are refining models of how pollutants move. The monitoring work will be repeated in Shanghai, which will host the World Expo in 2010.

CAS put a prototype of its network through its paces last August, including a 4-day period when Beijing ordered cars with license plates ending in even numbers off the street one day and odd numbers the next. During the test, which idled up to 1.3 million cars a day, NO_2 concentrations fell 26%—to levels lower than in the surrounding countryside, says Liu. SO_2 and PM_{10} also declined, but ozone levels rose—a disturbing phenomenon seen in other cities that have brought pollution levels down, Brasseur says.

In a less encouraging assessment, Wang Wen-xing and colleagues at the Chinese Research Academy of Environmental Sciences in Beijing, during a monitoring campaign in Beijing from 7 August to 30 September 2007, measured ozone and PM_{10} levels that were "much higher" than China's standards, they reported in the June issue of *Air Quality, Atmosphere & Health*. "This study is a bombshell," says Andrews, in that the observed pollution levels "vary drastically" from what EPB reported: for example, 50% higher for PM_{10} and 33% higher for SO_2.

Air Quality Index	NUMBER OF POLLUTED DAYS AT GIVEN AQI 2005	2006	2007	Prominent Pollutant	
0–50	36	26	32	--	GOOD AIR
51–100	197	215	214	PM_{10}, SO_2	MODERATE AIR
101–150	91	75	74	PM_{10}, SO_2	UNHEALTHY
151–200	31	30	34	PM_{10}, NO_2	TO
201–300	3	11	8	PM_{10}	HAZARDOUS
300–500	6	10	3	PM_{10}	AIR

SOURCE: ENVIRONMENTAL PROTECTION AGENCY

Business as usual?

Looking beyond the Olympics, scientists predict that hard-won improvements will go up in smoke when traffic returns to normal and industries rev back up after the Paralympics end here in September. Beijing's air quality tends to worsen in autumn, when high-pressure air can linger for days on end, potentially amplifying a rebound effect. "We will be watching if the pollution comes back again," says Wang Yuesi.

"Clearly, China needs to establish a long-term plan," says Brasseur. A good first step would be a thorough analysis of the chemical composition of Beijing's pollutants, he says: "Every megacity has a different spectrum." Once the ingredients of the witches' brew are known, CAS scientists hope Beijing can follow the trajectory of Los Angeles, which has tamed its once fearsome smog. "We want to learn from L.A.," says Wang Yuesi. Getting there, for starters, will take huge reductions in auto and industrial emissions. But CAS, with a mandate limited to analyzing pollution levels, cannot compel municipalities to adopt control measures.

In the meantime, all eyes are on how the athletes cope with the smog. On 20 July, in a final push to bring down PM_{10} levels before the Olympics opening ceremony on 8 August, nonessential industries in Beijing ground to a halt and the odd-even license-plate prohibition came into force. Reliable weather forecasts will come only a few days before the big event. "We hope the wind will be coming from the northwest," says Wang Yuesi. Or, as Rahn puts it, "It's time to start praying to the Mongolian weather gods."

–RICHARD STONE

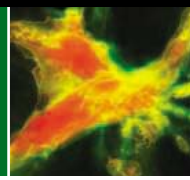

LETTERS

edited by Jennifer Sills

The Cost Benefits of Early Detection

IN HIS NEWS FOCUS STORY ("A BRUISING battle over lung scans," 2 May, p. 600), E. Marshall reports on the issue of screening smokers and patients at high risk for lung cancer with the use of computed tomography (CT)—an x-ray technique that visualizes internal structures in cross section. Opponents object to this procedure because it is "costly." Although conventional x-ray screening was dismissed in the article, it is an economical first step, and if suspicious indications are seen, it should be followed by a CT scan. It is possible, or even probable, that this would allow early detection and surgical removal of the cancer followed by a single course of chemotherapy. This management is not costly compared with extensive, and often futile, chemotherapy at later stages of the disease.

WARREN G. GUNTHEROTH

Department of Pediatrics, University of Washington, Seattle, WA 98195, USA. E-mail: wgg@u.washington.edu

Policy Forum Offered New Ideas

WE WISH THAT THE LETTER BY E. C. ELLIS ("Environmental revolution starts at home," 20 June, p. 1587), which we did not see prior to publication, had been based on a more careful reading of our Policy Forum ("Revolutionizing China's environmental protection," 4 January, p. 37). The main message of his Letter is that other countries have affected China's environment and that they should share responsibility for its environmental improvement. We certainly agree, as witnessed both by the Policy Forum that he criticizes and by our previous publication on these issues (*1*).

The Letter by Ellis also states that our suggestion to reform China's environmental governance is "nothing new." However, the reference used to support this claim (*2*) is 15 years old and does not address reforming the administrative system, as we did in our Policy Forum. Our article also provides new perspectives that reflect the current status of China's environment and governance. We understand that it was considered sufficiently new by the Chinese government that it immediately became the subject of a special report for high-level government leaders by China's official Xinhua News Agency. Following its publication, China's State Environmental Protection Administration was promoted to the Ministry of Environmental Protection (*3*), and environmental performance has been increasingly used as a criterion for evaluating government leaders [(e.g., (*4*)]. We also stressed the need to integrate multiple approaches at local to global levels, because no single approach at one location alone is sufficient to overcome complex environmental challenges.

JIANGUO LIU[1,2,3]* AND JARED DIAMOND[4]

[1]Center for Systems Integration and Sustainability, Michigan State University, East Lansing, MI 48823–5243, USA. [2]Guest Professor, Research Center for Eco-Environmental Sciences, Chinese Academy of Sciences, Beijing, China. [3]Adjunct Professor, Fudan University, Shanghai, China. [4]Department of Geography, University of California, Los Angeles, CA 90095–1524, USA.

*To whom correspondence should be addressed. E-mail: jliu@panda.msu.edu

References

1. J. Liu, J. Diamond, *Nature* **435**, 1179 (2005).
2. V. Smil, *China's Environmental Crisis: An Inquiry into the Limits of National Development* (M. E. Sharpe, Armonk, NY, 1993).
3. China's Ministry of Environmental Protection, www.sepa.gov.cn/xcjy/zwhb/200803/t20080327_119735.htm (2008) (in Chinese).
4. Xinhua News Agency, www.gov.cn/jrzg/2008-04/03/content_936002.htm (2008) (in Chinese).

Survey Says: Name a Role Model

"SCIENCE OFF THE AIR" (RANDOM SAMPLES, 28 March, p. 1741) analyzes a survey's results without paying attention to the actual question asked. The article discusses whether Americans "can" or "cannot" name living scientists. You would expect, then, that the survey question actually asked the respondents to name a living scientist. In fact, it asked "...who would you say are the science role models for the youth of today in America?" (*1*). The question did not ask for a specific person, it did not ask for a living person, and it did not ask for a scientist. It asked for "science role models." Why can't the life and career of a deceased scientist (such as Albert Einstein) serve as a model for today? Why can't an advocate of science (such as Al Gore) be a science role model for the youth of America, most of whom will not become scientists but will affect science through their votes? These were two common and entirely appropriate answers to the survey question, but are treated as disturbing by the article.

As a chemist, I would have no difficulty thinking of names of living scientists, but for a survey question asking about science role models of young Americans, I would probably pick "teachers." It would be interesting to see the results of a survey asking

Americans to name a living scientist, and it might well be disappointing, but that question was not asked in the survey. The survey results were interesting enough without sloppy analysis.

MICHAEL R. WEBB

Department of Chemistry, Tufts University, Medford, MA 02155, USA.

Reference

1. "The state of science in America," survey conducted by Harris Interactive for the Museum of Science and Industry, Chicago, IL (2008); www.stateofscience.org.

Gene Mutations and Cognitive Delay

WE CONGRATULATE T. WALSH *ET AL.* FOR A beautifully designed and executed study ("Rare structural variants disrupt multiple genes in neurodevelopmental pathways in schizophrenia," Reports, 25 April, p. 539). The demonstration that the frequency of gene deletions and duplications is elevated in schizophrenia as well as in autism and many forms of mental retardation must raise suspicions that such genomic variants are not really specific for a particular disease. Buried in the Supporting Online Material is the astonishing fact that 47% of the patients with poor cognitive function (IQ < 80) had these variants, compared with only 11% of the patients with normal IQ. Poor cognitive function is a common feature of these developmental disorders and is associated with similar anatomical anomalies across a range of disorders (*1*–*3*). Perhaps genomic deletions and duplications have a nonspecific effect—restricting the flexibility of coping responses during development, constraining neuroplasticity, and rendering cognitive function more dependent on intrinsic neurobiology.

CHRISTIANA M. LEONARD AND JOHN M. KULDAU

Departments of Neuroscience and Psychiatry, McKnight Brain Institute, University of Florida, Gainesville, FL 32610, USA, and Veterans Health Administration Research Service, Gainesville, FL 32610, USA.

References

1. C. M. Leonard *et al.*, *Biol. Psych.* **46**, 374 (1999).
2. C. M. Leonard, M. Eckert, B. Givens, V. Berninger, G. Eden, *Brain* **129**, 3329 (2006).
3. C. M. Leonard *et al.*, *Neuropsychology* **22**, 147 (2008).

Response

WE AGREE WITH LEONARD AND KULDAU THAT the association between cognitive delays and rare structural mutations in our sample is striking, although the numbers are very small. Of the 15 patients with schizophrenia who were diagnosed with cognitive delays by full assessment, 6 carried chromosomal deletions or duplications. These mutations included some of the largest deletions and duplications that we observed. The co-occurrence of schizophrenia and intellectual deficits in these patients may reflect dosage effects of more than one gene in a large genomic region—i.e., a contiguous gene effect. If so, then the smaller genomic copy number variants that involve individual genes may have effects more specifically related to psychosis.

The neurodevelopmental impact of any one structural mutation can vary remarkably among individuals. For example, in the Scottish pedigree harboring the *DISC1* translocation, 29 translocation carriers presented variously with schizophrenia or bipolar disorder or major depressive disorder or no mental illness (*1*). Just as individuals with different neuropsychiatric illnesses may harbor mutations in the same gene, individuals with the same disorder may carry different mutations in the same gene or in different genes in convergent pathways. The elucidation of critical pathways disrupted in affected individuals will contribute substantially to our understanding of psychopathology and provide important targets for treatment development.

JON M. MCCLELLAN,[1] TOM WALSH,[2] SHANE E. MCCARTHY,[3] MARY-CLAIRE KING,[2,4] JONATHAN SEBAT[3]

[1]Department of Psychiatry, University of Washington, Seattle, WA 98195, USA. [2]Department of Medicine, University of Washington, Seattle, WA 98195, USA. [3]Cold Spring Harbor Laboratory, Cold Spring Harbor, NY 11724, USA. [4]Department of Genome Sciences, University of Washington, Seattle, WA 98195, USA.

Reference

1. J. E. Chubb, N. J. Bradshaw, D. C. Soares, D. J. Porteous, J. K. Millar, *Mol. Psychiatry* **13**, 36 (2008).

TECHNICAL COMMENT ABSTRACTS

Comment on "Magnetic Resonance Spectroscopy Identifies Neural Progenitor Cells in the Live Human Brain"

Jeffrey C. Hoch, Mark W. Maciejewski, Michael R. Gryk

Manganas *et al*. (Reports, 9 November 2007, p. 980) used nuclear magnetic resonance spectroscopy to identify a biomarker of neural progenitor cells. However, their analysis relies on spectral processing methods that are known to be problematic. Absent detection using alternate methods of spectrum analysis or controls to quantify the false discovery rate, their conclusions may be premature.

Full text at www.sciencemag.org/cgi/content/full/321/5889/640b

Comment on "Magnetic Resonance Spectroscopy Identifies Neural Progenitor Cells in the Live Human Brain"

Seth D. Friedman

Manganas *et al*. (Reports, 9 November 2007, p. 980) used a metabolic biomarker identified in vitro to characterize the existence of neural progenitor cells in vivo. Although their detailed experiments and general approach are laudable, aspects of their magnetic resonance spectroscopy data and analyses raise questions about their results.

Full text at www.sciencemag.org/cgi/content/full/321/5889/640c

Comment on "Magnetic Resonance Spectroscopy Identifies Neural Progenitor Cells in the Live Human Brain"

Jacobus F. A. Jansen, John D. Gearhart, Jeff W. M. Bulte

Manganas *et al*. (Reports, 9 November 2007, p. 980) reported the discovery of a biomarker specific for neural progenitor cells detectable using magnetic resonance spectroscopy. A new algorithm was developed to extract the biomarker from noisy in vivo data. We question how this algorithm was validated, because the biomarker overlaps with peaks from nonspecific lipid signals.

Full text at www.sciencemag.org/cgi/content/full/321/5889/640d

Response to Comments on "Magnetic Resonance Spectroscopy Identifies Neural Progenitor Cells in the Live Human Brain"

Petar M. Djurić, Helene Benveniste, Mark E. Wagshul, Fritz Henn, Grigori Enikolopov, Mirjana Maletić-Savatić

We reported on a neural progenitor cell biomarker, a lipid-based metabolite enriched in these cells, which we detected using spectroscopy both in vitro and in vivo, and singular value decomposition–based signal processing. The study provided an outline of our computational methodology. Herein, we report more extensively on the method of spectrum analysis used, demonstrating the specificity of our findings.

Full text at www.sciencemag.org/cgi/content/full/321/5889/640e

Letters to the Editor

Letters (~300 words) discuss material published in *Science* in the previous 3 months or issues of general interest. They can be submitted through the Web (www.submit2science.org) or by regular mail (1200 New York Ave., NW, Washington, DC 20005, USA). Letters are not acknowledged upon receipt, nor are authors generally consulted before publication. Whether published in full or in part, letters are subject to editing for clarity and space.

CORRECTIONS AND CLARIFICATIONS

Reports: "Generation of pluripotent stem cells from adult mouse liver and stomach cells" by T. Aoi *et al*. (1 August, p. 699). After publication of the *Science* Express version of our Report, it was brought to our attention that the number of integration sites shown at the bottom of the Southern blot of Fig. 3 differs from the number of visible bands. In addition, we found that genomic DNA of cell line iPS-Hep 98A2 was contaminated with DNA containing additional retroviral integrations. The incorrect version of Fig. 3 has been published in both the online *Science* Express version and the printed version of the paper. The correct Fig. 3, including Southern blots with lower background and with uncontaminated DNA of iPS-Hep 98A2, is shown here. In this corrected figure, corresponding adjustments have been made to the number of integration sites as indicated at the bottom of the blot. The numbers of insertion sites for iPS-Hep/Stm versus iPS-MEF range from 1 to 4 and 1 to 9, respectively (as opposed to 1 to 4 versus 1 to 12, as reported in the *Science* Express and printed versions of the manuscript).

Some errors present in the *Science* Express version of the paper are corrected in the print version and associated Supporting Online Material (SOM): the order of transgenic mouse crosses and greater explanation provided for mouse chimerism designated as "ND" (not determined) in table S2. (We thank Dr. Shi V. Liu, Eagle Institute of Molecular Medicine, for these clarifications.)

A revised version of the SOM is also available (www.sciencemag.org/cgi/content/full/1154884/DC2). Figures S5, S6, S8, and S9 reported data skewed by the contaminated DNA in the original inverse PCR experiments. We have repeated these experiments with uncontaminated DNA. The corrected versions of figs. S5, S6, S8, and S9, eliminating five integration sites that had been present due to iPS-Hep98A2 contamination, are shown in the revised SOM. In addition, the sequence of the primer Oct3/4R2 is 5′-AGGTGATCCTCTTCTGCTTCAG-3′, as opposed to 5′-TCCAATAAACCCTCTTGCAGTT-3′ described in the SOM.

The numbers of integration sites identified by Southern blots (Fig. 3) and inverse PCR (figs. S5 to S9) do not exactly correspond as a result of pseudogenes and overlapping bands or bands that are too big or too small for detection by Southern blot. Our Report stated that the generation of iPS-Hep and iPS-Stm cells does not require retroviral integration into specific sites. This conclusion is based on the data from four cell lines, so a more extensive analysis is needed to confirm this conclusion.

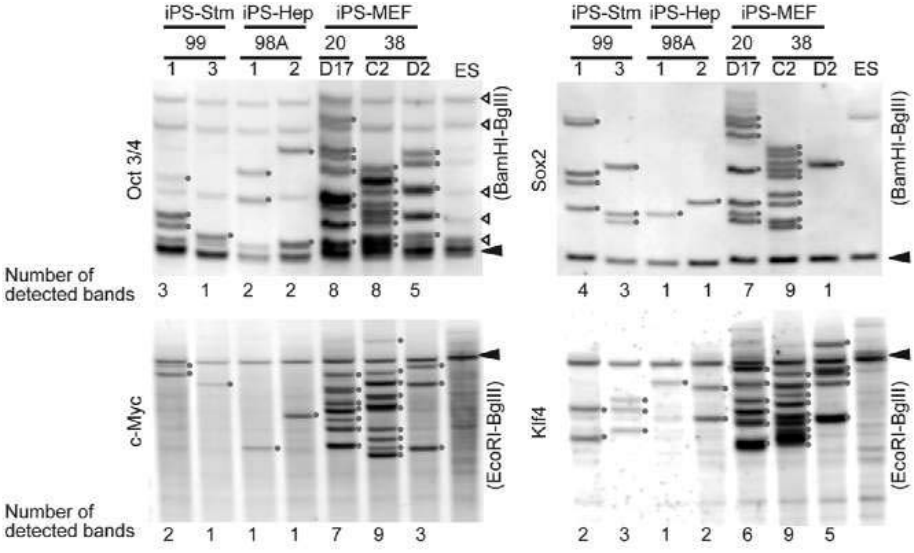

ECONOMICS

Rural Changes Stimulate Rising Giants

C. Peter Timmer

Rapid economic growth in China and India is the envy, and worry, of the world. Never in history have so many people been pulled out of poverty so quickly. But the newly emergent middle class in both countries has familiar desires: better diets, more comfortable housing, more pleasant places to shop, and more convenient transportation (including personal automobiles). The demands these rapidly expressed desires are placing on global resources have stirred new Malthusian fears. Is there enough food and fuel for China and India to live like Europe and the United States?

The Dragon and the Elephant
Agricultural and Rural Reforms in China and India

Ashok Gulati and Shenggen Fan, Eds

Johns Hopkins University Press, Baltimore, 2007. 574 pp. $75. ISBN 9780801887864. Paper, $38. ISBN 9780801887871. Published for the International Food Policy Research Institute.

The Dragon and the Elephant: Agricultural and Rural Reforms in China and India is a good place to start to understand how to answer that question. Edited by leading agricultural economists from India (Ashok Gulati) and China (Shenggen Fan), the volume is the product of a massive collaborative research effort that must have been incredibly difficult to arrange and manage. The International Food Policy Research Institute (Washington, DC), home base for both editors, deserves real credit for pulling this off.

Interestingly, the volume does not address the global resource dimensions of the Chinese and Indian growth successes. Instead, it seeks to understand the foundations of the successes themselves and finds them, not surprisingly, in efforts in both countries to revitalize their rural economies. Such revitalization was essential, the various authors argue, if the massive and impoverished populations in each country were to have any hope of higher living standards, including enough food to eat. The specter of hunger was a basic driver of reform policy in both China and India.

Three main themes drive the story of rural reforms in the two countries. First, China started in 1950 well behind India in terms of poverty, institutional infrastructure, and mechanisms of governance. Both countries struggled for 30 years to find a path to inclusive modernization. But to most observers' surprise, China found the path sooner, exploited it faster, and has roared past India in nearly all indicators of economic success. Only India's democratic form of governance (flawed as it is) holds promise for convergence in the future.

Second, and no doubt controversially, China's "initial conditions" laid down during the Maoist era are now seen to provide substantial advantages in managing rapid, inclusive growth. Greater gender equality, increased investments in rural human and physical capital, and even the capacity to control policy from the center now make the Maoist experiment with collectivization and rigid central planning seem not the disaster it appeared to be in the late 1970s.

Third, details matter. They matter at both a strategic level and at the level of commodity-specific, region-specific approaches to agricultural development. Here, the volume is rich in specificity about contrasts between China's and India's approaches to the "big" rural reform issues: trade policy (China opted early on for a much more open approach); poverty alleviation (China opted for rapid growth in rural areas, whereas India retained a state-provided safety net that has become increasingly cumbersome and expensive); rural nonfarm economy (India is only now beginning to facilitate the natural dynamism of rural entrepreneurs investing to service their agricultural neighbors).

Naturally, in a volume as long and complex as this—with 36 different authors contributing to 22 chapters—problems arise. It was clearly difficult and sometimes evidently impossible to get the Chinese and Indian authors to use common definitions and approaches, even when writing about the same topic. A particularly important example is the discussion of agricultural diversification. The chapter by Funing Zhong and Jing Zhu contains a careful statistical decomposition of sources of growth in Chinese agriculture. The companion chapter by P. K. Joshi and Ashok Gulati, however, is an impassioned plea for a more open regulatory environment to permit large foreign firms to enter the Indian market as a way to speed vertical integration—the only way, in the authors' minds, to build efficient links between "plate and plow." Each contribution is interesting on its own, but readers will gain little or no comparative insights from reading the pair.

In marked contrast, the two chapters on the rural nonfarm sector are built on a common framework that permits easy comparison. The econometrics Linxiu Zhang, Scott Rozelle, Jikun Huang, and Alan de Brauw apply to the Chinese development are based on better data than G. K. Chadha's more impressionistic analysis of the sector in India. But the Indian study is placed more carefully in a macroeconomic setting so that the overall income and employment effects can be judged easily. These are two of the most insightful chapters in the volume.

Looking forward, it is hard to miss the pessimism of the Indian authors as they view their country's rural reforms and progress compared with those of China. The contribution by V. S. Vyas, the "dean" of agricultural economists in India, is titled "Market Reforms in Indian Agriculture: One Step Forward, Two Steps Back." This chapter highlights the not-so-hidden agenda of the volume: the final sentence of the Acknowledgments declares "We are most grateful to Indian Prime Minister Manmohan Singh, the architect of economic reforms in India, who inaugurated the first conference in New Delhi and is still keen to know what each country can learn from the other." *The Dragon and the Elephant* is filled with such learning, revealing that competition works in powerful ways, even in the world of political economy.

CREDIT: JOAN STEPHENS/FROM *THE DRAGON AND THE ELEPHANT*

The reviewer is at the Program in Food Security and the Environment, Stanford University, Stanford, CA 94305, USA. E-mail: ptimmer@cgdev.org

10.1126/science.1160704

SCIENCE FESTIVALS

Celebrating Science as Culture

Lawrence M. Krauss

Even as many of us bemoan the sorry state of scientific literacy among the general population, the public nevertheless remains fascinated by science. The proof of this is the remarkable success of a relatively new phenomenon cropping up in cities around the world: science festivals. From Genoa to Edinburgh, from Ireland to the United States, such gatherings of scientists and the public are drawing hundreds of thousands of visitors, who are treated to everything from popular lectures to science-related operas. For periods ranging from a weekend to a full week, cities are transformed into places where science briefly attains what should be its natural place in popular culture.

This year witnessed the newest, and perhaps flashiest, entry into this club: the World Science Festival in New York City (*1*, *2*). Named with characteristic American hubris, the activities in New York were as much a "world" festival as baseball's "World Series" is a true world championship. Never mind that, though. During 4 days (Thursday, 29 May, to Sunday, 1 June), some 42 sold-out events, at over 20 locations around the city, drew some 25,000 people, and an estimated 100,000 people attended the festival's science street fair that weekend. Given the media clout of New York, and the efforts of the two chief festival organizers (mathematician-physicist Brian Greene and his wife, Tracy Day, a former TV producer), attendees were treated to events that included scientist-presenters as well as Hollywood types—from Sam Shepard to Alan Alda, who himself played a major role in helping organize and promote the festival.

The organizers scrambled to put together a program at what seemed (from a participant's perspective) to be a nerve-racking last-minute pace, but all of this was invisible to the paying public. The event I appeared in was tightly produced and choreographed—a general characteristic of the polished and entertaining menagerie of performances, readings, panel discussions, and lectures that made up the festival, which led to rave reviews from critics and audiences alike.

The New York festival differed from many of its European counterparts by charging up to $40 for a single event, whereas many of the European events were free or had minimal entry fees. But for New York audiences used to spending hundreds of dollars for Broadway plays and concerts, the ticket prices proved to be no barrier. And this is what makes the science festival phenomenon so exciting. Each one seems to be naturally tailored to the cultural milieu in which it is produced.

CREDIT: ©BEN AUSTIN FOR WORLD SCIENCE FESTIVAL

Lining up for science. After all 680 seats for the World Science Festival's event "Invisible Reality: The Wonderful Weirdness of the Quantum World" were reserved, more than 300 people waited for extra tickets or no-shows.

Over the years, I have been fortunate enough to participate in five festivals: the Genoa Science Festival (*3*), the Trieste International Science Media Fair (*4*), Science Week Ireland (*5*), the Edinburgh International Science Festival (*6*), and New York. The New York festival was patterned on that in Genoa, Italy, one of the oldest and most popular. In a city of merely 300,000, each year over 250,000 visitors enjoy at least one of the events taking place in palaces, churches, art galleries, and concert halls sprinkled throughout the city (so Genoa is literally taken over by the festival). When I arrived to present my lecture, I was flabbergasted to find over 1000 people who had been waiting for up to 2 hours to enter the hall. What all of these science festivals have done is to let people indulge their natural inner fascination with the world around us in a context that is neither intimidating nor culturally remote, as a university lecture hall too often seems.

What works particularly well—and was common to Trieste, Genoa, and New York—is to intersperse very different types of standard events (like lectures and panels) with musical compositions or storytelling and to ensure that each day there are hands-on activities for children. Both Genoa and Trieste set up central halls with interactive exhibitions for kids that remained open throughout the festival.

Probably the biggest concern, which each festival dealt with in different ways and with varying degrees of success, is to try and ensure that the science does not get completely subsumed by the spectacle. A similar problem occurs in many science museums, where the effort to demonstrate that science can be fun sometimes gives the sense that it is primarily a series of experiential games. Properly conveying the process of science is the hardest aspect of popularization, but it may also be the most important.

Every major urban center boasts concert halls, art galleries, and theaters. In forcing us to reexamine our place in the universe, science is fundamentally no different from music, art, and literature, and it should be equally integrated into our cultural fabric. All should be celebrated for demonstrating the unique features of the human intellect that make up what we commonly refer to as culture.

Music festivals, film festivals, and art openings are so common as to be unremarkable. It is high time that our scientific cultural heritage was similarly experienced as entertainment, worth devoting one's weekend to enjoying. One can only hope that science festivals will become so varied and so common that no one would feel it necessary to remark upon their existence in a magazine such as this.

The author, who was on the advisory board for the World Science Festival, is at the Center for Education and Research in Cosmology and Astrophysics, Case Western University. This month, he is moving to the School of Earth and Space Exploration, Arizona State University, Box 871404, Tempe, AZ 85287–1404, USA. E-mail: lawrence.krauss@asu.edu

References and Notes

1. www. worldsciencefestival.com.
2. AAAS is among the World Science Festival's 23 program partners.
3 http://festivalscienza.it.
4. www.festrieste.it.
5. www.scienceweek.ie.
6. www.sciencefestival.co.uk.

10.1126/science.1160396

RESEARCH FUNDING

Structural Disequilibria in Biomedical Research

Many current problems for U.S. biomedical research can be attributed to fundamental structural elements of the NIH funding system.

Michael S. Teitelbaum

Many are calling for large increases in the budget for the National Institutes of Health (NIH) to address the damaging effects on biomedical research resulting from recent flat funding levels. Yet politicians respond with skepticism, as the NIH budget is already very large and was doubled over the 5-year period 1998 to 2003 (*1*). What is often left unsaid is that the fundamental problems are structural in nature—biomedical research funding is both erratic and subject to positive-feedback loops (*2*, *3*) that together drive the system ineluctably toward damaging instability. It may be possible to create broad political support for large annual NIH funding increases into the indefinite future. But if not, objective analyses of systemic instabilities, followed by incremental adjustments, would be strongly in the interest of maintaining the quality of U.S. biomedical research.

Concerns about crises and discouragement resulting from flat funding levels for the National Institutes of Health (NIH) over the last 5 years (*4*) are valid and widely shared. Special worries are being expressed by NIH leadership about "the impact of this difficult situation on junior scientists, and on the ability of established investigators to maintain their laboratories" (*5*).

Crisis Despite the Doubling

NIH research funding is more difficult to get now than it was before the NIH budget doubled, especially for early-career researchers. In 1998, about 32% of NIH competing Research Project Grant (RPG) applications were successful; by 2007 the comparable success rate had declined to 21% (*6*). The percentage of NIH awardees aged 40 or under, already less than 23% in 1998, declined to just over 15% by 2005 (*7*).

Some of the reasons are well understood: First, adjusting for inflation, the value of the NIH budget has declined by about 13% from its peak in 2003 (*8*). Second, the rapid annual increases from 1998 to 2003 were followed by 5 years of small annual decreases (*7*). The inflation-adjusted budget today is not much higher than it would have been had smaller NIH budget increases, common before 1998, been sustained from 1998 to 2008 (*9*–*11*). Third, the number of applications for new and competing NIH research grants nearly doubled, from about 24,000 in 1998 to more than 47,000 in 2007. This was due primarily to a near-doubling of grant applicants, many of whom were trained under NIH research funding—from nearly 20,000 in 1998 to nearly 39,000 in 2007. In addition, the number of applications per applicant also increased somewhat (*12*).

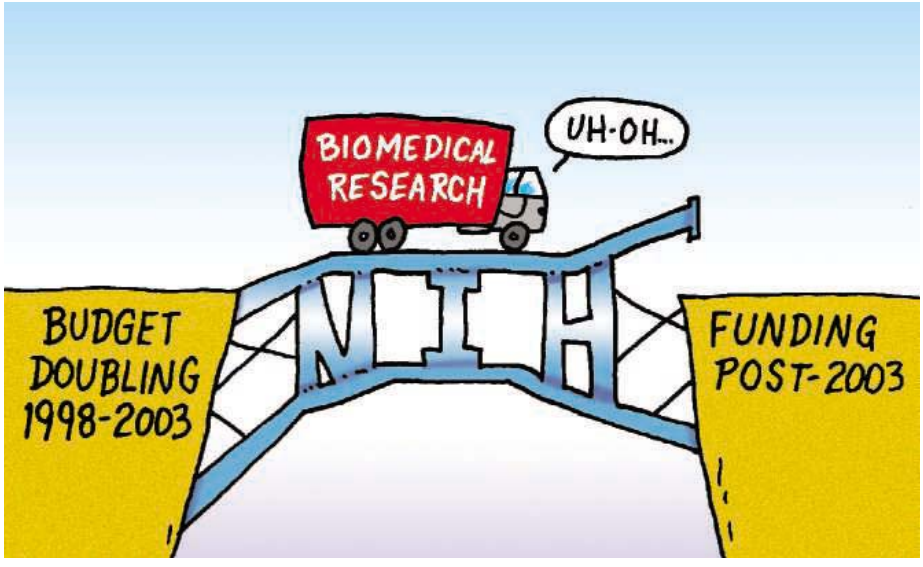

CREDIT: JOE SUTLIFF

Problems Fundamentally Structural

What is too often left unsaid is that these trends are fundamentally structural. This makes sustainable solutions exceptionally difficult to find. In the absence of careful adjustments to the current structure, these problems are unlikely to be solved by increases in NIH funding over the coming decades.

Symptoms of structural malaise were amply reported well before the NIH budget doubling began in 1998 (*13*). Indeed, the 1998 to 2003 budget doubling was intended in part to mitigate some of these symptoms. Rapid increases in research funding initially did have such effects, but only temporarily. A 2002 *Science* article (*10*) was prescient in concluding that biomedical research had become dependent on at least 6% annual budget increases. As if on cue, damaging crises emerged when the increases from 2003 onward proved to be smaller than 6%.

The harsh impacts of these structural problems now are being felt by research institutions and individual biomedical researchers. Yet, none of these institutions or individuals has it within their power to modify the key structural elements of the system in which they find themselves. These can be addressed only at the level of policy and administrative practice by the Congress and NIH itself.

Positive Feedback in the System

For NIH, more research funding does produce increased research output, as intended. Yet, because the system as currently structured employs graduate and postdoctoral research assistants to do much of the laboratory work, increased research funding also produces (after a multiyear lag) additional Ph.D.-level applicants for NIH grants. No effective mechanisms are in place to align these increased numbers with expanding career opportunities (*14*).

In theory, the resulting chilly job markets for recent biomedical Ph.D.'s should generate negative feedback that would tend toward more stable equilibria. In a closed system, and one with full information available to prospec-

Alfred P. Sloan Foundation, 630 Fifth Avenue, New York, NY 10011, USA; E-mail: teitelbaum@sloan.org. The views expressed are the author's and not necessarily those of the Alfred P. Sloan Foundation.

tive graduate students, some fraction of undergraduates who might otherwise consider becoming Ph.D. students and postdocs would correctly perceive the difficult career paths and would pursue other options.

In practice, however, the system is not closed. Given increased research funding, additional graduate students and postdocs can be readily recruited from large potential pools in countries with fewer such opportunities—precisely what took place as the NIH budget was rapidly doubled (*15*). Nor is there anything even approximating full information about career prospects available to prospective entrants, whether domestic or foreign.

The employment and career implications of such a positive-feedback structure were modeled during the 1990s (*16*). One simulation (for mathematics) assumed a 2% real increase in annual research funding for 5 years, followed by stabilization. The result was short-term improvement in employment prospects for recent mathematics Ph.D.'s, followed by deteriorating career prospects that ended up worse than before the funding increases began, even with the assumption of a permanent 10% increase in real research funding (*16*).

The 1998 to 2003 budget doubling resulted in other kinds of positive feedback. In particular, it offered incentives for expansion by U.S. academic medical centers, many of which encouraged their faculty to recover more of their compensation from external sources (*17*). Academic biomedical research facilities also were expanded, in expectation of overhead payments from increased research grant funding: Facilities investments rose from a predoubling average of about $348 million per year to $760 million per year during 1998 to 2003, to $1.1 billion per year from 2003 to 2007 (all figures in constant 1990 dollars) (*18*). Much of the expansion capital apparently was borrowed, in part because federal rules allow inclusion of debt service in NIH grant overhead calculations while excluding overhead claims for the imputed value of equity. In financial terms, one might say that the system became more highly leveraged, rendering it more vulnerable to unanticipated downward deflection of the increase in federal research funds.

What Can and Should Be Done?

Strong lobbying for increases in the NIH budget is under way. Yet, if current and prospective federal fiscal constraints preclude sustained budget increases of 6% or more, the system needs to be guided toward more stable equilibria. More stability would be in the interest of research institutions and established researchers, would facilitate medical progress and, over time, might make biomedical research careers more attractive to U.S. students.

This is, of course, far easier said than done. The current system has evolved over decades, has produced outstanding research and valuable returns to the world, and has served the interests of research institutions and senior researchers.

NIH's Office of Extramural Research could help greatly by convening a strong advisory committee of biomedical researchers and analysts of the NIH research and training system. Its charge would be to identify elements of the current structure that render it prone to instability and to suggest prudent sustainability strategies that would reduce the system's vulnerability to destructive booms, busts, and funding crises. Adjustments warranting assessment include the following:

» *Ways to attenuate the currently strong positive feedback between research funding and financial support for additional graduate students and postdocs,*

More support for NIH's Ph.D. "training" functions (*19*), with proportionately less for graduate students and postdocs financed under NIH research grants—long discussed, but not yet implemented (*20*).

» *New mechanisms to better align the Ph.D.-postdoc systems with demand in the labor market for their graduates, e.g.,*

a. Providing more current data on biomedical labor market conditions to prospective domestic and foreign entrants;

b. Allowing increases in NIH research funds to support career-path biomedical research positions (e.g., professional staff scientist positions) at research institutions rather than depending on temporary students and/or trainees.

c. Reconsidering the goals and career impacts of unlimited numbers of temporary visas for Ph.D. students and postdocs financed by NIH research funding.

» *Assessment of possible mechanisms for NIH funding increases that would be less destabilizing than the budget doubling, e.g.,*

a. Avoiding rapid acceleration and deceleration of NIH budget increases, aiming instead at sustained increases in excess of inflation and keyed to gross domestic product growth (*11*).

b. Limiting the percentage of a faculty members' salary that can be paid by NIH research grants (*17*);

c. Adjusting overhead rules regarding debt service for research facilities;

d. Designing creative financial mechanisms to stabilize or buffer erratic annual federal budget decisions. One suggestion worthy of analysis is an extra "stabilization overhead" that grantee institutions would reserve to provide bridge funding for biomedical researchers facing funding gaps (*11*).

References and Notes

1. The current FY 2008 budget for NIH is $29.457 billion, up by about $2.2 billion and 8% from the 2003 level; http://officeofbudget.od.nih.gov/ui/2008/Summary%20of%20FY%202009%20BudgetPress%20Release.pdf.
2. The concepts of positive and negative feedback are commonly associated with the work of Norbert Weiner (*3*).
3. Norbert Weiner, *Cybernetics: Or the Control and Communication in the Animal and the Machine* (MIT Press, Cambridge, MA, 1948).
4. "A broken pipeline? Flat funding of NIH puts a generation of science at risk," from a collaborative consisting of Brown University, Duke University, Harvard University, Ohio State University, Partners Healthcare, University of California at Los Angeles, and Vanderbilt University, March 2008; www.BrokenPipeline.org.
5. E. A. Zerhouni, *Science* **314**, 1088 (2006).
6. National Institutes of Health, "Success rates," at *NIH External Data Book 2007* (NIH, Bethesda, MD, 2007); slide 25 http://grants2.nih.gov/grants/award/Research_Training_Investment/Research_Training_Investment.cfm.
7. National Institutes of Health, Office of External Research, presentation to Association of Independent Research Institutes, Phoenix, AZ, 3 October 2006, slide 25; http://grants.nih.gov/grants/award/trends/airi2006.ppt.
8. The real value of the budget was based on the Biomedical Research and Development Price Index (BRDPI), the standard price index for biomedical research. Both increases and declines are "real," i.e., adjusted for biomedical cost inflation using the BRDPI. See http:// officeofbudget.od.nih.gov/UI/GDP_FromGenBudget.htm. The BRDPI measure has a number of acknowledged imperfections, e.g., that it adjusts for the costs of research inputs but not for the cost of outputs.
9. S. J. Heinig, J. Y. Krakower, H. B. Dickler, D. Korn, *N. Engl. J. Med.* **357**, 1042, fig. 1 (2007).
10. D. Korn *et al*., *Science* **296**, 1401 (2002).
11. R. Freeman, J. Van Reenen, "What if Congress doubled R&D spending on the physical sciences?" presented at the National Bureau of Economic Research Conference on *Innovation Policy and the Economy*, Washington, DC, 15 April 2008.
12. NIH, "Research project grants," at *NIH External Data Book 2007*, http://grants2.nih.gov/grants/award/Research_Training_Investment/Research_Training_Investment.cfm.
13. National Research Council, *Trends in the Early Careers of Life Scientists* (National Academy Press, Washington, DC, 1998).
14. Some see solutions in special funding programs focused on young investigators. While these may have a place, they cannot preempt negative countermessages conveyed by career crises being faced by more senior researchers.
15. National Science Board (NSB), *Science and Engineering Indicators 2008* (NSB 08-01; NSB 08-01A, National Science Foundation, Arlington, VA, 2008), figs. 2-12 and 2-32.
16. C. A. Goldman, W. E. Massy, *The PhD Factory: Training and Employment of Science and Engineering Doctorates in the United States* (Anker, Bolton, MA, 2000).
17. S. A. Bunton, W. T. Mallon, *Acad. Med.* **82**, 282 (2007).
18. S. J. Heinig, J. Y. Krakower, H. B. Dickler, D. Korn, *N. Engl. J. Med.* **357**, 1042 (2007).
19. Under the Ruth L. Kirschstein National Research Service Award program.
20. National Research Council, *Addressing the Nation's Changing Needs for Biomedical and Behavioral Scientists* (National Academy Press, Washington, DC, 2000).

10.1126/science.1160272

IMMUNOLOGY

A Splicing Switch for T Cells

A single ribonucleoprotein has been identified that triggers RNA splicing changes upon T cell activation.

Nick Holmes

The ability of T lymphocytes to divide and differentiate in response to specific antigen is critical to the immune defense of vertebrates. A major remodeling of gene and protein expression accompanies T cell activation. The latter is shaped not only by the turning on and off of dozens of genes but also by changes in the splicing of precursor messenger RNA (mRNA), which produces a shift in the mRNA and protein isoforms that are expressed (*1*). The alteration of alternative splicing in the transmembrane protein CD45 has been widely used to distinguish naïve T cells from recently activated cells and their descendants (antigen-experienced cells) (*2*). On page 686 of this issue, Oberdoerffer *et al*. (*3*) identify a protein, heterogeneous ribonucleoprotein L-like (hnRNPLL), whose increased expression during human T cell activation alters CD45 splicing.

By analyzing the global effects of inhibiting hnRNPLL in primary T cells ($CD4^+$ subtype) with the use of exon arrays (a systematic assay to assess the expression of alternative spliced forms of genes), Oberdoerffer *et al*. identified 131 other genes whose splicing was altered. Splicing of only 36 of these 132 genes was also altered in $CD4^+$ T cells from umbilical cord blood (assumed to be all naïve) that were activated by an antibody to the T cell antigen receptor. However, some of the unshared genes that were identified may be genuine targets whose splicing is altered in antigen-experienced T cells. A key aspect of the new work is that manipulating the expression of hnRNPLL predicts splicing of precursor mRNA from the endogenous CD45 gene.

Precursor mRNA splicing in metazoa involves its interaction with protein factors that enhance or inhibit individual exon splicing. Cis-acting sequences are found in both exons and introns (coding and noncoding regions of a gene, respectively), and the effects of individual proteins are context-dependent, so that the same factor can promote exclusion or inclusion of different exons (*4*). Previous work suggested that the closely related factor hnRNPL and several other hnRNP and serine-arginine-rich proteins are involved in the alternative splicing of CD45 (*5*, *6*). However, hnRNPL expression is unaltered by T cell activation, although the protein may undergo posttranslational modification (*5*).

Oberdoerffer *et al*. do not pin down the mechanism by which hnRNPLL exerts its effect. To understand this, it will be necessary to establish how hnRNPLL interacts with the other splicing factors involved. For example, is hnRNPLL binding dependent on, or exclusive of, hnRNPL? A global splicing factor called polypyrimidine tract binding protein–associated splicing factor also promotes activation-specific CD45 exon 4 exclusion (*5*). Does this effect depend on hnRNPLL?

CD45 is the major receptor phosphotyrosine phosphatase expressed by T cells. It is essential for T cell development and activation, probably through control of Src-family kinases (which phosphorylate protein substrates) (*2*). One complicating factor is that all cell types express more than a single CD45 isoform (see the figure). For example, mature $CD4^+$ T cells express the RB, RAB, RBC, and RO isoforms; naïve T cells have more RB than RO; and recently activated T cells have more RO than RB (*7*). Furthermore, expression of any single isoform alone produces fully functional T cells in vivo. Even the quantitative effects of CD45 expression on T cell development and activation fail to distinguish between isoforms (*8*). Moreover, there are marked glycosylation differences between cells expressing the same CD45 isoform, which may be of fundamental importance because all known CD45 ligands are lectins. These glycosylation differences certainly affect the ability of CD45 to dimerize, which has been proposed to regulate CD45 phosphatase activity and to explain the functional importance of isoforms (*9*), although both propositions are still uncertain.

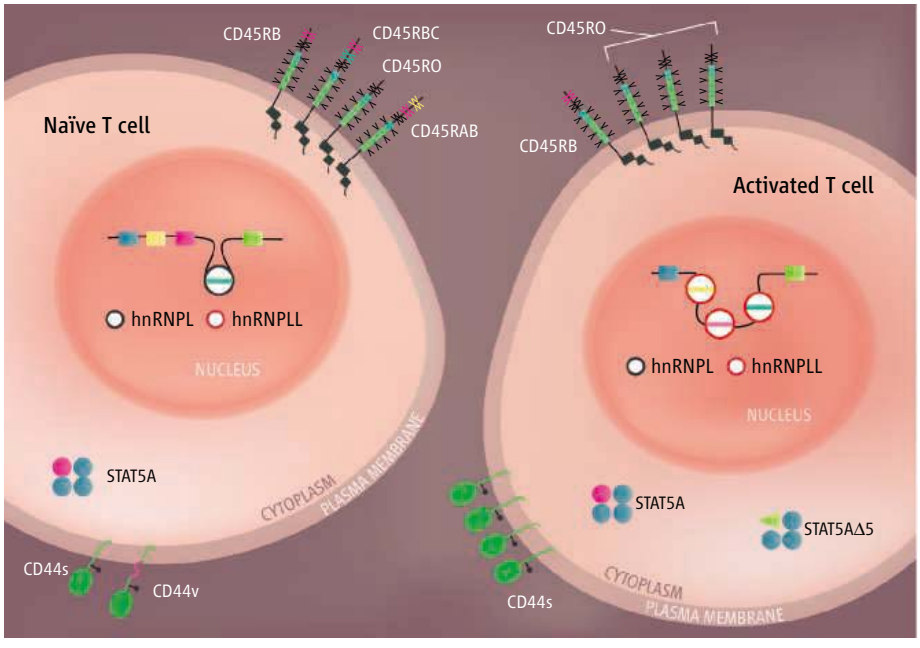

Master splicing regulator? The amount of hnRNPLL protein increases when T cells are activated. Precursor mRNAs encoding CD45, CD44, and STAT5A are among its targets, but the mechanism by which hnRNPLL controls alternative splicing (to generate different protein isoforms, as shown) remains unknown. Other factors (not shown) also control mRNA splicing.

Several single-nucleotide polymorphisms that alter splicing of CD45 have been identified in humans. Some reports found associations between such polymorphisms and susceptibility to a number of autoimmune and infectious diseases, but other studies have failed to find the same associations (*10*). Nonetheless, association of these mutations, particularly the mutation in exon 6 A138G that is linked to resistance to Graves' disease and hepatitis (*11*), would benefit from much larger studies. It would also be interesting to examine the interaction of these variants with hnRNPLL.

Division of Immunology, Department of Pathology, Cambridge University, Cambridge CB2 1QP, UK. E-mail: nh106@cam.ac.uk

CREDIT: ADAPTED BY N. KEVITIYAGALA/SCIENCE

Other intriguing precursor mRNAs whose splicing is controlled by hnRNPLL are CD44 and STAT5A. The details and consequences of CD44 isoform variation for T cell function are poorly understood. The best established fact about its expression in T cells is that naïve T cells express low amounts of CD44, whereas activated or antigen-experienced T cells express higher amounts. Whether hnRNPLL affects CD44 protein levels is unknown.

Initial concepts of cell type–specific single switches that propagate broad alternative splicing changes have been borne out in only a few cases (*4*). The identification of hnRNPLL as a putative "master regulator" of activation-induced splice changes in T cells should therefore provide new opportunities for work on the mechanism of splicing regulation and its functional consequences. Deleting the gene encoding hnRNPLL from the germline or from specific cell lineages in mouse models may test its importance in T cell function. Such experiments will not help to resolve the specific role of the change in CD45 isoforms if, as Oberdoerffer *et al*. suggest, hnRNPLL regulates a multiplicity of targets. Exon-specific mutations may be informative, although there is probably some coordinate regulation of CD45 splicing between the three variable exons (exons 4, 5, and 6), which share critical sequence motifs and binding of some splicing factors (*6*, *12*). Mutations that reduce hnRNPL binding by at least a factor of 10 have been described (*5*). If mutations can be identified that specifically affect hnRNPLL binding, then the introduction of such mutations into selected exons should help elucidate hnRNPLL function in vitro and the role of specific isoforms of CD45, and other target genes, in vivo.

References and Notes

1. J. Y. Ip *et al*., *RNA* **13**, 563 (2007).
2. M. L. Hermiston, Z. Xu, A. Weiss, *Annu. Rev. Immunol.* **21**, 107 (2003).
3. S. Oberdoerffer *et al*., *Science* **321**, 686 (2008); published online 10 July 2008 (10.1126/science.1157610).
4. A. J. Matlin, F. Clark, C. W. J. Smith, *Nat. Rev. Mol. Cell Biol.* **6**, 836 (2005).
5. A. A. Melton, J. Jackson, J. Wang, K. W. Lynch, *Mol. Cell. Biol.* **27**, 6972 (2007).
6. G. B. ten Dam *et al*., *J. Immunol.* **164**, 5287 (2000).
7. M. Hargreaves, E. B. Bell, *Immunology* **91**, 323 (1997).
8. R. J. Salmond, L. McNeill, N. Holmes, D. R. Alexander, *Int. Immunol.* **20**, 819 (2008).
9. Z. Xu, A. Weiss, *Nat. Immunol*. **3**, 674 (2002).
10. M. Gomez-Lira *et al*., *J. Neuroimmunol.* **140**, 216 (2003).
11. S. Boxall *et al*., *Hum. Mol. Genet.* **13**, 2377 (2004).
12. A. Tong, J. Nguyen, K. W. Lynch, *J. Biol. Chem.* **280**, 38297 (2005).

13. I thank A. Cooke, C. W. J. Smith, and J. Kaufman for comments.

10.1126/science.1162294

ASTRONOMY

The Cosmic Rosetta Stone

Numerical simulations of the first stars to appear in the universe may illuminate the general processes of star formation.

Volker Bromm

Cosmologists have made great strides in tracing the entire history of the universe, but there remains one crucial gap: the first billion years after the Big Bang when the first stars lit up the universe. Before the formation of the first stars, the universe was extremely simple, but evolved toward a state of increasing complexity. On page 669 of this issue, Yoshida *et al.* (*1*) present simulations of the initial steps in this grand cosmic transition, showing how tiny density fluctuations that were created through quantum processes in the early universe grew under the influence of gravity to eventually seed the formation of the very first stars.

The first stars are so important for cosmology because their emergence fundamentally changed the early universe at the end of the cosmic dark ages, setting the stage for the entire subsequent history of structure formation (*2*). Theoretical astrophysicists have constructed a "standard model" of how the first stars formed (*3*), with the main result that they typically had masses a few hundred times that of our Sun (*4*, *5*). This prediction derives from the inability of the primordial gas, consisting only of the hydrogen and helium synthesized in the Big Bang, to efficiently cool. The thermal pressure in the star-forming gas thus was considerably larger than in the present-day universe, where coolants composed of heavy chemical elements allow gas temperatures to drop to much lower values. For gravity to overwhelm the higher thermal pressure, the mass of the first stars must therefore have been large.

All previous first-star formation simulations, however, had to rely on a number of idealizations and extrapolations in arriving at the final mass estimate, rendering the standard model prediction still somewhat uncertain. Yoshida *et al.* have now carried out a key step toward the ambitious goal of simulating the formation of a primordial star in a completely ab initio, first-principle–based manner, without having to rely on approximations. This mind-boggling endeavor is made possible by the extraordinary simplicity in the early universe. We know both the initial conditions for the formation of the first stars, provided by the well-constrained cold dark matter (CDM) model of cosmological structure formation (*6*), and the relevant laws of physics that govern the evolution of the dark matter and the hydrogen-helium gas.

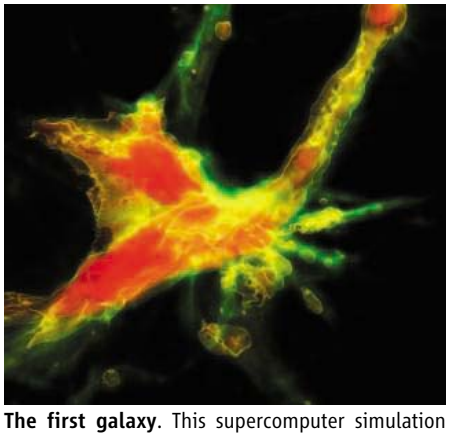

The first galaxy. This supercomputer simulation shows how one of the first galaxies was assembled at the end of the cosmic dark ages. Primordial matter flows along the filaments (red and yellow) toward the center where a cluster of primordial stars is likely to form. The assembly process sensitively depends on the properties of the first stars, in particular their mass.

CREDIT: CHRIS BURNS, THOMAS H. GREIF, JARRETT L. JOHNSON, RALF S. KLESSEN, VOLKER BROMM/TEXAS ADVANCED COMPUTING CENTER

This situation is in marked contrast to what theorists are confronted with in their attempt to understand star formation in the local universe (*7*). The initial conditions in the giant molecular clouds that are embedded in the disks of galaxies such as our Milky Way, where stars are born today, are exceedingly complex. These clouds are pervaded by strong magnetic fields, interacting with velocity fields that are organized by supersonic turbulence. The physics governing the star-formation process is of similar complexity. As a result, we still lack a complete theoretical model for how stars form in the present-day universe, despite the guidance from a huge body of observational data. The unique conditions in the early universe, where the initial conditions and governing physics are simple, may thus provide us with a cosmic Rosetta stone, enabling us to finally unlock the age-old problem of star formation.

Department of Astronomy, University of Texas, Austin, TX 78712, USA. vbromm@astro.as.utexas.edu

Yoshida *et al.* have reached a crucial halfway point by pushing their simulation all the way toward the formation of a primordial protostar, the small core inside the collapsing primordial cloud, where for the first time stellar densities, close to that of liquid water on Earth, are reached and where hydrostatic equilibrium is established, the almost exact balance between gravity and thermal pressure. This protostar will subsequently grow by accreting material from the surrounding envelope until the accretion flow is shut off by the ever more intense radiation emitted by the protostar (*8*, *9*). The protostellar accretion problem marks the next frontier in the field, but the present study provides a firm foundation for addressing this challenge. The ultimate goal of predicting the mass and properties of the first stars is now within reach.

The course of early cosmic history depends on this prediction. Specifically, if the first stars were indeed very massive, they were copious producers of heavy chemical elements that were rapidly dispersed into the cosmic matter in the wake of the first supernova explosions, and of ultraviolet photons that were energetic enough to ionize hydrogen, the most abundant element in the universe. The first stars therefore began the extended process of "reionization," which transformed the universe from a completely neutral state during the dark ages, when the universe was cold and contained no stars, into a fully ionized medium today. Observations of the degree of polarization, resulting from photons scattering off free electrons, in the cosmic microwave background, carried out by the Wilkinson Microwave Anisotropy Probe (WMAP), place constraints on the onset of reionization. The WMAP result indicates that about 30% of the total signal was produced by still unobserved stars during the first billion years after the Big Bang (*6*).

Once we understand the first stars, we can then begin to meaningfully consider the formation of the first galaxies (see the figure), which would contain clusters of many primordial stars (*10*, *11*). These small galaxies are believed to be the most distant sources that can be detected with the upcoming James Webb Space Telescope (JWST), planned for launch around 2013, and it is therefore important to predict their properties, such as colors, sizes, and luminosities. Their assembly is strongly influenced by the feedback from the first stars that formed during the process, due to the radiation and heavy elements produced by them. Again, the character and strength of the stellar feedback during the formation of the first galaxies sensitively depend on the mass distribution of the primordial stars.

Even before the JWST, we can test our theoretical predictions for the first stars by hunting for fossils from the dark ages in our local cosmic neighborhood. In this "stellar archaeology" approach, large surveys of low-mass stars are carried out in our Milky Way that contain only a tiny amount of heavy elements. These would carry the imprint of the first stars that produced those elements with an abundance pattern that strongly depends on their mass (*12*, *13*). Until now, the simulations were not detailed enough to make predictions with the required degree of precision, but Yoshida *et al.* have paved the way for stellar archaeology to fulfill its great potential. The combination of cutting-edge supercomputer simulations, large surveys of low-mass fossils in the Milky Way, and the deep images from the JWST promises to close the final gap in our cosmic worldview in the decade ahead. We are clearly entering a period of rapid discovery.

References and Notes

1. N. Yoshida, K. Omukai, L. Hernquist, *Science* **321**, 669 (2008).
2. R. Barkana, A. Loeb, *Phys. Rep.* **349**, 125 (2001).
3. V. Bromm, R. B. Larson, *Annu. Rev. Astron. Astrophys.* **42**, 79 (2004).
4. T. Abel, G. L. Bryan, M. L. Norman, *Science* **295**, 93 (2002).
5. V. Bromm, P. S. Coppi, R. B. Larson, *Astrophys. J.* **564**, 23 (2002).
6. D. N. Spergel *et al.*, *Astrophys. J. Supp.* **170**, 377 (2007).
7. C. F. McKee, E. C. Ostriker, *Annu. Rev. Astron. Astrophys.* **45**, 565 (2007).
8. K. Omukai, F. Palla, *Astrophys. J.* **589**, 677 (2003).
9. C. F. McKee, J. Tan, *Astrophys. J.* **681**, 771 (2008).
10. T. H. Greif, J. L. Johnson, R. S. Klessen, V. Bromm, *Mon. Not. R. Astron. Soc.* **387**, 1021 (2008).
11. J. H. Wise, T. Abel, *Astrophys. J.* **665**, 899 (2007).
12. T. C. Beers, N. Christlieb, *Annu. Rev. Astron. Astrophys.* **43**, 531 (2005).
13. A. Frebel, J. L. Johnson, V. Bromm, *Mon. Not. R. Astron. Soc.* **380**, L40 (2007).
14. V.B. acknowledges support from the U.S. National Science Foundation and NASA.

10.1126/science.1161710

CELL SIGNALING

"Make and Brake" in Signaling

Aristides G. Eliopoulos

Proteolysis of one component of a receptor-bound complex releases the complex from the cell surface to the cytoplasm to activate kinase signaling.

Understanding how cytokines and growth factors trigger intracellular signal transduction is a major challenge in cell biology. Of particular interest is the tumor necrosis factor (TNF)/TNF receptor superfamily, which encompasses more than 20 different ligands and 30 receptors involved in fundamental biological processes including apoptosis, immunity, inflammation, and organogenesis. Ligand binding triggers assembly of multiprotein complexes at the corresponding receptor intracellular domains. The cellular signaling pathways that dictate the biological outcome of ligand binding are thought to be initiated within the receptor-bound complexes and terminated by complex dissociation. A paper by Matsuzawa *et al.* on page 663 of this issue (*1*) suggests otherwise. By studying the signaling requirements for CD40, a TNF receptor family member with a prominent role in immune regulation and homeostasis, the authors elegantly demonstrate that activation of the c-Jun N-terminal kinase (JNK) and p38 mitogen-activated protein kinase (MAPK) cascades occurs only upon release of a CD40-tethered signaling complex. This two-step mechanism of signal initiation provides new insight into the intricate regulation of receptor-mediated signal transduction.

A major component of signaling by members of the TNF receptor superfamily is a group of cytoplasmic adaptor proteins known as TNF receptor–associated factors (TRAFs). Of the seven known mammalian TRAFs, CD40 directly binds TRAF2, TRAF3, and TRAF6 (*2*). TRAF2 and TRAF6 have attracted particular attention because although they lack intrinsic kinase activity, their ablation severely impairs CD40 signaling in lymphoid and nonhematopoietic cells (*3*–*5*). The contribution of TRAFs to signal transduction exceeds, however, their role as molecular bridges between TNF family receptors and intracellular signaling components. Indeed, both TRAF2 and TRAF6 possess E3 ubiquitin ligase activity and function together with the E2 ubiquitin-conjugating enzyme Ubc13 to catalyze the addition of lysine 63 (K63)–linked polyubiquitin chains to various protein kinases and cytoplasmic adaptors, including TRAFs themselves (*6*). Unlike lysine 48 (K48)–linked polyubiquitination, which signals for proteasome-

The University of Crete Medical School and Institute for Molecular Biology and Biotechnology, Foundation of Research and Technology Hellas, Heraklion, Greece. E-mail: eliopag@med.uoc.gr

dependent protein degradation, K63-linked polyubiquitination is nondestructive and activates protein kinases. Highlighting the significance of this modification in CD40 signal transduction, Ubc13-deficient B cells display impaired JNK and p38 MAPK activation in response to CD40 stimulation (*7*). Nevertheless, which protein kinase(s) in the signaling complex are targeted by TRAF2/Ubc13-dependent ubiquitination to activate MAPK signaling remains obscure.

Matsuzawa *et al.* analyzed the composition of the signaling complex assembled at the cytoplasmic tail of CD40 after receptor stimulation. The authors find that the binding of TRAF2 to CD40 is essential for recruitment of the K48-specific E3 ubiquitin ligase cellular inhibitor of apoptosis (c-IAP) and the K63 ligase Ubc13, followed by binding of IκB kinase γ (IKKγ) and MAP or extracellular signal–regulated kinase kinase 1 (MEKK1) (see the figure). IKKγ is best known as the regulatory subunit of the IκB kinase signaling complex involved in activation of the transcription factor nuclear factor κB (NF-κB). More recently, however, K63 ubiquitin-modified IKKγ has been found to influence MAPK activation induced by interleukin-1 and Toll-like receptor stimulation (*7*). Matsuzawa *et al.* show that the ubiquitination of IKKγ by TRAF2/Ubc13 is necessary for the recruitment of MEKK1 to the CD40-bound signaling complex (*1*). MEKK1 is a kinase operating at the start of MAPK cascades with a proven physiological role in CD40-induced MAPK signaling (*8*). It would thus be reasonable to predict that MEKK1 may be ubiquitinated by TRAF2/Ubc13 and activated within the CD40-bound signaling complex. Biological pathways are, however, notoriously unpredictable; thus, as Matsuzawa *et al.* report, MEKK1 associated with CD40 is neither ubiquitinated nor phosphorylated. Instead, ubiquitinated and phosphorylated MEKK1 is found in the cytosol in association with TRAF2, c-IAP, Ubc13, and IKKγ but not CD40. Within this complex, MEKK1 also interacts with and activates its substrates MKK4 and MKK3/6, which serve as JNK and p38 kinases, respectively. Thus, for MAPK signal activation, a complex assembled on CD40 must be released to the cytoplasm without dissociation.

What controls the release of this complex to the cytosol? The key here is shown to be TRAF3, which hetero-oligomerizes with TRAF2 but negatively regulates CD40-induced MAPK activation (*1*). Whereas TRAF2 undergoes both K63- and K48-linked polyubiquitination, TRAF3 undergoes only destructive K48-linked polyubiquitination that is catalyzed by c-IAPs and occurs rapidly at the level of the receptor. Concomitant with the proteasome-mediated degradation of TRAF3, the CD40-tethered signaling complex is released to the cytosol where MEKK1 is K63 polyubiquitin-modified by TRAF2/Ubc13 and activated (see the figure). TRAF2 therefore orchestrates MAPK signal initiation not only by nucleating an "effector" signaling complex at the cytoplasmic tail of CD40 but also by directing its release to the cytosol through the recruitment of c-IAP and the concomitant proteasome-mediated destruction of TRAF3. TRAF3 acts as a "brake" against premature signal initiation that is released when it is ubiquitinated.

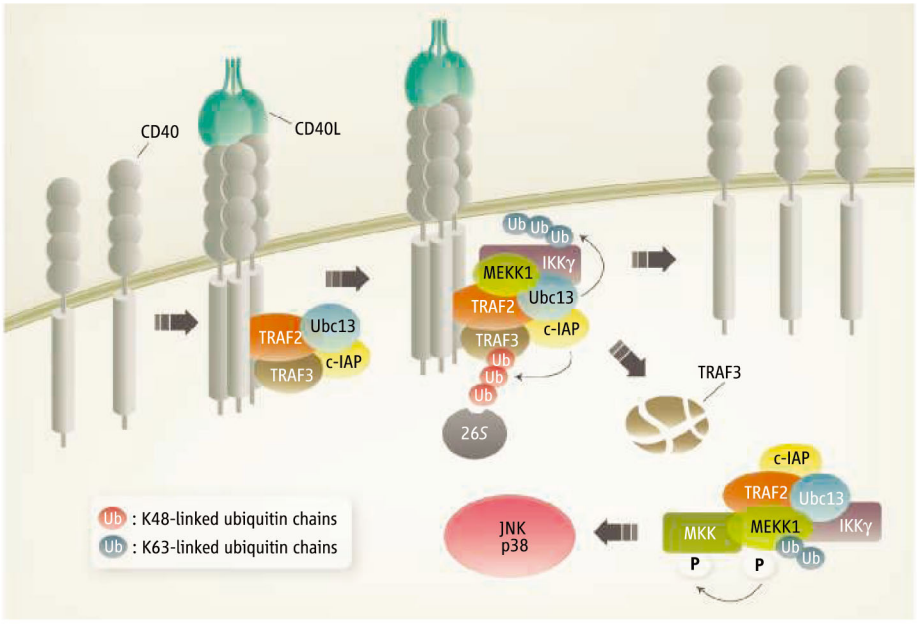

A two-stage mechanism of cytokine signaling. Matsuzawa *et al*. suggest that CD40 binding to the CD40 ligand (CD40L) stimulates receptor oligomerization and the formation of a CD40-tethered multiprotein signaling complex that is necessary but not sufficient for JNK and p38 MAPK activation. The latter requires the c-IAP–mediated K48-linked polyubiquitination of TRAF3 and its degradation by the proteasome (26*S*), which causes the release of the signaling complex from CD40 to the cytosol allowing activation of the MEKK1/MKK/MAPK module.

Matsuzawa *et al.* also study TRAF6 and show that it operates in a manner similar to TRAF2 but associates with the apical kinase transforming growth factor–β activated kinase 1 (TAK1) instead of MEKK1 to activate MAPK signaling in CD40-stimulated B cells. Whether the TRAF2 and TRAF6 complexes share components or are formed independently to activate the MAPK pathways remains to be seen (*4*). Moreover, the fate of the cytoplasmic TRAF complexes in the context of signal termination needs to be defined. Although TRAF2 degradation and complex disassembly may determine the termination phase, a role for deubiquitinating enzymes in silencing MAPK signaling cannot be excluded. Further studies are also required to define the mechanism of CD40-induced NF-κB activation, which is critically controlled by TRAF6 (*3*, *4*) but, unlike MAPK, is initiated exclusively at the level of the receptor (*1*). Given that TRAF expression substantially varies among cell lines and tissues (*9*), it is tempting to speculate that the pleiotropic and even biologically opposed consequences of CD40 stimulation may reflect differences in complex assembly and disassembly. There are tantalizing indications that the proposed two-step mechanism of MAPK activation might be more general. Matsuzawa *et al.* show that, similar to CD40, TNF receptor I–mediated MEKK1 and TAK1 phosphorylation are c-IAP–dependent and previous work has demonstrated that TNF stimulates the formation of two TNF receptor signaling complexes: a plasma membrane, receptor-bound complex that rapidly induces NF-κB activation and a slowly formed cytoplasmic complex that mediates apoptotic responses (*10*). Further studies are needed to place a two-step model of MAPK signaling in the context of these findings

References

1. A. Matsuzawa *et al.*, *Science* **321**, 663 (2008).
2. G. A. Bishop, *Nat. Rev. Immunol.* **4**, 775 (2004).
3. M. A. Lomaga *et al.*, *Genes Dev.* **13**, 1015. (1999).
4. C. C. Davies, T. W. Mak, L. S. Young, A. G. Eliopoulos, *Mol. Cell. Biol.* **25**, 9806 (2005).
5. L. T. Nguyen *et al.*, *Immunity* **11**, 379 (1999).
6. L. Deng *et al.*, *Cell* **103**, 351 (2000).
7. M. Yamamoto *et al.*, *Nat. Immunol.* **7**, 962 (2006).
8. E. Gallagher *et al.*, *Nat. Immunol.* **8**, 57 (2007).
9. J. M. Zapata *et al.*, *J. Immunol.* **165**, 5084 (2000).
10. O. Micheau, J. Tschopp, *Cell* **114**, 181 (2003).

10.1126/science.1162212

CLIMATE CHANGE

Did You Say "Fast"?

Greenland ice-core data show that large climatic shifts can occur within just 1 to 3 years.

Jacqueline Flückiger

When Manhattan froze in a day in the movie *The Day After Tomorrow* as a result of an abrupt change in the Atlantic meridional overturning circulation, scientists emphasized the physical impossibility of this scenario. Now some might be stunned by how quickly climate can change. On page 680 of this issue, Steffensen *et al.* (*1*) zoom in on three climatic shifts recorded in the NGRIP ice core from central Greenland (see the photo) (*2*) and show that the atmospheric circulation at mid to high northern latitudes changed within just 1 to 3 years.

The authors study the onset of the Bølling-Allerød warm period (~14,700 years ago) and the onset (~12,850 years ago) and termination (~11,700 years ago) of the Younger Dryas cold period. For each shift, they present reconstructions with subannual resolution of $\delta^{18}O$ (a proxy for local temperature), deuterium excess (a proxy for ocean surface temperature at the source region of the NGRIP precipitation), dust and calcium (originating from low-latitude Asian deserts), sodium (a marine sea salt indicator), and local accumulation rates. The high resolution of the records allows them to precisely define the duration of the shifts, and because all measurements were done along the same ice core, the sequence of events in different proxies can be compared without uncertainty in the relative timing.

How climate shifts. The ice core drilled at NGRIP in central Greenland revealed rapid climatic shifts in the past. Steffensen *et al.* now report a multiproxy analysis of the ice that sheds detailed light on their timing and mechanisms.

The surprising result is that the deuterium excess shifts within 1 to 3 years. The authors interpret the deuterium excess data as a reorganization of the atmospheric circulation in mid to high northern latitudes, leading to a spatial shift in the source region and, therefore, the source temperature of the precipitation. The deuterium excess shift happens very early, whereas the other records continue to change gradually over the subsequent 50 to 150 years.

Generally, abrupt climatic events such as those studied by Steffensen *et al.* are associated with changes in the strength of the Atlantic meridional overturning circulation (*3*). Steffensen *et al.* hypothesize that additionally, the Northern Hemisphere atmospheric circulation had a very sensitive threshold, which led to the observed fast reorganization. The slower changes found in Greenland temperature and dust might be dominated by the effects of the slower changing ocean circulation and its far-field effects.

Are these ice-core results supported by other paleorecords? A reorganization of the atmospheric circulation implies changes in wind fields, which will affect paleo-archives sensitive to wind-driven upwelling. Examples in the North Atlantic region are varved sediments from lakes (*4*) and laminated marine deposits such as those from the Cariaco Basin (*5*). So far, the resolution of the published records from these archives is insufficient to conclude that changes happened within just a few years, but annual resolution is within reach.

A reorganization of the atmospheric circulation may also influence the monsoon systems. Speleothems in Asia have revealed precipitation shifts lasting only a decade at the end of the Younger Dryas (*6*). In the hunt for annually resolved speleothems, Treble *et al.* (*7*) found one very abrupt shift 16,070 years ago, lasting only a few years. They hypothesize that the event is related to a reorganization of the atmospheric circulation during Heinrich event 1, a strong ice discharge event in the North Atlantic. Although Heinrich events are usually not seen in Greenland ice cores, it may be worth searching for an abrupt deuterium excess shift, especially because the low-resolution deuterium-excess record measured along the GRIP ice core shows a substantial change around the same time (*8*).

But rapid change is not the whole story. For the onset of the Bølling-Allerød and the termination of the Younger Dryas, Steffensen *et al.* find that the dust starts to decrease about a decade before the rapid deuterium-excess shift. This implies that the precipitation in Asia intensified before the reorganization of the atmospheric circulation at mid- to high latitudes. The first sign of climatic change may thus originate from Asia and not from the North Atlantic region.

Other records also show precursor events to the North Atlantic changes. One example is the atmospheric N_2O record measured along the GRIP and NGRIP ice cores for a series of warm events—called Dansgaard-Oeschger events—that were similar to the Bølling-Allerød but took place during the last glacial period. The N_2O concentration variations resemble the pattern of Northern Hemisphere climate events, but the N_2O concentration starts to rise a few centuries before the Greenland warming (*9*). Early changes for the same events are also found in intermediate-water-temperature tracers measured along a marine core from the Santa Barbara Basin (*10*). These records indicate that parts of the climate system started to move toward a new state before the abrupt transition in the North Atlantic.

Global coupled climate models provide one way to study the complex mechanisms that underlie climate shifts. Simulated climate shifts are, however, considerably slower than the observed ones, lasting a hundred to a few hundred years (*11*, *12*). This might be due to missing feedbacks, the wrong forcing of the abrupt shifts, or a misguided focus on changes in ocean circulation or temperature, rather than other aspects of the climate system. A closer look at wind patterns and atmospheric circulation in models will either reveal faster shifts and help clarify the underlying mechanisms, or tell us that better models are needed to study that question.

Environmental Physics, Institute of Biogeochemistry and Pollutant Dynamics, ETH Zürich, Universitätstrasse 16, 8092 Zürich, Switzerland. E-mail: jacqueline.flueckiger@env.ethz.ch

We should keep in mind that we only know the relative timing for three events so far, and that each of them looks somewhat different (*1*). Greenland ice cores offer the opportunity to study the 24 Dansgaard-Oeschger events of the last glacial period at a similar resolution. The data from all events, in combination with annually resolved records from other archives and improved models, will help to elucidate the dynamics of these events, revealing what they have in common, and what parts of the shifts are random.

The data reported by Steffensen *et al.* underscore the fact that the atmospheric circulation may shift from one state to another within just 1 year. With ongoing global warming, the climate system might therefore hold some surprises.

References

1. J. P. Steffensen *et al., Science* **321**, 680 (2008); published online 19 June 2008 (10.1126/science.1157707).
2. North Greenland Ice Core Project members, *Nature* **431**, 147 (2004).
3. S. Rahmstorf, *Nature* **419**, 207 (2002).
4. A. Brauer *et al.*, *Quat. Sci. Rev.* **18**, 321 (1999).
5. L. C. Peterson, G. H. Haug, K. A. Hughen, U. Röhl, *Science* **290**, 1947 (2000).
6. Y. J. Wang *et al.*, *Science* **294**, 2345 (2001).
7. P. C. Treble *et al.*, *Chem. Geol.* **238**, 197 (2007).
8. V. Masson-Delmotte *et al.*, *Science* **309**, 118 (2005).
9. J. Flückiger *et al.*, *Global Biogeochem. Cycles* **18**, GB1020 (2004).
10. I. L. Hendy, J. P. Kennett, *Quat. Sci. Rev.* **22**, 673 (2003).
11. R. J. Stouffer *et al.*, *J. Clim.* **19**, 1365 (2006).
12. J. Flückiger, R. Knutti, J. W. C. White, H. Renssen, *Clim. Dyn.* 10.1007/s00382-008-0373-y (2008).

10.1126/science.1159821

MATERIALS SCIENCE

Electrochemical Capacitors for Energy Management

Rapid storage and efficient delivery of electrical energy in heavy-duty applications are being enabled by electrochemical capacitors.

John R. Miller[1] and Patrice Simon[2]

Energy storage technology is a key element in harvesting the kinetic energy that is wasted whenever vehicles or large machines must be slowed or stopped. Although batteries have been successfully used in light-duty vehicles, hybrid platforms for trucks and buses will require storage and delivery of much higher currents than can be accommodated readily by batteries. Unlike batteries, electrochemical capacitors (ECs) can operate at high charge and discharge rates over an almost unlimited number of cycles and enable energy recovery in heavier-duty systems.

Like all capacitors, ECs (also called supercapacitors or ultracapacitors because of their extraordinarily high capacitance density) physically store charge. Conventional electrostatic and electrolytic capacitors store charge on low-surface-area plates, but ECs store charge in an electric double layer set up by ions at the interface between a high-surface-area carbon electrode and a liquid electrolyte (*1*, *2*). ECs first appeared on the market in 1978 as farad-sized devices to provide computer memory backup power.

A simple EC can be constructed by inserting two conducting rods in a beaker of salt water. During charging, charge separation occurs at each liquid-solid interface and potential builds up between the rods. Solvated ions in the electrolyte are rapidly attracted to the solid surface by an equal but opposite charge in the solid. These two parallel regions of charge are the source of the term "double layer." This process in effect creates two capacitors, connected in series by the electrolyte, that stay charged after the circuit is opened. Because the surface area of activated carbon electrode material can be thousands of square meters per gram, a 5000-farad EC (a million times the capacitance offered by typical electrostatic or electrolytic capacitors) can be small enough to be handheld.

This very high capacitance comes at a cost: The operating voltage of an EC cannot exceed the potential at which the electrolyte undergoes chemical reactions (typically 1 to 3 V per cell). For high-voltage applications, EC cells, like batteries, can be series-connected.

ECs at work. Hybrid diesel/electric rubber-tired gantry crane with DLCAP electrochemical capacitor energy storage system (fuel savings of 40% are typical).

Property	Battery	Electrochemical capacitor
Storage mechanism	Chemical	Physical
Power limitation	Reaction kinetics, mass transport	Electrolyte conductivity
Energy storage	High (bulk)	Limited (surface area)
Charge rate	Kinetically limited	High, same as discharge rate
Cycle life limitations	Mechanical stability, chemical reversibility	Side reactions

Comparison of properties of rechargeable batteries and electrochemical capacitors.

One of the most important advantages of batteries over ECs is that for a given volume, they can store 3 to 30 times more charge. However, ECs can deliver hundreds to many thousands of times the power of a similar-sized battery. In addition, the highly reversible electrostatic charge storage in ECs does not produce the changes in volume that usually accompany the redox reactions of the active masses in batteries. Such volume changes are the main cause of

[1]JME Inc., 17210 Parkland Drive, Shaker Heights, OH 44120, USA. [2]Université Paul Sabatier, CIRIMAT UMR-CNRS 5085, 31062 Toulouse, France. E-mail: jmecapacitor@att.net; simon@chimie.ups-tlse.fr

PHOTO CREDIT: NIPPON CHEMI-CON CORPORATION

the limited cycle life of batteries (generally several hundred to a few thousand cycles), compared to demonstrated full charge-discharge cycles for ECs into the many millions. The major differences between rechargeable (secondary) batteries and ECs, and their important fundamental properties, are compared in the table.

An important related class of energy storage devices are pseudocapacitors, which undergo electron transfer reactions but behave like capacitors. These materials store energy through highly reversible surface redox (faradic) reactions in addition to the electric double-layer storage. Materials that exhibit such pseudocapacitive storage (*1*) range from conducting polymers to a variety of transition metal oxides (*3*–*5*). The RuO_2 pseudocapacitor has the highest specific capacitance (~1000 F/g) in this class, but is prohibitive in price (a vehicle-sized EC of RuO_2 would cost more than $1 million). Efforts to develop more practical pseudocapacitive materials are now quite active.

The second generation of ECs used symmetric designs and organic electrolytes—typically an ammonium salt dissolved in an organic solvent such as propylene carbonate—which increased the rated cell voltage from under 1 V to ~2.5 V per cell. The most recent EC designs, which date from Russian patents in the mid-1990s, are asymmetric. One electrode is identical to those used in symmetric ECs, whereas the other is battery-like (relying on electron charge transfer reactions) but has much greater capacity and higher operating voltage. Asymmetric capacitors with specific energies of >10 watts-hour/kg are commercially available (*6*) and are well suited for transportation (traction) applications. Charging times for such systems are ~10 min.

Several asymmetric EC designs under development (*7*–*9*) use a lithium-ion intercalation electrode with an activated carbon electrode in an organic electrolyte (*7*) or an activated carbon electrode with a lead dioxide battery-like electrode and sulfuric acid as the electrolyte, with the potential of specific energies in excess of 20 watts-hour/kg at very low cost (*8*). Each of these designs can provide high cycle life relative to that of a battery because of the electrode capacity asymmetry. Capacity asymmetry reduces the depth of discharge of the battery-like electrode, thereby increasing its cycle life and power performance.

Symmetric ECs with specific energies of ~5 watts-hour/kg and response times of 1 s are widely available and can be used to store and release regenerative braking energy efficiently in vehicles and industrial equipment. They can also be used for load leveling—delivering power above the average value provided by a distributed generator (such as a fuel cell) and storing excess energy when power levels are below average.

Although lithium-ion batteries have advanced greatly in recent years, they still require 3 to 5 min for charging, versus ~1 s for an EC. Thus, battery systems generally must be grossly oversized in such applications to improve their efficiency and to lengthen their cycle life. Also, ECs are generally much safer than batteries during high-rate charge and discharge.

Finally, ECs are being used across a vast swath of commercial and industrial equipment. One example is a seaport rubber-tired gantry crane (see the figure) that has a capacitor system to store energy during load lowering. The use of ECs has reduced its energy usage by 40%.

References and Notes

1. B. E. Conway, in *Electrochemical Supercapacitors: Scientific Fundamentals and Technological Applications* (Kluwer Academic/Plenum, New York, 1999).
2. J. Chmiola *et al.*, *Science* **313**, 1760 (2006); published online 16 August 2006 (10.1126/science.1132195).
3. I. D. Raistrick, R. J. Sherman, in *Proceedings of the Symposium on Materials for Energy Conversion and Storage*, S. Srinivasan, S. Wagner, H. Wroblowa, Eds. (Electrochemical Society, Pennington, NJ, 1987), pp. 582–593.
4. M. Mastragostino, K. Arbizzani, F. Soavi, *Solid State Ionics* **148**, 493 (2002).
5. M. S. Hong, S. H. Lee, S. W. Kim, *Electrochem. Solid State Lett.* **5**, A227 (2002).
6. Available from JSC ESMA, OKB FIAN, Troitsk 142190, Russia (www.esma-cap.com).
7. T. Morimoto, paper presented at the International Conference on Advanced Capacitors, 28 to 30 May 2007, Kyoto, Japan.
8. S. A. Kazaryan *et al.*, *J. Electrochem. Soc.* **153**, A1655 (2006).
9. A. Balducci *et al.*, *Electrochim. Acta* **50**, 2233 (2005).

10.1126/science.1158736

CLIMATE CHANGE

Ecosystem Disturbance, Carbon, and Climate

Steven W. Running

Models of climate change effects should incorporate land-use changes and episodic disturbances such as fires and insect epidemics.

The terrestrial carbon cycle provides a sink for about 25% of the anthropogenic carbon emissions that increase atmospheric CO_2. Comprehensive models based on a detailed understanding of this carbon sink are needed to inform mitigation strategies aimed at stabilizing climate and adaptation strategies to minimize biospheric impacts. Can current models represent the full global range of ecosystem dynamics and both interannual and episodic variabilities that determine the strength of the terrestrial sink?

In early global climate models, or general circulation models (GCMs), the land surface was merely a necessary boundary condition influencing momentum dissipation, energy balance, and moisture content of the atmosphere. In 1983, Robert Dickinson was the first to explicitly represent the biophysics of ecosystems in a GCM. The next generation of land models in GCMs—used in the Intergovermental Panel on Climate Change (IPCC) Fourth Assessment (*1*)—incorporated biogeochemical principles of ecosystems, notably the carbon cycle and vegetation controls on the water cycle. Photosynthesis was explicitly computed from principles grounded in cellular biochemistry, with important sensitivity to changing atmospheric CO_2. Ecosystem releases of CO_2 from plant respiration and decomposition of dead material were incorporated in the models to complete land carbon balances.

Yet, a recent intercomparison illuminated a distressing disagreement of 11 land models attempting to simulate future atmospheric CO_2 with interactive terrestrial carbon balances (*2*). Some models predicted dramatic enhancements in photosynthesis for a doubled-CO_2 atmosphere, whereas others computed enhanced respiration and decomposition from the higher temperatures. The model responses of annual net primary production (NPP) for a doubled-CO_2 atmosphere ranged from near zero to 60%, with the average response about 40%. However, none of these models had nitrogen limitations.

To allow more confidence in future simulations, field programs are being used to improve these land models. For example, the

Numerical Terradynamic Simulation Group, College of Forestry, University of Montana, Missoula, MT 59812, USA. E-mail: swr@ntsg.umt.edu

FLUXNET global network of eddy-covariance flux towers provides full daily and seasonal cycles of net ecosystem carbon flux in multiple biome types and climates worldwide. Testing the NCAR Community Land Model against carbon and water flux data from 15 diverse FLUXNET sites revealed a need for improved water balance calculations that can simulate soil water deficits more accurately and highlighted nitrogen limitations on photosynthetic capacity (*3*). Combining seasonal eddy flux data, satellite greenness index data, and atmospheric CO_2 concentration data has illustrated some surprising carbon cycle feedbacks. Warming temperatures in the Northern Hemisphere have lengthened frost-free growing seasons and favor enhanced photosynthesis in the spring, but also enhanced respiration in the autumn, virtually canceling out any net gain in the annual terrestrial carbon sink (*4*). Land models must accurately represent this intricate seasonal balance between photosynthesis and respiration.

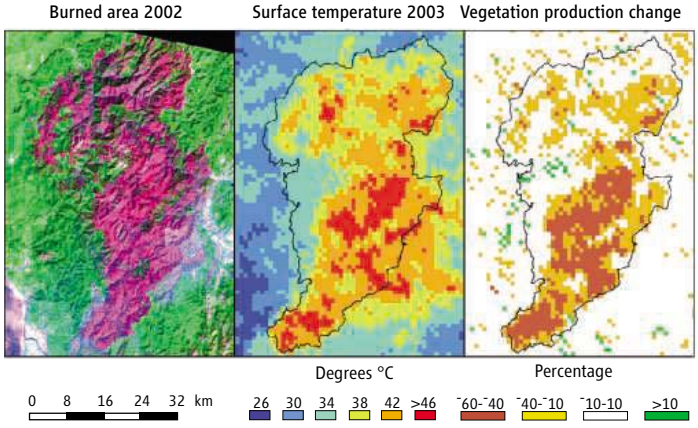

Impact of fire disturbance on land surface energy and carbon balances. In the summer of 2002, the Biscuit Fire in Oregon destroyed 2000 km^2 of temperate evergreen forests (**left**). A Moderate Resolution Imaging Spectroradiometer (MODIS) satellite image taken on 28 July 2003 (**middle**) shows land surface radiometric temperatures of 46° to 50°C in the area burned the summer before, whereas temperatures in the adjacent unburned forests range from 27° to 32°C. Annual vegetation production measured from MODIS (*4*) (**right**) was 20 to 60% lower in the burned area in 2003 to 2004 than before the wildfire.

The latest challenge is to expand flux tower–based measurements to global scales across the full range of biomes and climates. Currently, the only terrestrial carbon flux variable measured globally on a regular basis is NPP (*5*). A new modeling test, C-LAMP (Carbon Land Model Intercomparison Project), compares annual NPP from the current-generation GCM land models with global satellite derived NPP; correlations of 0.85 to 0.91 clearly show the models are improving (*6*).

A recent FLUXNET synthesis found that disturbance was the primary mechanism that changes ecosystems from carbon sinks to sources (*7*). Disturbances like fire change the energy, water, and carbon balances of a land surface dramatically and often instantly. In tropical areas, cropland and grazing fields are burned annually to clear away unwanted plant debris and stimulate new plant growth. A fire first releases a pulse of carbon and then reduces the albedo of a surface from 15 to 20% to around 4% (*8*). The blackened surface absorbs much more incident solar energy, and with little live vegetation remaining for evaporative cooling, midday surface temperatures can easily reach 50°C (see the figure). Albedo may recover from resprouting vegetation within a few months in a tropical grassland, but require decades in a boreal forest. Global fires burn an estimated 3.0 to 4.5 million km^2 per year—about 4% of vegetated land surfaces—and emit 2 to 3 Pg of carbon into the atmosphere annually, equivalent to 30% of fossil-fuel emissions (*9*). A recent analysis of accelerating wildfire trends completely reversed the earlier expectation that Canadian forests would be a future net carbon sink as warming temperatures extend the boreal growing season (*10*).

Less extreme disturbances like windstorms or insect epidemics do not change the surface albedo dramatically but shift trees from live carbon sinks to dead and slowly decaying carbon sources over substantial areas. In 2005, Hurricane Katrina killed an estimated 320 million trees in the southeastern United States; these trees became a carbon source of about 0.1 Pg, nullifying the entire annual terrestrial carbon sink of the rest of U.S. forests for that year (*11*). An unprecedented mountain pine beetle epidemic in western North America that started in 1999 in British Columbia is flipping an estimated 470,000 km^2 of forest land from a small annual carbon sink to a nearly equivalent carbon source from dead trees that will decompose over decades (*12*, *13*). Current land models cannot recreate such episodic ecosystem disturbances mechanistically with proper climatic triggers, and no systematic global monitoring of disturbance exists, although prototypes are under development (*14*).

The next generation of GCMs must additionally represent the human-driven biogeographical dynamics of land cover and land-use change through urbanization, agricultural land conversion and grazing, deforestation, episodic disturbances, and the feedback responses of these processes to the atmosphere. According to current satellite-based estimates, 17 million km^2, or 14% of the land surface, has been changed by human agricultural activity, and another 28% is used for domestic animal grazing (*15*). Every year, new human land-use activities are adding 1.1 Pg of carbon to the atmosphere, in addition to the 8 Pg per year of fossil fuel carbon emissions; this trend will probably accelerate with growing population (*16*). GCM runs can be initialized with satellite data sets of existing land cover, but must then simulate both future climates and changing land-use patterns.

It is unlikely that all these new ecosystem details can be added to the land models of leading GCMs in time for the IPCC Fifth Assessment simulations that are expected to start within the next 2 years. Predicting specific disturbance events is not necessary for global science; regional average occurrence rates should suffice. The GCMs must then represent the pulse of carbon emission and subsequent recovery in ecosystem biogeochemistry, and the probabilities of extreme climatic events that trigger these disturbances. The most socially important question is whether these disturbance rates will increase in the future.

References

1. IPCC, *Climate Change 2007: The Physical Science Basis. Contribution of Working Group I to the Fourth Assessment Report of the Intergovernmental Panel on Climate Change*, S. Solomon *et al.*, Eds. (Cambridge Univ. Press, Cambridge, UK, and New York, NY, 2007).
2. P. Friedlingstein *et al.*, *J. Climate* **19**, 3337 (2006).
3. R. Stockli *et al.*, *J. Geophys. Res.* **113**, G01025 (2008).
4. S. Piao *et al.*, *Nature* **451**, 49 (2008).
5. S. W. Running *et al.*, *Bioscience* **54**, 547 (2004).
6. Carbon-Land Model Intercomparison Project; www.climatemodeling.org/c-lamp.
7. D. Baldocchi, *Australian J. Botany* **56**, 1 (2008).
8. J. T. Randerson *et al.*, *Science* **314**, 1130 (2006).
9. K. Tansey *et al.*, *Geophys. Res. Lett.* **35**, L01401 (2007).
10. W. A. Kurz, G. Stinson, G. J. Rampley, C. C. Dymond, E. T. Wilson, *Proc. Natl. Acad. Sci. U.S.A.* **105**, 1551 (2008).
11. J. Q. Chambers *et al.*, *Science* **318**, 1107 (2007).
12. K. F. Raffa *et al.*, *Bioscience* **58**, 501 (2008).
13. W. A. Kurz *et al.*, *Nature* **452**, 987 (2008).
14. D. J. Mildrexler, M. Zhao, F. A. Heinsch, S. W. Running, *Ecological Appl.* **17**, 235 (2007).
15. J. A. Foley *et al.*, *Science* **309**, 570 (2005).
16. K. M. Strassman, F. Joos, G. Fischer, *Tellus B;* 10.1111/j.1600-0889.2008.00340.x (2008).

10.1126/science.1159607

Hopping Hotspots: Global Shifts in Marine Biodiversity

W. Renema,[1,4*] D. R. Bellwood,[2] J. C. Braga,[3] K. Bromfield,[4] R. Hall,[5] K. G. Johnson,[6] P. Lunt,[7] C. P. Meyer,[8] L. B. McMonagle,[6,9] R. J. Morley,[5,10] A. O'Dea,[11] J. A. Todd,[6] F. P. Wesselingh,[1] M. E. J. Wilson,[12] J. M. Pandolfi[4]

Hotspots of high species diversity are a prominent feature of modern global biodiversity patterns. Fossil and molecular evidence is starting to reveal the history of these hotspots. There have been at least three marine biodiversity hotspots during the past 50 million years. They have moved across almost half the globe, with their timing and locations coinciding with major tectonic events. The birth and death of successive hotspots highlights the link between environmental change and biodiversity patterns. The antiquity of the taxa in the modern Indo-Australian Archipelago hotspot emphasizes the role of pre-Pleistocene events in shaping modern diversity patterns.

One of the most striking patterns in marine biogeography is the tropical center of maximum diversity in the Indo-Australian Archipelago (IAA). Many coral reef groups reach their greatest diversity here (*1*, *2*), a pattern that is also reflected in a wide range of taxa in other shallow marine ecosystems (*3*–*5*). This taxonomic richness pattern has been related to a multitude of mechanisms, usually associated with the spatial distribution of modern parameters or processes, and has engendered vigorous debate (*3*, *6*–*9*). It is the focus of numerous evolutionary and ecological theories (*8*, *10*–*13*) and has underpinned strategies for current conservation efforts (*14*). The potential role of the IAA as a museum or cradle for biodiversity has highlighted the importance of the history of the region (*12*, *15*). Moreover, recent discoveries that incorporate the fossil record and evolutionary history of taxa in the IAA hotspot provide an insightful perspective of the history of biodiversity hotspots, that is, geographical areas of maximal biodiversity in a given time interval.

The combination of molecular evidence and the fossil record provides a powerful tool for understanding the spatial and temporal dynamics leading to current biodiversity patterns (*4*, *16*, *17*). Despite the apparent complexity of the IAA, our knowledge of the fossil record of this region is expanding rapidly as new collections clarify taxonomic, paleoenvironmental, and chronostratigraphic relationships. These recent advances have revealed a striking pattern of profound importance for our understanding of the evolutionary history of the IAA hotspot. Its presence has traditionally been attributed to either a speciation pump, as a result of the relationship between Pleistocene sea level changes and the complex geography of the area, or as a result of accumulation, reflecting the exceptional environmental features of the region (*1, 3, 7, 13, 18*). These hypotheses are derived from analysis of present-day richness patterns. However, this approach is spatially and temporally constrained. Here, we review recent evidence showing that biodiversity hotspots have moved across almost half the globe over the past 50 million years (My) and that the age of the taxa characterizing the modern IAA biodiversity hotspot is much older than previously thought.

Hopping Hotspots

The biogeography of large benthic foraminifera through time shows remarkable similarities with that of other tropical shallow marine organisms (*19*). This is not surprising but does show that large benthic foraminifera can be used for measuring overall diversity in tropical marine environments, not least because of their high abundance and good fossil record (*19*). During the Eocene, global α-diversity (number of genera found at a single location) peaked in southwest Europe, northwest Africa, and along the eastern shore of the Arabian Peninsula, Pakistan, and West India (*20*) (Fig. 1A). Likewise, the fossil record of mangroves and reef corals suggests maximal global diversity in this West Tethyan hotspot during the Eocene, and the diversity of mollusk assemblages was highest at the northwest margin of the West Tethyan region (*5*, *15*, *21*–*24*).

By the Late Eocene, the highest α-diversity is recorded in the Arabian hotspot (*20*, *25*), centered around the Middle East. The Late Eocene Arabian hotspot has an overlapping taxonomic composition with the earlier West Tethyan hotspot, and the Miocene Arabian and IAA hotspots also have broadly overlapping taxonomic compositions (Fig. 1B). For both large benthic foraminifera genera and mangrove pollen types, the Miocene is the most diverse period in southeast Asia, centered around the Philippines–Papua New Guinea region, partly because of the overlapping occurrence of Paleogene and extant taxa (*20*, *23*). Habitat loss, largely due to regional uplift during the Arabia-Eurasia collision, resulted in extensive faunal depletion and the demise of the Arabian hotspot during the Middle to Late Miocene. Similarly, the cowrie gastropods largely disappeared from Europe and the Middle East during the Late Miocene (*22*). The area of maximal diversity of tridacnine bivalves likewise shows an eastward shift, with a diverse West Tethyan fauna from the Eocene and a modern fauna with highest diversity in the IAA (*24*).

With the loss of the Arabian hotspot, the modern configuration appeared (Fig. 1C). The fossil record of large benthic foraminifera, mangrove pollen types, gastropods, and corals shows that this high α-diversity was present at least since the Early Miocene [20 million years ago (Ma)]. These patterns indicate the surprising antiquity of the IAA hotspot. To explore this antiquity, we turn to the ages of the modern taxa inhabiting this region (Fig. 2).

Origins of IAA Biodiversity: Heat in the Miocene

Contrary to previous expectations (*26*–*28*), the vast majority of extant IAA taxa for which a fossil record is available first occurred before the Pleistocene (Fig. 3). All but one of the 24 extant large benthic foraminifera genera originated during the Pliocene or earlier, with seven genera having an Eocene or earlier origin and two occurring for the first time during the Oligocene (*20*). Likewise, all modern mangrove pollen types have been present in the IAA since the Late Miocene, with most genera extending back to the Eocene (*5*, *6*, *23*) and all mangrove species, where they can be identified on pollen characters, extending to the Miocene (*23*, *29*). In the corals, the modern subgenus *Acropora* (*Acropora*) was represented by the precursors of 9 out of 20 currently recognized morphological groups during the Eocene in the Paris Basin, and the earliest occurrence of this genus in the IAA is from the Early Miocene (*21*). In the cowries, 9 out of 12 IAA genera with a known fossil record are first recorded from the Miocene (*22*). Finally, of the 69 extant IAA tonnoid species with a fossil record, 67 have their first occurrence in the Miocene (*30*). These patterns are particularly striking given the potential dampening effect of the "pull of the recent," causing the extension of stratigraphic ranges of fossil taxa by the relatively complete sampling of the Recent biota (*31*).

[1]Nationaal Natuurhistorisch Museum, Naturalis, 2300 RA, Leiden, Netherlands. [2]Australian Research Council Centre of Excellence for Coral Reef Studies, School of Marine and Tropical Biology, James Cook University, Townsville, QLD 4811, Australia. [3]Departamento de Estratigrafia y Paleontologia, Universidad de Granada, 18002 Granada, Spain. [4]Australian Research Council Centre of Excellence for Coral Reef Studies, Centre for Marine Studies, University of Queensland, Brisbane, QLD 4072, Australia. [5]Southeast Asia Research Group, Royal Holloway University of London, Egham, Surrey TW20 0EX, UK. [6]Department of Paleontology, The Natural History Museum, London SW7 5BD, UK. [7]Murphy Oil, Kuala Lumpur 50088, Malaysia. [8]National Museum of Natural History, Smithsonian Institution, Washington, DC 20013, USA. [9]Department of Earth Sciences, University of Durham, Durham DH1 3LE, UK. [10]Palynova, Littleport CB6 1PY, UK. [11]Smithsonian Tropical Research Institute, Balboa, Ancón, Republic of Panamá. [12]Department of Applied Geology, Curtin University, Perth, WA 6845, Australia.

*To whom correspondence should be addressed. E-mail: Renema@naturalis.nl

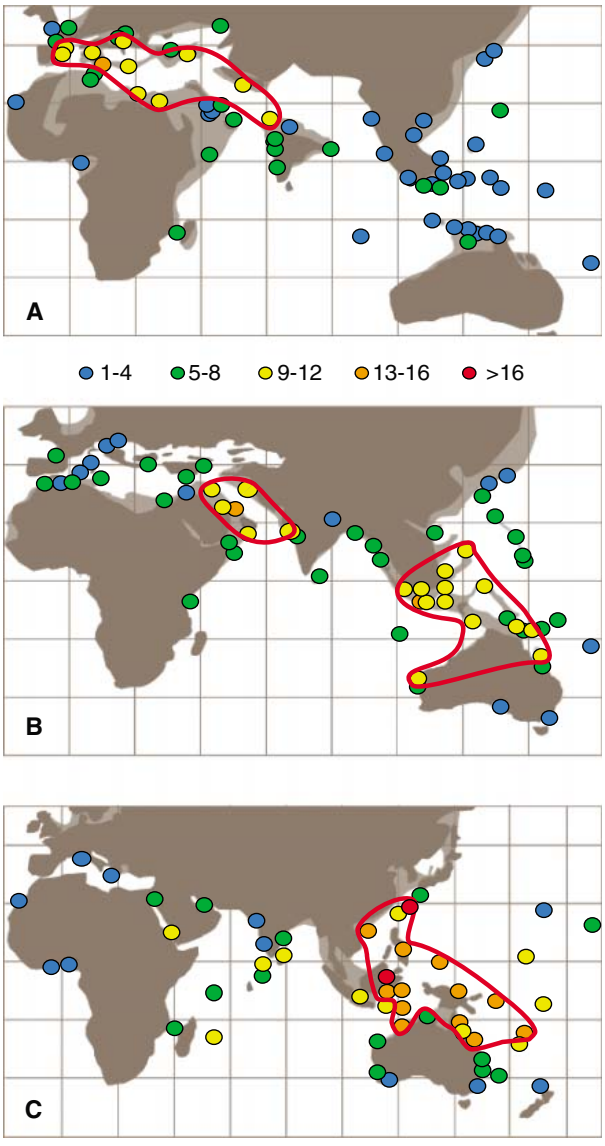

Fig. 1. Generic α-diversity of large benthic foraminifera in (**A**) the late Middle Eocene (42 to 39 Ma), (**B**) the Early Miocene (23 to 16 Ma), and (**C**) the Recent. Solid lines delimit the West Tethys, Arabian, and IAA biodiversity hotspots (tables S1 to S3). Note the relocation of hotspots across the globe. Where multiple studies occurred at a single locality, the highest recorded diversity is reported. Paleogeographic reconstructions modified after (*41*, *42*).

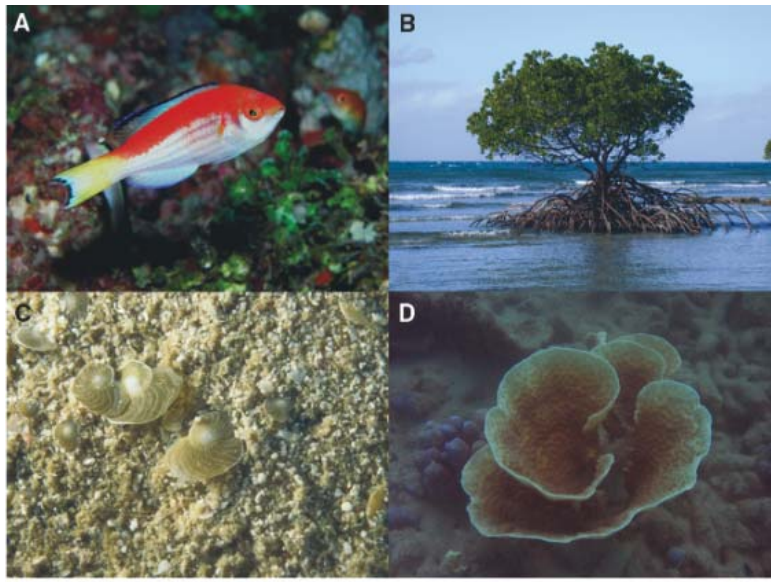

Fig. 2. Congruent biogeographic patterns are characterized by multiple taxa within the IAA biodiversity hotspot. Evidence exists from the molecular genetics of (**A**) fishes and the fossil record of (**B**) mangroves, (**C**) larger benthic foraminifera, and (**D**) corals.

The pattern of first occurrences provided by the fossil evidence is strongly supported by molecular data. Several recent molecular studies have provided crucial insights into the nature and timing of IAA origins by using a combination of comprehensive species-level phylogenies and geographic distributions. Estimated minimum divergence ages of extant cowrie lineages suggest that the majority of extant species originated in the Miocene, with only a single IAA species arising in the Pleistocene (*32*). Similarly, divergence ages of periwinkle gastropods are estimated to fall in the range of 10 to 47 Ma, with no evidence for speciation in the Plio-Pleistocene (*4*). Most lineages of coral reef fishes arose in the Late Miocene to Pliocene. A few species have been identified that diverged in the Pleistocene, but, as in the cowries, these young species are found throughout the Indo-Pacific and are not concentrated in the IAA (*33*–*38*). Similar ages of origination have been reported for the symbiotic dinoflagellate *Symbiodinium* (*39*), echinoids (*40*), and corals (*16*).

In summary, the molecular and fossil evidence from a range of taxa contradicts the notion of Pleistocene origins of the modern marine IAA fauna and flora and points to the presence of a high diversity of extinct and extant lineages from at least the Miocene onwards. Fossil data further establish that the IAA has not always been the center of marine biodiversity but that earlier centers of marine biodiversity occurred in at least two additional places during the past 50 My. There appear to have been three distinct hotspot locations. However, the component taxa may shift from one location to another, demonstrating the differences in behavior between hotspots and their component taxa: hotspots hop and taxa shift.

A Role for Plate Tectonics in the Generation and Senescence of Biodiversity Hotspots?

Our review has identified the presence of three spatially distinct biodiversity hotspots with differing biotic and environmental histories through time. Comparisons of these replicate hotspots provide a robust framework for evaluating the wide range of parameters that have been associated with their formation and maintenance. However, because of the temporal sequence now available, we are also able for the first time to examine the relationship between hotspots and factors operating over the past 50 My. One of the most striking features of these three hotspots is that each in turn marks the location of a major collision between tectonic plates.

The Eocene West Tethyan and Arabian hotspots lie within the convergence zone between the African and European continents, separated by the Tethys Ocean and a mosaic of microcontinental fragments (*41*). Important tectonic phases are the onset of counterclockwise rotation of Africa, resulting in the domination of contraction over extension between the Late Cretaceous and Early Eocene (99 to 42 Ma) coinciding with the formation and expansion of the West Tethys hotspot. Continent-continent collision progressed from west to east, resulting in emergence and mountain building in southwestern Europe coinciding with the contraction of the eastern part of the West Tethys hotspot. About 33 to 30 Ma, rifting in the Red Sea region formed the Arabian plate. The progressive rotation of the Arabian plate resulted in collision with Anatolia (*41*), starting ~20 Ma, again coinciding with an increase in diversity in the Arabian hotspot. Mountain building in Anatolia and Iran and the loss of shallow marine habitats terminated the Arabian hotspot. Finally, the IAA hotspot lies in the region of convergence between Eurasia, Australia, and the Pacific/Philippine Sea plates, where there is a complex mosaic of oceanic, arc, and microcontinental fragments. Here, three critical phases are: (i) the onset of subduction of the Australian and Pacific plate below the continental part of southeast Asia ~45 Ma, (ii) the collision of Australia with Pacific arcs and the southeast Asian margin ~23 Ma, and (iii) regional changes of plate motions at the Eurasian continental margin in the

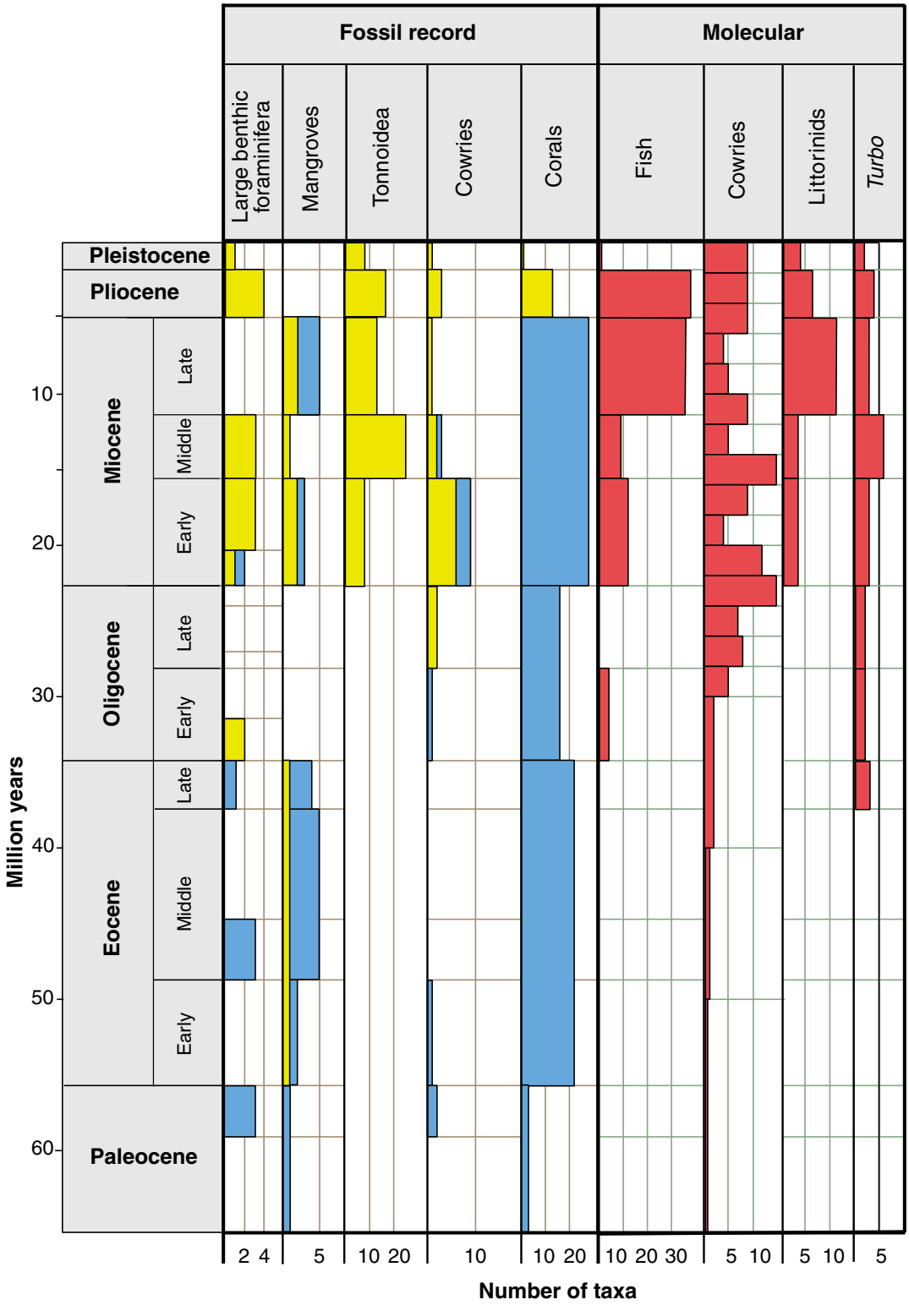

Fig. 3. The earliest records and estimated age of tropical marine taxa occurring in the modern IAA biodiversity hotspot from fossil and molecular evidence, respectively. In all of the taxa examined, numbers of first occurrences are higher in the pre-Pleistocene interval than in the Pleistocene, demonstrating the antiquity of most of the taxonomic diversity in the biodiversity hotspot. The first recorded occurrences of large benthic foraminifera genera (*20*), mangrove pollen types (table S4), tonnoid gastropod species (*30*), cowrie gastropod genera (*22*), and coral genera (*48*) are derived from the fossil record (yellow, first record inside the IAA; blue, first record outside the IAA). In each case, the data are derived from the lowest taxonomic level currently available in the literature. Minimum divergence ages of sister species of fish, cowries, littorinids, and *Turbo* gastropods are based on molecular evidence (*4*, *17*, *32*, *34*–*38*). Studies were selected where there was relatively complete sampling in the focal clades.

West Pacific about 5 Ma, initiating the recent tectonic regime (*42*). It was in phase (ii) that the most extensive creation of new islands and shallow seas corresponded with the observed formation of the IAA hotspot.

The strong correlation between the presence of hotspots and major tectonic events suggests that the primary drivers may operate over time scales beyond those traditionally used to examine diversity. Nevertheless, the geological processes must be expressed through ecological mechanisms that continue to act in extant ecosystems. Plate tectonic movements control the area and variability of suitable shallow marine habitat. Subject to global climatic constraints, they will modulate ocean circulation, resulting in changes in surface water characteristics as well as altering connectivity between (meta)populations. All of these processes have been identified as key drivers in the origination, maintenance, and extinction of marine taxa (*1*–*4*, *7*, *13*). The early phase of plate collision is characterized by the appearance of, and an increase in, new shallow water habitats. The formation of islands will provide new opportunities for isolation and disruption of genetic connectivity. Also, accumulation of diversity as a result of the juxtaposition of communities by accretion of tectonic terranes is most likely to occur in a compressive tectonic setting. All of these changes will serve to increase the biodiversity in the region, either by the origination of new species or through the accumulation of species from elsewhere. For example, in the West Tethys hotspot, the approach of the African plate led to the creation of numerous shallow marine platforms in southern Europe and was associated with a rapid surge in biodiversity throughout the region. High levels of biodiversity were maintained for millions of years while the collision matured, during which habitat area and complexity peaked. The late phase of plate collision is characterized by continent-continent contact, resulting in the rise of mountains, gradual elimination of shallow seas, closure of seaways,

and increased terrestrial runoff. All of these processes provide a mechanism to reduce the regional biodiversity. In the West Tethys hotspot, as the continents of Africa and Europe came closer together, these changes would underpin regional declines in diversity. Acting in concert with climate cooling (*43*) and a decrease in dispersal into the region with the final closure of the Tethyan seaway (*44*), these changes herald the senescence of the West Tethys biodiversity hotspot.

Conclusions

Combined evidence from fossil and molecular studies provides a new perspective on the nature of biodiversity hotspots. The evidence reveals that biodiversity hotspots occurred at different places through time. Today's hotspot in the IAA is not a unique feature but is the latest manifestation of a pattern that has been present for at least 50 My. This long time frame provides a new understanding of the nature of biodiversity hotspots and emphasizes that these phenomena are a product of ecological processes operating over geological time scales. Moreover, hotspots can be studied from their initiation to their termination. The critical role of tectonic events emphasizes the importance of abiotic factors in shaping the world's biotic realm. They drive and underpin the birth, life, and senescence of biodiversity hotspots.

A synthesis of the paleontological and molecular data, interpreted in an ecological context, has enabled us to understand the true antiquity of hotspots and their component species. However, future studies are clearly needed as global threats to marine biodiversity put the spotlight on the vulnerability of coral reef ecosystems. We now realize that human-induced changes are operating on time scales far removed from those that have created these hotspots (*45*–*47*). An improved understanding of the nature of biodiversity hotspots, be they terrestrial or marine, will require

(i) A clearer understanding of the geographic and environmental context of taxonomic turnover driving the origination, maintenance, and diminution of hotspots over extensive time scales. It is critical to distinguish between the movement of a single hotspot across the globe and the successive origination and extinction of hotspots.

(ii) An understanding of the ecological and environmental processes operating during the natural senescence of biodiversity hotspots to place the current threats to global biodiversity in perspective. It is important to identify the factors that in the past have resulted in the demise of hotspots.

(iii) Multidisciplinary studies integrating large-scale high-resolution data from the geosciences, evolutionary biology, and ecological sciences. This approach can foster the necessary synergies to understand the complexity of global biodiversity patterns over broad spatial and temporal scales.

References

1. B. R. Rosen, in *The Evolving Biosphere,* P. L. Forey, Ed. (Cambridge Univ. Press, Cambridge, 1981), pp. 103–129.
2. D. R. Bellwood, T. P. Hughes, *Science* **292**, 1532 (2001).
3. B. W. Hoeksema, in *Biogeography, Time and Place*, W. Renema, Ed. (Springer, Dordrecht, 2007), pp. 117–178.
4. S. T. Williams, D. G. Reid, *Evolution Int. J. Org. Evolution* **58**, 2227 (2004).
5. A. M. Ellison, E. J. Farnsworth, R. E. Merkt, *Glob. Ecol. Biogeogr.* **8**, 95 (1999).
6. J. C. Briggs, *Evolution Int. J. Org. Evolution* **53**, 326 (1999).
7. D. R. Bellwood, T. P. Hughes, S. R. Connolly, J. Tanner, *Ecol. Lett.* **8**, 643 (2005).
8. S. R. Palumbi, *Coral Reefs* **16**, S47 (1997).
9. P. H. Barber, S. R. Palumbi, M. V. Erdmann, M. K. Moosa, *Nature* **406**, 692 (2000).
10. S. Connolly, T. P. Hughes, D. R. Bellwood, R. Carlson, *Science* **309**, 1363 (2005).
11. R. H. Karlson, H. V. Cornell, T. P. Hughes, *Nature* **429**, 867 (2004).
12. D. Jablonski, K. Roy, J. W. Valentine, *Science* **314**, 102 (2006).
13. P. Jokiel, F. J. Martinelli, *J. Biogeogr.* **19**, 449 (1992).
14. C. M. Roberts *et al*., *Science* **295**, 1280 (2002).
15. M. E. J. Wilson, B. R. Rosen, in *Biogeography and Geological Evolution of Southeast Asia,* R. Hall, J. D. Holloway, Eds. (Backhuys, Leiden, 1998), pp. 165–195.
16. H. Fukami *et al*., *Nature* **427**, 832 (2004).
17. S. T. Williams, *Biol. J. Linn. Soc.* **92**, 573 (2007).
18. J. C. Briggs, *J. Biogeogr.* **32**, 1517 (2005).
19. Materials and methods are available as supporting material on *Science* Online.
20. W. Renema, in *Biogeography, Time and Place*, W. Renema, Ed. (Springer, Dordrecht, 2007), pp. 179–215.
21. C. C. Wallace, B. R. Rosen, *Proc. R. Soc. Lond. B Biol. Sci.* **273**, 975 (2006).
22. E. A. Kay, in *Origin and Evolutionary Radiation of the Mollusca,* J. Taylor, Ed. (Oxford Univ. Press, Oxford, 1996), pp. 211–220.
23. R. J. Morley, *Origin and Evolution of Tropical Rain Forests* (Wiley, London, 2000).
24. M. Harzhauser *et al*., *Zool. Anz.* **246**, 241 (2007).
25. L. Hottinger, *Notebooks on Geology* **CG2007-A06**, 1 (2007).
26. D. C. Potts, *Proc. Fifth Int. Coral Reef Congr. Tahiti* **4**, 127 (1985).
27. P. H. Barber, S. R. Palumbi, M. V. Erdmann, M. K. Moosa, *Nature* **406**, 692 (2000).
28. H. A. Lessios, B. D. Kessing, J. S. Pearse, *Evolution Int. J. Org. Evolution* **55**, 955 (2001).
29. R. J. Morley, in *Tropical Rainforest Responses to Climatic Change,* M. Bush, J. R. Flenley, Eds. (Springer, Dordrecht, 2007), pp. 1–31.
30. A. G. Beu, *Scripta Geol.* **130**, 1 (2005).
31. D. Jablonski *et al*., *Science* **300**, 1133 (2003).
32. C. Meyer, *Biol. J. Linn. Soc.* **79**, 401 (2003).
33. M. E. Alfaro, F. Santini, C. D. Brock, *Evolution Int. J. Org. Evolution* **61**, 2104 (2007).
34. S. McCafferty *et al*., *Mol. Ecol.* **11**, 1377 (2004).
35. G. Bernardi, S. J. Holbrook, R. J. Schmitt, N. L. Crane, E. DeMartini, *Mar. Biol. (Berl.)* **144**, 369 (2004).
36. S. O. Klanten, L. van Herwerden, J. H. Choat, D. Blair, *Mol. Phylogenet. Evol.* **32**, 221 (2004).
37. P. H. Barber, D. R. Bellwood, *Mol. Phylogenet. Evol.* **35**, 235 (2005).
38. C. I. Read, D. R. Bellwood, L. van Herwerden, *Mol. Phylogenet. Evol.* **38**, 808 (2006).
39. T. C. LaJeunesse, *Mol. Biol. Evol.* **22**, 570 (2005).
40. H. A. Lessios *et al*., *Evolution Int. J. Org. Evolution* **53**, 806 (1999).
41. J. Dercourt *et al*., Eds., *Atlas Peri-Tethys. Palaeogeographical Maps* (Commission for the Geological Map of the World, Paris, 2000).
42. R. Hall, *J. Asian Earth Sci.* **20**, 353 (2002).
43. J. C. Plaziat, C. Cavagnetto, J.-C. Koeniguer, F. Baltzer, *Wetlands Ecol. Manage.* **9**, 161 (2001).
44. M. Harzhauser, W. E. Piller, F. F. Steininger, *Palaeogeogr. Palaeoclimatol. Palaeoecol.* **183**, 103 (2002).
45. T. P. Hughes *et al*., *Science* **301**, 929 (2003).
46. J. B. C. Jackson *et al*., *Science* **293**, 629 (2001).
47. J. M. Pandolfi *et al*., *Science* **301**, 955 (2003).
48. J. E. N. Veron, *Corals of the World* (Australian Institute of Marine Science, Townsville, 2002).

Supporting Online Material

www.sciencemag.org/cgi/content/full/321/5889/654/DC1
Materials and Methods
Tables S1 to S4
References

10.1126/science.1155674

Evidence of Global Chlorophyll d

Y. Kashiyama,[1]* H. Miyashita,[2] S. Ohkubo,[2] N. O. Ogawa,[1] Y. Chikaraishi,[1] Y. Takano,[1] H. Suga,[1] T. Toyofuku,[1] H. Nomaki,[1] H. Kitazato,[1] T. Nagata,[3]† N. Ohkouchi[1]

We chemically detected chlorophyll d (Chl d) and its derivatives [e.g., pheophytin d (Phe d) and pyropheophytin d (PPhe d) (fig. S1)] directly from sedimentary samples, demonstrating that Chl d synthesis is widespread in oceanic and lacustrine environments covering a range of temperatures and salinities. Briefly, surface sediments were collected from (i) temperate coastal basins (Otsuchi Bay, Sagami Bay, Tokyo Bay, and Uchiura Bay, Japan), (ii) subarctic to Arctic pelagic basins (Bering Sea and Arctic Sea), (iii) Antarctic saline lakes (Lake Hunazoko and Lake Suribati), and (iv) a temperate freshwater lake (Lake Biwa, Japan) (tables S1 and S2). All samples contained pristine Chl d, Phe d, and PPhe d, as well as more polar equivalents (possibly chlorophyllone d and its analogs) and a less polar equivalent with an undetermined structure (fig. S1) lacking pyrochlorophyll d (PChl d) (Fig. 1 and fig. S1). This composition of degraded products parallels that of other chlorophylls, including Chl a (Fig. 1 and fig. S1), and indicates that Chl d experiences similar chemical and biochemical regimes. Concentrations of Chl a, Phe a, Chl d, and Phe d were measured on the basis of absorption chromatograms at 660, 660, 702, and 696 nm (width = 2 nm), respectively (table S1).

Among these samples, concentrations of Chl d and Phe d relative to Chl a and Phe a, respectively, are high, reaching up to 4% (table S1). The relative abundance of pigments in the surface sediment estimates the relative production rates between Chl a and Chl d [see supporting online material (SOM) text for methods and controls]. These production rates in turn are proportional to the rates of photosynthetic production of the respective chlorophylls because the quantum requirement of Chl d–based photosynthesis is equivalent to that of Chl a–based photosynthesis (*1*). Although Chl d derivatives can be hemisynthetically derived from Chl a derivatives in the laboratory (*2*), this conversion requires strong oxidants (e.g., $NaIO_4$) and is highly unlikely to occur in natural environments. Thus, these Chl d–related compounds appear to be derivatives produced by phototrophic organisms in the water column.

Our study extends the potential habitat of Chl d–producing phototrophs. Although *Acaryochloris marina* has only been reported from benthic habitats in littoral settings [e.g., (*3*–*6*)], our data indicate that Chl d–producing phototrophs also dwell offshore in hemipelagic to pelagic oceans, as well as in saline to freshwater lakes, and potentially thrive in most aquatics environments on Earth that receive near-infrared light.

Sediment core samples from Lake Biwa demonstrate marked variations in relative Chl d production over time (0.3 to 1.1%), whereas saline Antarctic lakes produced between 1.9 to 3.0% Chl d. These values are comparable to reported average Chl d abundances that were about 1% that of Chl a in underwater seaweed beds (table S3). Therefore, a similar order of Chl d–based aquatic primary production is observable regardless of geographic and ecological setting. The presence of these organisms may be attributed either to *Acaryochloris*, with its metabolic adaptations to diverse conditions (*7*), or to unknown taxa producing Chl d. Regardless of what organism produces Chl d, Chl d–based photosynthesis needs to be properly re-evaluated in estimating global primary production.

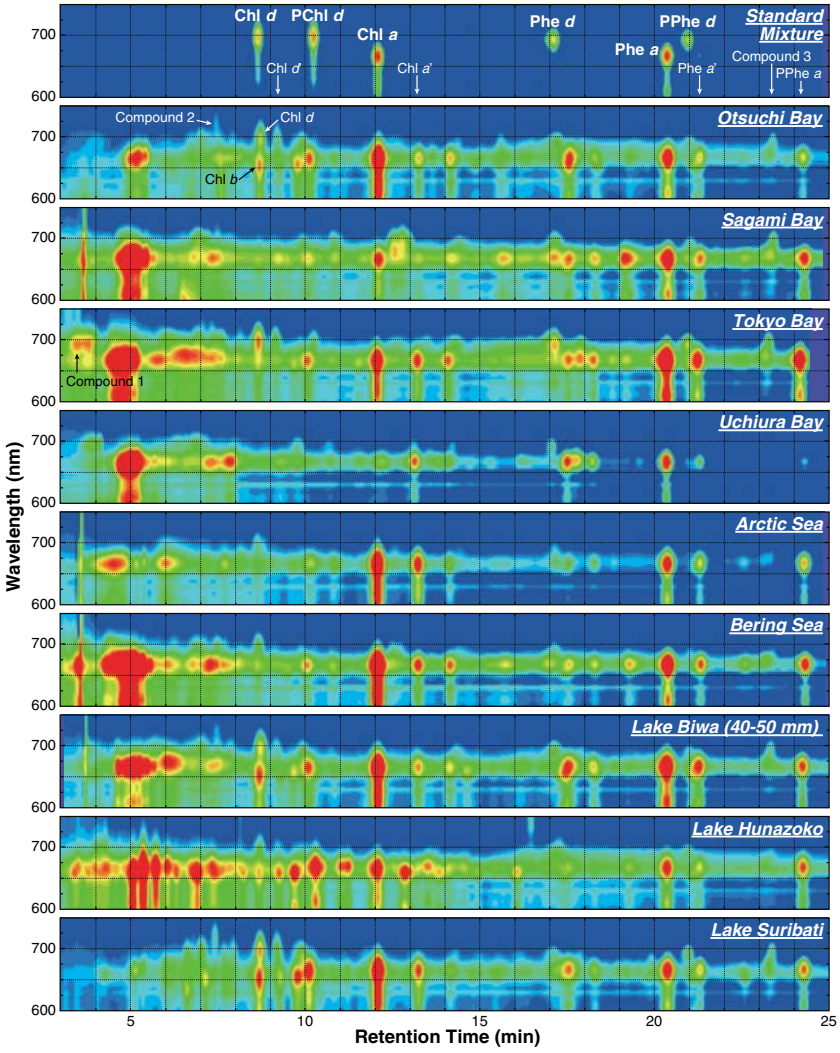

Fig. 1. Three-dimensional chromatograms of pigment analysis. Retention times and absorption of Chl a, Chl d, PChl d, Phe a, Phe d, and PPhe d and respective isomers Chl a′, Chl d′, and Phe a′ are indicated by the chromatogram of the standard mixture. Retention times of other major pigments are also indicated. Note that Chl b and Chl d are co-eluted but are distinguished by absorption peaks. Compounds 1 to 3 have absorption maxima around 690 to 700 nm and might also be derivatives of Chl d. Compound 1 was tentatively assigned on the basis of its mass spectrum (fig. S2).

References

1. S. Miyachi, K. Strassdat, H. Miyashita, H. Senger, *Z. Naturforsch. Teil C* **52**, 636 (1997).
2. T. Mizoguchi *et al.*, *Photochem. Photobiol. Sci.* **5**, 291 (2006).
3. H. Miyashita *et al.*, *Nature* **383**, 402 (1996).
4. A. Murakami, H. Miyashita, M. Iseki, K. Adachi, M. Mimuro, *Science* **303**, 1633 (2004).
5. M. Kuhl, M. Chen, P. J. Ralph, U. Schreiber, A. W. D. Larkum, *Nature* **433**, 820 (2005).
6. S. R. Miller *et al.*, *Proc. Natl. Acad. Sci. U.S.A.* **102**, 850 (2005).
7. W. D. Swingley *et al.*, *Proc. Natl. Acad. Sci. U.S.A.* **105**, 2005 (2008).

Supporting Online Material

www.sciencemag.org/cgi/content/full/321/5889/658/DC1
Materials and Methods
SOM Text
Figs. S1 to S4
Tables S1 to S3
References and Notes

7 April 2008; accepted 29 May 2008
10.1126/science.1158761

[1]Institute for Research on Earth Evolution, Japan Agency for Marine-Earth Science and Technology, Yokosuka 237-0061, Japan. [2]Department of Interdisciplinary Environment, Graduate School of Human and Environmental Studies, Kyoto University, Kyoto 606-8501, Japan. [3]Center for Ecological Research, Kyoto University, Otsu 520-2113, Japan.

*To whom correspondence should be addressed. E-mail: chiro@jamstec.go.jp
†Present address: Ocean Research Institute, University of Tokyo, Tokyo 164-8639, Japan.

Crystal Structure of the Termination Module of a Nonribosomal Peptide Synthetase

Alan Tanovic, Stefan A. Samel, Lars-Oliver Essen,* Mohamed A. Marahiel*

Nonribosomal peptide synthetases (NRPSs) are modular multidomain enzymes that act as an assembly line to catalyze the biosynthesis of complex natural products. The crystal structure of the 144-kilodalton *Bacillus subtilis* termination module SrfA-C was solved at 2.6 angstrom resolution. The adenylation and condensation domains of SrfA-C associate closely to form a catalytic platform, with their active sites on the same side of the platform. The peptidyl carrier protein domain is flexibly tethered to this platform and thus can move with its substrate-loaded 4′-phosphopantetheine arm between the active site of the adenylation domain and the donor side of the condensation domain. The SrfA-C crystal structure has implications for the rational redesign of NRPSs as a means of producing novel bioactive peptides.

Nonribosomal peptide synthetases (NRPSs) are modular multidomain enzymes that catalyze up to several dozen reactions in a highly coordinated manner to generate peptides of remarkable structural and functional diversity. The NRPS assembly line logic is analogous to that of other megasynthetases such as polyketide synthases (PKSs) and fatty acid synthases (FASs) (*1*, *2*), except that in nonribosomal peptide synthesis, the monomers are in general proteinogenic and nonproteinogenic amino acids, whereas PKSs and FASs assemble acyl–coenzyme A monomers, activated as the corresponding malonyl–coenzyme A derivatives. In each case, multidomain catalytic units designated as modules catalyze the successive copolymerization of the thioester-activated building blocks to yield linear peptides, polyketides, or fatty acids.

A prototypical NRPS module responsible for the elongation of a peptide intermediate is composed of at least an adenylation (A) domain, a peptidyl carrier protein (PCP) domain, and a condensation (C) domain in the order C-A-PCP. Each A domain (~550 amino acids) recognizes a specific amino acid building block that it activates by adenylation and then transfers to the terminal thiol of the 4′-phosphopantetheine (Ppan) arm of the downstream PCP domain (~80 amino acids). When the PCP domains of two neighboring modules are loaded with their cognate substrates, the C domain (~450 amino acids) located between these PCP domains catalyzes peptide bond formation by transferring the growing peptidyl or aminoacyl group from the donor PCP domain onto the amino group of the aminoacyl intermediate that is bound to the acceptor PCP domain. The unidirectionality of the condensation reaction guarantees the downstream-directed synthesis of the NRPS product. Finally, the growing peptide chain is translocated toward a termination module, where, after a last elongation step, the product is usually released by peptide cyclization catalyzed by a C-terminal thioesterase (TE) domain.

Although x-ray and nuclear magnetic resonance (NMR) structures of all essential NRPS domains have been solved (*3*–*7*), including that of a PCP-C bidomain (*8*) covering the border between two adjacent modules, no structural data have been reported for a complete and functionally intact NRPS module. In contrast to FASs, PKSs, or hybrid PKS/NRPSs, which form homo- and hetero-oligomeric complexes (*9*–*11*), NRPS assembly lines exist as monomers in solution (*12*). Given that the prosthetic Ppan group spans ~20 Å, this raises the question of how the PCP domain with its tethered reaction intermediates can reach the active sites of at least three domains: the A domain and the upstream and downstream C domains.

SrfA-C from *Bacillus subtilis* ATCC 21332 (1274 amino acids, 144 kD; Fig. 1, A and B), which serves as the termination module (C-A-PCP-TE) of the surfactin biosynthetic cluster, catalyzes the addition of L-leucine to the hexapeptide precursor as well as the cyclization of the resultant product to the lipoheptapeptide lactone surfactin, one of the most potent biosurfactants (Fig. 1A). Here, we present at 2.6 Å resolution the crystal structure of SrfA-C, whose conformational state provides insight into how successive catalytic steps are coordinated within a NRPS module.

Overall organization of SrfA-C. We obtained diffraction-quality crystals of recombinant SrfA-C (*13*) by using a Ser^{1003} → Ala mutant that lacks the attachment site for the prosthetic Ppan arm at Ser^{1003} of the PCP domain (fig. S1). The structure of SrfA-C was solved at 2.8 Å resolution by multiple anomalous dispersion (MAD) from selenomethionine-labeled crystals, using a partial model obtained by molecular replacement with the A domain of GrsA (PheA) (*3*) and the C domain of the sixth module of tyrocidine synthetase III (TycC6) (*8*) to localize the 30 selenium sites for phasing. The final atomic model refined at 2.6 Å resolution covers the entire SrfA-C molecule (Met^{1} to Val^{1274}) and includes an additional C-terminal stretch (Thr^{1269} to Glu^{1290}) that is derived from a *myc*-his_6 affinity tag (Fig. 1, B and C). Accordingly, the overall structure of SrfA-C can be divided into three distinct regions: (i) the elongation module harboring the tightly associated C, A, and PCP domains with an outer dimension of 130 Å by 64 Å by 54 Å; (ii) the TE domain at the C terminus of SrfA-C, which, in keeping with its role as a termination module, catalyzes the cyclization and release of the lipopeptide surfactin; and (iii) the nonfunctional C-terminal *myc*-his_6 peptide tag. The TE domain is structurally almost identical to the crystal structure of the isolated SrfA-C TE domain in its open state (*14*), with a root mean square deviation (RMSD) of 0.72 Å for 201 C_α positions. In our SrfA-C structure, however, several loop regions (Leu^{1156} to Thr^{1160}, Asn^{1175} to Glu^{1181}, and Ile^{1202} to Gln^{1206}) of the TE domain are not resolved because of enhanced disorder (fig. S2) resulting from a lack of packing interactions between the TE domain and the remaining crystal lattice.

Apart from the TE domain, the C-A-PCP domain order of SrfA-C prevails in the elongation modules of most NRPSs responsible for the synthesis of several hundred currently known nonribosomal peptide products (*15*). The elongation module of SrfA-C has roughly the shape of a rectangular box in which the C domain and the core of the A domain, which together constitute 83% of the total mass of the elongation module (118 kD), associate to form a catalytic platform (Fig. 1C). On the surface of this platform, two smaller domains—the PCP domain (Asn^{971} to Gly^{1041}) and the C-terminal A subdomain (Asp^{861} to Pro^{955})—are docked to the C and A domains, respectively. The catalytic centers of the condensation and activation domains are separated by more than 63 Å, as indicated by the location of the His^{147} catalytic residue of the C domain and the A domain–bound substrate leucine (Fig. 1C). This separation indicates that large conformational domain rearrangements must occur during the catalytic peptide elongation step and that the observed SrfA-C structure corresponds to one of the intermediary steps.

Catalytic domains. Like previously reported C domain structures (*5*, *8*), the SrfA-C condensation domain consists of two structurally similar subdomains (Met^{1} to Gln^{193}, Asp^{194} to Pro^{432}) comparable to the chloramphenicol acetyltransferase (CAT) fold. These N- and C-terminal subdomains are arranged in a V shape, and there

Biochemistry, Department of Chemistry, Philipps University Marburg, Hans-Meerwein-Strasse, D35032 Marburg, Germany.

*To whom correspondence should be addressed. E-mail: essen@chemie.uni-marburg.de (L.-O.E.); marahiel@chemie.uni-marburg.de (M.A.M.)

is a rotational offset between SrfA-C's subdomains along a hinge at Lys[192] relative to those of the condensation domain VibH (19°) and that of TycC6 (8°, fig. S3). Between these subdomains, whose relative orientation might be affected by either substrate binding or domain interactions, runs a canyon with the catalytic His[147] located at its midpoint. Thus, the C domain is accessible to substrates that are attached to the Ppan arms of the corresponding upstream (donor site) or downstream (acceptor site) PCP domains. In the SrfA-C structure, only the acceptor site is partly covered by the PCP domain.

The A domain is subdivided into a major N-terminal domain (A_{core}) and a C-terminal catalytic subdomain (A_{sub}) (*3*, *6*, *16*). The C-terminal subdomain can adopt multiple orientations relative to the N-terminal domain during the catalytic cycle of the A domain. An open A domain state promotes substrate entry. This is followed by a two-step reaction involving adenylation of the incoming substrate (closed state) and transfer of the aminoacyl moiety to the reactive thiol group of the Ppan arm that is tethered to the subsequent PCP domain (open state). The A_{sub} domain of SrfA-C does not adopt any of the previously observed open or closed orientations. Relative to structures of A domains in their closed state—for example, the PheA domain of the gramicidin S biosynthesis cluster (*3*) (Fig. 2)—the A_{sub} domain with its catalytic loop (Leu[943] to Gly[947]) moves ~16 Å out of the active site of the A_{core} domain. The active-site cleft of the A domain in SrfA-C is occupied by a leucine substrate molecule. Accordingly, subsequent binding of adenosine triphosphate may trigger a reorientation of the C-terminal A_{sub} domain.

Linkers and domain-domain interfaces. The fully defined linker regions within the SrfA-C termination module (Fig. 3 and fig. S4) give a clear view into how linker regions facilitate the organization of the domains of NRPS elongation modules (fig. S5). The C domain–A domain interface differs from other domain-domain interactions within SrfA-C by the multitude of interactions between the C and A domains, so that 1621 Å^2 of the domain surfaces are occluded from solvent access (Fig. 4A). Furthermore, the L-shaped C-A linker between the C and A domains (Asp[433] to Lys[464]) is well defined in the crystal structure by being intimately associated with both domains. Its N-terminal

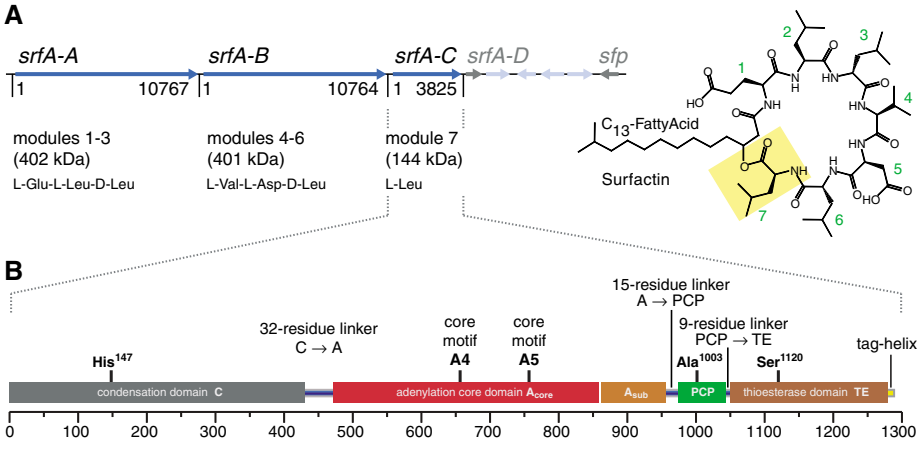

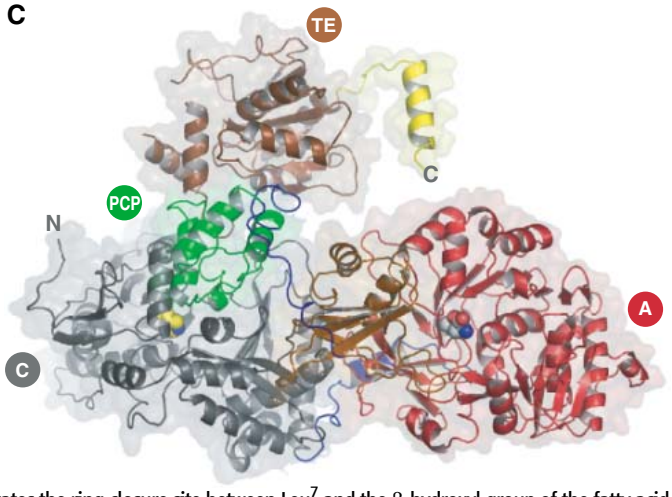

Fig. 1. Organization and overall structure of the synthetase SrfA-C, the termination module of the surfactin biosynthesis cluster from *B. subtilis* ATCC 21332. (**A**) The surfactin biosynthetic operon [including *srfA-A*, 10,767 base pairs (bp); *srfA-B*, 10,764 bp; *srfA-C*, 3825 bp] encoding the nonribosomal peptide synthetases SrfA-A, B, and C and associated genes (*srfA-D* and *sfp*). The chemical structure of the lipoheptapeptide product surfactin is shown on the right. The yellow box indicates the ring closure site between Leu[7] and the β-hydroxyl group of the fatty acid catalyzed by SrfA-C. (**B**) Schematic illustration of the terminal synthetase SrfA-C comprising the condensation domain (C, gray), adenylation domain (A, red and orange), peptidyl carrier protein domain (PCP, green), and thioesterase domain (TE, brown). Linkers are blue; the C-terminal tag helix is yellow. (**C**) Overall structure of SrfA-C at 2.6 Å resolution. The C domain's catalytically active residue His[147] and a leucine residue bound in the A domain's active site are shown in space-filling representation. Coloring of the domains is according to (B). See fig. S6 for stereoviews of the total SrfA-C structure. All figures were made with PYMOL 1.0 (*20*).

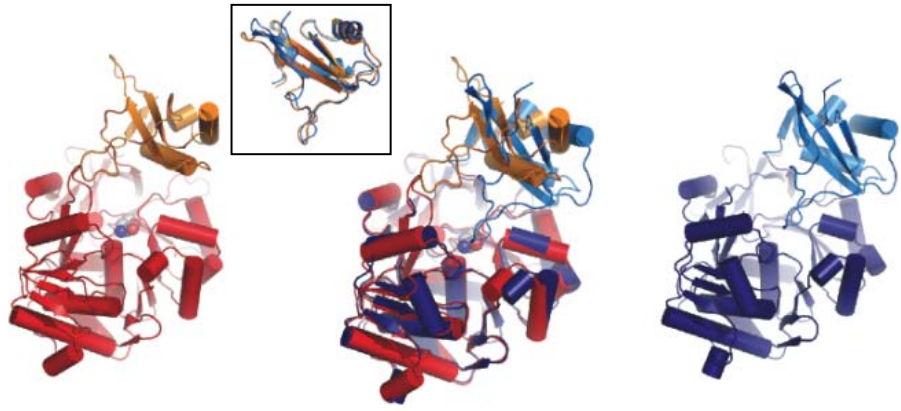

Fig. 2. Superposition of the SrfA-C adenylation domain and PheA (*3*). Whereas the core domains fit well, the smaller C-terminal subdomains (A_{sub}) point in different directions. Various relative domain orientations have been found in structurally related enzymes and have been assigned to different stages of the catalytic cycle. However, the relative arrangement observed in SrfA-C differs from the previously reported A domain structures (*3*, *16*, *21*). As shown in the inset, the excised C-terminal subdomains (A_{sub}) of SrfA-C (residues 861 to 955) and PheA (residues 430 to 530) superpose well onto each other with an RMSD of only 1.06 Å for 87 C_α positions. Consequently, there are no prominent structural differences for the C-terminal subdomains that cause the different arrangement relative to the core region.

part (Asp^{433} to Arg^{445}) stabilizes the C domain–A domain interactions by running along the C-A interface before turning into a helical segment that is associated with the A domain surface (Fig. 3). In the C-A interface, the loop βA16-βA17 (Lys^{791} to Gly^{804}, Fig. 4A) of the N-terminal A_{core} domain serves not only as a docking site for the C-A linker but also stacks against the C-terminal helix αC13 and the αC8-βC9 loop of the C domain. On the basis of the large number of residues involved, we expect that this set of C domain–A domain interactions remains invariant during the catalytic cycle. In contrast, another set of interactions made by βA22-βA23 (Ile^{866} to His^{869}) and βA24-βA25 (Arg^{895} to Ala^{901}) of the C-terminal A_{sub} domain and a stretch in the C domain (Glu^{207} to Gln^{212}) can only be transient, given the requirement of the A_{sub} domain to adopt at least two distinct orientations during the catalytic action of the A domain.

In summary, the C domain and a major part of the A domain are closely enough engaged to form a stable platform, on which the PCP domain and the A_{sub} domain can rearrange to promote loading of the PCP domain with the cognate amino acid via the A domain and its condensation with a precursor peptide through the action of the C domain. Such an enhanced structural variability of the PCP domain and the C-terminal A_{sub} domain is indicated in our SrfA-C structure. In contrast to the C domain–A domain interface, the A-PCP linker between the A_{sub} domain and the PCP domain lacks any contacts with the catalytic platform, despite being only half the size (15 residues) of the C-A linker (Fig. 3). The same holds true for the shorter PCP-TE linker with nine residues (Fig. 3). The rigid nature of the C-A catalytic platform and the stretched A-PCP linker implies that the catalytic cycle at the A domain sterically controls the interaction of the PCP domain along the acceptor side of the C domain. Accordingly, an uncharged PCP domain with a diminished tendency to position its charged Ppan arm onto a C domain could allow free rotation of the A_{sub} domain so that an incoming substrate molecule can be adenylated and, after further reorientation of the A_{sub} domain and the PCP domain, be transferred to the latter.

PCP domain interactions. PCP domains shuffle reaction intermediates among different catalytic NRPS domains and are apparently capable of adopting alternative conformational states (*7*). During a catalytic cycle, at least three functionally relevant and distinct orientations must be adopted by the PCP domain within an elongation module. One orientation would permit aminoacyl transfer onto the thiol group of the Ppan arm by association with the A domain. In the SrfA-C structure, the observed distance of 57 Å between the attachment site for the Ppan arm and the leucine within the active site of the A domain (Fig. 5) clearly exceeds the maximum distance that can be spanned by an extended Ppan arm (~20 Å). There are two remaining orientations within an elongation module: the approach of the PCP domain to the previous condensation domain at its acceptor site and to the following C domain at its donor site. Although a PCP-attached Ppan arm is missing in the SrfA-C structure, the observed domain arrangement is compatible with the PCP domain stalled in the C domain's acceptor site. Here, helices αP2 and αP3 of the PCP domain are docked to the L shape–arranged helices αC1 and αC10 of the C domain, thus protecting 975 Å^2 of the PCP and C domain surfaces from solvent access (Fig. 4B). The PCP helices αP2 and αP3 include three residues that were previously identified by Lai *et al*. to be crucial for productive PCP domain–C domain interaction in EntB, a NRPS of the enterobactin biosynthesis cluster (*17*). Two of the corresponding residues within the PCP domain, Met^{1007} and Phe^{1027}, form hydrophobic interactions with the C domain, particularly with Phe^{24} and Leu^{28} of

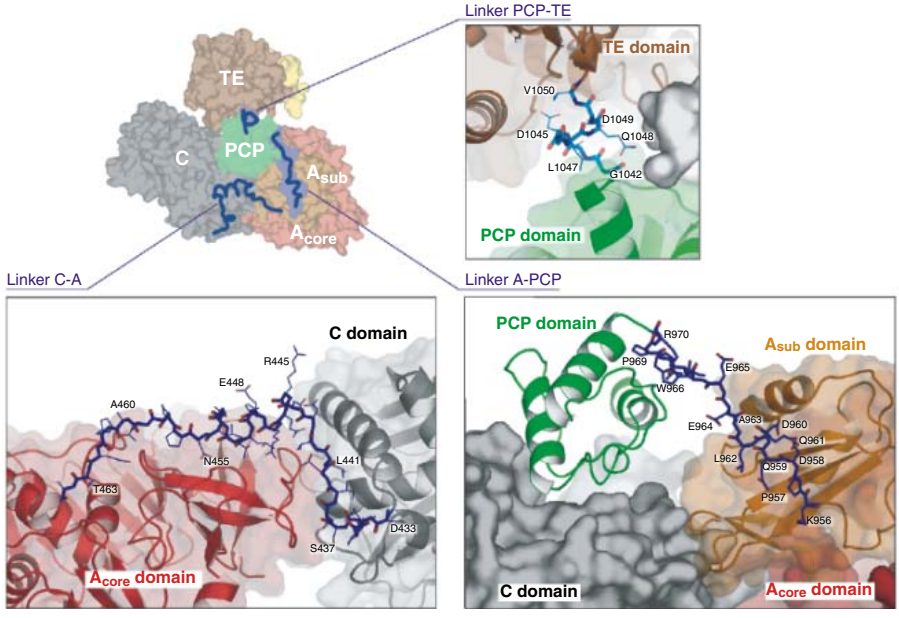

Fig. 3. Interdomain linkers of the module SrfA-C. Linker regions are shown in blue (*22*). The C-A linker connects the condensation (C) and adenylation (A) domains. It consists of 32 residues (Fig. 1B), 11 of which form an α-helical segment. The A-PCP linker between the A_{sub} and PCP domains is 15 residues in length and is devoid of interdomain contacts, with the exception of one H bond between the side chain of Gln^{961} and the main chain of A_{sub} domain residue Phe^{935}. The PCP-TE linker joining the PCP and TE domains is merely nine residues in length and shows few interactions with the PCP domain.

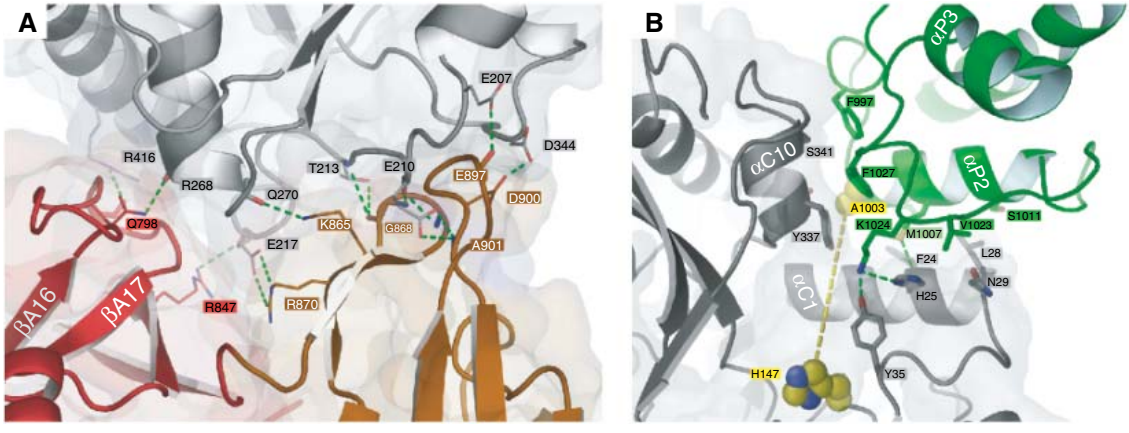

Fig. 4. Domain interfaces in SrfA-C. (**A**) The C domain–A domain interface exhibits numerous interactions of the C domain with both the A_{core} and A_{sub} domains. H bonds (distance $d < 4$ Å) are shown and respective residues are labeled (*22*). (**B**) Close domain interactions between the PCP domain and the C domain at its acceptor side that places the two domains' catalytic residues, Ala^{1003} and His^{147}, at a distance of 16 Å.

helix αC1 and Tyr^{337} of αC10, respectively. The attachment site of the prosthetic Ppan arm, a serine mutated to Ala^{1003} in our structure, would be suitably positioned at the acceptor entry site of the C domain to project the tip of its Ppan arm with an attached aminoacyl group over a distance of 16 Å into the active site close to His^{147} (Fig. 4B). NMR studies performed by Koglin *et al.* (*7*) showed that a Ser^{45} → Ala mutation in the dissected PCP domain of the third module of tyrocidine synthetase C (TycC$_3$-PCP) induces a conformational exchange from a compact A/H state to a more relaxed A state (*7*). In contrast, a Ser^{1003}→ Ala mutation in SrfA-C shows the PCP conformation in the A/H state (*4*, *7*).

NRPS-NRPS interactions. Finally, we found an unexpected but structurally well-defined interaction between a helical segment partly derived from the C-terminal *myc*-his$_6$ tag (tag helix Ser^{1275} to Ala^{1290}) and the condensation domain of a neighboring module (Fig. 6A). This is of considerable interest, because the SrfA-C C domain is known to interact with a segment that is predicted to adopt a helical structure, the COM helix, which protrudes from the C-terminal epimerization (E) domain of SrfA-B, the module that is immediately upstream of SrfA-C in the surfactin biosynthesis cluster. Close inspection of the tag sequence and comparison with those of the COM helices identified by Hahn and Stachelhaus (*18*) indeed showed an overall relationship in terms of sequence similarity and amphiphilicity (Fig. 6B). In the SrfA-C structure, the tag-derived helix is enwrapped by a hand-shaped motif of the condensation domain that is part of the N-terminal CAT-like subdomain. This helix projects several residues (Phe^{1279}, Glu^{1280}, Val^{1283}, and Leu^{1287}) toward the mostly hydrophobic floor of this motif. Apart from Glu^{1280}, these residues are mostly similar to the C-terminal SrfA-B COM helix (Fig. 6B). In the model of NRPS-NRPS interaction (*18*), it was postulated that a C-terminal COM helix aligns with an N-terminal COM helix derived from the first C domain of the following NRPS.

On the basis of the SrfA-C structure, we suggest that the C domain provides a more complex motif, the COM hand, as a docking site for COM helices. This motif comprises the N terminus and a three-stranded β sheet (βC1-βC3-βC4) that is distinct from the remaining N-terminal CAT-like subdomain but is well preserved among other structurally known condensation domains.

Implications for the construction of chimeric NRPS proteins. One appealing aspect of NRPS organization is the possibility of constructing chimeric enzymes, where intact modules or even single domains are exchanged to allow the biosynthesis of novel nonribosomal peptides. In the past this approach has faced serious problems, mostly due to insufficient activity of the NRPS chimeras. Our structure of SrfA-C indicates that an intact C domain–A domain interface might be crucial for maintaining the integrity of the catalytic platform. Given the complex nature of this interface, it might prove difficult to exchange individual A domains on a broad scale to alter the product spectrum, although this has been successfully accomplished in some cases (*19*). An alternative route would be the exchange of C domain–A domain pairs. In this case, the heterologous PCP domain–C domain interaction has yet to be optimized, but given the available model for the interaction between a C domain and an acceptor PCP domain, this should now be a feasible approach.

References and Notes

1. C. T. Walsh, *Science* **303**, 1805 (2004).
2. K. J. Weissman, R. Müller, *ChemBioChem* **9**, 826 (2008).
3. E. Conti, T. Stachelhaus, M. A. Marahiel, P. Brick, *EMBO J.* **16**, 4174 (1997).
4. T. Weber, R. Baumgartner, C. Renner, M. A. Marahiel, T. A. Holak, *Structure* **8**, 407 (2000).
5. T. A. Keating, C. G. Marshall, C. T. Walsh, A. E. Keating, *Nat. Struct. Biol.* **9**, 522 (2002).

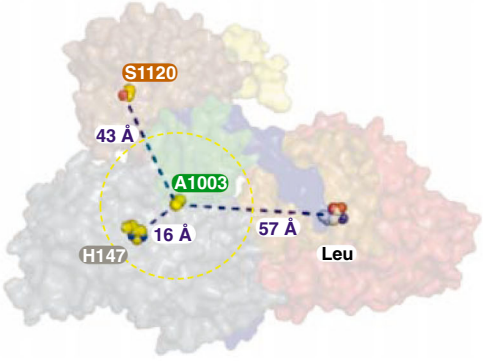

Fig. 5. Distances between the catalytic center of the PCP domain at Ala^{1003} and those of the C domain (His^{147}), the A domain (Leu residue in the active site), and the TE domain (Ser^{1120}), respectively. The dashed yellow circle has a radius of 20 Å, corresponding to the distance that a 4′-phosphopantetheine cofactor can span. Because of perspective, the interdomain distances appear shorter than they are.

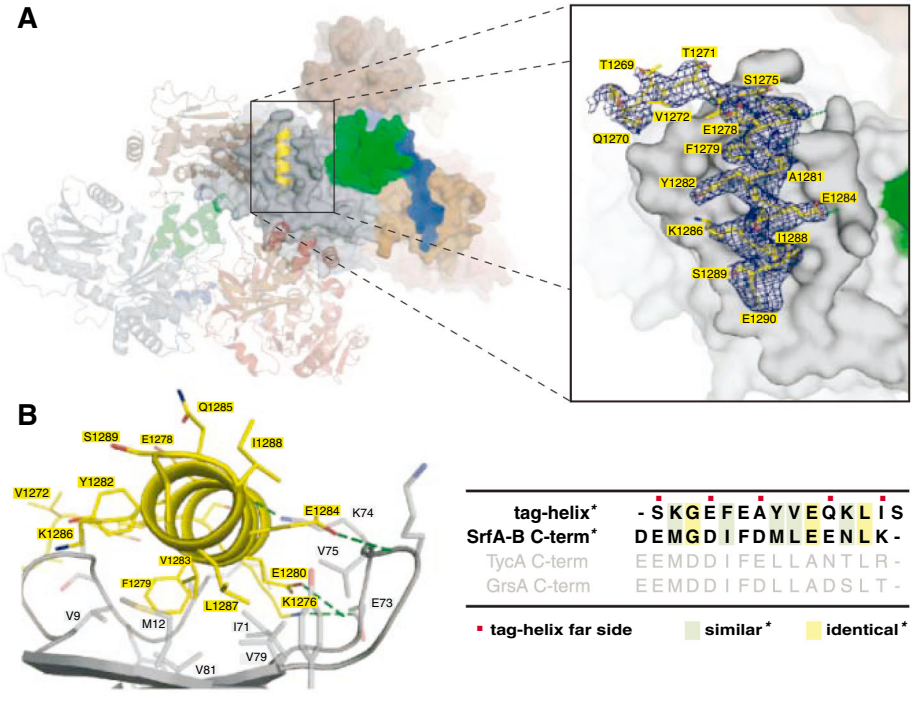

Fig. 6. Intermolecular interactions between the SrfA-C C domain and the C-terminal peptide tag (yellow) as observed in the crystal structure. (**A**) The fusion peptide attached to the C terminus of SrfA-C adapts an α-helical conformation and shares sequence similarity with the C-terminal α-helical COM region of the synthetase SrfA-B. The inset shows electron density for the C-terminal peptide region and its surface complementarity to the C domain (*22*). (**B**) The hand-shaped COM region of the N-terminal C domain poses apolar residues on its bottom (formed by β strands βC1, βC3, and βC4) and mostly polar residues on flanking regions. H bonds and salt bridges (d < 4 Å) between the COM hand and the C-terminal fusion peptide of a symmetry-related SrfA-C molecule are marked. The multiple sequence alignment on the right side indicates similarity between the observed helical segment docked to the COM hand and the putative COM helices at the C-terminal ends of surfactin (SrfA-B) as well as the noncognate tyrocidine (TycA) and gramicidin (GrsA) synthetases (gray) that were shown to interact with SrfA-C (*18*). Residues of the tag helix that are located on the far side with respect to the COM hand are marked by red dots.

6. J. J. May, N. Kessler, M. A. Marahiel, M. T. Stubbs, *Proc. Natl. Acad. Sci. U.S.A.* **99**, 12120 (2002).
7. A. Koglin *et al.*, *Science* **312**, 273 (2006).
8. S. A. Samel, G. Schönafinger, T. A. Knappe, M. A. Marahiel, L.-O. Essen, *Structure* **15**, 781 (2007).
9. S. Jenni, M. Leibundgut, T. Maier, N. Ban, *Science* **311**, 1263 (2006).
10. T. Maier, S. Jenni, N. Ban, *Science* **311**, 1258 (2006).
11. Y. Tang, C.-Y. Kim, I. I. Mathews, D. E. Cane, C. Koshla, *Proc. Natl. Acad. Sci. U.S.A.* **103**, 11124 (2006).
12. S. A. Sieber *et al.*, *Chem. Biol.* **9**, 997 (2002).
13. See supporting material on *Science* Online.
14. S. D. Bruner *et al.*, *Structure* **10**, 301 (2002).
15. S. Caboche *et al.*, *Nucleic Acids Res.* **36**, D326 (2008).
16. A. M. Gulick, V. J. Starai, A. R. Horswill, K. M. Homick, J. C. Escalante-Semerena, *Biochemistry* **42**, 2866 (2003).
17. J. R. Lai, A. Koglin, C. T. Walsh, *Biochemistry* **45**, 14869 (2006).
18. M. Hahn, T. Stachelhaus, *Proc. Natl. Acad. Sci. U.S.A.* **101**, 15585 (2004).
19. T. Stachelhaus, A. Schneider, M. A. Marahiel, *Science* **269**, 69 (1995).
20. W. L. DeLano, DeLano Scientific LLC, San Carlos, CA, 2002 (www.pymol.org).
21. E. Conti, N. P. Franks, P. Brick, *Structure* **4**, 287 (1996).
22. Abbreviations for amino acid residues: A, Ala; C, Cys; D, Asp; E, Glu; F, Phe; G, Gly; H, His; I, Ile; K, Lys; L, Leu; M, Met; N, Asn; P, Pro; Q, Gln; R, Arg; S, Ser; T, Thr; V, Val; W, Trp; Y, Tyr.
23. We thank U. Linne for mass spectrometric analysis of SrfA-C; C. Petosa for support at synchrotron beam line ID14-2 at European Synchrotron Radiation Facility, Grenoble; and S. Russo at X06SA, Swiss Light Source, Villigen. Supported by Deutsche Forschungsgemeinschaft grants ES152-4 and MA811-14 and by the European Community and Fonds der Chemischen Industrie. Coordinates and structure factors of SrfA-C are deposited in the RCSB protein data bank (accession number 2vsq).

Supporting Online Material
www.sciencemag.org/cgi/content/full/1159850/DC1
Materials and Methods
Figs. S1 to S7
Table S1
References

30 April 2008; accepted 16 June 2008
Published online 26 June 2008;
10.1126/science.1159850
Include this information when citing this paper.

Essential Cytoplasmic Translocation of a Cytokine Receptor–Assembled Signaling Complex

Atsushi Matsuzawa,[1]* Ping-Hui Tseng,[1]* Sivakumar Vallabhapurapu,[1] Jun-Li Luo,[1] Weizhou Zhang,[1] Haopeng Wang,[2] Dario A. A. Vignali,[2] Ewen Gallagher,[3] Michael Karin[1]†

Cytokine signaling is thought to require assembly of multicomponent signaling complexes at cytoplasmic segments of membrane-embedded receptors, in which receptor-proximal protein kinases are activated. Indeed, CD40, a tumor necrosis factor receptor (TNFR) family member, forms a complex containing adaptor molecules TRAF2 and TRAF3, ubiquitin-conjugating enzyme Ubc13, cellular inhibitor of apoptosis proteins 1 and 2 (c-IAP1/2), IκB kinase regulatory subunit IKKγ (also called NEMO), and mitogen-activated protein kinase (MAPK) kinase kinase MEKK1 upon ligation. TRAF2, Ubc13, and IKKγ were required for complex assembly and activation of MEKK1 and MAPK cascades. However, these kinases were not activated unless the multicomponent signaling complex translocated from CD40 to the cytosol upon c-IAP1/2–induced degradation of TRAF3. This two-stage signaling mechanism may apply to other innate immune receptors, accounting for spatial and temporal separation of MAPK and IKK signaling.

Cytoplasmic segments of cytokine, growth factor, and antigen receptors serve as assembly sites for complexes containing adaptor proteins, protein kinases, and other signaling factors (*1*, *2*). Ligand-induced assembly of such complexes is thought to concentrate and subsequently activate protein kinases on the receptor, thereby triggering a plethora of effector pathways that control metabolism, proliferation, and survival. Among cytokine receptors, the tumor necrosis factor receptor (TNFR) family contains members of biomedical importance that bind trimeric ligands (*3*, *4*). TNFR engagement results in assembly of multicomponent receptor-associated signaling complexes that activate inhibitor of nuclear factor κB (IκB) kinase (IKK) and mitogen- or stress-activated protein kinase (MAPK/SAPK) cascades (*3*, *5*). Key players in TNFR signaling are TNF receptor–associated factors (TRAFs), serving as E3 ubiquitin ligases and adaptors that recruit and activate protein kinases that act at the apex of effector pathways (*3*, *5*–*7*). These protein kinases include transforming growth factor–β activated kinase 1 (TAK1) and MAP or extracellular signal–regulated kinase kinase kinase 1 (MEKK1), which in turn activate IKK (*8*), and the MAPK/SAPKs c-Jun N-terminal kinase (JNK) and p38 (*5*, *9*). Most TRAF proteins contain an N-terminal RING finger required for signal transduction and formation of K63-linked polyubiquitin chains conjugated through the C-terminal glycine of the added ubiquitin moiety and K63 of the protein-attached ubiquitin (*6*), and a C-terminal TRAF domain involved in self-association and binding to receptor and adaptor proteins (*3*).

Much of our knowledge of TNFR signaling comes from studies of type I TNF receptor (TNFR1), which interacts with TRAF2 and TRAF5 through the adaptor protein TRADD (*10*). Receptor recruitment of TRAF2 results in inclusion of the cellular Inhibitors of Apoptosis (c-IAP) 1 and c-IAP2 proteins in a signaling complex that also contains the protein kinase RIP1 (*11*). This complex, named complex I, was suggested to activate IKK, JNK, and p38 while associated with membrane-embedded TNFR1 (*12*, *13*). IKK activation was proposed to depend on its binding to receptor-associated TRAF2 (*14*) and K63-mediated polyubiquitination of RIP1 that results in recruitment of TAK1, a putative IKK kinase (*15*, *16*). IKK association with complex I may be stabilized by binding of IKKγ, its regulatory subunit (*17*), to K63-polyubiquitinated RIP1 (*18*, *19*). However, it has not been formally demonstrated that kinase activity of TAK1 is actually stimulated upon receptor engagement and if so, where and when the kinase is activated.

TNFR1-induced JNK activation depends in part on the MAPK kinase kinase (MAP3K) MEKK1 (*20*). MEKK1 is also a major contributor to activation of JNK and p38 by two B cell TNFR family members: CD40 and BAFF receptor (BAFF-R) (*9*), which recruit TRAF2, TRAF3, and TRAF6 directly (*21*). CD40 and BAFF-R are critical for B cell maturation, survival, proliferation, and immune functions (*22*). Some of these functions also depend on MEKK1 (*9*). We find that CD40-induced activation of MEKK1 and its downstream targets requires assembly of a receptor-associated multicomponent complex. But, MEKK1 is not activated unless the receptor-anchored complex is released to the cytosol via a proteolytic step. A similar mechanism accounts for activation of TAK1. These results outline an unprecedented two-stage signaling mechanism in which membrane-anchored receptors nucleate a multicomponent signaling complex, but actual MAP3K activation requires complex release into the cytoplasm, where MAP3K substrates are located.

TRAF requirements for MEKK1 activation in CD40-stimulated B cells. CD40 transduces signals through TRAF proteins (*22*). To identify the TRAFs responsible for MEKK1 activation in

[1]Laboratory of Gene Regulation and Signal Transduction, Departments of Pharmacology and Pathology, School of Medicine, University of California San Diego, 9500 Gilman Drive, La Jolla, CA 92093–0723, USA. [2]Department of Immunology, St. Jude Children's Research Hospital, Memphis, TN 38105–2794, USA. [3]Department of Immunology, Imperial College, London, Faculty of Medicine, Norfolk Place, London W2 1PG, UK.

*These authors contributed equally to this work.
†To whom correspondence should be addressed. E-mail: karinoffice@ucsd.edu

CD40-stimulated B cells, we reconstituted irradiated mice with wild-type (WT), *Traf2*$^{-/-}$, *Traf3*$^{-/-}$, and *Traf6*$^{-/-}$ stem cells and isolated splenic B cells that were stimulated with a CD40 agonistic antibody. Activation of MEKK1, measured by reactivity with a phospho-specific antibody that recognizes phospho-Thr^{1381} in its activation loop (*9*) or a kinase activity assay, was impaired in *Traf2*$^{-/-}$ cells, but not in *Traf3*$^{-/-}$ or *Traf6*$^{-/-}$ cells (Fig. 1A and fig. S1A). Correspondingly, phosphorylation of JNK and p38 and JNK activity were decreased in *Traf2*$^{-/-}$ cells by ~75% (fig. S1B). TRAF6 ablation also decreased MAPK phosphorylation and JNK activity by ~50%, suggesting that TRAF6 activates JNK and p38 through another MAP3K, most likely TAK1, whose activation was diminished in *Traf6*$^{-/-}$, but not in *Traf2*$^{-/-}$ or *Traf3*$^{-/-}$ cells (Fig. 1A). Curiously, the absence of TRAF3 resulted in earlier MAP3K and MAPK phosphorylation and activation, which were nearly maximal at the 5-min time point (Fig. 1A and fig. S1, A and B). Indeed, a JNK kinase assay revealed near-maximal JNK activation at 5 min in *Traf3*$^{-/-}$ cells, whereas in WT cells, JNK activity peaked around 30 min (Fig. 1A and fig. S1B). Depletion of TRAF2, TRAF3, and TRAF6 by lentivirus-mediated transduction of short hairpin RNAs (shRNAs) produced similar results: CD40-induced MEKK1 activation was barely detected in TRAF2-deficient cells, whereas TRAF6 depletion prevented TAK1 activation (Fig. 1, B and C). Notably, TRAF3 depletion accelerated MAP3K and MAPK activation. CD40 ligation induces MEKK1 ubiquitination (*9*), a modification that was dependent on TRAF2, but not on TRAF3 or TRAF6 (fig. S2).

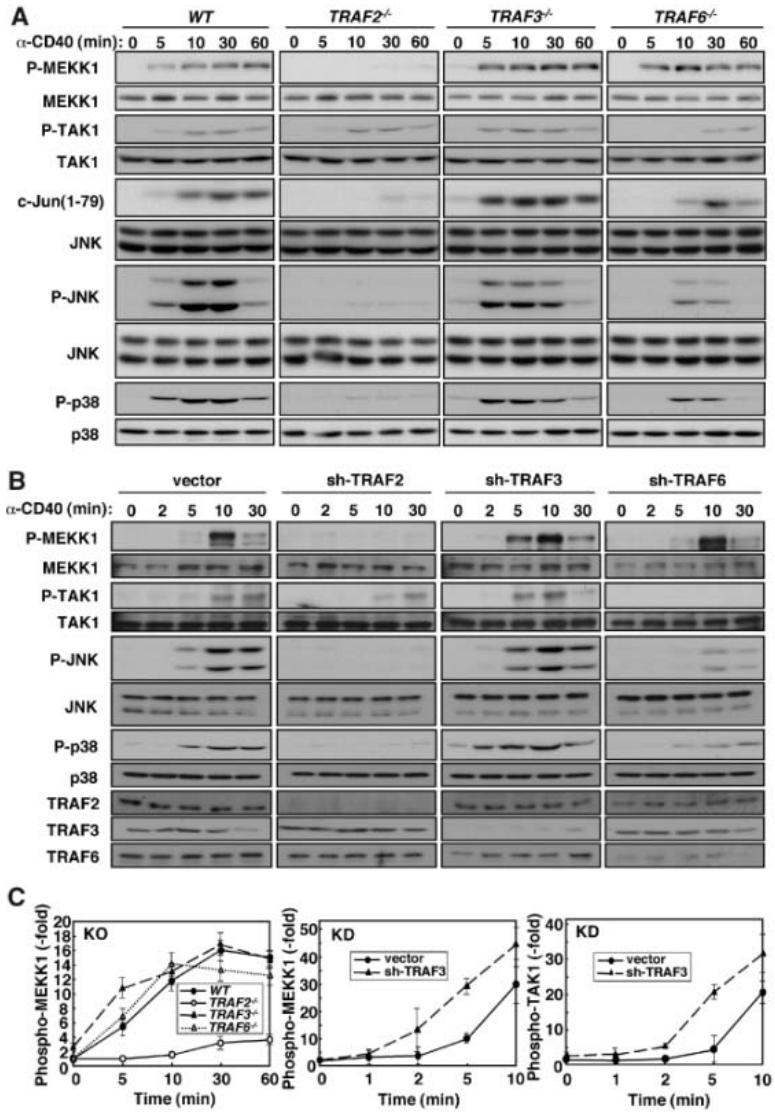

Fig. 1. Requirement of TRAF2 for CD40-mediated activation of MEKK1. (**A**) MEKK1 activation in B cells. Splenic B cells from mice reconstituted with WT, *Traf2*$^{-/-}$, *Traf3*$^{-/-}$, and *Traf6*$^{-/-}$ fetal liver were stimulated with CD40 agonistic antibody. Cell lysates were prepared at the indicated times and phosphorylation of MEKK1, TAK1, JNK, and p38 was analyzed by immunoblotting. The kinase activity of immunoprecipitated JNK was measured by phosphorylation of glutathione *S*-transferase (GST)-c-Jun(1-79). Immunoblotting with anti-JNK served as the loading control. (**B**) MEKK1 activation in a B cell line. A20 B cells transduced with lentiviruses containing no insert or shRNAs to TRAF2, 3, or 6 were stimulated with anti-CD40. MEKK1, TAK1, JNK, and p38 phosphorylation and TRAF2, 3, or 6 expression were analyzed by immunoblotting. (**C**) Kinetics of CD40-induced phosphorylation of MEKK1 and TAK1. Phosphorylation kinetics of MEKK1 in WT and TRAF knockout (KO) B cells were determined by densitometric analysis of two separate experiments as in (A). The early kinetics of MEKK1 and TAK1 phosphorylation in control and TRAF3 knockdown (KD) A20 B cells were determined in two separate experiments similar to the one shown in (B).

Requirement of Ubc13 and IKKγ for MEKK1 activation. Ubc13, which together with Uev1a forms an E2 ubiquitin-conjugating enzyme that selectively catalyzes K63 polyubiquitination, is critical for CD40 signaling (*23*). We explored its role in MEKK1 activation by transducing A20 B cells with control or Ubc13 shRNA lentiviruses. CD40-induced phosphorylation of MEKK1 and JNK was abrogated upon depletion of Ubc13 (Fig. 2A). Ubc13 deficiency had only a minor effect on IKK activation and IκBα degradation (*23*). RING-dependent MEKK1 self-ubiquitination (*24*) was Ubc13-dependent (fig. S3).

Ubc13-dependent ubiquitination of IKKγ was proposed to function in IL-1 and TLR-mediated activation of JNK (*23*). Indeed, MEKK1, its substrate MKK4, and both JNK and p38 were no longer activated by CD40 in IKKγ-deficient 1.3E2 cells derived from the 70Z3 B cell lymphoma (Fig. 2B). IKKγ itself is polyubiquitinated upon CD40 engagement and this was TRAF2- and Ubc13-dependent (fig. S4, A and B). A portion of IKKγ is tightly bound to IKKα and IKKβ (*17*), but its involvement in MEKK1 activation suggested it might also have an IKK-independent function. We separated IKK-associated IKKγ from other forms in lysates of splenic B cells from WT or MEKK1 kinase domain–deficient (*Mekk1*$^{\Delta KD/\Delta KD}$) mice by sequential immunoprecipitation. Kinase activity of MEKK1 was required for CD40-induced ubiquitination only of IKKγ that was not associated with other IKK subunits (fig. S5).

A multicomponent signaling complex is formed after CD40 engagement and undergoes membrane-to-cytosol translocation. CD40 immunoprecipitated from stimulated B cells was associated with TRAF2, MEKK1, IKKγ, Ubc13, c-IAP1, and c-IAP2 (Fig. 2C). This complex included trace amounts of the MEKK1 substrates MKK4 and MKK7, and at 10 min after receptor engagement did not contain detectable IKKα and IKKβ. Immunoprecipitation of MEKK1 from whole-cell lysates also revealed formation of a CD40-induced multiprotein complex containing CD40, TRAF2, c-IAP1/2, Ubc13, IKKγ, and MEKK1 itself (Fig. 2D). With anti-CD40 as the immunoprecipitating antibody, the amounts of most complex components declined between 10 and 30 min after stimulation. This apparent dissociation of

the complex was not seen in MEKK1 immune complexes.

We also observed transient CD40-induced membrane association of MEKK1, TRAF2, IKKγ, and Ubc13 (fig. S6). We therefore fractionated splenic B cells at various time points after stimulation as previously done in studies of TNFR1 signaling (*12*). In this protocol, nuclei and other heavy organelles are removed first, and the remaining extract is divided into soluble (cytosol) and nonsoluble (membrane-containing) fractions. The multiprotein complex isolated with either CD40, IKKγ, or MEKK1-specific antibodies was present in the membrane-containing fraction at 10 min after stimulation but was barely detected after 30 min (Fig. 3 and fig. S6 for loading control). By contrast, a complex, containing TRAF2, MEKK1, IKKγ, and Ubc13, but not CD40, was detected in the soluble cytosol fraction within 10 min, and most of its components were relatively stably associated for up to 60 min after

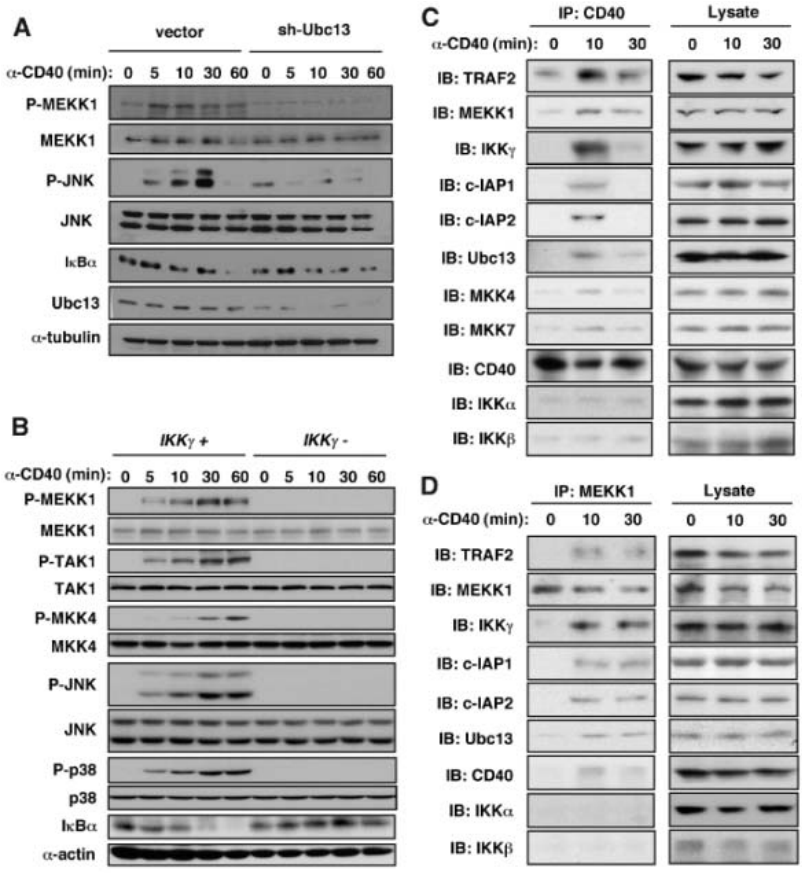

Fig. 2. Dependence of MEKK1 activation on Ubc13 and IKKγ and association with formation of a multicomponent signaling complex. (**A**) A20 B cells transduced with lentiviruses with no insert or Ubc13 shRNA were stimulated with anti-CD40. Lysates were immunoblotted to detect phosphorylation of MEKK1, JNK, and p38, degradation of IκBα, and expression of Ubc13. (**B**) *Ikkγ*-null 1.3E2 B cells and parental 70Z3 cells were stimulated with anti-CD40. At the indicated times, lysates were prepared and analyzed by immunoblotting for MAP3K and MAPK phosphorylation and IκBα degradation. (**C** and **D**) Splenic B cells were stimulated with anti-CD40. At the indicated times, cell lysates were prepared and immunoprecipitated (IP) with anti-CD40 (C) or anti-MEKK1 (D). The gel-separated immune complexes were immunoblotted (IB) with the indicated antibodies.

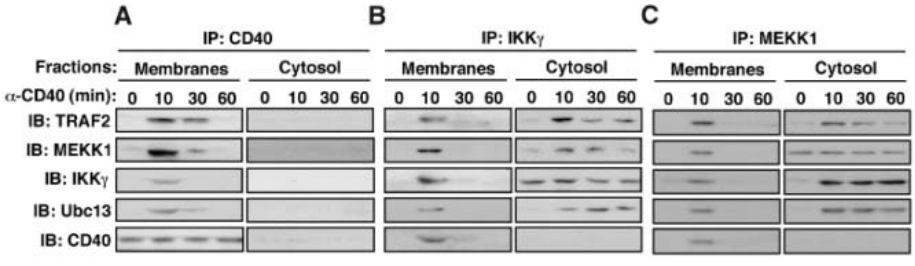

Fig. 3. Release of the receptor-associated signaling complex to the cytosol. Splenic B cells were stimulated with anti-CD40, and membrane and cytosolic fractions were prepared at the indicated times. CD40 (**A**), IKKγ (**B**), or MEKK1 (**C**) were immunoprecipitated (IP) from lysates of each fraction, and the gel-separated immune complexes were immunoblotted (IB) with the indicated antibodies. The amounts of the analyzed proteins in total B cell lysates and the subcellular fractions are shown in fig. S7.

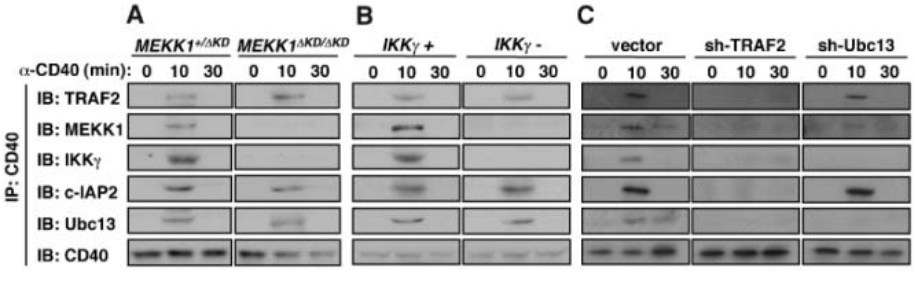

Fig. 4. Role of individual components in assembly of the CD40-associated signaling complex. (**A**) Role of MEKK1. *Mekk1*$^{+/\Delta KD}$ or *Mekk1*$^{\Delta KD/\Delta KD}$ B cells were stimulated with anti-CD40, and the membrane fraction was immunoprecipitated with anti-CD40. (**B**) Role of IKKγ. 70Z3 and 1.3E2 B cells were stimulated and analyzed as above. (**C**) Roles of TRAF2 and Ubc13. A20 B cells transduced with lentiviruses containing no insert or shRNAs for TRAF2 or Ubc13 were stimulated and analyzed as above. After washing, the CD40 immunecomplexes in all three experiments were gel-separated and immunoblotted with the indicated antibodies.

CD40 engagement. CD40 itself remained in the membrane fraction and its amount did not decline during this time.

Complex assembly occurs in two steps. We investigated which components were critical for assembly of the CD40-anchored complex. In B cells lacking MEKK1 kinase domain, TRAF2, c-IAP2, and Ubc13 were still recruited to CD40, but IKKγ was not (Fig. 4A). Likewise, IKKγ was

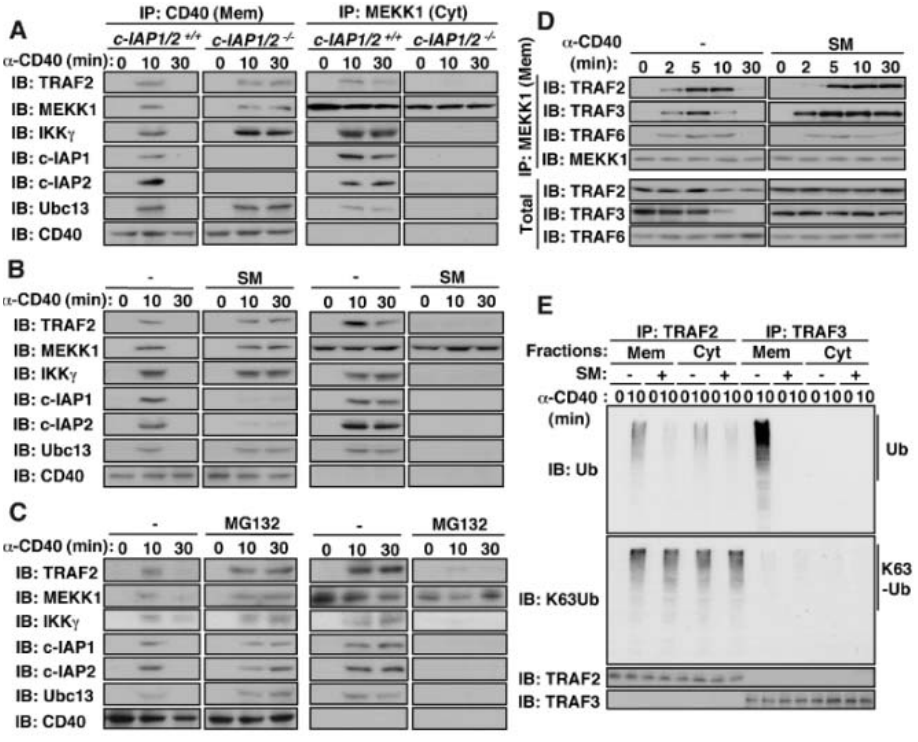

Fig. 5. Requirement of c-IAP and proteasome activity for cytosolic translocation of the receptor-associated signaling complex and TRAF3 degradation. (**A** and **B**) Requirement of c-IAP1/2. c-IAP–deficient and control multiple myeloma cells (A), or splenic B cells treated with or without the c-IAP inhibitor Smac mimic (SM) for 4 hours (B), were stimulated with anti-CD40. (**C**) Requirement of proteasome activity. Splenic B cells were treated with or without the proteasome inhibitor MG132 for 30 min before anti-CD40 stimulation. All cells were divided into membrane (Mem) and cytosolic (Cyt) fractions that were immunoprecipitated with anti-CD40 and anti-MEKK1, respectively. The gel-separated immune complexes were immunoblotted with the indicated antibodies. (**D**) Degradation of membrane- and MEKK1-associated TRAF3 in a c-IAP1/2–dependent manner. Splenic B cells were treated or not treated with SM as in (B) and stimulated with anti-CD40. At the indicated times, the cells were divided into membrane and cytosolic fractions. MEKK1 was immunoprecipitated, and presence of indicated proteins in the immune complexes and total cell lysate was examined. (**E**) Requirement of c-IAP1/2 for TRAF2 and TRAF3 ubiquitination. B cells preincubated without or with SM were stimulated with anti-CD40 for 10 min. Cells were divided into membrane and cytosol fractions. TRAF2 and TRAF3 were immunoprecipitated from both fractions, extensively washed, gel-separated, and analyzed by immunoblotting with conventional or K63-specific anti-ubiquitin.

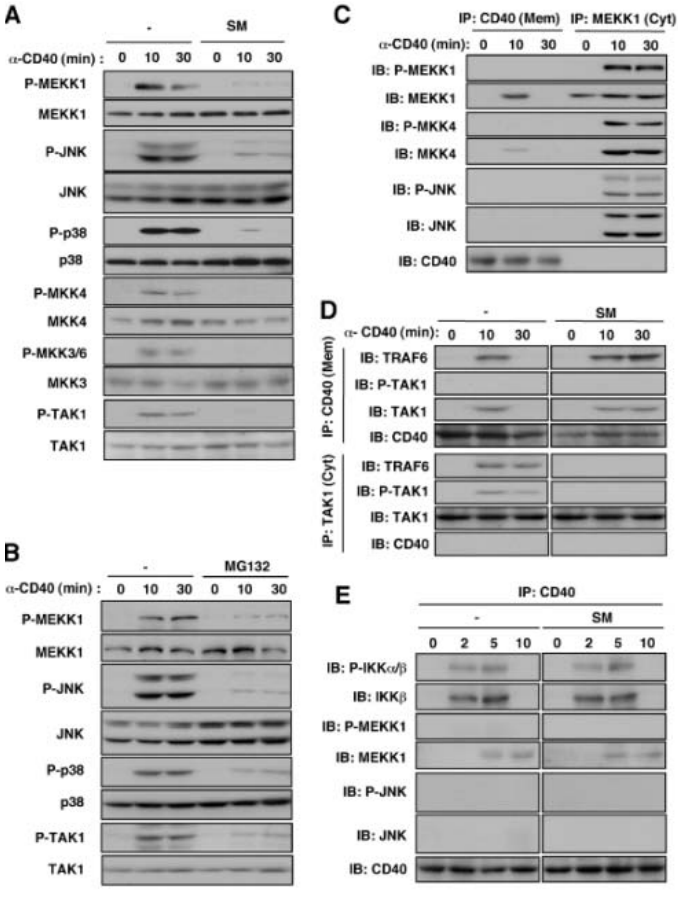

Fig. 6. Requirement of c-IAP and proteasome activity for cytosolic activation of MAP3K signaling modules. (**A** and **B**) Splenic B cells were treated with or without SM (A) or MG132 (B) for 4 hours and 30 min, respectively, before anti-CD40 stimulation. Kinase phosphorylation/activation was monitored by immunoblotting. (**C**) Subcellular location of MEKK1 module activation. Splenic B cells were stimulated with anti-CD40 and divided at the indicated times into membrane and cytosolic fractions that were immunoprecipitated with anti-CD40 or anti-MEKK1, respectively, and separated on the same gel. Kinase phosphorylation/activation was monitored by immunoblotting. (**D**) Requirement of c-IAP1/2 for cytosolic translocation of the TRAF6-TAK1 signaling complex. Splenic B cells treated with or without SM were stimulated with anti-CD40. Cells were divided into membrane and cytosolic fractions that were immunoprecipitated with anti-CD40 and anti-TAK1, respectively. The gel-separated immune complexes were blotted with the indicated antibodies. (**E**) Splenic B cells were pretreated with or without SM and stimulated with anti-CD40. At the indicated times, membranes were isolated, lysed and immunoprecipitated with anti-CD40. The gel-separated immune complexes were analyzed as above.

required for recruitment of MEKK1, but not for recruitment of TRAF2, c-IAP2, or Ubc13 (Fig. 4B). As predicted by its direct binding to CD40 (*25*), depletion of TRAF2 from cells abolished complex assembly (Fig. 4C). Depletion of Ubc13, however, did not interfere with recruitment of TRAF2 and c-IAP2, but prevented inclusion of MEKK1 and IKKγ (Fig. 4C). Hence, the first step in complex formation is binding of TRAF2 and c-IAP1/2, followed by recruitment of Ubc13. Once this initial complex is formed, IKKγ and MEKK1 are recruited into it interdependently.

Requirement of c-IAP and proteasome activity for cytosolic translocation of the receptor-bound complex and degradation of TRAF3. To examine the role of c-IAP1 and c-IAP2, we used multiple myeloma cells lacking these proteins as a result of an oncogenic deletion encompassing the linked *c-IAP1* and *c-IAP2* loci (*26*). Surprisingly, absence of c-IAP1/2 had no effect on complex assembly, but completely prevented its translocation to the cytosol (Fig. 5A). To further examine the role of c-IAP1/2 in complex release, we used a small-molecule mimic of the pro-apoptotic protein Smac (SM), which binds to c-IAP1/2 and induces their rapid degradation (*27*, *28*). SM also prevented cytosolic translocation of the receptor-associated signaling complex (Fig. 5B). c-IAP1 and c-IAP2 are K48-specific E3 ubiquitin ligases (*29*, *30*). Proteasomal degradation of a c-IAP–targeted protein appeared to be required for cytosolic translocation of the signaling complex, because the proteasome inhibitor MG132 prevented complex release (Fig. 5C).

To understand the role of c-IAP1/2 in complex release, we searched for a component of the receptor-associated complex that was rapidly degraded in a c-IAP1/2–dependent manner. Our first candidate was TRAF2 because it binds directly to CD40 and its degradation may cause complex release. Although CD40 engagement resulted in reduced TRAF2 abundance that was inhibited by SM (Fig. 5D), it was not sufficiently rapid to account for complex release, and ample TRAF2 remained in the cytosolic complex (fig. S7). We therefore shifted our attention to TRAF3 because it can bind to the same site on CD40 as TRAF2, with which it may hetero-oligomerize (*21*, *22*). Furthermore, the absence of TRAF3 accelerated MAP3K and MAPK activation (Fig. 1C). Receptor-recruited TRAF3 was rapidly degraded but was completely stabilized in cells depleted of c-IAP1/2 (Fig. 5D). Moreover, TRAF3 was only present in the membrane-associated MEKK1 complex and was not part of the cytosolic complex (fig. S7).

Whereas polyubiquitinated TRAF2 was detected both in the membrane and cytosol fractions after CD40 engagement, polyubiquitinated TRAF3 was seen only in the membrane fraction and its appearance was completely inhibited by pretreatment with SM (Fig. 5E). Using a monoclonal antibody specific for K63-linked polyubiquitin (*31*), we found K63-linked polyubiquitin on TRAF2 both in the membrane and cytosol, and the extent of this modification was not inhibited by pretreatment with SM, which did reduce the amount of polyubiquitinated TRAF2 detected by a conventional antibody to ubiquitin (Fig. 5E). No K63-linked polyubiquitinated TRAF3 could be detected. We interpret these results to suggest that TRAF3 is subjected only to degradative K48-linked polyubiquitination that is c-IAP1/2–dependent. By contrast, TRAF2 is subjected to both K63-linked and K48-linked polyubiquitination, and only the K48-linked conjugates were c-IAP1/2–dependent.

Requirement of complex release for MEKK1 and MAPK activation. c-IAP and proteasome activity also appeared to be required for activation of MAP3Ks and MAPKs. Phosphorylation of MEKK1, TAK1, MKK4, MKK3/6, JNK, and p38 was inhibited in splenic B cells that were treated with c-IAP or proteasome inhibitors (Fig. 6, A and B). Similar results were obtained in c-IAP1/2–deficient cells (fig. S8).

These results indicate that MEKK1 and TAK1 and their signaling modules are not activated unless the CD40-assembled signaling complex leaves the receptor and translocates to the cytosol. To investigate this point, we examined the site of kinase activation. No phosphorylation of any relevant kinase was detected in the membrane fraction, whereas the cytosolic complex contained

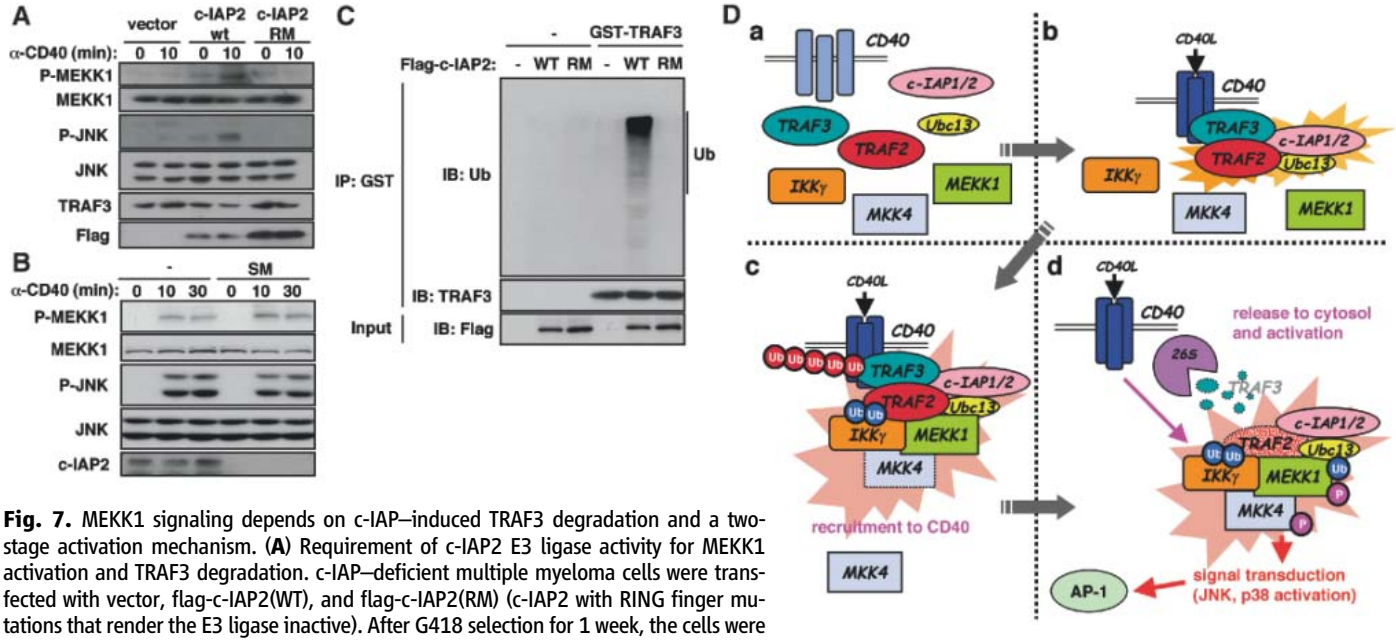

Fig. 7. MEKK1 signaling depends on c-IAP–induced TRAF3 degradation and a two-stage activation mechanism. (**A**) Requirement of c-IAP2 E3 ligase activity for MEKK1 activation and TRAF3 degradation. c-IAP–deficient multiple myeloma cells were transfected with vector, flag-c-IAP2(WT), and flag-c-IAP2(RM) (c-IAP2 with RING finger mutations that render the E3 ligase inactive). After G418 selection for 1 week, the cells were stimulated with anti-CD40. Lysates were analyzed by immunoblotting with the indicated antibodies. (**B**) TRAF3 deficiency renders MEKK1 signaling c-IAP1/2–independent. TRAF3 knockdown A20 cells were incubated with or without SM and stimulated with anti-CD40. At the indicated times, MEKK1 and JNK activation were analyzed by immunoblotting. (**C**) TRAF3 ubiquitination by c-IAP2. Cell lysates were prepared as in (A). c-IAP2 WT and RM were immunoprecipitated, washed, and incubated with or without GST-TRAF3 in a reaction mixture containing ubiquitin, adenosine 5′-triphosphate, E1, and a mixture of E2 ubiquitin-conjugating enzymes. After 30 min, GST-TRAF3 was immunoprecipitated, gel-separated, and analyzed by immunoblotting with anti-ubiquitin and anti-TRAF3. Amounts of c-IAP2 WT and RM were examined with anti-Flag. (**D**) A two-stage signaling mechanism. (a) In nonstimulated B cells, only CD40 is membrane-associated. (b) Receptor engagement induces trimerization and recruitment of TRAF2, TRAF3, c-IAP1/2, and Ubc13. (c) Next to be recruited into this complex are IKKγ and MEKK1. Interactions between IKKγ and MEKK1 and K63-linked polyubiquitin chains catalyzed by TRAF2 and Ubc13 stabilize the complex. (d) c-IAP1/2 catalyze K48-linked polyubiquitination of TRAF3 whose proteasomal (*26S*) degradation results in translocation of the receptor-assembled signaling complex into the cytosol where MEKK1 is activated and in turn activates downstream components of its signaling module.

phosphorylated (and thus, activated) MEKK1, MKK4, and JNK (Fig. 6C). CD40-associated JNK1 and JNK2 were not detected in the membrane fraction, whereas these kinases were readily detected in the cytosolic MEKK1 complex. The cytosolic complex also contained higher relative amounts of MKK4 than did the receptor-associated complex.

TAK1 and TRAF6, which also contribute to MAPK activation (Fig. 1, A and B), were also recruited to CD40 upon its engagement, and a complex containing TAK1 and TRAF6 was released to the cytosol (Fig. 6D). Pretreatment of cells with SM prevented the release of this complex and inhibited CD40-induced phosphorylation of TAK1, which was detected only in the cytoplasm.

IKKβ was recruited to the CD40 signaling complex as early as 2 min after receptor engagement. Maximum amounts were present at 5 min, and IKKβ was no longer detected in the CD40 complex after 10 min (Fig. 6E). IKKβ was activated at the receptor and was insensitive to SM. MEKK1 recruitment was considerably slower: Activated MEKK1 was first detected at 5 min after receptor engagement in the cytoplasm, and its activation peaked at 10 min, the first time point at which activated JNK was detected (fig. S9). Activation of MEKK1 and JNK, as well as MEKK1 ubiquitination, which was also restricted to the cytosolic complex (fig. S10), was inhibited by SM pretreatment. SM also inhibited TNF-induced activation of MEKK1, TAK1, and JNK, but had no effect on activation of IKK (fig. S11). By contrast, depletion of TRAF3, which accelerated MAPK activation, also accelerated recruitment of MKK4, MKK7, and JNK to MEKK1 but had no effect on TRAF2 recruitment to CD40 (fig. S12).

We further examined the role of c-IAP1/2 in CD40 signaling. Reconstitution of c-IAP–deficient multiple myeloma cells with c-IAP2 restored CD40-induced phosphorylation of MEKK1 (Fig. 7A). This appeared to require c-IAP2 catalytic activity because no phospho-MEKK1 was detected in cells expressing RING finger mutated c-IAP2 (*32*). Indeed, in vitro ubiquitination assay revealed that c-IAP2 served as a TRAF3 ubiquitin ligase and this activity depended on its RING finger (Fig. 7C). Supporting the notion that TRAF3 is the "brake" that prevents complex release and kinase activation, MAPK signaling in TRAF3-deficient cells was insensitive to SM (Fig. 7B).

Discussion. Growth factor, cytokine, and immune receptors use MAPK cascades to control many biological outcomes of receptor occupancy (*33*). Activation of receptor-proximal MAP3Ks that lie at the apex of MAPK cascades is thought to require assembly of multiprotein signaling complexes at receptor intracellular domains, and dissociation of receptor-associated complexes has been linked to signal termination. Our results suggest otherwise. Whereas CD40-induced MEKK1 or TAK1 activation requires assembly of a multiprotein complex at the receptor, it is the release of this complex into the cytosol that causes kinase activation. These results indicate that MAPK signaling, at least by CD40 and other TNFRs, follows a two-stage mechanism based on assembly of a multiprotein complex at the receptor that primes MAP3Ks for activation, but in which kinase activation is delayed until the complex is released to the cytoplasm (Fig. 7D).

Whereas TAK1 activation is TRAF6-dependent, activation of MEKK1 depends on TRAF2, which is directly recruited, probably as a TRAF2:3 hetero-oligomer (*22*), to CD40 trimers (*25*). TRAF2 and TRAF3 play opposing but complementary roles in MEKK1 and MAPK activation. In addition to initiating complex assembly, TRAF2 is responsible for recruitment of c-IAP1/2. Although c-IAP1/2 are dispensable for MEKK1 or TAK1 recruitment, they are critical for their activation because they are needed for degradation of TRAF3, which acts as a "brake" that prevents release of the receptor-associated complexes to the cytoplasm (Fig. 7D). In this two-stage mechanism, assembly of the membrane receptor–associated signaling complex (stage I) can be separated in two steps: recruitment of TRAF2:TRAF3 (or TRAF6:TRAF3 for TAK1), c-IAP1/2, and Ubc13, followed by recruitment of IKKγ and MEKK1. Given that IKKγ can bind K63-linked polyubiquitin (*18*, *19*), which decorates TRAF2, it is plausible that Ubc13 and TRAF2 catalyze synthesis of the polyubiquitin chains to which IKKγ binds to promote MEKK1 recruitment. MEKK1 also contains a ubiquitin interaction motif (*24*), which may further contribute to complex stabilization. Consistent with this notion, Ubc13 is obligatory for MAPK activation by several immune receptors (*23*).

Assembly of the receptor-associated signaling complex is insufficient for MAP3K and MAPK activation. Activation requires translocation to the cytosol, which depends on K48-linked polyubiquitination of TRAF3 catalyzed by c-IAP1/2 and subsequent proteasomal degradation (Fig. 7D). In the absence of TRAF3, which cannot activate MAPK or IKK signaling upon overexpression (*34*), complex release and MAPK activation are accelerated and are rendered c-IAP1/2-independent. Therefore, the signaling function of TRAF3 is entirely different from that of TRAF2 or TRAF6. Whereas the latter promote kinase activation through their adaptor and ubiquitin ligase functions, TRAF3 prevents complex release and premature activation.

Although it remains to be seen whether the two-stage signaling mechanism applies to activation of MAP3Ks by other cytokine and immune receptors, IKK activation depends on a different mechanism. It occurs at the receptor with considerably faster kinetics and is c-IAP1/2–independent. Spatial and temporal separation of IKK activation from MAPK activation may be related to their different cellular functions.

References and Notes

1. J. Schlessinger, *Cell* **103**, 211 (2000).
2. T. Pawson, G. D. Gish, P. Nash, *Trends Cell Biol.* **11**, 504 (2001).
3. G. Chen, D. V. Goeddel, *Science* **296**, 1634 (2002).
4. J. L. Bodmer, P. Schneider, J. Tschopp, *Trends Biochem. Sci.* **27**, 19 (2002).
5. V. Baud, M. Karin, *Trends Cell Biol.* **11**, 372 (2001).
6. Z. P. Xia, Z. J. Chen, *Sci. STKE* **2005**, pe7 (2005).
7. M. Rothe, S. C. Wong, W. J. Henzel, D. V. Goeddel, *Cell* **78**, 681 (1994).
8. J. Ninomiya-Tsuji *et al.*, *Nature* **398**, 252 (1999).
9. E. Gallagher *et al.*, *Nat. Immunol.* **8**, 57 (2007).
10. H. Hsu, H. B. Shu, M. G. Pan, D. V. Goeddel, *Cell* **84**, 299 (1996).
11. M. Rothe, M. G. Pan, W. J. Henzel, T. M. Ayres, D. V. Goeddel, *Cell* **83**, 1243 (1995).
12. O. Micheau, J. Tschopp, *Cell* **114**, 181 (2003).
13. J. R. Muppidi, J. Tschopp, R. M. Siegel, *Immunity* **21**, 461 (2004).
14. A. Devin *et al.*, *Immunity* **12**, 419 (2000).
15. C. Wang *et al.*, *Nature* **412**, 346 (2001).
16. H. Hacker, M. Karin, *Sci. STKE* **2006**, re13 (2006).
17. D. M. Rothwarf, E. Zandi, G. Natoli, M. Karin, *Nature* **395**, 297 (1998).
18. C. K. Ea, L. Deng, Z. P. Xia, G. Pineda, Z. J. Chen, *Mol. Cell* **22**, 245 (2006).
19. C. J. Wu, D. B. Conze, T. Li, S. M. Srinivasula, J. D. Ashwell, *Nat. Cell Biol.* **8**, 398 (2006).
20. V. Baud *et al.*, *Genes Dev.* **13**, 1297 (1999).
21. S. S. Pullen, T. T. Dang, J. J. Crute, M. R. Kehry, *J. Biol. Chem.* **274**, 14246 (1999).
22. G. A. Bishop, *Nat. Rev. Immunol.* **4**, 775 (2004).
23. M. Yamamoto *et al.*, *Nat. Immunol.* **7**, 962 (2006).
24. Z. Lu, S. Xu, C. Joazeiro, M. H. Cobb, T. Hunter, *Mol. Cell* **9**, 945 (2002).
25. H. Ye, Y. C. Park, M. Kreishman, E. Kieff, H. Wu, *Mol. Cell* **4**, 321 (1999).
26. J. J. Keats *et al.*, *Cancer Cell* **12**, 131 (2007).
27. L. Li *et al.*, *Science* **305**, 1471 (2004).
28. S. L. Petersen *et al.*, *Cancer Cell* **12**, 445 (2007).
29. D. L. Vaux, J. Silke, *Nat. Rev. Mol. Cell Biol.* **6**, 287 (2005).
30. X. Li, Y. Yang, J. D. Ashwell, *Nature* **416**, 345 (2002).
31. The monoclonal antibody has been generated against a branched peptide corresponding to the region containing K63 of one ubiquitin chain and the C-terminal portion of another chain. It does not recognize ubiquitin attached to any other lysine residue of ubiquitin including K48.
32. H. Huang *et al.*, *J. Biol. Chem.* **275**, 26661 (2000).
33. L. Chang, M. Karin, *Nature* **410**, 37 (2001).
34. H. Hacker *et al.*, *Nature* **439**, 204 (2006).

35. We thank V. M. Dixit (Genentech) for his excellent suggestions, X. Wang (University of Texas Southwestern Medical School) for SM, J. DiDonato (Cleveland Clinic) and G. Courtois (INSERM U697) for IKKγ-deficient cells, R. Fonseca (Mayo Clinic) for c-IAP–deficient cells, and J. Reed and Z. Ronai (Burnham) for c-IAP2 and TRAF2 expression vectors, respectively. Work was supported by NIH grant AI043477 and a Leukemia and Lymphoma Society SCOR (7332-06) project to M.K., who is an American Cancer Society Research Professor. A.M., P.-H.T., and J.-L.L. were supported in part by The Mochida Memorial Foundation for Medical and Pharmaceutical Research, American Lung Association of California, and Life Science Foundation, respectively. H.W. and D.A.A.V were supported by the NIH (AI52199), a Cancer Center Support CORE grant (CA21765), and the American Lebanese Syrian Associated Charities (ALSAC).

Supporting Online Material

www.sciencemag.org/cgi/content/full/1157340/DC1
Materials and Methods
Figs. S1 to S12
References

4 March 2008; accepted 17 June 2008
Published online 17 July 2008;
10.1126/science.1157340
Include this information when citing this paper.

Protostar Formation in the Early Universe

Naoki Yoshida,[1]* Kazuyuki Omukai,[2] Lars Hernquist[3]

The nature of the first generation of stars in the universe remains largely unknown. Observations imply the existence of massive primordial stars early in the history of the universe, and the standard theory for the growth of cosmic structure predicts that structures grow hierarchically through gravitational instability. We have developed an ab initio computer simulation of the formation of primordial stars that follows the relevant atomic and molecular processes in a primordial gas in an expanding universe. The results show that primeval density fluctuations left over from the Big Bang can drive the formation of a tiny protostar with a mass 1% that of the Sun. The protostar is a seed for the subsequent formation of a massive primordial star.

Large ground-based telescopes have discovered distant astronomical objects such as galaxies and quasars (*1*, *2*) that were in place when the universe was less than 1 billion years old, or about 5% of its current age. Moreover, these studies have shown that other luminous objects must have been present even earlier. For example, the most distant known quasar, SDSS-J4010, contains substantial amounts of heavy elements such as carbon, oxygen, and iron as well as dust grains (*3*). These heavy elements are not of cosmic origin, but must have been formed earlier in massive stars before being expelled by supernovae and stellar winds, and then incorporated into the material that later condensed to produce this quasar.

Recently, stars with extremely low heavy-element content were discovered in the halo of our Galaxy (*4*, *5*). The observed elemental abundance patterns indicate several possibilities for the nature of their ancestors (*6*, *7*). One interesting scenario is that supernova explosions of massive primordial stars enriched the parent gas clouds from which these halo stars were born.

Theoretical analyses hold promise for revealing the process of primordial star formation for two main reasons: (i) The initial conditions, as determined cosmologically, are well established, so that statistically equivalent realizations of a standard model universe can be accurately generated; and (ii) the important basic physics such as gravitation, hydrodynamics, and atomic and molecular processes in a hydrogen-helium gas are understood. Other complications that plague investigations of star formation in the local universe, such as the presence of strong magnetic fields or heavy elements, can be neglected at these early times.

Here, we report supercomputer simulations of the development of cosmic structure in the early universe and the formation of primordial stars. Our simulations achieve a dynamic range in spatial scale of ~10^{13}, resolving small-scale structures having sizes of a fraction of a solar radius (~10^{10} cm) within cosmological volumes hundreds of kiloparsecs in length (~10^{23} cm). The smallest length scale—the so-called local Jeans length, set by the action of gravity and hydrodynamic pressure—is fully resolved throughout the simulation volume at all times.

We do not assume any a priori equation of state for the gas. The thermal and chemical evolution of the gas is determined fully by molecular and atomic processes, which are treated in a direct, self-consistent manner. The spatial resolution and the accurate implementations of the physical processes allow us to follow the collapse of a gas to stellar densities, and thus our calculations offer a detailed picture of how the first cosmological objects—primordial protostars—form from chemically pristine gas.

We set up cosmological initial conditions such that the statistical properties of the density and velocity fields are matched to those given by the standard model of the universe (*8*), according to which the energy density is dominated by dark energy and cold dark matter. We follow the gravitational collapse of dark matter and the hydrodynamics of primordial gas through simulations of cosmic structure formation. Below, we provide details on one simulation, which followed the evolution of dark matter and gas in a cube 200 comoving kiloparsecs on a side. We focus our attention on a gravitationally bound dark-matter

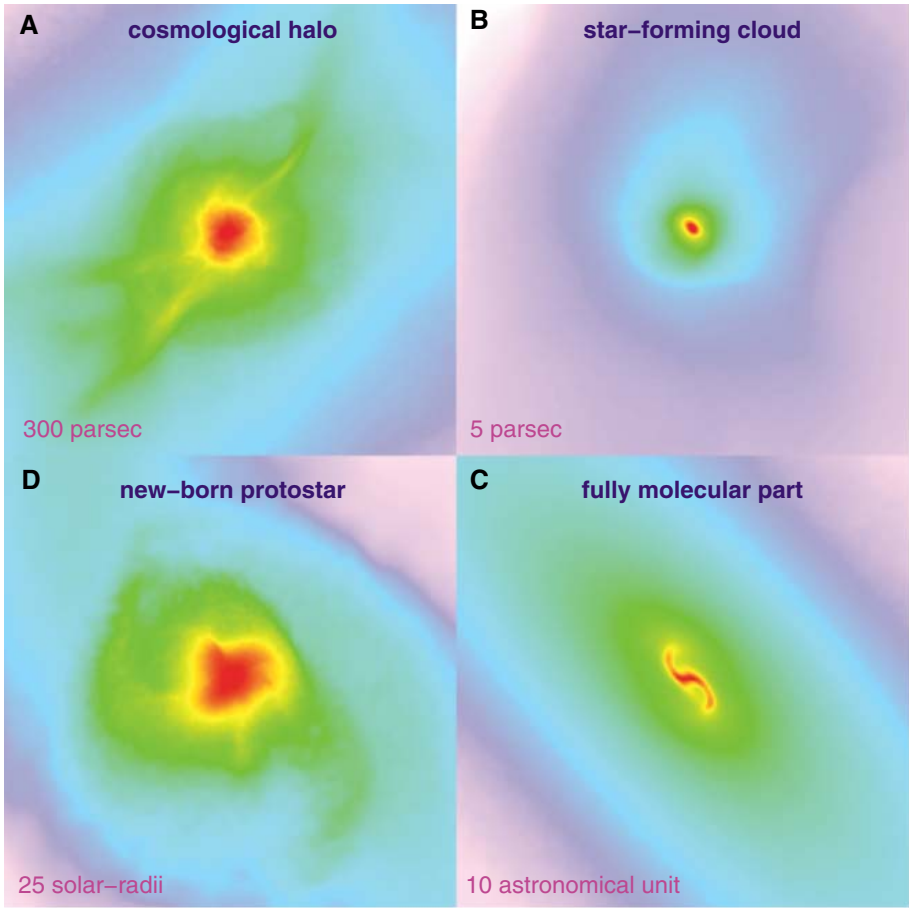

Fig. 1. Projected gas distribution around the protostar. (**A**) The large-scale gas distribution around the cosmological halo (300 pc on a side). (**B**) A self-gravitating, star-forming cloud (5 pc on a side). (**C**) The central part of the fully molecular core (10 astronomical units on a side). (**D**) The final protostar (25 solar radii on a side). The color scale from light purple to dark red corresponds to logarithmically scaled hydrogen number densities from 0.01 to 10^3 cm^{-3} (A), from 10 to 10^6 cm^{-3} (B), and from 10^{14} to 10^{19} cm^{-3} (C). The color scale for (D) shows the density-weighted mean temperature, which scales from 3000 to 12,000 K.

[1]Department of Physics, Nagoya University, Furocho, Chikusa, Nagoya, Aichi 464-8602, Japan. [2]National Astronomical Observatory of Japan, Osawa, Mitaka, Tokyo 181-8588, Japan. [3]Harvard-Smithsonian Center for Astrophysics, 60 Garden Street, Cambridge, MA 02138, USA.

*To whom correspondence should be addressed. E-mail: nyoshida@a.phys.nagoya-u.ac.jp

halo that formed in this volume at an epoch when the cosmological redshift was $z = 14$ (Fig. 1). The mass of this halo (500,000 solar masses, $M_\odot$) and the physical conditions within it are particularly conducive for it to host a primordial star (*9*–*11*). The gas within this halo had a temperature of ~1000 K, and a small mass of hydrogen molecules (~10^{-4} in number fraction) had already formed, enabling efficient radiative cooling.

Through the action of radiative cooling, a star-forming gas cloud collected in the host dark halo. We tracked the subsequent thermal and chemical evolution of the primordial gas cloud for more than 20 decades in density up to the epoch of protostar formation. We accounted for (i) the chemistry at both low and high densities, including molecular hydrogen formation; (ii) transfer of molecular line photons and accompanying radiative cooling; and (iii) transfer of collisionally induced continuum radiation and resulting radiative cooling. In the final phase of the collapse, the temperature increased adiabatically as a result of the absence of radiative and chemical cooling. This continued until the contraction of the central part was halted by strong thermal pressure. At this time, strong hydrodynamic shocks formed, marking the moment of the formation of a protostar. We could not follow the evolution after this epoch accurately without implementing radiative effects from the post-shock high-temperature gases, and thus we stopped the simulation at this point.

The structure in and around the newly formed protostar was rather complex (Fig. 1D). At this time, there were substantial variations in density and temperature even in the innermost (10 solar radii) region. Clearly, the primordial protostar was not simply a sphere surrounded by a single accretion shock.

The cloud evolution was dictated by several important physical processes. First, a fully molecular cloud with mass ~1 $M_\odot$ formed (*10*, *12*, *13*) when the gas density was sufficiently high (>10^8 cm^{-3}) that three-body chemical reactions converted nearly all the hydrogen into molecules. Efficient cooling by rovibrational transitions of hydrogen molecules caused the first small dip at a radius $R \sim 10^{16}$ cm in the radial temperature profile (Fig. 2). When the dense, molecular part contracted further, it became optically thick to hydrogen molecular rovibrational lines, and then the efficiency of radiative cooling saturated (dot-dashed lines in Fig. 2). At still higher densities, frequent collisions between hydrogen molecules led to efficient emission of continuum radiation via collision-induced emission. By this rapid cooling occurring at densities greater than ~10^{14} cm^{-3}, a small central part with ~0.1 $M_\odot$ cooled efficiently to form a flattened disk-like structure. In the flattened gas cloud, radiation escaped preferentially in the direction where contraction was fastest, because the velocity gradient was large and the continuum optical depth was small in this direction (*14*) (figs. S1 and S2). This combined effect of gravitational contraction and direction-dependent radiative cooling accelerated the deformation of the cloud core to a disk structure. The disk structure had a radius of ~10^{13} cm and a mass of ~0.1 $M_\odot$, where the cooling time and the local dynamical time are comparable. While the innermost portion further contracted slowly, spiral density waves were excited, yielding two arms (Fig. 1C).

When the central density reached $n \sim 10^{18}$ cm^{-3}, the gas became completely optically thick to continuum radiation, and at this point radiative cooling no longer operated efficiently (long dashed lines in Fig. 2). Further collapse and the associated dynamical heating triggered full-scale dissociation of hydrogen molecules in the central part (see also Fig. 3). After most of the hydrogen molecules were collisionally dissociated, the gas could not lose its thermal energy either radiatively or by dissociating molecules. The resulting effective equation of state became progressively more stiff, making the gas cloud resist gravitational deformation and fragmentation (*15*, *16*). The gas then contracted adiabatically, and its temperature quickly increased above several thousand kelvin while the density exceeded $n \sim 10^{20}$ cm^{-3}. The strong thermal pressure finally stopped the gravitational collapse, and hydrodynamic shocks were generated (solid lines in Fig. 2). We define a constant-density atomic gas core as a protostar that is pressure-supported. At the final output time, a protostar formed with a mass of just 0.01 $M_\odot$. It had an initial radius of ~5×10^{11} cm, similar to that of present-day protostars in theoretical calculations (*17*). The central particle number density of the protostar was ~10^{21} cm^{-3} and the temperature was well above 10,000 K.

At the time of protostar formation, the central temperature was so high that almost all the molecules were collisionally dissociated within an enclosed mass M_{enc} of 0.01 $M_\odot$ (Fig. 3A). A slight degree of ionization was also seen in the innermost high-pressure part of the atomic core. There was a small variation in the atomic hydrogen fraction at ~0.1 $M_\odot$; a small fraction of hydrogen molecules were dissociated when the gas temperature reached ~2000 K (*12*, *18*), but the molecular fraction increased again when the density increased and efficient continuum cooling brought the gas temperature temporarily below 2000 K (see the second temperature dip at $R \sim 10^{13}$ cm in Fig. 2).

The protostar accreted the ambient gas in a complicated way (Fig. 3B). In the direction vertical to the disk plane, gas falling in at a velocity exceeding 10 km/s was suddenly stopped at the location of a shock at $M_{enc} \sim 0.01\ M_\odot$. Figure 3B also shows the degree of rotational support of the gas, defined as $f_{rot} = (L/r)/v_{Kep}$, where L is the spe-

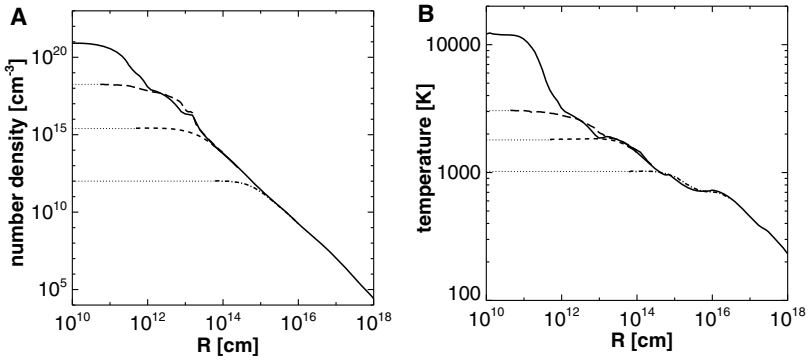

Fig. 2. Evolution of spherically averaged radial density profile (**A**) and temperature profile (**B**) around the protostar. Epochs are shown when the central core became optically thick to molecular lines (dot-dashed lines), when cooling by collision-induced emission kicked in (short dashed lines), when the core became optically thick to continuum (long dashed lines), and when full-scale dissociation was completed and a pressure-supported core formed (solid lines).

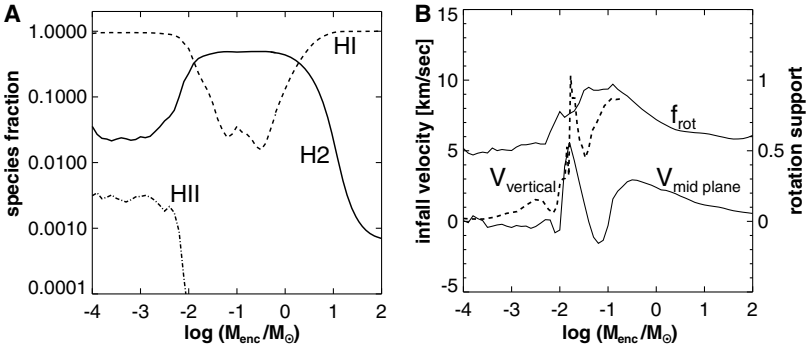

Fig. 3. Structure of the protostar. (**A**) The number fractions of atomic hydrogen (dashed line), molecular hydrogen (solid line), and ionized hydrogen (dot-dashed line). (**B**) The gas infall velocity in one direction perpendicular to the disk plane (dashed line) and an azimuthally averaged inflow velocity at the midplane (solid line). The thin solid line shows the degree of rotational support f_{rot} as defined in the text.

cific angular momentum of the gas within radius r, and v_{Kep} is the Keplerian velocity at that radius.

Within a mass of ~0.1 $M_\odot$, two spiral arms rotated rapidly; the outer part (~0.05 to 0.1 $M_\odot$) appeared nearly centrifugally supported, whereas the central part had gravitationally collapsed. The central core lost part of its angular momentum via gravitational torques exerted by nonaxisymmetric perturbations. The newly born protostar was supported by both thermal pressure and rotation. The overall velocity structure was characteristic of a collapsing gas with an initially slow rotation, as reported in previous studies of both present-day and primordial star formation (*19*, *20*).

A long-standing question is whether a primordial gas cloud such as that studied here experiences vigorous fragmentation by thermal instability during its evolution. In our simulation, a single small protostellar core formed first and the central part did not fragment into multiple objects before protostar formation. At all phases, the locally estimated growth time for isobaric perturbations was longer than, or only comparable to, the local dynamical time for collapse. Hence, the cloud core did not fragment by thermal instability, but instead its collapse accelerated. It has been suggested that the central part of primordial gas clouds may break up into smaller clumps during the subsequent accretion phase (*20*, *21*). We examined a core fragmentation model of (*19*) by measuring Ωt_{dyn}, where Ω is the mean angular velocity and the local dynamical time $t_{dyn} = 1/[(4\pi G\rho)^{1/2}]$ (where G is the gravitational constant and ρ is the gas density). The central ~0.01 $M_\odot$ portion had a value of $\Omega t_{dyn} = 0.25$, which is large and close to the critical value for fragmentation. Thus, the formation of multiple stellar systems may be possible, although not very likely, during later accretion phases.

The instantaneous gas mass accretion rate at the time of protostar formation was as large as 0.01 to 0.1 $M_\odot$ per year within the innermost 10 $M_\odot$. If the gas in the inner portion accreted efficiently, the protostar would quickly grow to be as massive as 10 $M_\odot$ within 1000 years (*22*). Even if multiple stellar seeds formed, there would be at least one main accreting protostar. A detailed protostellar calculation for a similarly large accretion rate predicts that the mass of the star when it lands on the main sequence will be ~100 $M_\odot$ (*13*, *23*).

Feedback effects, in particular those from ionizing photons emitted by the protostar, work to evaporate the surrounding gas and to halt gas accretion. A semianalytic calculation including this radiative feedback and the effect of rotation shows that the final stellar mass can still be greater than a few tens of solar masses in a reasonable parameter space of the model (*24*). If instead mass accretion is unimpeded throughout the star's evolution, the final stellar mass can be very large, possibly exceeding a few hundred solar masses (*22*, *23*). Such very massive stars ionize a large volume of the surrounding gas. Because of the different thermal evolution of an initially ionized gas (*25*), second-generation primordial stars formed under such conditions are predicted to be several tens of solar masses (*26*, *27*). Therefore, in either case, our model provides a viable scenario for the early chemical enrichment in the universe by massive primordial stars (*6*), which is necessary for the formation of later populations of ordinary stars.

The basic properties of the particular star-forming cloud we simulate, such as physical size and mass, are characteristic for cosmological primordial gas clouds, and the object is indeed similar in many aspects to those found in previous work (*10*, *11*, *28*). The final evolution of the central high-density part will likely be affected by its angular momentum content (*20*). However, because the bulk of the cloud core is assembled from material with low angular momentum (*13*), it generally has a slow initial spin, and thus the evolution of prestellar gas is expected to be similar to what is presented here. Our simulation thus offers a complete picture of how a primordial protostar may have formed from tiny cosmological density fluctuations. Primordial star formation for different cosmological models has been explored (*29*, *30*). The particle properties of dark matter may be another important factor in star formation in the early universe.

References and Notes

1. X. Fan *et al.*, *Astron. J.* **125**, 1649 (2003).
2. M. Iye *et al.*, *Nature* **443**, 186 (2006).
3. F. Walter *et al.*, *Nature* **424**, 406 (2003).
4. N. Christlieb *et al.*, *Nature* **419**, 904 (2002).
5. A. Frebel *et al.*, *Nature* **434**, 871 (2005).
6. N. Iwamoto *et al.*, *Science* **309**, 451 (2005); published online 2 June 2005 (10.1126/science.1112997).
7. Y. Komiya *et al.*, *Astrophys. J.* **658**, 367 (2007).
8. D. N. Spergel *et al.*, *Astrophys. J.* **424**, 406 (2007).
9. V. Bromm, P. S. Coppi, R. B. Larson, *Astrophys. J.* **527**, L5 (1999).
10. T. Abel, G. L. Bryan, M. L. Norman, *Science* **295**, 93 (2002); published online 15 November 2001 (10.1126/science.1063991).
11. V. Bromm, P. S. Coppi, R. B. Larson, *Astrophys. J.* **564**, 23 (2002).
12. K. Omukai, R. Nishi, *Astrophys. J.* **508**, 141 (1998).
13. N. Yoshida, K. Omukai, L. Hernquist, T. Abel, *Astrophys. J.* **652**, 6 (2006).
14. See supporting material on *Science* Online.
15. T. Hanawa, T. Matsumoto, *Pub. Astron. Soc. Jpn.* **52**, 241 (2000).
16. K. Omukai, T. Tsuribe, R. Schneider, A. Ferrara, *Astrophys. J.* **626**, 627 (2005).
17. R. B. Larson, *Mon. Not. R. Astron. Soc.* **145**, 271 (1969).
18. E. Ripamonti, F. Haardt, A. Ferrara, M. Colpi, *Mon. Not. R. Astron. Soc.* **334**, 401 (2002).
19. T. Matsumoto, T. Hanawa, *Astrophys. J.* **595**, 913 (2003).
20. M. N. Machida, K. Omukai, T. Matsumoto, S. Inutsuka, *Astrophys. J.* **677**, 813 (2008).
21. P. C. Clark, S. C. O. Glover, R. S. Klessen, *Astrophys. J.* **672**, 757 (2008).
22. V. Bromm, A. Loeb, *New Astron.* **353**, 364 (2004).
23. K. Omukai, F. Palla, *Astrophys. J.* **589**, 677 (2003).
24. C. F. McKee, J. Tan, *Astrophys. J.* **681**, 771 (2008).
25. H. Uehara, S. Inutsuka, *Astrophys. J.* **531**, L91 (2000).
26. J. L. Johnson, V. Bromm, *Mon. Not. R. Astron. Soc.* **366**, 247 (2006).
27. N. Yoshida, K. Omukai, L. Hernquist, *Astrophys. J.* **667**, L117 (2007).
28. B. O'Shea, M. L. Norman, *Astrophys. J.* **654**, 66 (2007).
29. L. Gao, T. Theuns, *Science* **317**, 1527 (2007).
30. D. Spolyar, K. Freese, P. Gondolo, *Phys. Rev. Lett.* **100**, 051101 (2008).

31. We thank M. Machida and T. Matsumoto for fruitful discussions on gas cloud evolution. Supported by Grants-in-Aid for Young Scientists 17684008, 18740117, and 19047004 from the Ministry of Education, Culture, Science, and Technology of Japan and by the Mitsubishi Foundation (N.Y. and K.O.).

Supporting Online Material

www.sciencemag.org/cgi/content/full/321/5889/669/DC1
Materials and Methods
Figs. S1 and S2
References

9 May 2008; accepted 12 June 2008
10.1126/science.1160259

High Rates of Oxygen Reduction over a Vapor Phase–Polymerized PEDOT Electrode

Bjorn Winther-Jensen,* Orawan Winther-Jensen, Maria Forsyth, Douglas R. MacFarlane

The air electrode, which reduces oxygen (O_2), is a critical component in energy generation and storage applications such as fuel cells and metal/air batteries. The highest current densities are achieved with platinum (Pt), but in addition to its cost and scarcity, Pt particles in composite electrodes tend to be inactivated by contact with carbon monoxide (CO) or by agglomeration. We describe an air electrode based on a porous material coated with poly(3,4-ethylenedioxythiophene) (PEDOT), which acts as an O_2 reduction catalyst. Continuous operation for 1500 hours was demonstrated without material degradation or deterioration in performance. O_2 conversion rates were comparable with those of Pt-catalyzed electrodes of the same geometry, and the electrode was not sensitive to CO. Operation was demonstrated as an air electrode and as a dissolved O_2 electrode in aqueous solution.

Both fuel-cell technology for power generation and metal-air batteries for energy storage require an efficient electrode for O_2 reduction. Such air electrodes are usually a Pt catalyst embedded in a porous carbon electrode. Despite having a high current density suitable for high-power applications such as vehicle drive systems (*1*–*4*), a number of issues with these elec-

trodes may ultimately limit the use and lifetime of the fuel cell or the storage battery, despite recent improvements (*5*, *6*). For example, the cost of the Pt alone in a polymer membrane fuel cell for a small 100-kW passenger vehicle is substantially greater (at March 2008 prices) than the current cost of an entire 100-kW gasoline engine (*7*). Several technical issues also arise with the use of Pt catalysts. The Pt particles present in the composite electrode are not fixed in place, and a well-known drift phenomenon (*8*) by which the particles diffuse and agglomerate over time ultimately diminishes the performance of the fuel cell. Further, Pt is very sensitive to deactivation in the presence of CO, either in the air supply or as a by-product from the use of methanol in the direct methanol fuel cell (*9*–*13*).

Other metallic electrode materials, such as cobalt and Ru/Pt alloys (*14*, *15*), have been explored to overcome some of these problems, but in all cases one or more of the issues remain. In particular, the sensitivity to CO is a particularly difficult problem to overcome. In this work, we have developed a Pt-free air electrode based on a nanoporous, intrinsically conductive polymer (ICP) multilayer structure that offers performance similar to that of Pt-catalyzed electrodes under parallel testing. Because the material is homogeneous, the drift issue is avoided and, being nonmetallic, the catalyst is not sensitive to CO poisoning.

The use of ICPs for catalytic electrodes was investigated early in the history of conducting polymer research and applications. However, success was limited by low conductivity and efficiency, and the instability of the ICP in the environment required for the catalysis (*16*–*18*). By incorporation of traditional catalytic centers such as Pt into ICPs, a range of catalytic electrodes have been reported (*14*, *19*, *20*), but these materials all suffer from many of the same problems as the Pt-C electrode. Recently, the development of chemical polymerization [in particular, a process known as vapor phase polymerization (VPP)] and "designed" ICP derivatives has produced materials with high conductivity, improved ordering and stability, and controllable porosity at the nanoscale (*21*–*24*). These properties improve the potential of these materials for electrocatalytic applications. Previous studies of PEDOT (*25*) have not been able to demonstrate catalysis of oxygen reduction; however, the improved thin-film properties obtained via VPP prompted us to reexamine its potential as an electrocatalytic material.

One of the key features of an air electrode is that it must establish a high–surface area boundary between the three active phases: air, the electrolyte, and the catalyst/conductor. To achieve this three-phase interface, we coated a PEDOT electro-active layer onto one side of a hydrophobic, porous membrane (Goretex). The procedure developed here involves plasma polymerization of a binding layer to the polytetrafluoroethylene (PTFE) membrane, followed by VPP of the 3,4-ethylenedioxythiophene monomer to form the PEDOT conducting polymer (see fig. S1 for further details).

A schematic of the cross-sectional structure of the electrode in Fig. 1A shows the intended three-phase interface in the circled region. The designed structure allows access of the air stream from one side of the electrode to a high–surface area, electrochemically active layer of the PEDOT, which is simultaneously in contact with the electrolyte. The Goretex membrane provides a good, although not entirely optimized, starting point because it is highly porous at the micrometer level and, being hydrophobic, does not allow penetration of the aqueous electrolyte into the pores of the membrane. Because the electrical conductivity of PEDOT is still not high enough to provide a low-resistance path to the external circuit, a more electronically conductive underlayer was used. Coating one face of this membrane with a ~40-nm layer of gold provided the conductor layer without altering the structure of the membrane (Fig. 1B). In the next stage, a 400-nm PEDOT layer is created on one side by VPP (Fig. 1C). The structure of the underlying membrane is still visible after these deposition steps, which indicates that the three-phase boundary has been obtained over a substantial fraction of the membrane. An image of the cross-sections of the complete membrane assembly (Fig. 1D) shows the thin PEDOT layer on the surface of the structure.

From the thickness measurements, the mass of the PEDOT can be determined to be 0.05 mg/cm^2 for the optimum layer for this particular Goretex membrane; this optimal thickness will change with pore size and shape of the membrane.

The Goretex/PEDOT electrode was subjected to testing as an air electrode at various pH levels and potentials in a cell that allowed direct contact with air from one side and electrolyte from the other (see fig. S2 for detailed experimental setup). The air reduction current under standard conditions (Fig. 2) shows that the electrode performs well over a wide pH range. The PEDOT membrane provides substantial oxygen reduction current densities at all of the pH conditions studied with the potential of onset of the reduction currents shifting as a function of pH in the expected way. To demonstrate that the underlying gold layer was not actively involved in the catalytic process, we conducted a separate experiment (fig. S3) using a Goretex membrane coated only with gold; this electrode produced substantially lower currents.

Continuous operation in air was achieved at −0.3 V versus saturated calomel electrode (SCE) for more than 1500 hours at pH = 1; 3 A·hour/cm^2 of charge was passed during this test. Testing of the electrochemical characteristics of the electrode after 1500 hours showed no change as a result of this period of operation (fig. S4).

Electrodes were constructed with PEDOT thicknesses ranging from around 40 to 1300 nm. It appears that the 400-nm coating shown in Figs. 1 and 2 is nearly optimal for this membrane pore size. When thicker coatings are applied, the diffusion of species, either in the electrolyte, or of oxygen through the PEDOT, becomes limiting and leads to lower currents.

For comparison purposes, we created a Pt-catalyzed electrode by depositing a 45-nm Pt

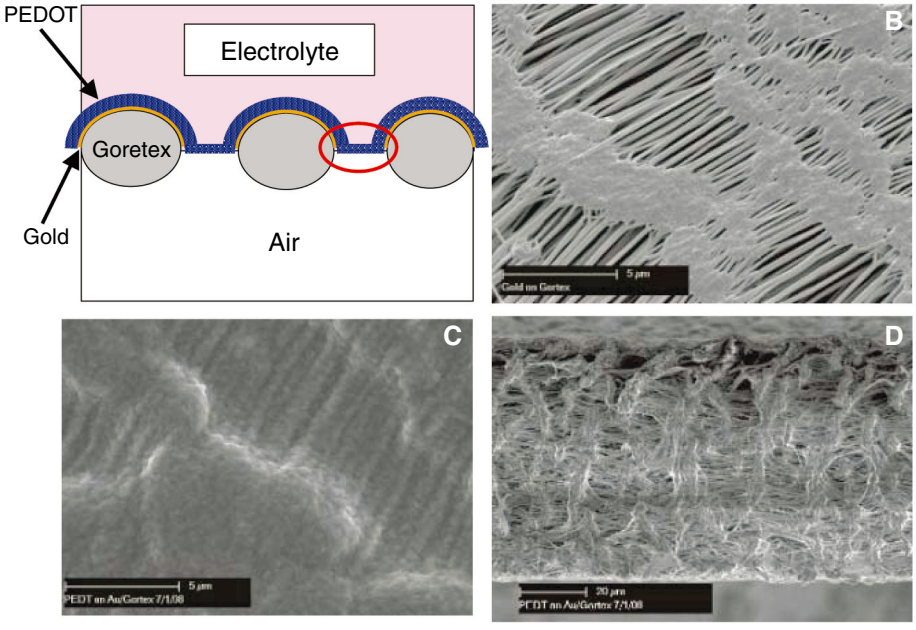

Fig. 1. (**A**) Schematic representation of the PEDOT/Goretex air electrode. (**B** to **D**) Scanning electron micrograph images: (B) The Goretex membrane coated with gold. Scale bar, 5 μm. (C) The PEDOT/Goretex structure. Scale bar, 5 μm. (D) Cross-section of the electrode with thickness measurements of the PEDOT layer. Scale bar, 20 μm.

Australian Centre for Electromaterials Science, Monash University, Clayton, Victoria 3800, Australia.

*To whom correspondence should be addressed. E-mail: bjorn.winther-jensen@eng.monash.edu.au

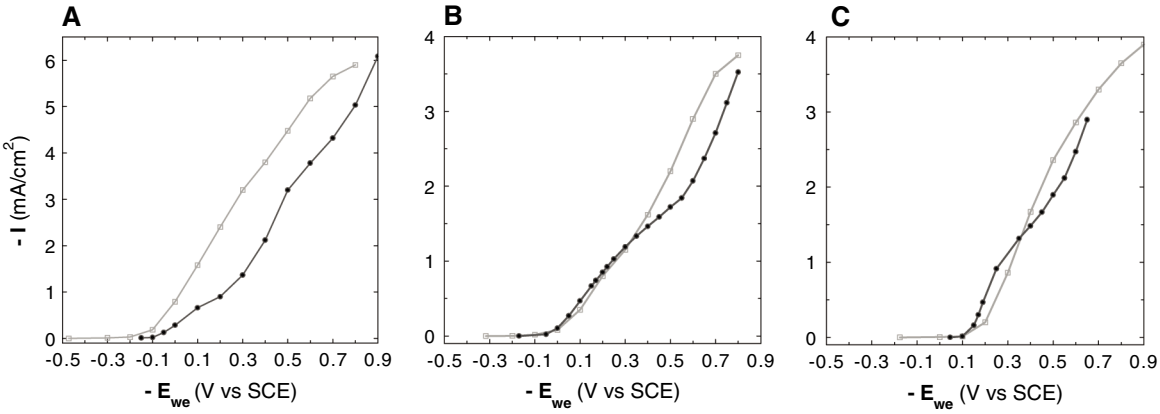

Fig. 2. Steady-state measurements (each point after 1 hour of continuous operation) of the conversion current versus potential at different pH values (black line: 400-nm PEDOT/Goretex; gray line: 45-nm Pt/Goretex). (**A**) pH 1, (**B**) pH 7, and (**C**) pH 13 for oxygen reduction from air.

layer onto the Au layer. The magnitudes of the conversion currents delivered by the PEDOT electrode are comparable to those of Pt for the same geometrical (membrane) area (Fig. 2). At pH 1, the Pt seems to perform better than the PEDOT electrode by a factor of ~2, whereas at pH 7 and pH 13, the conversion currents are similar. The active surface area is actually considerably higher in the Pt case, because of the pore-filling effect of the thicker PEDOT layer in the Goretex membrane. It is also interesting that, although the thicknesses are different for the Pt (45 nm) and PEDOT (400 nm) layers, the difference in their densities (21.1 g/cm^3 for Pt and ~1.2 g/cm^3 for PEDOT) means that the mass loading of active material is actually lower in the PEDOT case by a factor of ~2. The electrocatalytic performance of the PEDOT material (up to ~0.2 A/mg) is also similar to that of other recently reported cobalt-based materials (*14*).

The highest room-temperature current density observed with the membranes described here is ~6 mA/cm^2. This value is sufficient for some metal/air batteries and a number of fuel-cell technologies including small direct methanol fuel cells, micro fuel cells, and the various biofuel cell concepts (*9*, *26*). Higher–current density fuel-cell application of the PEDOT electrocatalyst concept would require extension of the three-phase interface into a thicker membrane structure.

The performance of the PEDOT and Pt-based assemblies is compared in Fig. 3A for different levels of CO contamination in the air supply; the PEDOT electrode is not affected, whereas the Pt electrode is poisoned very rapidly under identical conditions. The formation of carbonyl complexes of Pt at the surface that poisons its activity is unlikely with PEDOT. The effect of oxygen partial pressure in the gas supply (air = 20%) (Fig. 3B) demonstrates that the electrode is capable of even higher currents than are generated in air and that no limit related to processes within the PEDOT is being reached over the range of oxygen contents probed.

In a similar series of tests, the sensitivity of the electrode to the presence of methanol in the electrolyte was examined. Methanol crossover from the anode to the cathode is a major issue in the direct methanol fuel cell. The oxidation of methanol is seen to be a competitive reaction to O_2 reduction on the cathode side (*9*). In the present work, a 1% addition of methanol was found to decrease the steady-state current at −0.3 V versus SCE by 20%, at which point the current again reached a steady value. Removal of the methanol brought the current back to its original value, indicating that no permanent damage to the electrode had been caused.

Further insight into the mechanism of the processes taking place in these PEDOT electrode assemblies is provided by Fig. 4, which shows the electronic conductivity of the membrane as a function of the applied potential in an aqueous system. PEDOT in the absence of O_2 adopts a variable state of oxidation as a function of potential between about −0.5 to +0.5 V versus Ag/AgCl in aqueous solution (fig. S5). It is transformed from a low-conductivity material in its reduced state to a highly conductive material in its fully oxidized state. Operating the PEDOT air electrode at various potentials shows a conductiv-

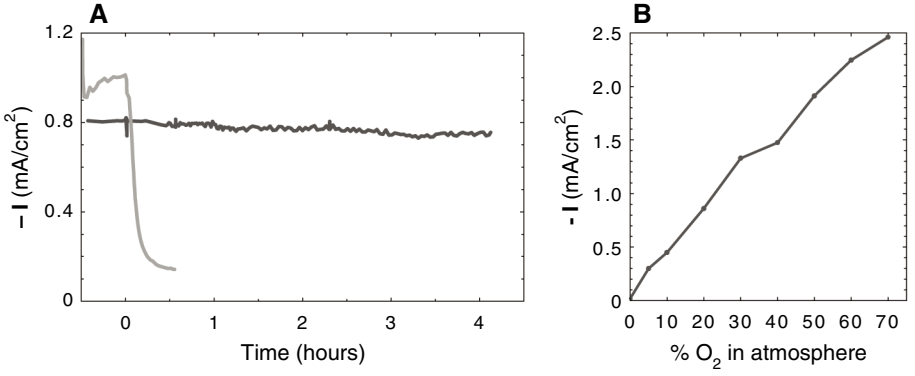

Fig. 3. Response of the PEDOT air electrode (black line) to different gas supplies (−0.3 V versus SCE, 0.1 M phosphate buffer, pH 7). (**A**) Current versus time in air contaminated by 10% CO compared to a similar Pt-catalyzed electrode (gray line). (**B**) Current as a function of oxygen content in the gas supply.

Fig. 4. Conductivity (σ) versus potential (*E*): Conductivity in PEDOT air electrode (0.1 M phosphate buffer, pH 7).

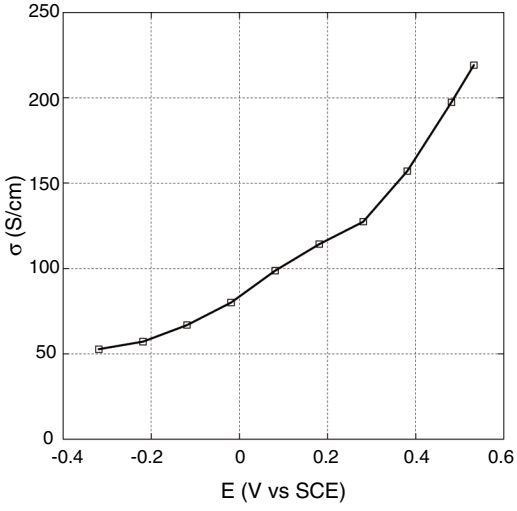

ity profile with much higher conductivity at lower potentials (Fig. 4) compared to PEDOT in the absence of air (fig. S5), indicating that the PEDOT is reaching a steady-state oxidation level according to the applied potential, which is greater in the presence of air. The mechanism of the air reduction electrocatalysis likely involves a redox cycling process where the PEDOT, which naturally rests in an oxidized form, is momentarily reduced by the action of the electrochemical cell. An O_2 molecule then absorbs onto the surface of the PEDOT and rapidly reoxidizes the PEDOT to its preferred oxidized state and is itself reduced in the process. The role of the counterion in this mechanism, if any, is still unclear.

Given the similarity between the Pt and PEDOT responses in Fig. 2, it seems likely that the O_2 reduction proceeds via the four-electron pathway as it does on Pt, because there is no sign of an additional process that might indicate a contribution from H_2O_2 formation. Further investigation of the type described by Halseid *et al.* (*27*) is under way to probe the selectivity with respect to the four-electron pathway. Recent reports (*28*) describe efficient iron-loaded graphite catalysts for oxygen reduction. Given the very low Fe loadings involved, we cannot exclude the possibility of a role for residual Fe, at levels below the limit of x-ray photoelectron spectroscopy detection, in the mechanism reported here. However, iron-based catalytic centers would normally be expected to show signs of poisoning in the presence of CO; the resistance to CO poisoning seen here (Fig. 3) thus suggests that iron centers do not play a notable role.

A laboratory Zn/air battery was also constructed based on this PEDOT air-electrode assembly and a 1 M KOH electrolyte. An open-circuit voltage of 1.44 V was measured, comparable with other examples of this cell (*29*, *30*). Discharge characteristics (fig. S6) as a function of current density and over a 48-hour continuous test were superior to similar devices constructed with a Pt/Goretex air electrode.

The electrode described here provides only a partial solution to some of the problems with the use of Pt discussed in the introduction, because Pt is also used in the anode (fuel) electrode in the fuel cell. However, the fundamental mode of catalysis at work in the present materials may be able to be extended to other reactions, such as the hydrogen oxidation reaction, by careful choice of the ICP. ICPs can be successfully used as a substitute for Pt in dye-sensitized solar cells for the I^-/I_3^- redox reaction (*31*). Thus, the development of the gas-ICP-electrolyte three-phase interface electrode reported here may provide a platform for a new generation of metal-free electrocatalysts.

References and Notes

1. T. Teratani, R. Mizutani, K. Yamamoto, T. Anegawa, *IEEJ Trans. Electr. Electron. Eng.* **3**, 162 (2008).
2. P. Agnolucci, *Int. J. Hydrogen Energy* **32**, 3526 (2007).
3. E. Pucher, A. Sekanina, *Elektrotechnik und Informationstechnik* **123**, 410 (2006).
4. K. Jorgensen, *Utilities Policy* **16**, 72 (2008).
5. V. R. Stamenkovic *et al.*, *Science* **315**, 493 (2007).
6. J. Zhang, K. Sasaki, E. Sutter, R. R. Adzic, *Science* **315**, 220 (2007).
7. University of Houston, "Fuel Cells Gearing Up To Power Auto Industry," *ScienceDaily*, 31 October 2007, retrieved 14 April 2008; www.sciencedaily.com/releases/2007/10/071030121117.htm.
8. X. Yu, S. Ye, *J. Power Sources* **172**, 145 (2007).
9. A. S. Arico, S. Srinivasan, V. Antonucci, *Fuel Cells* **1**, 133 (2001).
10. D. J. Ham, Y. K. Kim, S. H. Han, J. S. Lee, *Catal. Today* **132**, 117 (2008).
11. M. Winter, R. J. Brodd, *Chem. Rev.* **104**, 4245 (2004).
12. R. Liu *et al.*, *J. Phys. Chem. B* **104**, 3518 (2000).
13. J. S. Lee, S. Locatelli, S. T. Oyama, M. Boudart, *J. Catal.* **125**, 157 (1990).
14. R. Bashyam, P. Zelenay, *Nature* **443**, 63 (2006).
15. A. Garsuch *et al.*, *J. Electrochem. Soc.* **155**, B236 (2008).
16. R. C. M. Jakobs, L. J. J. Janssen, E. Barendrecht, *Electrochim. Acta* **30**, 1313 (1985).
17. N. F. Atta *et al.*, *J. Chem. Soc. Chem. Commun.*, 1347 (1990).
18. M. Somasundrum, J. V. Bannister, *J. Chem. Soc. Chem. Commun.*, 1629 (1993).
19. M. C. Lefebvre, Z. Qi, P. G. Pickup, *J. Electrochem. Soc.* **146**, 2054 (1999).
20. G. Tourillon, F. Garnier, *J. Phys. Chem.* **88**, 5281 (1984).
21. B. Winther-Jensen, K. West, *Macromolecules* **37**, 4538 (2004).
22. D. M. de Leeuw, P. A. Kraakman, P. F. G. Bongaerts, C. M. J. Mutsaers, D. B. M. Klaassen, *Synth. Met.* **66**, 263 (1994).
23. B. Winther-Jensen *et al.*, *Org. Electron.* **8**, 796 (2007).
24. B. Winther-Jensen *et al.*, *Polymer* **49**, 481 (2008).
25. V. Khomenko, V. Barsulov, A. Katashinskii, *Electrochim. Acta* **50**, 1675 (2005).
26. D. Ivnitski, B. Branch, P. Atanassov, C. Apblett, *Electrochem. Commun.* **8**, 1204 (2006).
27. R. Halseid, M. Heinen, Z. Jusys, R. J. Behm, *J. Power Sources* **176**, 435 (2008).
28. E. Proietti, S. Ruggeri, J. P. Dodelet, *J. Electrochem. Soc.* **155**, B340 (2008).
29. A. A. Mohamad, *J. Power Sources* **159**, 752 (2006).
30. W. K. Chao, C. M. Lee, S. Y. Shieu, C. C. Chou, F. S. Shieu, *J. Power Sources* **177**, 637 (2008).
31. Y. Saito, W. Kubo, T. Kitamura, Y. Wada, S. Yanagida, *J. Photochem. Photobiol. Chem.* **164**, 153 (2004).

32. Funding of this work by the Australian Research Council (ARC) Centre of Excellence in Electromaterials Science is gratefully acknowledged, as is ARC Fellowship support for B.W.-J. (Australian Postdoctoral Fellowship) and D.R.M. (Federation Fellowship).

Supporting Online Material

www.sciencemag.org/cgi/content/full/321/5889/671/DC1
Materials and Methods
Figs. S1 to S6
References

17 April 2008; accepted 23 June 2008
10.1126/science.1159267

Structures of Neutral Au_7, Au_{19}, and Au_{20} Clusters in the Gas Phase

Philipp Gruene,[1] David M. Rayner,[2] Britta Redlich,[3] Alexander F. G. van der Meer,[3] Jonathan T. Lyon,[1] Gerard Meijer,[1] André Fielicke[1]*

The catalytic properties of gold nanoparticles are determined by their electronic and geometric structures. We revealed the geometries of several small neutral gold clusters in the gas phase by using vibrational spectroscopy between 47 and 220 wavenumbers. A two-dimensional structure for neutral Au_7 and a pyramidal structure for neutral Au_{20} can be unambiguously assigned. The reduction of the symmetry when a corner atom is cut from the tetrahedral Au_{20} cluster is directly reflected in the vibrational spectrum of Au_{19}.

Haruta *et al.*'s finding that dispersed gold nanoparticles show pronounced catalytic activity toward the oxidation of CO has triggered a gold rush in cluster chemistry (*1*). Although bulk gold is a classic example of chemical inertness (*2*), many later studies have confirmed the size-dependent reactivity of deposited gold clusters (*3*–*6*). Small particles of gold differ from the bulk because they contain edge atoms that have low coordination (*7*) and can adopt binding geometries that lead to a more reactive electronic structure (*8*). Thus, the secret of the catalytic properties of gold nanoparticles lies at least partly in their geometric structure. Structural information for deposited gold mono- and bilayers on titania has been obtained by using high-resolution electron energy–loss spectroscopy on CO adsorbates (*9*). Determining the three-dimensional (3D) structure of deposited gold nanoparticles is more challenging, but recently has been achieved for clusters containing around 310 atoms by means of aberration-corrected scanning transmission electron microscopy (*10*).

The geometry of nanoparticles can also be studied in the gas phase. The advantages of this approach are the exact knowledge of the clusters' size and the absence of any interaction with the surrounding environment. The properties of such well-defined species can thus be modeled very precisely with quantum-mechanical calculations. Different experimental techniques exist for the study of free clusters. By measuring the mobility of size-selected gold anions and cations in helium, a transition from 2D to 3D structures has been found (*11*, *12*). This transition appears at different cluster sizes for cations and anions and is yet to be determined experimentally for neutral species. A combination of photoelectron spectroscopy and quantum-mechanical calculations has revealed fascinating structures of anionic gold species—for example, cages for clusters containing 16 to 18 atoms (*13*), a tetrahedral pyramid for Au_{20}^- (*14*), and a possibly chiral structure for Au_{34}^- (*15*). These structural motifs have been confirmed by measurement of the electron diffraction pattern of size-selected trapped anions (*15*, *16*). Although ion mobility measurements, photoelectron spectrosco-

[1]Fritz-Haber-Institut der Max-Planck-Gesellschaft, 14195 Berlin, Germany. [2]Steacie Institute for Molecular Sciences, Ottawa, Ontario K1A 0R6, Canada. [3]Stichting voor Fundamenteel Onderzoek der Materie (FOM) Institute for Plasma Physics Rijnhuizen, 3439 MN Nieuwegein, Netherlands.

*To whom correspondence should be addressed. E-mail: fielicke@fhi-berlin.mpg.de

py, and trapped-ion electron diffraction have all substantially added to the understanding of the geometric properties of free nanoparticles, these methods are restricted to the investigation of charged species.

We investigated neutral gold clusters in the gas phase by means of vibrational spectroscopy, which is inherently sensitive to structure. In infrared (IR) absorption spectroscopy, the number of allowed transitions is restricted by selection rules, and thus directly reflects the symmetry of the particle. Far-IR multiple-photon dissociation (FIR-MPD) spectroscopy is a proven technique for obtaining the vibrational spectra of gas-phase metal clusters and, hence, by comparison with calculated spectra, their geometries (*17*, *18*). It is the only technique for determining the structure of free metal clusters that is not limited to charged species. We explored three representative sizes of neutral gold clusters. With Au_7, we investigated the structure in a size region in which the anions and cations are known to adopt planar structures, and we thereby addressed a controversy in theoretical studies. With Au_{20}, we confirmed that the neutral cluster retains the symmetrical pyramid geometry established for the anion. With Au_{19}, we directly observed the reduction of symmetry when one of the corner atoms is removed from Au_{20}.

Details of the technique of FIR-MPD have been described elsewhere (*17*, *19*). Neutral gold clusters are produced by means of laser vaporization from a gold rod in a continuous flow of He and Kr (1.5% Kr in He) at 100 K. Under these conditions, complexes of the bare metal clusters with one or two Kr ligands are formed. The molecular beam is overlapped with a pulsed FIR beam delivered by the Free Electron Laser for Infrared eXperiments (FELIX) (*20*). The neutral complexes are ionized by an F_2-excimer laser (7.9 eV per photon) and mass-analyzed in a time-of-flight mass spectrometer. Resonance of the FIR light with an IR-active vibrational mode of a given neutral cluster may lead to the absorption of several photons. The subsequent heating of the complex results in the evaporation of a loosely bound Kr ligand and a depletion of the corresponding mass spectrometric signal. Recording the mass-spectrometric signal while scanning the wavelength of FELIX leads to depletion spectra, from which absorption spectra $\sigma(\tilde{\nu})$ are reconstructed (*21*).

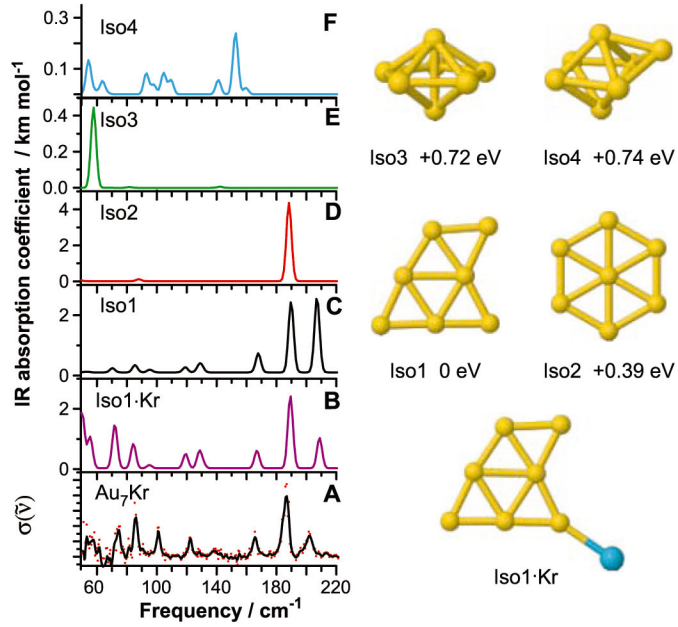

Fig. 1. Vibrational spectra of neutral Au_7. (**A**) The FIR-MPD spectrum of Au_7Kr. The red dots represent relative cross sections, $\sigma(\tilde{\nu})$, the average of up to ~1000 single laser shots at a fixed frequency, whereas the black line interconnects a binomially weighted five-point running average, thus accounting for the spectral bandwidth of the IR laser. It is compared with the spectra of four low-lying isomers (Iso1 to 4) (**C** to **F**) obtained by DFT calculations. The peak positions in the experiment are in best agreement with a planar structure of C_s symmetry (Iso1). Including the Kr ligand in the calculation does not substantially change the structure of the cluster or the positions of the resonances (Iso1 • Kr) (**B**), but has an effect on the IR intensities, which become very similar to those in the experimental spectrum.

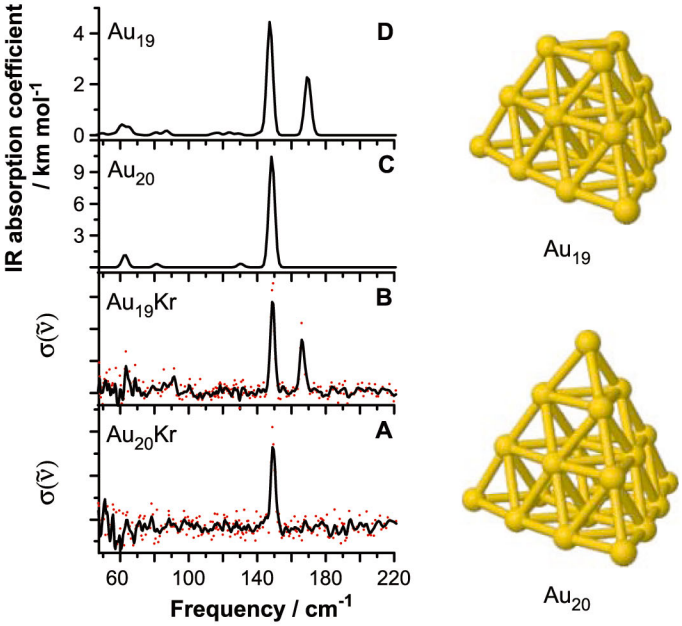

Fig. 2. Vibrational spectra of neutral Au_{19} and Au_{20}. (**A** and **B**) The FIR-MPD spectra of $Au_{20}Kr$ and $Au_{19}Kr$, respectively. (**C** and **D**) Calculated spectra for pyramidal geometries Au_{20} and Au_{19} are in excellent agreement with the experiment. The splitting of the degenerate resonance at 148 cm^{-1} for Au_{20} into two peaks at 149 cm^{-1} and 166 cm^{-1} for Au_{19} is due to the lowering of symmetry when going from the tetrahedron to the truncated pyramid.

Figure 1A shows the vibrational spectrum of neutral Au_7 obtained with FIR-MPD of its complex with one Kr ligand. A number of bands were found in the region between 47 and 220 cm^{-1}, usually having a full width at half maximum of less than 4 cm^{-1} (*21*). This is close to the spectral bandwidth of FELIX, which is about 2 to 3 cm^{-1} and nearly constant over the whole tuning range. The number of peaks implies a rather nonsymmetric structure for neutral Au_7. The geometry of Au_7 was established by comparing the experimental spectrum with the calculated vibrational spectra for multiple isomers predicted by density functional theory (DFT) calculations within the generalized gradient approximation (*21*, *22*). We found a planar edge-capped triangle with C_s symmetry (Iso1) to be lowest in energy. This structure has been previously reported as the global minimum (*23*). A hexagonal planar structure (Iso2) (*24*) and a 3D structure (Iso3) (*25*) have been proposed as lowest-energy structures as well, but were computed to be higher in energy in the present study.

The experimental vibrational spectrum unambiguously tested the reliability of the theoretical methods. The calculated spectra were distinctive in the range between 150 and 220 cm^{-1}. The peak positions of Iso1 fit with experimental absorptions at 165, 186, and 201 cm^{-1}. Only the relative intensities of the bands did not agree completely; the central band at 186 cm^{-1} was much more pronounced in the experiment. Figure 1B shows the calculated absorption spectrum of the complex Iso1·Kr, in which Kr is bound to the energetically most favorable position of the Iso1 cluster with a bond dissociation energy of 0.09 eV. The positions of the resonances were not changed, but the relative intensities were substantially affected. The three bands were then in excellent agreement with the experiment, and, furthermore, all absorptions between 50 and 150 cm^{-1} became more pronounced (*26*). The calculations show that all of these vibrational modes are highly delocalized and involve the motion of all atoms in the cluster [see normal mode displacement vectors for the three highest-energy vibrations of Au_7 (all in-plane) in fig. S3].

In principle, multiple isomers can be present in the molecular beam, in which case the spectrum would represent a superposition of their individual contributions. Iso2 has one strong absorption at

185 cm^{-1}, and its presence in the molecular beam could also explain the pronounced intensity of the central peak in the experimental spectrum. Ion mobility measurements, however, excluded the presence of major amounts of additional isomers for cationic and anionic Au_7. For experimental modes that were not present in the calculated spectrum of hexagonal Iso2—for example, at 165 cm^{-1} and 201 cm^{-1}—the mass-spectrometric intensity of Au_7Kr went down to below 30% of its original value when irradiated by FELIX, which set the upper limit for the abundance of other isomers. Therefore, although a minor contribution of Iso2 could not be ruled out, the capped triangle could be assigned as the dominant structural isomer of neutral Au_7 present in our experiment.

On comparison with the experimentally determined structures of the corresponding ionic species, we found that Au_7 is a cluster size, which changes its geometries for each charge state. Although the cation is highly symmetric and corresponds to the D_{6h} structure Iso2 (*12*), the anion forms a threefold edge-capped square (*11*). We found this structure to be a saddle point in our calculations for neutral Au_7 that relaxes into Iso1. The geometrical change as a function of cluster charge corresponds to a lessening of the average coordination as the electron density increases. Although the gold atoms in the cation have on average 3.43 nearest neighbors, this value decreases to 3.14 and 2.85 for the neutral and the anion, respectively. With additional electrons, the clusters favor more open structures.

Having shown that the experimental spectrum, in combination with theory, can be used to identify the geometry of the Au_7 cluster, we moved on to bigger sizes. Photoelectron spectroscopy and quantum-mechanical calculations have shown that anionic Au_{20}^- is a pyramid and has T_d symmetry (*14*). This structure has also been suggested to be the global minimum for neutral Au_{20} (*14*). The FIR-MPD spectrum we measured of the $Au_{20}Kr$ complex (Fig. 2A) was very simple, with a dominant absorption at 148 cm^{-1}, which already pointed to a highly symmetric structure. The calculated spectrum of tetrahedral Au_{20} was in agreement with the experiment (Fig. 2C, and see fig. S4 for the IR spectra of less stable isomers). In the FIR-MPD spectrum of $Au_{20}Kr_2$, weaker features occurred at low frequencies and were well reproduced by theory when the Kr ligands are included in the calculations (fig. S1). The strong absorption at 148 cm^{-1} corresponds to a triply degenerate vibration (t_2) in bare Au_{20} with T_d symmetry.

Theory predicts a truncated trigonal pyramid to be the minimum energy structure for neutral Au_{19} (*27*), for which the removal of a corner atom of the Au_{20} tetrahedron reduces the symmetry from T_d to C_{3v}. As a direct consequence, the degeneracy of the t_2 vibration of Au_{20} is lifted, and this mode splits into a doubly degenerate vibration (e) and a nondegenerate vibration (a_1) in Au_{19}. This splitting was observed in the vibrational spectrum of neutral Au_{19} (Fig. 2). The e vibration lies at 149 cm^{-1} and is hardly shifted as compared with the t_2 mode of Au_{20}. The a_1 vibration is blue-shifted by 18 cm^{-1} relative to the t_2 vibration in Au_{20}. The truncated pyramidal structure of Au_{19} can thus be inferred directly from the IR spectrum. We also found the C_{3v} structure of Au_{19} to be a minimum in our calculations, and the calculated vibrational spectrum fits the experimental one in terms of peak positions and relative intensities (Fig. 2D, and see fig. S5 for IR spectra of less-stable isomers). Again, the modifications in peak intensities induced by the Kr ligands agree well between theory and experiment (fig. S2).

We have shown that detailed structural information on small neutral gold nanoparticles can be obtained by means of vibrational spectroscopy. FIR-MPD is the only size-selective experimental technique available to date that allows for the structure determination of neutral metal clusters in the gas phase. It can be used to study the transition of 2D structures to 3D structures for neutral gold clusters as well as to study, for instance, ligand-induced geometrical modifications that are highly relevant in catalysis. With improved sensitivity for heavier masses, it will be possible to extend these measurements to larger clusters. Although spectral congestion may prohibit detailed analysis of nonsymmetric structures, we can expect symmetric and near-symmetric structures to remain identifiable, as they do for Au_{20} and Au_{19}. For instance, it should be possible to answer questions such as, is neutral Au_{55} icosahedral, or does it have a low-symmetry structure such as has been indicated for the anion (*28*)?

References and Notes

1. M. Haruta, N. Yamada, T. Kobayashi, S. Iijima, *J. Catal.* **115**, 301 (1989).
2. B. Hammer, J. K. Nørskov, *Nature* **376**, 238 (1995).
3. M. Valden, X. Lai, D. W. Goodman, *Science* **281**, 1647 (1998).
4. B. Yoon *et al.*, *Science* **307**, 403 (2005).
5. C. T. Campbell, *Science* **306**, 234 (2004).
6. P. P. Edwards, J. M. Thomas, *Angew. Chem. Int. Ed.* **46**, 5480 (2007).
7. C. Lemire, R. Meyer, S. Shaikhutdinov, H.-J. Freund, *Angew. Chem. Int. Ed.* **43**, 118 (2004).
8. G. Mills, M. S. Gordon, H. Metiu, *J. Chem. Phys.* **118**, 4198 (2003).
9. M. S. Chen, D. W. Goodman, *Science* **306**, 252 (2004).
10. Z. Y. Li *et al.*, *Nature* **451**, 46 (2008).
11. F. Furche *et al.*, *J. Chem. Phys.* **117**, 6982 (2002).
12. S. Gilb *et al.*, *J. Chem. Phys.* **116**, 4094 (2002).
13. S. Bulusu, X. Li, L.-S. Wang, X. C. Zeng, *Proc. Natl. Acad. Sci. U.S.A.* **103**, 8326 (2006).
14. J. Li, X. Li, H.-J. Zhai, L.-S. Wang, *Science* **299**, 864 (2003).
15. A. Lechtken *et al.*, *Angew. Chem. Int. Ed.* **46**, 2944 (2007).
16. X. Xing, B. Yoon, U. Landman, J. H. Parks, *Phys. Rev. B* **74**, 165423 (2006).
17. A. Fielicke *et al.*, *Phys. Rev. Lett.* **93**, 023401 (2004).
18. A. Fielicke, C. Ratsch, G. von Helden, G. Meijer, *J. Chem. Phys.* **122**, 091105 (2005).
19. A. Fielicke, G. von Helden, G. Meijer, *Eur. Phys. J. D* **34**, 83 (2005).
20. D. Oepts, A. F. G. van der Meer, P. W. van Amersfoort, *Infrared Phys. Technol.* **36**, 297 (1995).
21. Materials and methods are available as supporting material on *Science* Online.
22. The IR frequencies, calculated by DFT with TURBOMOLE V5.10 (*29*), were uniformly scaled by multiplication with a factor of 1.15.
23. V. Bonačić-Koutecký et al, *J. Chem. Phys.* **117**, 3120 (2002).
24. H. Häkkinen, U. Landman, *Phys. Rev. B* **62**, R2287 (2000).
25. J. Wang, G. Wang, J. Zhao, *Phys. Rev. B* **66**, 035418 (2002).
26. The influence of the rare-gas ligand on the IR absorption intensities is very similar to what has been found in photodissociation studies of cationic gold clusters in the visible region (*30*).
27. S. Bulusu, X. C. Zeng, *J. Chem. Phys.* **125**, 154303 (2006).
28. W. Huang *et al.*, *ACS Nano* **2**, 897 (2008).
29. R. Ahlrichs, M. Bär, M. Häser, H. Horn, C. Kölmel, *Chem. Phys. Lett.* **162**, 165 (1989).
30. A. N. Gloess, H. Schneider, J. M. Weber, M. M. Kappes, *J. Chem. Phys.* **128**, 114312 (2008).

31. The authors acknowledge support from the Cluster of Excellence Unifying Concepts in Catalysis coordinated by the Technische Universität Berlin and funded by the Deutsche Forschungsgemeinschaft. This work is supported by FOM by providing beam time for FELIX. We thank the FELIX staff for their skillful assistance, in particular J. Pluijgers and R. van Buuren, as well as K. Rademann for providing the cluster source. P.G. thanks the International Max Planck Research School Complex Surfaces in Material Science, and J.T.L. thanks the Alexander von Humboldt Foundation for funding.

Supporting Online Material

www.sciencemag.org/cgi/content/full/321/5889/674/DC1
Materials and Methods
Figs. S1 to S5

30 May 2008; accepted 23 June 2008
10.1126/science.1161166

Colossal Ionic Conductivity at Interfaces of Epitaxial ZrO_2:Y_2O_3/$SrTiO_3$ Heterostructures

J. Garcia-Barriocanal,[1] A. Rivera-Calzada,[1] M. Varela,[2] Z. Sefrioui,[1] E. Iborra,[3] C. Leon,[1] S. J. Pennycook,[2] J. Santamaria[1]*

The search for electrolyte materials with high oxygen conductivities is a key step toward reducing the operation temperature of fuel cells, which is currently above 700°C. We report a high lateral ionic conductivity, showing up to eight orders of magnitude enhancement near room temperature, in yttria-stabilized zirconia (YSZ)/strontium titanate epitaxial heterostructures. The enhancement of the conductivity is observed, along with a YSZ layer thickness–independent conductance, showing that it is an interface process. We propose that the atomic reconstruction at the interface between highly dissimilar structures (such as fluorite and perovskite) provides both a large number of carriers and a high-mobility plane, yielding colossal values of the ionic conductivity.

Solid oxide fuel cells (SOFCs) have emerged as a promising nonpolluting technology for the short-to-medium–term substitution of fossil fuels (*1*–*4*). The conversion efficiency of chemical into electrical energy is limited by the transport of oxygen anions through an elec-

trolyte material. So far, yttria-stabilized zirconia $(Y_2O_3)_x(ZrO_2)_{1-x}$ (YSZ) is the material mostly used in SOFCs because of its mechanical stability, chemical compatibility with electrodes, and high oxygen ionic conductivity. It is well known that doping ZrO_2 with Y_2O_3 stabilizes the cubic fluorite structure of ZrO_2 at room temperature and supplies the oxygen vacancies responsible for the ionic conduction, resulting in high values of the oxygen conductivity at high temperatures (*5*–*7*). A maximum value of 0.1 S/cm (where 1 S = 1 A/V) at 1000°C is observed for the 8 to 9 mole percent (mol %) yttria content (*2*–*4*). A severe drawback toward the final implementation of SOFCs is the relatively low room temperature ionic conductivity of this material, which imposes rather high operational temperatures around 800°C (*1*–*4*). The search for alternative electrolytes has not yet been successful in reaching the conductivity value of 0.01 S/cm desired for room temperature operation (*1*–*4*).

Only modest reductions in the operation temperature of SOFCs (500° to 700°C) can be anticipated with the recently proposed optimized electrolytes such as gadolinia-doped ceria and lanthanum gallates (*8*–*11*). On the other hand, the one to two orders of magnitude increase of the electrical conductivity reported (*12*–*14*) in nanocrystalline samples as compared with single crystals outlines the importance of processing as an alternative route to increasing conductivity values toward the desired levels. Because modern thin film growth techniques allow a precise control of layer thickness and morphology, they provide a pathway for the production of solid electrolytes with optimized properties. Maier *et al.* found a substantial increase of the dc ionic conductivity of superlattices of CaF_2 and BaF_2 when the thickness of the individual layers was decreased down to 16 nm, assigned to a size effect due to the space charge regions being smaller than the layer thickness (*15*, *16*). Kosacki *et al.* have reported enhanced conductivity in highly textured thin films of YSZ with thicknesses between 60 and 15 nm, reaching 0.6 S/cm at 800°C (*17*). Because reducing film thickness (and therefore increasing the fraction of material near the interface) produces such a noticeable conductivity enhancement, the interfaces themselves would seem to play a determining role in the outstanding conductivity properties observed.

To search for interface effects, we fabricated heterostructures where YSZ layers (with 8 mol % nominal yttria content) in the thickness range from 62 nm down to 1 nm were sandwiched between two 10-nm-thick layers of insulating $SrTiO_3$ (STO). Also, superlattices were grown, alternating 10-nm-thick STO films with YSZ layers with thickness between 62 and 1 nm (*18*). Figure 1A displays a low-magnification (inset) and a high-resolution annular dark field (or Z-contrast) image of a $[YSZ_{1nm}/STO_{10nm}]_9$ superlattice (with nine repeats), showing the excellent crystalline quality of the sample. The layers appear continuous and flat over long lateral distances (a few microns). The interfaces between the STO and the YSZ are seen to be atomically flat. From the high-magnification image it is possible to count the number of unit cells of STO and YSZ, nominally 25 of STO and 2 of YSZ. Most importantly, the YSZ is perfectly coherent with the STO, in agreement with x-ray diffraction (XRD) results (fig. S1), meaning that the ultrathin layer of YSZ grows rotated by 45° around the *c* axis and strains to match the STO lattice. Because the bulk lattice constants of STO and YSZ are 0.3905 (*19*) and 0.514 nm (*20*), respectively, the epitaxial growth of the YSZ on top of the STO ensures a large, expansive strain in the thin YSZ layers of 7% in the *ab* plane. Increasing the thickness of YSZ (for constant STO thickness) results in a loss of structural coherence, as reflected by a reduction of superlattice satellites in XRD. Electron microscopy observations confirm that the release of strain results in a granular morphology, although the growth remains textured.

We plotted the lateral electrical conductivity (real part σ′) of the thinnest YSZ trilayer versus frequency in a double logarithmic plot (Fig. 2). The characteristic electrical response of ionic conductors (*21*–*23*) is observed in the figure. The long range or σ_{dc} ionic conductivity of the material is obtained from the plateau found in σ′ versus frequency plots. In the presence of blocking effects due to grain boundaries or electrodes, a further

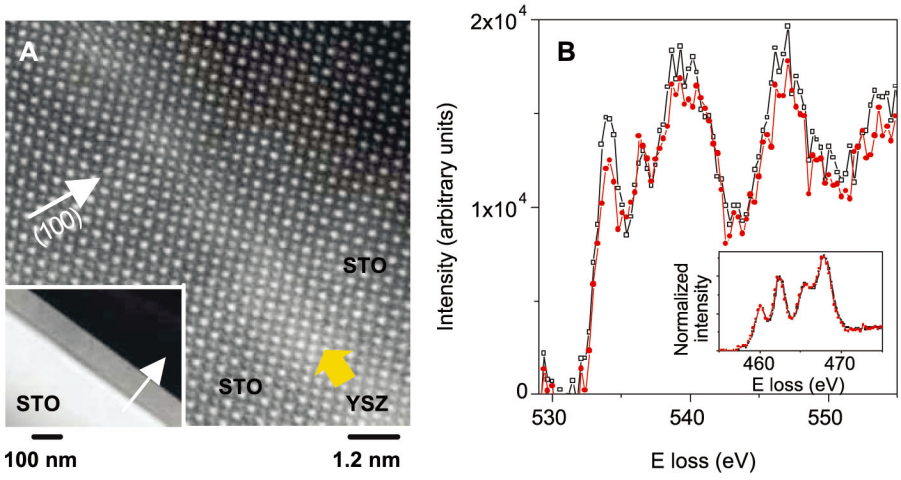

Fig. 1. (**A**) Z-contrast scanning transmission electron microscopy (STEM) image of the STO/YSZ interface of the $[YSZ_{1nm}/STO_{10nm}]_9$ superlattice (with nine repeats), obtained in the VG Microscopes HB603U microscope. A yellow arrow marks the position of the YSZ layer. (Inset) Low-magnification image obtained in the VG Microscopes HB501UX column. In both cases a white arrow indicates the growth direction. (**B**) EEL spectra showing the O K edge obtained from the STO unit cell at the interface plane (red circles) and 4.5 nm into the STO layer (black squares). (Inset) Ti $L_{2,3}$ edges for the same positions, same color code. All spectra are the result of averaging four individual spectra at these positions, with an acquisition time of 3 s each.

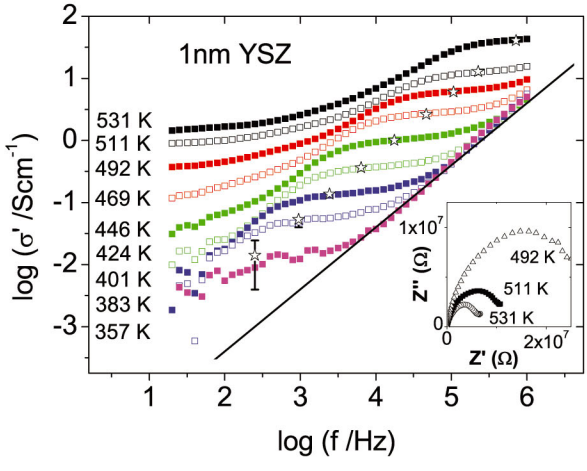

Fig. 2. Real part of the lateral electrical conductivity versus frequency of the trilayer with 1-nm-thick YSZ in a double log plot. Isotherms were measured in the range of 357 to 531 K. The solid line represents a NCL contribution ($\sigma' \sim A\omega$, where *A* is a temperature-dependent proportionality factor and ω is the angular frequency), as explained in the text. Stars identify the value of σ_{dc}. The uncertainty of conductance measurements is 1 nS (10^{-2} S/cm in conductivity for the sample shown, see error bar). (**Inset**) Imaginary versus real part of the impedance (Nyquist) plots at 492, 511, and 531 K. Whereas the high-frequency contribution is a Debye-like process characterized by a conductivity exponent $n = 0$, the "grain boundary" term observed in the Nyquist plots shows a clear deviation from a Debye behavior, as reflected by the distorted impedance arcs.

[1]Grupo de Física de Materiales Complejos, Universidad Complutense de Madrid, Madrid 28040, Spain. [2]Materials Science and Technology Division, Oak Ridge National Laboratory, Oak Ridge, TN 37831, USA. [3]Escuela Técnica Superior de Ingenieros de Telecomunicaciones, Universidad Politécnica de Madrid, Madrid 28040, Spain.

*To whom correspondence should be addressed. E-mail: jacsan@fis.ucm.es

decrease of σ′ (below bulk σ_{dc} values) may occur toward lower frequencies. For clarity, the value of σ_{dc} has been identified by using stars. The σ_{dc} value is found to be thermally activated, so when the temperature is reduced the conductivity curves shift downwards in Fig. 2. The inset in Fig. 2 displays Nyquist plots for the same sample. To determine the nature of the charge carriers, we measured the conductance of the samples by means of dc measurements. As can be observed in fig. S2, the dc conductance (open circles) is three to four orders of magnitude lower than the values obtained from ac measurements (solid squares) in the entire temperature measurement range. This result indicates that the electronic contribution to the ac measurements can be considered negligible, and thus, the measured ac transport is attributable to an ionic diffusion process.

In Fig. 3, the temperature dependence of the σ_{dc} of $[STO_{10nm}/YSZ_{Xnm}/STO_{10nm}]$ trilayers is shown together with data corresponding to a single crystal and the 700-nm thin film from (*7*). Whereas the "bulklike" samples (the thin film and the single crystal) show the well-known Arrhenius behavior with an activation energy of ~1.1 eV, the trilayers show much larger conductivity values and smaller values of the activation energy. The thickest trilayer (62-nm YSZ) already shows an increase of about two orders of magnitude in the high-temperature dc conductivity, and the dc activation energy decreases to 0.72 eV. When decreasing the thickness of the YSZ layer to 30 nm, the dc conductivity increases another three orders of magnitude, and the activation energy decreases to 0.6 eV. The high values of the pre-exponential factor of $\sim 10^7$ $(ohm \cdot cm)^{-1}$ are comparable to those found in other ion conductors (*24*) [see supporting online material (SOM) text]. If the thickness is further reduced all the way down to 1 nm (two unit cells of YSZ), the conductivity is observed to increase as the inverse of the YSZ layer thickness, but the conductance is essentially thickness-independent (bottom inset in Fig. 3). We can think of three parallel conduction paths due to the interfaces and the bulk YSZ and STO layers. The bulk conductivity of YSZ is 10^{-7} S/cm at 500 K, which would yield a conductance value of $\sim 10^{-14}$ S for 1-nm-thick layers. This value is much lower than the 10^{-6} S value measured with the ac technique. If we instead assume that the high conductance ($G = 10^{-6}$ S) is due to electronic conduction in the STO, both ac and dc techniques would provide this same value, contrary to what is observed (fig. S2). Moreover, reported conductivity values in STO thin films (*25*) are also much lower than those necessary to explain the high conductance observed. Because bulk YSZ or STO contributions can be ruled out, an interface conduction mechanism is inferred.

To further test this scenario, we grew superlattices repeating the $[YSZ_{1nm}/STO_{10nm}]$ growth unit. We found (top inset in Fig. 3) that conductance scales now with the number of interfaces up to a number of eight (four bilayer repetitions). There is a scaling breakdown in the figure, observed for a larger number of bilayer repetitions, most likely resulting from disorder building up in this highly strained structure. The experimental data indicates that the first STO/YSZ interface does not contribute to the large ionic conductivity observed in the samples, probably because the first STO layer is somehow different from the others as it is grown directly on the substrate. This scaling, together with the invariance of the conductance with the thickness of the YSZ, shows that the large conductivity values in these heterostructures originate truly at the interfaces between YSZ and STO. Our results indicate a superposition of two parallel contributions—one due to the bulk and one attributable to the interface—and the colossal ionic conductivity is observed as long as the interface conductance is larger than that of the bulk. The abrupt conductivity decrease when the thickness changes from 30 to 62 nm is most likely due to a degraded interface structure when the YSZ layers exceed the critical thickness.

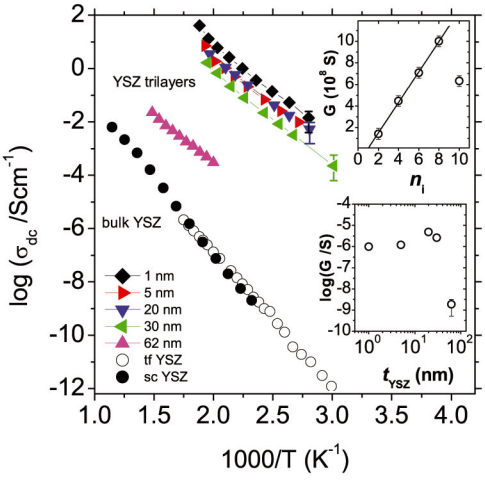

Fig. 3. Dependence of the logarithm of the long-range ionic conductivity of the trilayers STO/YSZ/STO versus inverse temperature. The thickness range of the YSZ layer is 1 to 62 nm. Also included are the data of a single crystal (sc) of YSZ and a thin film (tf) 700 nm thick [taken from (*7*)] with the same nominal composition. (**Top inset**) 400 K conductance of $[YSZ_{1nm}/STO_{10nm}]_{(ni/2)}$ superlattices as a function of the number of interfaces, n_i. (**Bottom inset**) Dependence of the conductance of $[STO_{10nm}/YSZ_{Xnm}/STO_{10nm}]$ trilayers at 500 K on YSZ layer thickness. Error bars are according to a 1 nS uncertainty of the conductance measurement.

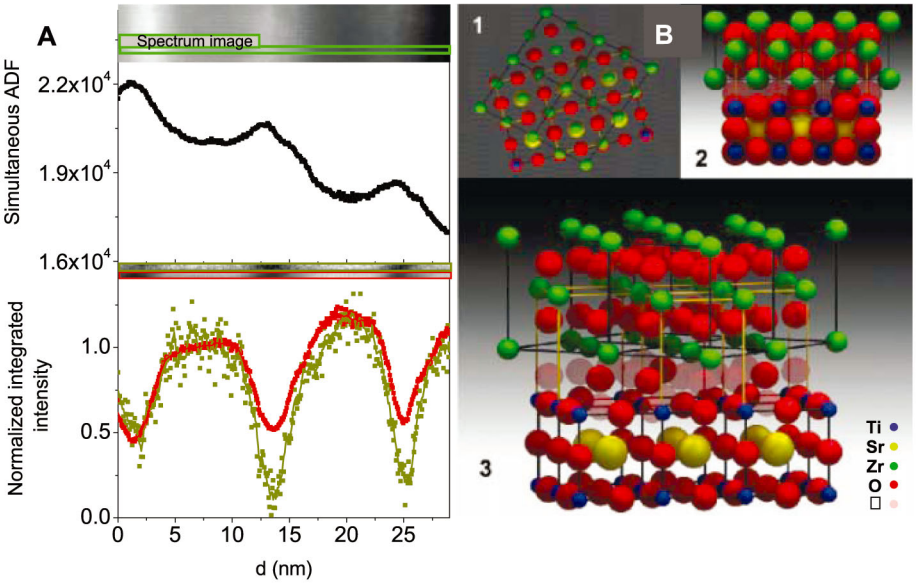

Fig. 4. (**A**) EELS chemical maps. The ADF image in the upper panel shows the area used for EELS mapping (spectrum image, marked with a green rectangle) in the $[YSZ_{1nm}/STO_{10nm}]_9$ superlattice. The middle panel shows the averaged ADF signal acquired simultaneously with the EEL spectrum image, showing the STO (low-intensity regions) and YSZ (higher-intensity) layers. The lower panel shows the Ti (red) and Sr (dark yellow) EELS line traces across several consecutive interfaces. These line traces are averaged from the elemental 2D images shown in the insets, each framed with the same color code (red for Ti, dark yellow for Sr). Data was obtained in the VG Microscopes HB501UX. Because the STEM specimen was relatively thick (several tens of nanometers), the wide chemical interface profiles are most likely attributable to beam broadening. (**B**) Solid spheres model of the YSZ/STO interface showing: (1) The compatibility of the perovskite and fluorite (rotated) structures. (2) A side view of the interface between STO (at the bottom) and YSZ (on top) with realistic ionic radius. The shaded oxygen positions in the interface plane are presumed absent or displaced because of volume constraints, enabling the high ionic conductivity. (3) A 3D view of the interface, with the ionic radius reduced by half to better visualize the plane of oxygen vacancies introduced in the interface. The square symbol in the legend indicates the empty positions available for oxygen ions at the interface.

The dc conductivity of the 1-nm YSZ layer shows a record value of 0.014 S/cm at 357 K, with an activation energy of 0.64 eV and an extrapolated value of 0.003 S/cm at 300 K. Thus, the threshold for the conductivity value that defines the feasibility for practical applications, 0.01 S/cm, is reached in these ultrathin films just slightly above room temperature. Previous enhancements of the conductivity in nanoscopic systems have been explained in terms of size effects (*13*–*16*) and overlapping of space charge regions. However, the screening or Debye length in ionic conductors with high carrier concentrations, such as YSZ, is on the order of 0.1 nm (*26*). The conductivity values found here are in good agreement with a recent prediction of Kosacki *et al*. (*17*), who analyzed thicker YSZ thin films (15 nm) grown on MgO substrates, discussing the possible existence of an interface diffusion mechanism that would yield a dc conductivity ~0.001 S/cm at room temperature, with an activation energy of 0.45 eV for a film thickness ~1.6 nm. Consequently, and considering the good epitaxial quality of the heterostructures, we believe that strain and especially interfacial effects are at the origin of the enhanced conductivity.

To further investigate the role of the interfaces in the observed increase of ~eight orders of magnitude in the ionic conductivity with respect to bulk YSZ values, we next present a detailed analysis of the YSZ/STO interfaces using atomic column resolution electron energy-loss spectroscopy (EELS). Figure 4A shows line traces corresponding to elemental concentrations of Ti and Sr obtained from EELS spectrum images of the $[YSZ_{1nm}/STO_{10nm}]_9$ superlattice across several bilayers. The YSZ layers are the bright bands observed in the annular dark field (ADF) picture in the upper inset, which also shows in a green rectangle the area used for EELS analysis. The lower panel shows the normalized integrated intensity under the Sr M_3 (dark yellow) and the Ti $L_{2,3}$ (red) absorption lines. The resulting two-dimensional (2D) images are shown in the inset. It can be observed that the Ti intensity is clearly higher than that of Sr in all of the interfaces, indicating that the STO termination layer is always a (TiO_2) plane. YSZ grows epitaxially, rotating its cell 45° to accommodate half of the diagonal of the YSZ conventional unit cell [$a_{YSZ}/\sqrt{2}$ = 0.361 nm (a_{YSZ} = 0.514 nm), where a is the lattice parameter] to the STO perovskite unit cell (a_{STO} = 0.390 nm) with a 7% in plane tensile strain on the YSZ. In this configuration, both structures are compatible because the FCC fluorite structure of YSZ keeps the positions of the atoms in the ab plane, the only difference being that the oxygen atoms of the fluorite are not in the z = 0 plane but are displaced to z = 1/4 along the c direction (Fig. 4B). The first YSZ plane in the (001) stacking sequence should be an O plane at $c_{YSZ}/4$, but these O sites are directly above the O atoms of the last TiO_2 plane. Presumably, these sites are either vacant or the O atoms are displaced from their normal positions (as suggested by the shaded sites in Fig. 4B). Therefore, this interfacial O plane is likely to be highly disordered, even though the cation lattice remains coherent, which would thereby enable the enhancement in ionic conductivity.

Further evidence for this interface structure comes from a close inspection of the fine structure of the O K edge (oxygen/potassium absorption edge) at the STO interface plane (Fig. 1B), which shows noticeable changes when compared to the O K edge from the middle of the STO layer. These changes are consistent with an enhanced density of O vacancies in this plane (*27*). However, we could not detect any change in the oxidation state of Ti at the interface (it is +4), which is in good agreement with the lack of electronic conduction observed (inset in Fig. 1B). Additionally, the fine structure of the O K edge within the YSZ ultrathin layers is completely different from that of bulk YSZ, as a consequence of the severe structural distortions in the oxygen octahedra attributable to the large strain accumulated (fig. S3 and SOM text). Thus, these results point to partial occupancy and high disorder in the interface oxygen plane, resulting in the introduction of a large number of interfacial oxygen vacancies and a substantial decrease in the activation energy for O migration. The STO side of the YSZ/STO interface may play a role in stabilizing disorder in the anionic sublattice, as has been recently reported for the $LaAlO_3/SrTiO_3$ interface (*28*, *29*).

The analysis of the high-frequency dispersive ac conductivity above the dc plateau of Fig. 2 may provide some further insight into the colossal ionic conductivity. In ionic conductors, the dc plateau crosses over into a dispersive conductivity regime depending on frequency as a power law with a fractional exponent n (n < 1). This contribution is usually known as Jonscher's response and reflects the influence of ion-ion correlations on ion motion (*21*–*23*, *30*, *31*). At even higher frequencies and lower temperatures, the power law dependence of the conductivity universally merges into an almost linear frequency-dependent term with n = 1, resulting in a regime with a nearly constant (dielectric) loss (NCL) (*32*, *33*). NCL is weakly temperature dependent and has been ascribed to caged dynamics of mobile ions at short times (high frequencies) (*34*). Both power law regimes are usually distinct, and they are observed in particular in bulk or "thick" thin films of YSZ, where the n exponent has a value of ~0.5 to 0.6 before merging into the NCL behavior (*6*, *7*). In the case of our ultrathin YSZ heterostructures, either the Jonscher's response is absent (n = 0) or n is a very small value (Fig. 2), as shown by the dc plateau directly merging into a NCL (n = 1) term, which is plotted in the figure as a solid line to guide the eye. This is a very anomalous result indicating an uncorrelated ion diffusion process. The absence of the fractional power law regime has only been observed in systems with a carrier concentration low enough so that the carriers do not interact with each other. Such an explanation can be ruled out in our samples where the large conductivity values do not, by any means, indicate a reduced carrier density. We believe that the uncorrelated ion diffusion at the interface is another manifestation of conduction along the oxygen depleted/disordered interface plane. In fact, the absence of ion-ion correlations may produce a decrease in the activation energy of the conductivity (*30*, *31*). The large in-plane expansive strain on the YSZ interface plane, together with the high concentration of vacant oxygen positions and probable positional disorder, surely contributes to the reduction in the activation energy and the resulting huge enhancement in ionic conductivity.

We have shown eight orders of magnitude enhancement of the ionic conductivity of YSZ in ultrathin films reaching values that enable practical application of the material in SOFCs slightly above room temperature. This result may have a special impact on single-chamber fuel cells where both electrodes are located on the same side of a thin electrolyte film deposited onto a substrate, and thus the ionic current flows in a lateral direction parallel to the substrate (*35*). The coherent interface between very dissimilar structures (in this case, fluorite and perovskite in YSZ/STO heterostructures) provides both a high carrier concentration and, simultaneously, a decreased activation energy, achieving a greatly enhanced mobility that accounts for the many orders of magnitude increase of the conductivity. The combination of epitaxial strain and suitable heterogeneous interfaces appears to be a key step in the design of artificial nanostructures with high ionic conductivity. This result is of major technological importance to achieve fast oxygen conduction at room temperature, and the outstanding electrical properties of the ultrathin YSZ/STO heterostructures may open the way to new and improved devices far beyond fuel cells.

References and Notes

1. B. C. H. Steele, A. Heinzel, *Nature* **414**, 345 (2001).
2. R. M. Ormerod, *Chem. Soc. Rev.* **32**, 17 (2003).
3. J. B. Goodenough, *Annu. Rev. Mater. Res.* **33**, 91 (2003).
4. J. W. Fergus, *J. Power Sources* **162**, 30 (2006).
5. W. Nernst, *Z. Elektrochem*. **6**, 41 (1899).
6. A. Pimenov, J. Ullrich, P. Lunkenheimer, A. Loidl, C. H. Ruscher, *Solid State Ionics* **109**, 111 (1998).
7. A. Rivera, J. Santamaria, C. Leon, *Appl. Phys. Lett.* **78**, 610 (2001).
8. N. P. Brandon, S. Skinner, B. C. H. Steele, *Annu. Rev. Mater. Res.* **33**, 183 (2003).
9. Z. Shao, S. M. Haile, *Nature* **431**, 170 (2004).
10. Y. Yoo, *J. Power Sources* **160**, 202 (2006).
11. H. Huang *et al*., *J. Electrochem. Soc.* **154**, B20 (2007).
12. I. Kosacki, B. Gorman, H. U. Anderson, *Electrochem. Soc. Proc.* **97**, 631 (1998).
13. T. Suzuki, I. Kosacki, H. U. Anderson, P. Colomban, *J. Am. Ceram. Soc.* **85**, 1492 (2002).
14. S. Azad *et al*., *Appl. Phys. Lett.* **86**, 131906 (2005).
15. J. Maier, *Solid State Ionics* **131**, 13 (2000).
16. N. Sata, K. Eberman, K. Eberl, J. Maier, *Nature* **408**, 946 (2000).
17. I. Kosacki, C. M. Rouleau, P. F. Becher, J. Bentley, D. H. Lowndes, *Solid State Ionics* **176**, 1319 (2005).
18. Materials and methods are available as supporting material on *Science* Online.
19. H. Swanson, R. K. Fuyat, *Natl. Bur. Stand. Circ. (US)* **3**, 44 (1954).
20. P. Li, I.-W. Chen, J. E. Penner-Hahn, *Phys. Rev. B* **48**, 10063 (1993).
21. A. K. Jonscher, *Nature* **267**, 673 (1977).
22. C. A. Angell, *Chem. Rev.* **90**, 523 (1990).
23. F. Kremer, A. Schönhals, Eds., *Broadband Dielectric Spectroscopy* (Springer, Berlin, 2003).

24. R. J. Cava, E. A. Rietman, *Phys. Rev. B* **30**, 6896 (1984).
25. C. Ohly, S. Hoffmann-Eifert, X. Guo, *J. Am. Ceram. Soc.* **89**, 2845 (2006).
26. A. Peters, C. Korte, D. Hesse, N. Zakharov, J. Janek, *Solid State Ionics* **178**, 67 (2007).
27. D. J. Wallis, N. D. Browning, *J. Am. Ceram. Soc.* **80**, 781 (1997).
28. W. Siemons *et al.*, *Phys. Rev. Lett.* **98**, 196802 (2007).
29. A. Kalabukhov *et al.*, *Phys. Rev. B* **75**, 121404(R) (2007).
30. K. L. Ngai, A. K. Rizos, *Phys. Rev. Lett.* **76**, 1296 (1996).
31. K. L. Ngai, G. N. Greaves, C. T. Moyhihan, *Phys. Rev. Lett.* **80**, 1018 (1998).
32. W. K. Lee, J. F. Liu, A. S. Nowick, *Phys. Rev. Lett.* **67**, 1559 (1991).
33. K. L. Ngai, *J. Chem. Phys.* **110**, 10576 (1999).
34. J. Habasaki, K. L. Ngai, Y. Hiwatari, *J. Chem. Phys.* **120**, 8195 (2004).
35. J. Fleig, H. L. Tuller, J. Maier, *Solid State Ionics* **174**, 261 (2004).
36. This work was supported by grants from the Spanish Ministry for Science and Innovation (MAT2005 06024, MAT2007 62162, and MAT 2008) and by the Madrid Regional Government Communidad Autónoma de Madrid through Universidad Complutense de Madrid Groups Programme. We thank U. Complutense–Centro de Asistencia a la Investigación de Técnicas Físicas for technical support. Research at Oak Ridge National Laboratory (M.V. and S.J.P.) was sponsored by the Division of Materials Sciences and Engineering of the U.S. Department of Energy. We are grateful to J. T. Luck for help with STEM specimen preparation and to F. de Andrés for help with the graphic design of the hard spheres model.

Supporting Online Material
www.sciencemag.org/cgi/content/full/321/5889/676/DC1
Materials and Methods
SOM Text
Figs. S1 to S3
References

12 February 2008; accepted 13 June 2008
10.1126/science.1156393

High-Resolution Greenland Ice Core Data Show Abrupt Climate Change Happens in Few Years

Jørgen Peder Steffensen,[1]* Katrine K. Andersen,[1] Matthias Bigler,[1,2] Henrik B. Clausen,[1] Dorthe Dahl-Jensen,[1] Hubertus Fischer,[2,3] Kumiko Goto-Azuma,[4] Margareta Hansson,[5] Sigfús J. Johnsen,[1] Jean Jouzel,[6] Valérie Masson-Delmotte,[6] Trevor Popp,[7] Sune O. Rasmussen,[1] Regine Röthlisberger,[2,8] Urs Ruth,[3] Bernhard Stauffer,[2] Marie-Louise Siggaard-Andersen,[1] Árný E. Sveinbjörnsdóttir,[9] Anders Svensson,[1] James W. C. White[7]

The last two abrupt warmings at the onset of our present warm interglacial period, interrupted by the Younger Dryas cooling event, were investigated at high temporal resolution from the North Greenland Ice Core Project ice core. The deuterium excess, a proxy of Greenland precipitation moisture source, switched mode within 1 to 3 years over these transitions and initiated a more gradual change (over 50 years) of the Greenland air temperature, as recorded by stable water isotopes. The onsets of both abrupt Greenland warmings were slightly preceded by decreasing Greenland dust deposition, reflecting the wetting of Asian deserts. A northern shift of the Intertropical Convergence Zone could be the trigger of these abrupt shifts of Northern Hemisphere atmospheric circulation, resulting in changes of 2 to 4 kelvin in Greenland moisture source temperature from one year to the next.

Ice core records from Greenland have been instrumental in investigating past abrupt climate change. As compared with other sedimentary records, the ice core records have unparalleled temporal resolution and continuity (*1*–*3*). The newest Greenland ice core, from the North Greenland Ice Core Project (NGRIP), has been measured at very high resolution for water isotope ratios, dust, and impurity concentrations. This allows researchers for the first time to follow the ice core proxies of Greenland temperature, accumulation, moisture origin, and aerosol deposition at subannual resolution over the very abrupt climate changes in the period from 15.5 to 11.0 thousand years ago (ka) (measured from 2000 AD throughout this study).

In the Northern Hemisphere, the last glacial period ended in a climatic oscillation composed of two abrupt warmings interrupted by one cooling event (*3*–*6*). The temperature changed rapidly from glacial to mild conditions in the Bølling and Allerød periods and then returned to glacial values in the Younger Dryas period before the onset of the present warm interglacial, the Holocene (Fig. 1, and see table S1 for classification of climate periods). The shape and duration of the abrupt climate change at the termination of the last glacial have previously been constrained by Greenland ice core records from DYE-3 (*4*, *7*), Greenland Ice Core Project (GRIP) (*8*) and Greenland Ice Sheet Project 2 (GISP2) (*3*, *6*, *9*), but sampling of these cores did not typically achieve a resolution sufficient to resolve annual layers. Because of new continuous flow analysis (CFA) systems (*10*–*12*), impurity and chemical records of the recent NGRIP ice core (*1*) have been obtained at subannual resolution, which allows for the multiple-proxy identification of annual-layer thickness and the construction of a new Greenland time scale, the Greenland Ice Core Chronology 2005 (GICC05) (*2*). Complementary highly detailed stable water isotope profiles ($\delta^{18}O$ and δD) have been measured on the NGRIP ice core covering the period from 15.5 to 11.0 ka at 2.5-to-5.0-cm resolution, corresponding to one to three samples per year. They were compared with the concentrations of insoluble dust, soluble sodium (Na^+), and calcium (Ca^{2+}), each measured with CFA at subannual resolution (*10*, *12*, *13*) (Fig. 2) and, when available, with the highest-resolution data from GRIP, GISP2, and DYE-3 ice cores on the GICC05 time scale.

Across the warming transitions, the records exhibit clear shifts between two climate states. We characterize a shift to be significant if the mean values of the climate states on each side of the shift differ by more than the statistical standard error of the noise of a 150-year period of these climate states. A simple but objective approach to finding the best timing of the transition is to characterize the shift observed in each proxy as a "ramp": a linear change from one stable state to another. We applied a ramp-fitting method (*14*) to determine the timing of the transitions. The method entails using weighted least-squares regression to determine the ramp location and a bootstrap simulation to estimate the uncertainty of the results [transition times are listed in Table 1; see supporting online material (SOM) methods and table S2 for more detailed information on the method and the ramp fit values and uncertainties (*15*)]. Data and fitted ramps are shown in Figs. 2 and 3. For annual layer thickness (λ), concentrations of dust, Ca^{2+}, and Na^+, logarithmic scales were used because these proxies are approximately log-normally distributed.

The $\delta^{18}O$ record is a proxy for past air temperature at the ice core site (*16*, *17*). Although the magnitude of Greenland $\delta^{18}O$ changes can be influenced by changing site and source temperatures and by snowfall seasonality (*16*, *18*, *19*), the timing of $\delta^{18}O$ changes is dominated by the changing site temperature (*18*). The $\delta^{18}O$ warming transition at 14.7 ka was the most rapid and occurred within a remarkable 3 years, whereas the

[1]Centre for Ice and Climate, Niels Bohr Institute, University of Copenhagen, Juliane Maries Vej 30, DK-2100 Copenhagen OE, Denmark. [2]Climate and Environmental Physics, Physics Institute, University of Bern, Sidlerstrasse 5, CH-3012, Switzerland. [3]Alfred-Wegener-Institute for Polar- and Marine Research (AWI), Postfach 120161, D-27515 Bremerhaven, Germany. [4]National Institute of Polar Research, Kaga 1-9-10, Itabashi-ku, Tokyo 173-8515, Japan. [5]Department of Physical Geography and Quaternary Geology, Stockholm University, S-106 91, Stockholm, Sweden. [6]Institut Pierre Simon Laplace/Laboratoire des Sciences du Climat et de l'Environnement, Commissariat à l'Énergie Atomique (CEA)–CNRS–Université de Versailles Saint Quentin en Yvelines, CEA Saclay, 91191 Gif-Sur-Yvette, France. [7]The Institute of Arctic and Alpine Research, Campus Box 450, University of Colorado, Boulder, CO 80309-0450, USA. [8]British Antarctic Survey, Natural Environment Research Council, High Cross, Madingley Road, Cambridge CB3 0ET, UK. [9]Raunvísindastofnun Háskólans, Dunhagi 3, Iceland.

*To whom correspondence should be addressed. E-mail: jps@gfy.ku.dk

warming transition at 11.7 ka lasted 60 years; both correspond to a warming of more than 10 K (*6*, *20*). $\delta^{18}O$ records from the GRIP (*9*, *21*), GISP2 (*9*), and DYE-3 (*7*, *17*) ice cores across the 11.7 ka transition show a similar duration. The $\delta^{18}O$ cooling transition at 12.9 ka lasted more than two centuries, much longer than the warming transitions, and does not meet the above criteria for being described as a ramp shift.

Annual layer thickness λ (estimated independently of $\delta^{18}O$ by annual layer counting) increased by 40% during the two warmings over 3 and 40 years, respectively. During the cooling, λ decreased by 33% over a period of 152 years. When corrected for strain, λ represents the annual precipitation rate, which is linked to site temperature and to synoptic weather patterns. Both Greenland site temperature and accumulation are expected to be strongly related to the extent of the northern sea ice (*22*).

The most abrupt transitions are those of the deuterium excess $d = \delta D - 8\delta^{18}O$, a second-order isotopic parameter that contains information on fractionation effects caused by the evaporation of source water (*16*, *18*, *23*). The excess is considered to be mainly a proxy of past ocean surface temperatures at the moisture-source region (*16*, *18*, *23*). Our dust record, not showing a similar abrupt transition as the excess, rules out the alternative explanation, that a rapid shift in *d* was linked with changes in cloud condensation nuclei and kinetic fractionation taking place during cloud ice-crystal formation (*24*, *25*). The excess record shows a 2 to 3 per mil (‰) decrease in *d* during the warmings, corresponding to a cooling by 2 to 4 K of the marine moisture-source region (*16*, *18*) over 1 to 3 years, and a 2 to 3‰ increase during the cooling transition. Figure 3 presents the rapid changes of *d* on a more highly resolved time axis in order to clearly show the rapid change between the climate states. The moisture-source evaporation conditions can change either because of a shift in atmospheric circulation, resulting in relocation of the moisture source, or because of changing sea surface temperature, humidity, or wind conditions at a stationary moisture source. The extremely rapid shifts in both warmings and coolings rule out an explanation that is purely in terms of sea-ice extent, because the northern sea ice extended far south during the final phase of the cold stadials and is not expected to have broken down in just 1 to 3 years (*26*, *27*). Finally, if *d* was reflecting only changes in weather pattern trajectories with respect to the NGRIP observation point, then it would be expected to detect simultaneous changes in other parameters, such as dust, Ca^{2+}, and λ, which is not the case. Thus, we interpret the rapid shifts in *d* to be more likely a consequence of changed source regions of the water vapor reaching Greenland. This points to a reorganization of atmospheric circulation from one year to the next.

The concentrations of insoluble dust and Ca^{2+} reflect both source strength and transport conditions from terrestrial sources, which for Greenland are the low-latitude Asian deserts (*10*, *28*). At the two warming events, the concentrations of dust and Ca^{2+} decreased by a factor of 5 to 7 within four decades, slightly preceding the *d* shift by 10 ± 5 years. In contrast, during the cooling event, the dust and Ca^{2+} concentrations increased by a factor of 5 over a period of more than a century, slightly lagging the *d* shift by 20 ± 10 years.

The concentration of Na^{+}, which is mainly a marine sea-salt indicator, shows only moderate changes at the transitions as compared with its interannual variability. Changes in sea-ice extent are expected to influence sea-salt export to Greenland through changing the distance to open water and altering sea-salt aerosol contributions from sea-ice and open-water sources. However, meteorological conditions play an important role in modulating the sea-salt uplift, transport, and deposition on the Greenland ice sheet (*29*). Although insufficient quantitative understanding of the processes involved is available, the lack of a fast response of the marine sea-salt proxy may be seen as a gradual change in sea ice or as a combination of changes in sea ice and meteorology, compensating for each other to some extent.

This high-resolution study shows a previously unkown sequence of events and gives insights into both the onset and evolution of a rapid climate shift. Our records demonstrate that the last two major warming events followed the same general pattern. During Greenland cold phases, the thermohaline circulation (THC) was reduced, northern sea ice extended far south, and the Intertropical Convergence Zone (ITCZ) was shifted southward, resulting in dry conditions at the low-latitude dust-source regions (*22*, *30*, *31*). Meanwhile, southern high latitudes and tropical oceans accumulated heat and underwent gradual warming as reflected in the bipolar seesaw pattern (*32*, *33*), because of a reduction in the North Atlantic overturning circulation. We suggest that this Southern Hemisphere/tropical warming induced first a northward shift of the ITCZ and, when a threshold was reached, an abrupt intensification of the Pacific monsoon. The wetter conditions at the Asian dust-source areas then caused decreased uplift and increased washout of atmospheric dust, leading to the first sign of change in Greenland: decreasing dust and Ca^{2+} concentrations. This reorganization of the tropical atmospheric circulation was followed by a complete reorganization of the mid- to high-latitude atmospheric circulation almost from one year to the next, as identified by the 1-to-3-year transitions in *d*. Sea ice then started retreating in the North Atlantic, associated with increased advection of atmospheric heat and moisture, as indicated by Greenland changes in $\delta^{18}O$ and λ (*22*, *34*).

Both abrupt warming events of the last termination are characterized by this sequence of events, even though they occurred at different stages of deglaciation. The 14.7-ka event followed Heinrich event H1 at a time when the ice sheets in the north were still extensive, whereas the north was more deglaciated at 11.7 ka (*35*), reducing the amount of ice discharge available to change the density of North Atlantic ocean waters and thereby the THC before the warming onset (*35*). The NGRIP ice core has also revealed that the very first interstadial of the last glacial cycle occurred at the inception of the glacial period 110 ka, before the ice sheets were fully developed and the climate system had cooled to full glacial conditions (*1*). The detailed sequence of events obtained here for the most recent warming events suggests that the classical bipolar seesaw concept (*32*) involving the ocean THC reorganization must include the role of abrupt atmospheric circulation changes from the tropics to the high

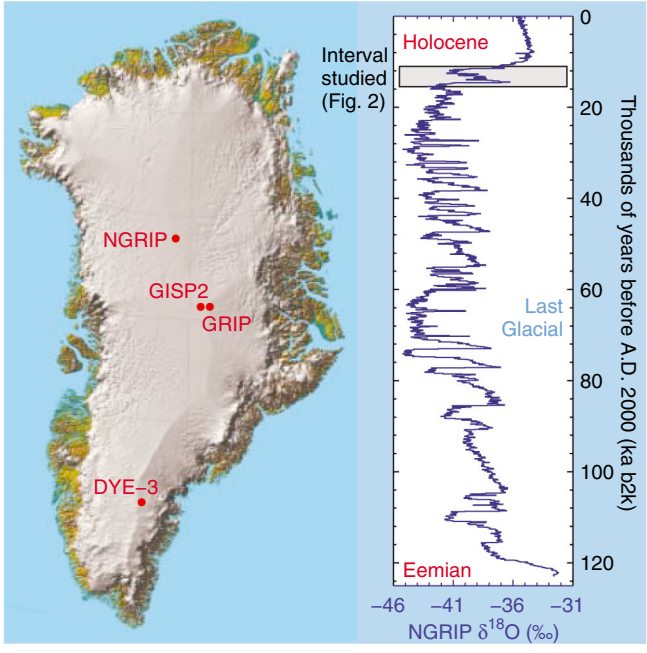

Fig. 1. (**Left**) Location of drill sites on the Greenland Ice Sheet: DYE-3 (65.15°N, 43.82°W), GRIP (72.59°N, 37.64°W), GISP2 (72.58°N, 38.46°W), and NGRIP (75.10°N, 42.32°W). (**Right**) The NGRIP stable water isotope profile ($\delta^{18}O$) on the GICC05 time scale (*1*, *2*). The zone studied (11.0 to 15.5 ka) is marked with gray shading.

northern latitudes in the onset of abrupt warmings seen in the North Atlantic region.

The cooling at 12.9 ka is characterized by relatively longer transition times for all parameters except for *d*, and the sequence of events is notably different. In this case, changes in *d* and $\delta^{18}O$ precede the dust and Ca^{2+} reactions. The centennial scale change in $\delta^{18}O$ follows anterior gradual cooling during the Allerød period, probably including gradual buildup of sea ice. Given the generally slow nature of the coolings, the persistent rapid switch of the atmospheric circulation as recorded by the excess is even more surprising and confirms the potential for extremely abrupt reorganizations of the Arctic atmospheric circulation, whether going from cold to warm or vice versa. The lag and longer duration of the dust and Ca^{2+} responses may be

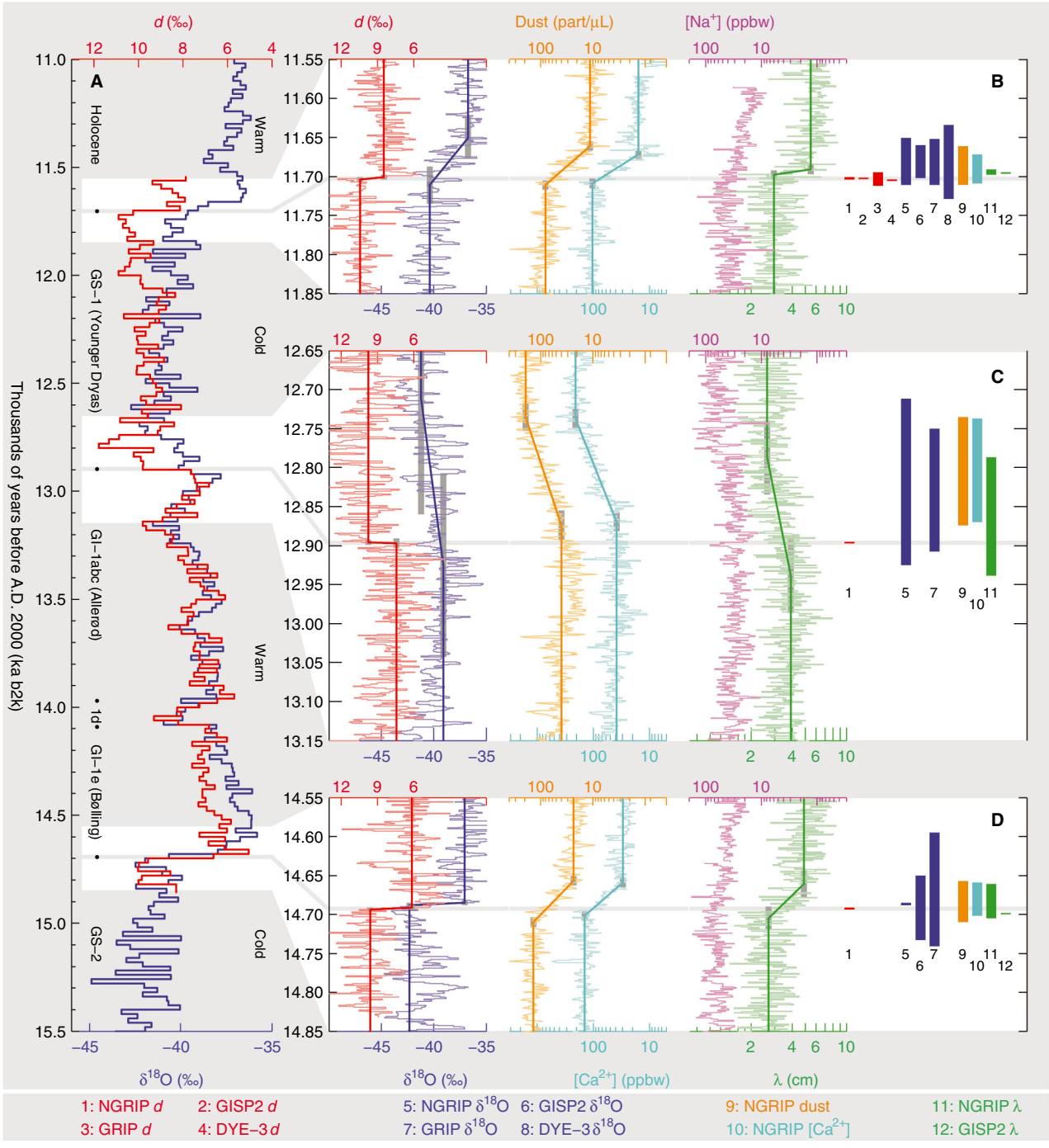

Fig. 2. Multiple-parameter records from the NGRIP ice core 11.0 to 15.5 ka. (**A**) *d* (red) and $\delta^{18}O$ (dark blue) at 20-year resolution over the entire period and details of the transition zones: (**B**) from GS-1 into the Holocene at 11.7 ka, (**C**) from GI-1a into GS-1 at 12.9 ka, and (**D**) from GS-2 into GI-1e at 14.7 ka. [Left part of (B) to (D)] NGRIP records of *d* (red), and $\delta^{18}O$ (dark blue) and logarithmic plots of dust content (yellow), calcium concentration ($[Ca^{2+}]$, light blue), sodium concentration ($[Na^{+}]$, purple), and annual layer thickness (λ, green) at annual resolution. Bold lines show the fitted ramp functions; gray vertical bars represent the 95% (2σ) confidence intervals of the ramp point locations. [Right part of (B) to (D)] Bars representing the locations of the fitted ramp functions for the NGRIP records shown to the left and for the corresponding results obtained using DYE-3, GRIP, and GISP2 data, where these are available at sufficient resolution (see list of records below the figure). See Table 1, SOM methods, and table S2 (*15*) for additional information on ramp fitting.

due to the inertia of land surfaces drying out and vegetation dying off in the dust-source regions before large fluxes of dust could be reestablished.

The high-resolution records from the NGRIP ice core reveal that polar atmospheric circulation can shift in 1 to 3 years, resulting in decadal- to centennial-scale changes from cold stadials to warm interstadials/interglacials associated with large Greenland temperature changes of 10 K (*6*, *20*). Neither the magnitude of such shifts nor their abruptness is currently captured by state-of-the-art climate models. We propose a series of events, beginning in the lower latitudes and leading to changes in the ocean and atmosphere, that reveals for the first time the anatomy of abrupt climate change. Although no large shifts in *d* can be identified over the course of the Holocene in the Greenland ice cores (*36*), past warming events now documented at subannual resolution offer important benchmarks with which to test climate models. If we are to be confident in the ability of those models to accurately predict the impacts of future abrupt change, their ability to match what we see in the past is crucial.

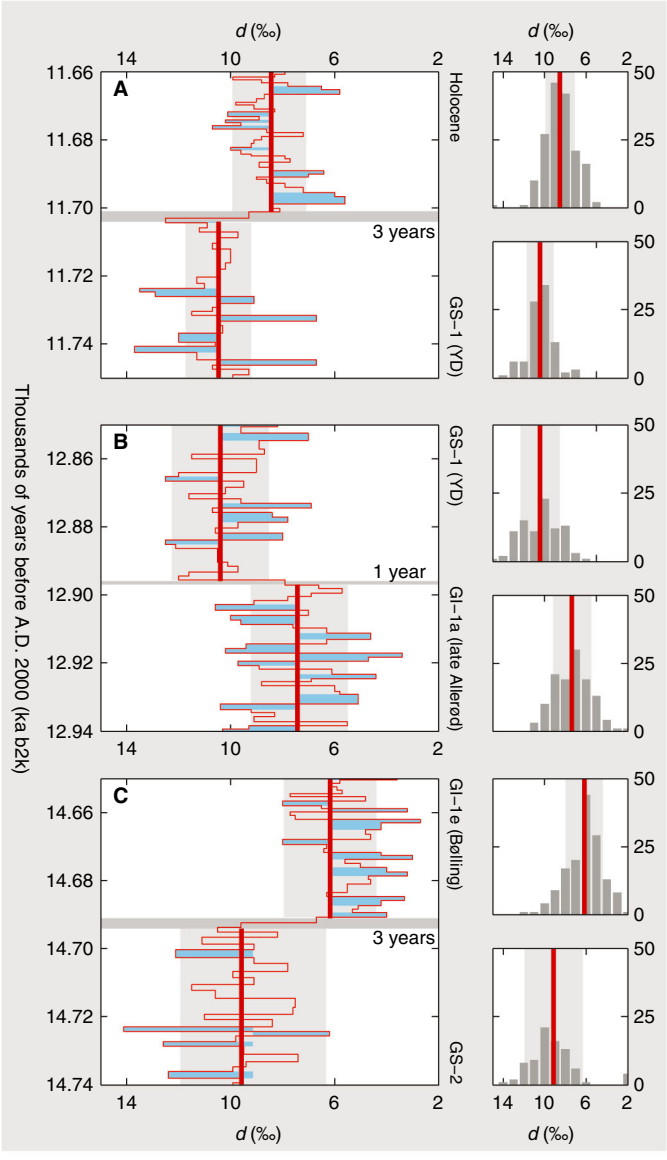

Fig. 3. (**A** to **C**) *d* (red) at measured resolution and the fitted ramp curves across the same transitions as shown in Fig. 2, B to D. The mean values over the 150 years before and after the transitions are shown as bold red lines. (Left) To visualize the shifts, the areas within 1 SD from the mean values are shaded light gray. Where the data values are more than 1 SD away from the mean, the zone is colored light blue. (Right) Histograms (gray) of the distribution of the *d* values in the states before and after the rapid shifts. The mean values are shown as bold red lines. Because of the abruptness of the *d* shifts, the ramp-fitting method produces results with very small uncertainties. Therefore, we suggest that the *d* record be used for defining transition points between different climatic episodes, especially for the transitions studied here (15.5 to 11.0 ka) but possibly also for those found in the older part of the NGRIP record (123.0 to 15.5 ka).

Table 1. Ramp-fitted transition times. Ramp-fitting results (*14*) for $\delta^{18}O$, *d*, dust content, Ca^{2+}, and λ over the three transitions from Greenland Stadial 1 (GS-1) into the Holocene at 11.7 ka, from Greenland Interstadial 1a (GI-1a) into GS-1 at 12.9 ka, and from GS-2 into GI-1e at 14.7 ka. The GICC05 time scale (*2*), produced by multiple-proxy identification of annual layers using NGRIP impurity records, provides the ages. The timing and standard error of the ramp points are listed at the onset and termination of the transitions. Times are in years before 2000 AD.

Period	$\delta^{18}O$	*d*	Dust	Ca^{2+}	λ
Start of Holocene	11,651 ± 13	11,701 ± 1.5	11,661 ± 3.0	11,672 ± 3.0	11,691 ± 3.0
End of GS-1	11,711 ± 12	11,704 ± 1.5	11,711 ± 3.0	11,709 ± 3.0	11,698 ± 3.0
Start of GS-1	12,712 ± 74	12,896 ± 1.5	12,735 ± 8.9	12,737 ± 8.9	12,787 ± 24
End of GI-1a	12,925 ± 59	12,897 ± 3.0	12,874 ± 9.6	12,870 ± 5.9	12,939 ± 24
Start of GI-1e	14,685 ± 1.5	14,691 ± 1.5	14,657 ± 3.0	14,659 ± 3.0	14,661 ± 8.9
End of GS-2	14,688 ± 1.5	14,694 ± 1.5	14,710 ± 3.0	14,702 ± 3.0	14,705 ± 7.4

References and Notes

1. North Greenland Ice Core Project Members, *Nature* **431**, 147 (2004).
2. S. O. Rasmussen *et al.*, *J. Geophys. Res.* **111**, D06102 (2006).
3. R. B. Alley *et al.*, *Science* **299**, 2005 (2003).
4. W. Dansgaard, J. W. C. White, S. J. Johnsen, *Nature* **339**, 532 (1989).
5. J. J. Lowe, M. J. C. Walker, *Reconstructing Quaternary Environments* (Pearson Higher Education, New Jersey, ed. 2, 1997).
6. J. P. Severinghaus, E. J. Brook, *Science* **286**, 930 (1999).
7. W. Dansgaard *et al.*, *Science* **218**, 1273 (1982).
8. S. J. Johnsen *et al.*, *J. Geophys. Res.* **102**, 26397 (1997).
9. P. M. Grootes, M. Stuiver, J. W. C. White, S. J. Johnsen, J. Jouzel, *Nature* **366**, 552 (1993).
10. U. Ruth *et al.*, *Geophys. Res. Lett.* **34**, L03706, 10.1029/2006GL027876 (2007).
11. R. Röthlisberger *et al.*, *Environ. Sci. Technol.* **34**, 338 (2000).
12. M. Bigler, thesis, University of Bern, Switzerland (2004).
13. U. Ruth, D. Wagenbach, J. P. Steffensen, M. Bigler, *J. Geophys. Res.* **108**, 4098 (2003).
14. M. Mudelsee, *Comput. Geosci.* **26**, 293 (2000).
15. Materials and methods are available as supporting material on *Science* Online.
16. V. Masson-Delmotte *et al.*, *Science* **309**, 118 (2005).
17. W. Dansgaard *et al.*, in *Climatic Processes and Climate Sensitivity, vol. Maurice Ewing 5*, J. E. Hansen, T. Takahashi, Eds. (American Geophysical Union, Washington, DC, 1984), pp. 288–298.
18. J. Jouzel *et al.*, *Quat. Sci. Rev.* **26**, 1 (2007).
19. M. Werner, M. Heimann, G. Hoffmann, *Tellus B Chem. Phys. Meteorol.* **53**, 53 (2001).
20. A. Landais, J. Jouzel, V. Masson-Delmotte, N. Caillon, *C. R. Geosci.* **337**, 947 (2005).
21. S. J. Johnsen *et al.*, *J. Quat. Sci.* **16**, 299 (2001).
22. C. Li, D. S. Battisti, D. P. Schrag, E. Tziperman, *Geophys. Res. Lett.* **32**, L19702, 10.1029/2005GL023492 (2005).
23. S. J. Johnsen, W. Dansgaard, J. W. C. White, *Tellus B Chem. Phys. Meteorol.* **41**, 452 (1989).
24. J. Jouzel *et al.*, *J. Geophys. Res.* **96**, 7495 (1991).
25. D. A. Fisher, *Tellus Ser. B Chem. Phys. Meteorol.* **43**, 401 (1991).
26. M. Winton, *Geophys. Res. Lett.* **33**, L23504 (2006).
27. C. Hillaire-Marcel, A. de Vernal, *Earth Planet. Sci. Lett.* **268**, 143 (2008).
28. A. Svensson, P. E. Biscaye, F. E. Grousset, *J. Geophys. Res.* **105**, 4637 (2000).
29. M. A. Hutterli *et al.*, *Clim. Dyn.*, 10.1007/s00382-006-0211-z (2006).
30. D. W. Lea, D. K. Pak, L. C. Peterson, K. A. Hughen, *Science* **301**, 1361 (2003).
31. J. W. Partin, K. M. Cobb, J. F. Adkins, B. Clark, D. P. Fernandez, *Nature* **449**, 452 (2007).
32. T. F. Stocker, S. J. Johnsen, *Paleoceanography* **18**, 1087 (2003).
33. EPICA Community Members, *Nature* **444**, 195 (2006).
34. J. C. H. Chiang, C. M. Bitz, *Clim. Dyn.* **25**, 10.1007/s00382-005-0040-5 (2005).
35. K. Lambeck, T. M. Esat, E.-K. Potter, *Nature* **419**, 199 (2002).
36. V. Masson-Delmotte *et al.*, *J. Geophys. Res.* **110**, D14102 (2005).
37. NGRIP is directed and organized by the Ice and Climate Research Group, Niels Bohr Institute, University of

Copenhagen. It is supported by funding agencies in Denmark (Forskningsrådet for Natur og Univers), Belgium (Fonds National de la Recherche Scientifique), France (Institut Polaire Française and Institut National des Science l'Univers/CNRS), Germany (AWI), Iceland (Rannís), Japan (Ministry of Education, Culture, Sports, Science and Technology), Sweden (Polarforskningssekretariatet), Switzerland (Der Schweizerische Nationalfonds) and the United States (NSF, Office of Polar Programs).

Supporting Online Material
www.sciencemag.org/cgi/content/full/1157707/DC1
Materials and Methods
Tables S1 and S2
Data

12 March 2008; accepted 12 June 2008
Published online 19 June 2008;
10.1126/science.1157707
Include this information when citing this paper.

The Global Stoichiometry of Litter Nitrogen Mineralization

Stefano Manzoni,[1] Robert B. Jackson,[2] John A. Trofymow,[3] Amilcare Porporato[1]*

Plant residue decomposition and the nutrient release to the soil play a major role in global carbon and nutrient cycling. Although decomposition rates vary strongly with climate, nitrogen immobilization into litter and its release in mineral forms are mainly controlled by the initial chemical composition of the residues. We used a data set of ~2800 observations to show that these global nitrogen-release patterns can be explained by fundamental stoichiometric relationships of decomposer activity. We show how litter quality controls the transition from nitrogen accumulation into the litter to release and alters decomposers' respiration patterns. Our results suggest that decomposers lower their carbon-use efficiency to exploit residues with low initial nitrogen concentration, a strategy used broadly by bacteria and consumers across trophic levels.

Plant residues deposited to the soil are subject to biological degradation (*1*–*3*). During this process, litter carbon (C) is respired to CO_2 while providing energy to the decomposers, whereas nutrient concentrations generally increase (*4*). Nutrients in mineral forms are taken up by the decomposers (immobilized) and thus accumulate in the litter. Typically, net nitrogen (N) release in mineral forms (ammonium and nitrate) from a given plant residue (net mineralization) only occurs after N concentration reaches a critical value (*1*). Knowledge of this threshold and how it is related to biogeochemical or climatic factors is essential to predict the patterns of nutrient cycling in natural and agricultural settings (*4*–*6*), to improve our understanding of ecosystem stoichiometry (*7*, *8*), and to constrain biogeochemical models (*9*). The biological degradation of litter is mainly carried out by microbial decomposers, including bacteria and fungi, and their grazers, which have higher N:C values compared with most litter types (*1*). This creates a high N demand, and, even though a considerable fraction of assimilated C is respired, the decomposers often still require some inorganic N uptake during at least the early phases of decomposition. The decomposer N:C and the respiration rate (complementary to the carbon-use efficiency) define the actual nutrient requirement of the decomposers (*9*–*11*). Although the decomposer N:C ratios have been observed to be relatively constant across ecosystems and litter types, the causes of patterns of variation in carbon-use efficiency are still unclear.

[1]Civil and Environmental Engineering Department, Duke University, Durham, NC 27708, USA. [2]Department of Biology and Nicholas School of the Environment, Duke University, Durham, NC 27708, USA. [3]Canadian Forest Service, Pacific Forestry Centre, Victoria, BC V8Z 1M5, Canada.

*To whom correspondence should be addressed. E-mail: amilcare@duke.edu

We analyzed litter decomposition data including the temporal evolution of both carbon and nitrogen, as measured in litterbags left to decompose in field conditions (*12*) or from chemical analysis of large branches and logs along decomposition chronosequences. On the basis of 55 litter types classified by initial N concentrations ranging from 0.03% to 3% (*13*), we show that the carbon-use efficiency tends to increase with higher initial substrate N:C ratio, which corresponds to a more-efficient nitrogen use and a less-efficient carbon use for N-poor substrates (i.e., litter with low N concentration and low N:C). In turn, low carbon-use efficiencies allow net mineralization to occur early during decomposition, even in relatively N-poor residues.

The dynamics of net N immobilization, accumulation, and mineralization have been described mathematically with mass balance equations (*9*, *11*, *14*). We developed a general set of such equations that allows us to obtain universal analytical curves of N accumulation and release during decomposition, when the decomposer characteristics can be assumed relatively constant in time (*13*). Specifically, the general expression for the fraction of initial litter nitrogen content, n, as a function of the fraction of remaining carbon content in the litter sample, c, can be written independently of the specific decomposition model as

$$n(c) = c\frac{r_B}{r_{L,0}} + \left(1 - \frac{r_B}{r_{L,0}}\right)c^{\frac{1}{1-e}} \qquad (1)$$

where $r_{L,0}$ is the initial litter N:C ratio, r_B is the decomposer biomass N:C, and e is the decomposer carbon-use efficiency (i.e., amount of C in new biomass per unit C decomposed). Thus, the N dynamics are represented in terms of the fraction of remaining litter C content, avoiding any explicit account of the temporal variability of decomposition rates caused by climatic factors or nutrient limitation. On the basis of data from 15 data sets containing observations at more than 60 sites worldwide (table S1), this universal representation of N immobilization and release curves appears to be valid across diverse terrestrial ecosystems and with different initial litter N:C values.

During decomposition, the fraction of remaining N and lost C move along the curves from left to right at a speed dictated by biogeochemical and environmental conditions (Fig. 1). All the curves show slower N loss than C loss, meaning that N tends to accumulate, and the N:C ratio of the litter increases throughout decomposition. Where the curves increase with respect to the initial condition, not only is N retained more efficiently than C, but net immobilization occurs. At the point on each curve where n is maximal, immobilization ends and net mineralization begins. Conversely, if the curve decreases monotonically there is no initial net immobilization, as in Fig. 1, A and B. The maximum of the N release curve thus corresponds to the litter critical N concentration, which can be expressed analytically in terms of N:C ratio as a function of the decomposer characteristics, $r_{CR} = e{\cdot}r_B$ (*9*, *10*). In general, the lower r_{CR} is, the earlier N release occurs, even in N-poor residues. Moreover, when $r_{CR} < r_{L,0}$, net release occurs from the beginning of decomposition. Conversely, if r_{CR} is high, large amounts of mineral N have to be immobilized to increase the litter N concentration to its critical value.

The litter decomposition observations and Eq. 1 can be used to study the patterns of variation of the litter r_{CR} and decomposer characteristics. Using the analytical N release curve provides a theoretical underpinning to previous estimates of the onset of mineralization based on regressions of field observations (*4*, *15*) and offers robust estimates of r_{CR} and the decomposer parameters, e and r_B. In particular, r_B does not vary systematically along gradients of organic matter and litter N:C and typically remains in the range of 0.07 to 0.2 [or C:N between 5 and 15 (*7*, *16*, *17*)]. We thus assumed an average value of $r_B = 0.1$ and fitted the remaining free parameter, e, for each litter type (*13*). For given values of r_B and e and applying a nonlinear transformation of Eq. 1, all observations of litter C and N content collapse well onto a single 1:1 curve (Fig. 2 and fig. S1), showing that the variation of e alone explains most of the variability in the data.

We assessed how r_{CR} and e, which are simply proportional when r_B is a constant, respond to changes in climatic variables and initial litter conditions. Parton *et al.* (*18*) and Moore *et al.* (*15*) noted that the N release patterns observed in two

continental-scale decomposition experiments do not depend on climatic variables. Our analysis, which includes many additional data sets (table S1), not only confirms the lack of a significant correlation between r_{CR} and mean annual precipitation or temperature but also reveals a significant power law relationship between r_{CR} and $r_{L,0}$ (Fig. 3A). This result shows that decomposers of low-N residues are able to begin mineralization even when the litter N concentration is still relatively low. In fact, for a given r_B, lower values of r_{CR} imply lower values of e (i.e., higher fractions of respired C), indicating that some decomposers with low energetic efficiency may be able to decompose low-N litter without necessarily having to immobilize much inorganic N. A low r_{CR} (and low e) also explains the low N immobilization observed during decomposition of N-poor wood (*19*). Apparently, decomposers are able to use the limited but relatively reliable N bound to organic compounds, thus reducing their dependence on the less-reliable or less-accessible inorganic pool. Nevertheless, because estimated values of r_{CR} are generally higher than $r_{L,0}$ (data points above the dashed line in Fig. 3A), some degree of immobilization remains necessary. For a given $r_{L,0}$, the variability in r_{CR} might be attributed to site effects. In fact, a trend for higher N accumulation in litters from sites with higher soil N:C ratios has been reported (*15*), although there are not enough data to test for such an effect globally.

Lastly, the pattern of decline in e as a function of $r_{L,0}$ appears to be independent of possible changes in r_B (shaded area in Fig. 3A). Remarkably, a similar pattern has also been observed [Fig. 3B; see also (*13*)] at different time scales and trophic levels in bacterial cultures (*20*), in aquatic bacteria (*21*), and in terrestrial and aquatic grazers (*22*–*25*). The generality of such a result hints at a common mechanism of carbon utilization across diverse ecosystems and trophic levels, where carbon "waste" occurs under restricted nutrient availability. From a metabolic perspective, the observation of low e may be related to regulation of catabolic reactions in low-nutrient conditions to maintain a stable cellular composition (*20*, *21*) or to increased C throughput by the decomposers or decomposer food web for obtaining N from recalcitrant substrates (*17*, *26*). A better understanding of the causes of this behavior is of fundamental interest and could reveal the constraints on decomposer community functioning under N-poor conditions, an important goal for improving biogeochemical modeling. In biogeochemical models of soil and litter, the carbon-use efficiency of decomposers is generally assumed constant or to decrease with substrate N:C, in agreement with our results (*14*, *17*, *27*). However, our estimates are generally lower than the efficiency values typically assumed, suggesting that current models might underestimate the heterotrophic respiration flux per unit mass of decomposed litter or organic matter.

In summary, the N-release patterns of decomposing litter appear to be regulated by the initial chemical composition of the litter and the stoichiometric requirements of the decomposers (Fig. 1). In particular, the critical N:C ratio, below which net immobilization occurs, is uncorrelated with climatic variables but strongly correlated with initial litter chemistry (Fig. 3A). Because decom-

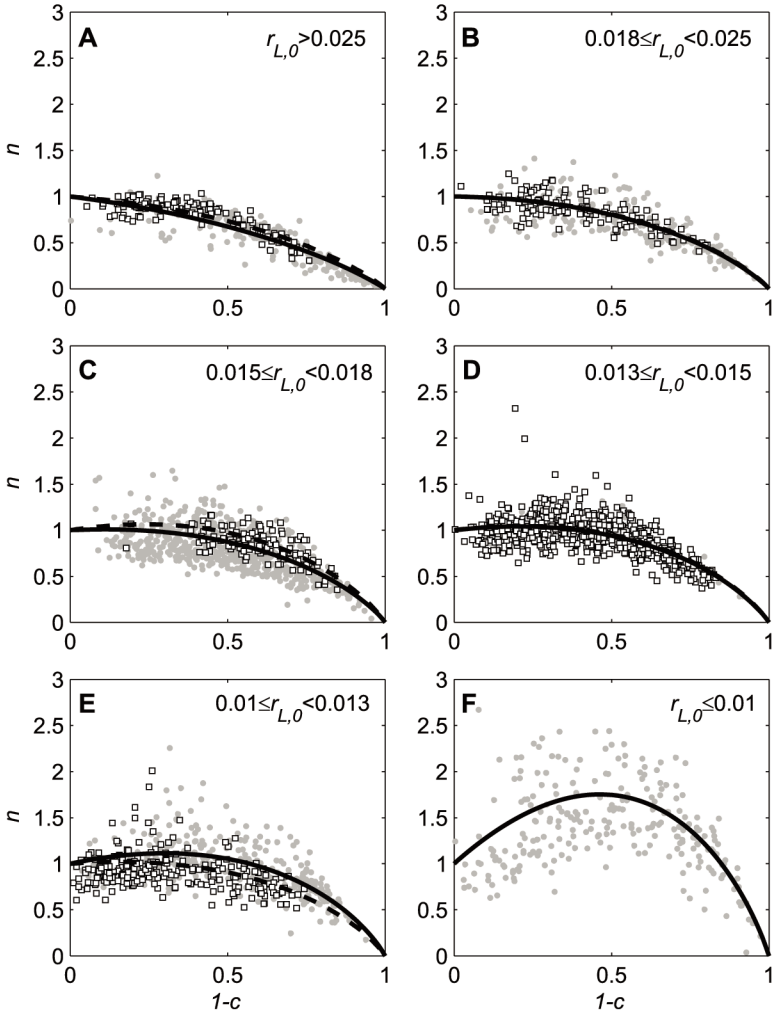

Fig. 1. Nitrogen release patterns across litter types. (**A** to **F**) Observed and modeled fractions of initial nitrogen, $n = N_L(t)/N_L(0)$, as a function of the decomposed fractions of initial carbon, $1 - c = 1 - C_L(t)/C_L(0)$, for leaf litter with decreasing values of $r_{L,0}$. Data and analytical N release curves for the LIDET data set (*18*, *28*, *29*) are represented by ● and solid lines; data from the CIDET data set (*12*, *15*), by □ and dashed lines.

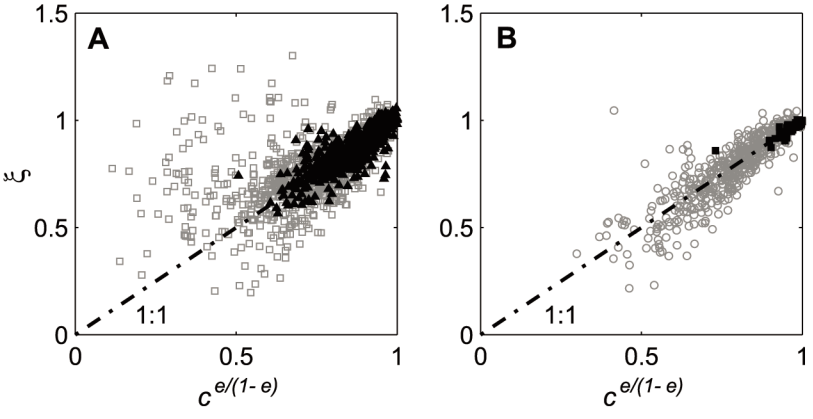

Fig. 2. Normalized representation of the nitrogen release curves. Plots of the normalized variable $\xi = (r_L - r_B)/(r_{L,0} - r_B)$ (eq. S5) against $c^{e/(1-e)}$ for litters of different origin [(**A**) broadleaved tree and shrub leaves, □, and conifer needles, ▲; (**B**) grass leaves, ○, and woody residues, ■], showing that the analytical N release curves (Eq. 1) fitted to the data with the only free parameter e is able to capture most of the variability in all litter types.

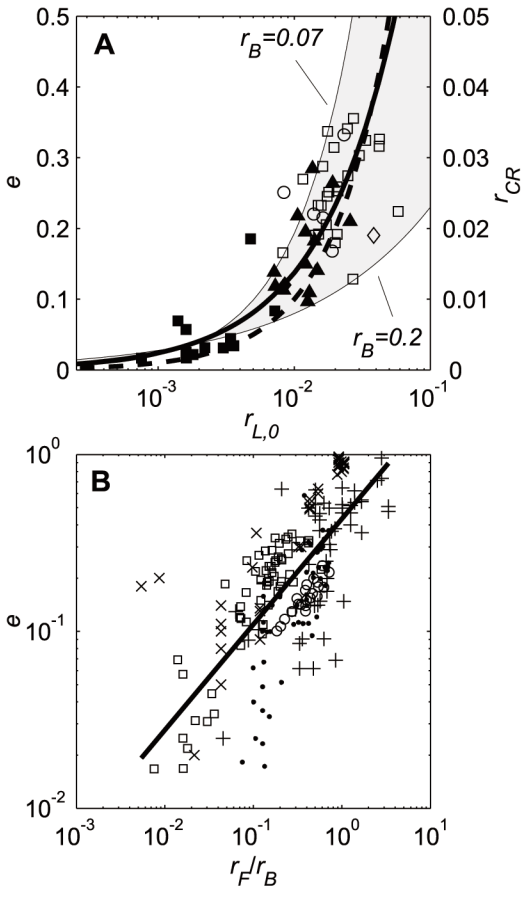

Fig. 3. Effect of litter quality on decomposer stoichiometry. (**A**) Decomposer efficiency, *e* (left), or r_{CR} (right) as a function of $r_{L,0}$ when r_B = 0.1. Symbols indicate different litter types as in Fig. 2; ◇ and ◆ refer to a decomposing log (r_B = 0.122) and the underlying soil (r_B = 0.135), respectively [data elaborated after (*16*, *30*)]. The solid line is a linear least square fit of the log-transformed r_{CR} and $r_{L,0}$ ($r_{CR} = 0.45 \times r_{L,0}^{0.76}$; $R = 0.88$; $P < 0.0001$). The shaded area shows the effects on *e* of different r_B around 0.1 (solid line). The dashed curve indicates points where $r_{CR} = r_{L,0}$: Litter points above this curve need to immobilize N; points below release N since the beginning of decomposition. (**B**) Estimates of *e* as a function of the ratio between food source N:C (r_F) and consumer N:C (r_B) at different trophic levels: □, terrestrial plant residue decomposers (this study); +, marine bacteria (*21*); ○, terrestrial larvae (*25*); ●, terrestrial insects (*23*); and ×, aquatic insects (*24*). The solid line is a linear least square fit of the log-transformed *e* and r_F/r_B [$e = 0.43 \times (r_F/r_B)^{0.60}$; $R = 0.72$; $P < 0.0001$].

poser N:C ratio is relatively constant, this pattern suggests that the decomposer communities are able to adapt partially to low-nitrogen substrates (i.e., low $r_{L,0}$) by decreasing their C-use efficiency and thus the critical N:C of the litter (Fig. 3A). Such a pattern has been observed in aquatic environments and at other trophic levels (*21*–*25*) and appears to be a universal response of decomposers in nutrient-poor conditions (Fig. 3B). Decreasing efficiency results in higher heterotrophic respiration per unit mass of litter humified or unit nutrient released, suggesting that the soil carbon cycle is likely more open than currently thought.

References and Notes

1. B. Berg, C. A. McClaugherty, *Plant Litter: Decomposition, Humus Formation, Carbon Sequestration* (Springer, Berlin, 2003).
2. M. J. Swift, O. W. Heal, J. M. Anderson, *Decomposition in Terrestrial Ecosystems*, vol. 5 of *Studies in Ecology* (Univ. of California Press, Berkeley, 1979).
3. S. A. Waksman, *J. Agric. Sci.* **14**, 555 (1924).
4. J. D. Aber, J. M. Melillo, *Can. J. Bot.* **60**, 2263 (1982).
5. G. Seneviratne, *Biol. Fertil. Soils* **31**, 60 (2000).
6. B. Berg, G. Ekbohm, *Ecology* **64**, 63 (1983).
7. C. C. Cleveland, D. Liptzin, *Biogeochemistry* **85**, 235 (2007).
8. R. W. Sterner, J. J. Elser, *Ecological Stoichiometry: The Biology of Elements from Molecules to the Biosphere* (Princeton Univ. Press, Princeton, NJ, 2002).
9. S. Manzoni, A. Porporato, *Soil Biol. Biochem.* **39**, 1542 (2007).
10. G. I. Ågren, E. Bosatta, *Theoretical Ecosystem Ecology: Understanding Element Cycles* (Cambridge Univ. Press, Cambridge, 1996).
11. E. Bosatta, H. Staaf, *Oikos* **39**, 143 (1982).
12. J. A. Trofymow, CIDET, "The Canadian Intersite Decomposition Experiment (CIDET): Project and site establishment report," *Tech. Rep. No. BC-X-378* (Pacific Forestry Centre, Victoria, Canada, 1998).
13. See supporting materials on *Science* Online.
14. W. J. Parton, D. S. Schimel, C. V. Cole, D. S. Ojima, *Soil Sci. Soc. Am. J.* **51**, 1173 (1987).
15. T. R. Moore, J. A. Trofymow, C. E. Prescott, J. Fyles, B. D. Titus, *Ecosystems* (*New York*) **9**, 46 (2006).
16. S. C. Hart, *Ecology* **80**, 1385 (1999).
17. H. W. Hunt *et al.*, *Biol. Fertil. Soils* **3**, 57 (1987).
18. W. Parton *et al.*, *Science* **315**, 361 (2007).
19. O. N. Krankina, M. E. Harmon, A. V. Griazkin, *Can. J. For. Res.* **29**, 20 (1999).
20. J. B. Russell, G. M. Cook, *Microbiol. Rev.* **59**, 48 (1995).
21. P. A. del Giorgio, J. J. Cole, *Annu. Rev. Ecol. Syst.* **29**, 503 (1998).
22. J. J. Elser *et al.*, *Nature* **408**, 578 (2000).
23. W. J. Mattson, *Annu. Rev. Ecol. Syst.* **11**, 119 (1980).
24. T. J. Pandian, M. P. Marian, *Freshw. Biol.* **16**, 93 (1986).
25. F. Slansky, P. Feeny, *Ecol. Monogr.* **47**, 209 (1977).
26. J. M. Craine, C. Morrow, N. Fierer, *Ecology* **88**, 2105 (2007).
27. W. B. McGill, H. W. Hunt, R. G. Woodmansee, J. O. Reuss, in *Terrestrial Nitrogen Cycles: Processes, Ecosystem Strategies and Management Impacts*, F. E. Clark, T. Rosswall, Eds. (Ecological Bulletins, Stockholm, 1981), vol. 33, pp. 49–115.
28. M. E. Harmon, Long-Term Ecological Research (LTER) Intersite Litter Decomposition Experiment (LIDET), Forest Science Data Bank code TD023, Corvallis, OR, 2007, www.fsl.orst.edu/lter/data/abstract.cfm?dbcode=TD023.
29. H. L. Gholz, D. A. Wedin, S. M. Smitherman, M. E. Harmon, W. J. Parton, *Glob. Change Biol.* **6**, 751 (2000).
30. S. C. Hart, G. E. Nason, D. D. Myrold, D. A. Perry, *Ecology* **75**, 880 (1994).

31. This research was supported by Department of Energy (DOE) Forest-Atmosphere Carbon Transfer and Storage project (FACT-1), NSF DEB 0235425 and 0717191, and DOE PER 64242-0012346. LIDET data sets were provided by the Forest Science Data Bank, a partnership between the Department of Forest Science, Oregon State University, and the U.S. Forest Service Pacific Northwest Research Station, Corvallis, Oregon. Significant funding for these data was provided by the NSF Long-Term Ecological Research program (DEB-02-18088). Funding for the CIDET experiment was provided by Climate Change and Ecosystem Processes Network of the Canadian Forest Service and Natural Resources Canada Panel on Energy Research Development. We also thank G. Katul, D. Richter, and two anonymous reviewers for useful comments.

Supporting Online Material

www.sciencemag.org/cgi/content/full/321/5889/684/DC1
Materials and Methods
Fig. S1
Table S1

29 April 2008; accepted 1 July 2008
10.1126/science.1159792

Regulation of CD45 Alternative Splicing by Heterogeneous Ribonucleoprotein, hnRNPLL

Shalini Oberdoerffer,[1] Luis Ferreira Moita,[2]* Daniel Neems,[1] Rui P. Freitas,[2]* Nir Hacohen,[2,3] Anjana Rao[1]†

The transition from naïve to activated T cells is marked by alternative splicing of pre-mRNA encoding the transmembrane phosphatase CD45. Using a short hairpin RNA interference screen, we identified heterogeneous ribonucleoprotein L-like (hnRNPLL) as a critical inducible regulator of CD45 alternative splicing. HnRNPLL was up-regulated in stimulated T cells, bound CD45 transcripts, and was both necessary and sufficient for CD45 alternative splicing. Depletion or overexpression of hnRNPLL in B and T cell lines and primary T cells resulted in reciprocal alteration of CD45RA and RO expression. Exon array analysis suggested that hnRNPLL acts as a global regulator of alternative splicing in activated T cells. Induction of hnRNPLL during hematopoietic cell activation and differentiation may allow cells to rapidly shift their transcriptomes to favor proliferation and inhibit cell death.

It is estimated that greater than 75% of genes yield alternative transcripts, contributing to considerable functional diversity within the genome (*1*, *2*). SR (serine-arginine rich) proteins are key positive regulators of alternative splicing that bind enhancer sequences on nascent tran-

scripts and recruit spliceosomal proteins to weak splice sites, thereby facilitating proximal spliceosome assembly (*3*). Heterogeneous nuclear ribonucleoproteins (hnRNPs) also regulate splicing by binding negative cis-regulatory elements and causing exon exclusion from mature mRNA (*3*). SR proteins and hnRNPs function as antagonists in alternative splicing, with binding of hnRNPs to silencer sequences inhibiting SR protein binding, thus forcing a shift of splicing to distal splice sites (*4*).

CD45 is an abundant transmembrane protein tyrosine phosphatase expressed at the surface of T cells, B cells, and other hematopoietic cells (*5*). CD45 transcripts undergo extensive alternative splicing in which exons 4, 5, and 6 are variably excluded (Fig. 1A) (*6*). Primary naive T cells and B cells express the larger isoforms and are referred to as RA^+. In contrast, activated and memory T cells express the shortest isoform, CD45RO (*5*). CD45 initiates signaling through antigen receptors by dephosphorylating the inhibitory tyrosine on Src-family kinases (*5*), but attributing specific functions to individual CD45 isoforms has been complicated by the high basal expression of CD45 in lymphocytes and its ability to dephosphorylate both inhibitory and activation-loop tyrosines of Src-family kinases (*7*–*9*). Stimulated T cells show a shift in CD45 alternative splicing that culminates in increased CD45RO and decreased $CD45RA^+$ transcripts within 24 hours, and this can be blocked by cycloheximide treatment, which suggests the involvement of de novo protein synthesis (*10*).

To identify trans-acting factors required for CD45RO expression in stimulated T cells, we performed an RNA interference (RNAi) screen in JSL1 T cells, which basally express both CD45RO and CD45RA, but in which phorbol 12-myristate 13-acetate (PMA) stimulation generates a relative increase in the ratio of RO to RA transcripts through alternative splicing (*10*). JSL1 cells were infected in duplicate with individual short hairpin RNAs (shRNAs) from a splicing factor–directed library (*11*, *12*), selected with puromycin, stimulated with PMA (40 hours), and assayed for CD45RO expression (Fig. 1B). Knockdown of a single candidate, hnRNPLL (heterogeneous ribonucleoprotein L-like), sub-

[1]Department of Pathology, Immune Disease Institute, Harvard Medical School, Boston, MA 02115, USA. [2]Center for Immunology and Inflammatory Diseases, Division of Rheumatology, Allergy, and Immunology, Massachusetts General Hospital, Charlestown, MA 02129, USA. [3]Broad Institute of Harvard and Massachusetts Institute of Technology, Cambridge, MA 02142, USA.

*Present address: Instituto de Medicina Molecular, Faculdade de Medicina, Universidade de Lisboa, 1649-028 Lisboa, Portugal.

†To whom correspondence should be addressed. E-mail: arao@idi.harvard.edu

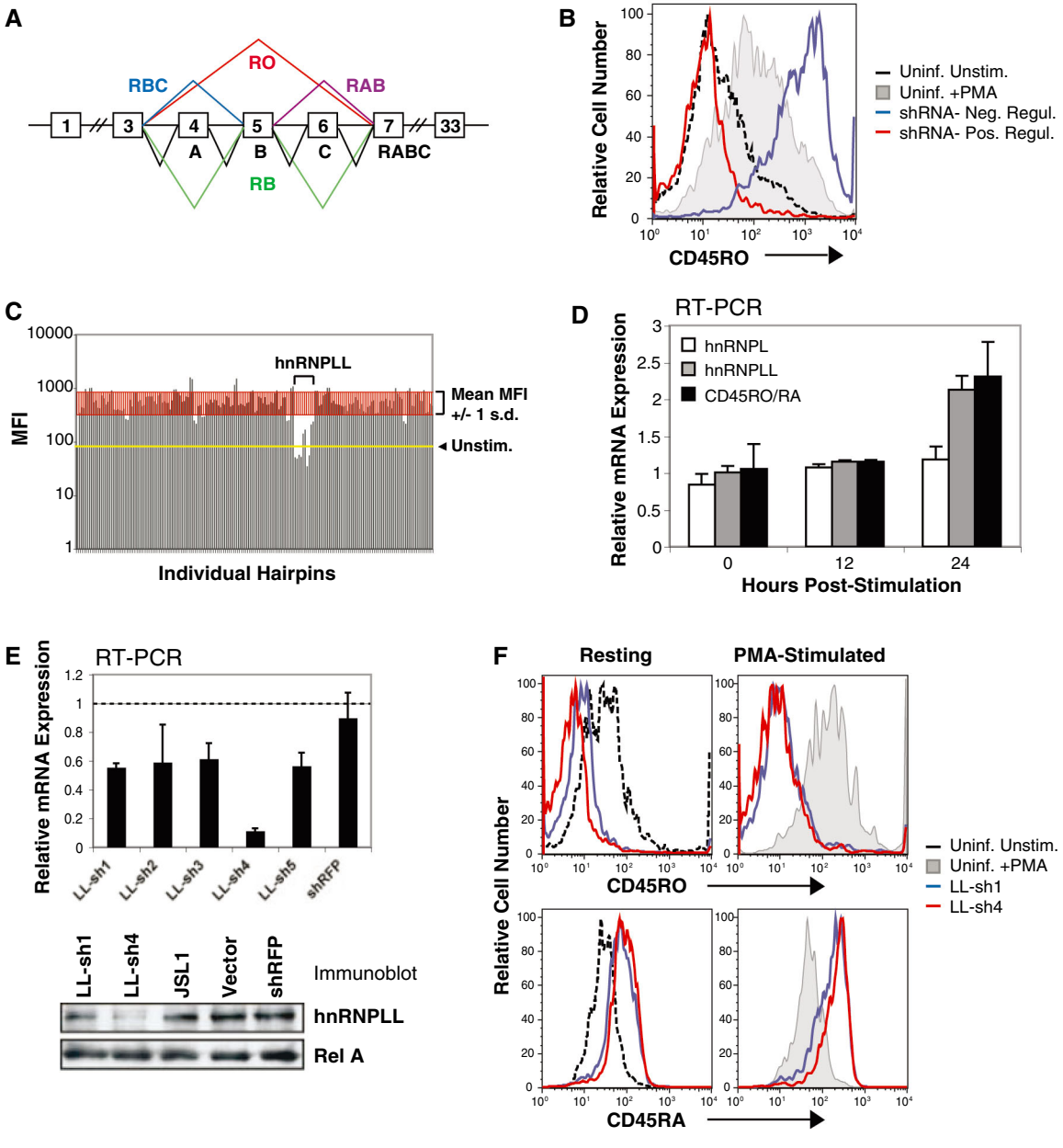

Fig. 1. Identification of hnRNPLL in an shRNA screen. (**A**) CD45 isoform nomenclature. (**B**) Sample histogram of cell surface-CD45RO expression in uninfected JSL1 cells with or without PMA stimulation and JSL1 cells transduced with lentiviral shRNAs. (**C**) Representative results from a single 96-well plate in the screen. All hnRNPLL hairpins decreased PMA-induced CD45RO expression. (**D**) Quantitative RT-PCR for hnRNPLL, hnRNPL, CD45RO, and CD45RA in JSL1 cells stimulated with PMA for 12 and 24 hours. PMA stimulation increases hnRNPLL expression and the ratio of CD45RO to RA transcripts. (**E**) Quantitative RT-PCR and anti-hnRNPLL immunoblot confirmed hnRNPLL depletion. (**F**) Cell-surface expression of CD45 isoforms assessed in PMA-stimulated JSL1 cells stably expressing LL-sh1 and LL-sh4. HnRNPLL depletion decreased CD45RO expression and increased CD45RA expression.

stantially reduced PMA-induced CD45RO expression, with three of the five hairpins reducing it to a level lower than the unstimulated control (Fig. 1C).

Concurrent with the increased ratio of CD45RO to RA transcripts, PMA stimulation of JSL1 cells increased hnRNPLL transcripts by a factor of ~2.0 in 24 hours (Fig. 1D), without affecting expression of its paralog hnRNPL (heterogeneous ribonucleoprotein L). These data are consistent with the hypothesis that hnRNPLL is the de novo synthesized factor that promotes alternative splicing in PMA-stimulated JSL1 cells (*10*).

In JSL1 cells engineered for stable expression of two of the five lentiviral shRNAs (LL-sh1 and LL-sh4), a substantial reduction of hnRNPLL protein expression was also observed (Fig. 1E). Cells expressing these shRNAs showed decreased CD45RO expression, and a concomitant increase in CD45RA expression, under both resting and stimulated conditions (Fig. 1F). This result is consistent with the notion that hnRNPLL mediates alternative splicing rather than repressing CD45 transcription.

To further examine the influence of hnRNPLL expression, JSL1 cells were transduced with a lentivirus encoding bicistronic hnRNPLL and internal ribosomal entry site–green fluorescent protein (IRES-GFP) as a means of tracking hnRNPLL expression in these cells. HnRNPLL overexpression was readily apparent in the total cell population (Fig. 2A), even though only ~35% of the cells were successfully transduced as judged by

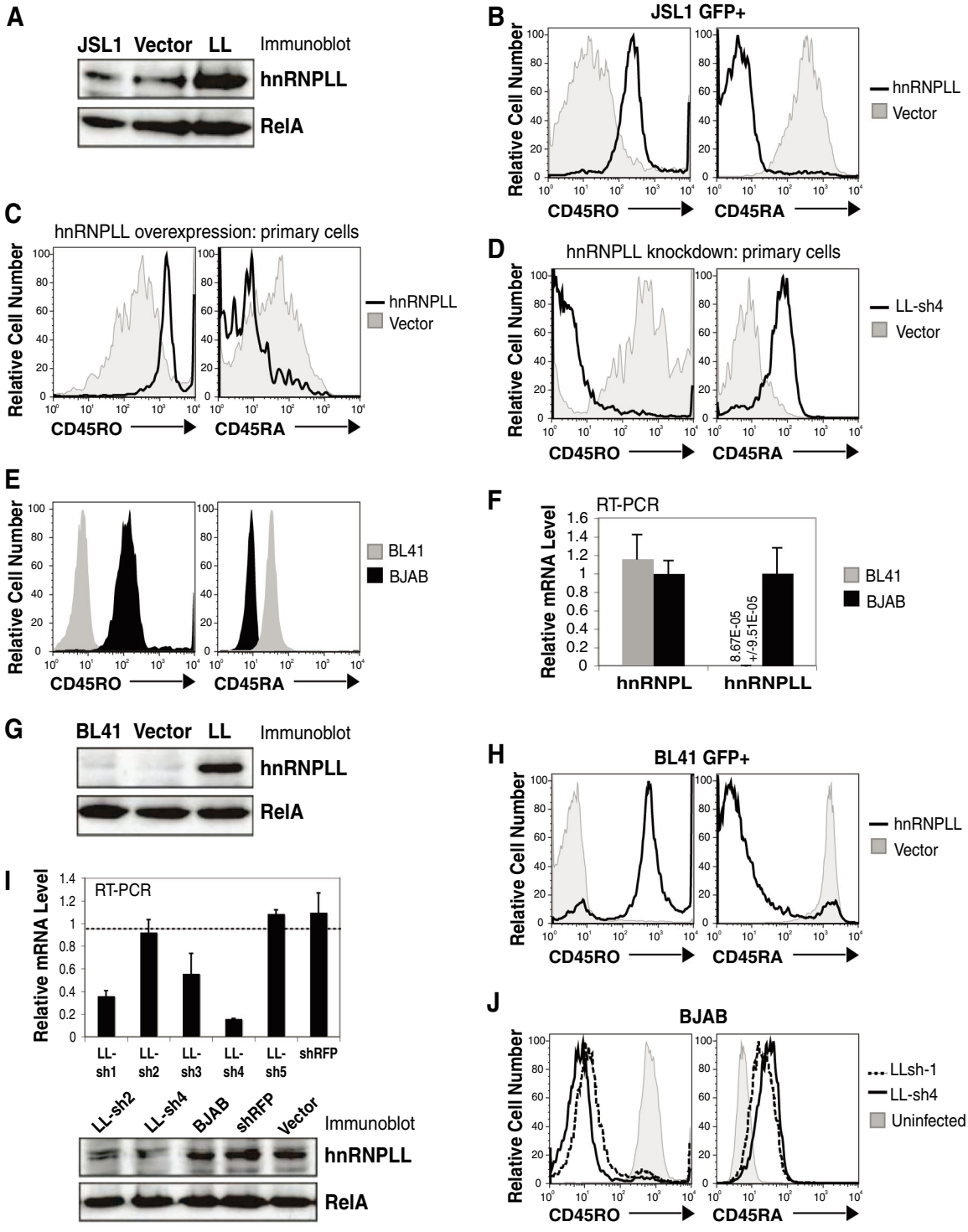

Fig. 2. Overexpression or knockdown of hnRNPLL influences CD45 alternative splicing. (**A**) Immunoblot for hnRNPLL expression in JSL1 cells retrovirally transduced with IRES-GFP hnRNPLL or empty vector. (**B**) HnRNPLL overexpression in GFP$^+$ JSL1 cells increased CD45RO and decreased CD45RA expression in the absence of stimulation. (**C**) Increased CD45RO expression and decreased CD45RA expression in GFP$^+$, hnRNPLL-transduced primary human CD4$^+$ T cells. (**D**) Reduced CD45RO expression and increased CD45RA expression in hnRNPLL-depleted primary CD4$^+$ T cells. (**E**) CD45 isoform expression in BJAB and BL41 B cell lines. (**F**) Detection of hnRNPLL transcripts in BJAB but not BL41 cells (value shown numerically) by quantitative RT-PCR. (**G**) Immunoblot for hnRNPLL expression in BL41 cells retrovirally transduced with IRES-GFP hnRNPLL or empty vector. (**H**) Increased CD45RO and decreased CD45RA expression in GFP$^+$ hnRNPLL-transduced BL41 cells. (**I**) Quantitative RT-PCR and immunoblot for hnRNPLL in knockdown BJAB cells. (**J**) Decreased CD45RO and increased CD45RA expression in LL-sh1 and LL-sh4 BJAB cells.

GFP expression (fig. S1). The entire population of hnRNPLL-expressing (GFP^+) cells up-regulated CD45RO, and CD45RA expression was eliminated (Fig. 2B). Thus, hnRNPLL expression is both necessary and sufficient for CD45 alternative splicing and CD45RO expression in JSL1 cells.

We next tested the ability of hnRNPLL to influence CD45 isoform expression in primary human $CD4^+$ T cells. Stimulated naïve $CD4^+$ T cells were infected with lentiviruses encoding IRES-GFP hnRNPLL (for overexpression) or LL-sh4 (for RNAi-mediated knockdown) and cultured in interleukin-2–containing medium for 5 to 7 days. As expected, mock-infected primary T cells up-regulated CD45RO and down-regulated CD45RA after activation, and this was also seen in hnRNPLL-expressing (GFP^+) T cells, but to a greater extent (Fig. 2C). In contrast, primary T cells depleted of hnRNPLL were 100% $CD45RO^-$ and $CD45RA^+$ (Fig. 2D).

Unlike T cells, which readily undergo CD45 alternative splicing upon activation, B cells are refractory to the CD45RA > RO switch, and PMA stimulation of B cell lines does not promote exon 4 to 6 exclusion and consequent CD45RO expression (*10*, *13*). Most B cell lines constitutively express high levels of the largest isoform, CD45RABC (B220) and do not express CD45RO (e.g., BL41) (Fig. 2E). While screening additional B cell lines for CD45 isoform expression, however, we found that BJAB B cells are 100% positive for CD45RO and do not express $CD45RA^+$ isoforms (Fig. 2E). HnRNPLL expression directly correlated with CD45 isoform expression in these two cell lines, with virtually undetectable CD45RO and hnRNPLL in BL41 cells (Fig. 2, E to G) and high levels of hnRNPLL and CD45RO in BJAB cells (Fig. 2, E, F, and I). Transcript levels of the paralog, hnRNPL, were similar in the two cell lines (Fig. 2F). When hnRNPLL was overexpressed in BL41 cells using an IRES-GFP lentiviral expression plasmid (Fig. 2G and fig. S1), a total population shift was seen, such that infected (GFP^+) cells uniformly expressed CD45RO and lost expression of $CD45RA^+$ isoforms (Fig. 2H). Conversely, depletion of hnRNPLL with LL-sh1 and LL-sh4 shRNAs in BJAB cells decreased hnRNPLL transcript and protein expression (Fig. 2I) and caused a total population shift of the infected cells to $CD45RO^{low}$ and $CD45RA^+$ (Fig. 2J). These data confirm an important role for hnRNPLL in CD45 alternative splicing in T cells and also in B cells.

The paralog of hnRNPLL, hnRNPL, was previously identified as binding to an exonic splicing silencer, ESS1, located in exon 4 of CD45 (*14*, *15*). However, it was not identified in our screen (fig. S2A), and we traced this to an inability to knock down hnRNPL protein expression effectively in JSL1 cells (fig. S2B). In BJAB cells however, L-sh2 substantially diminished hnRNPL expression (Fig. 3A, left), with no observable effect on CD45 isoform expression (Fig. 3B). Conversely, overexpression of hnRNPL, either in JSL1 or BL41 cells, had no effect on CD45 isoform expression (Fig. 3, C and D). Given the homology between hnRNPL and hnRNPLL (69% identity at the amino acid level) (*16*), we confirmed that hnRNPLL knockdown did not result in an "off-target" decrease in hnRNPL expression (fig. S2C).

We next used RNA-immunoprecipitation (RIP) (*17*) followed by quantitative reverse transcription polymerase chain reaction (RT-PCR) to test the association between hnRNPLL and CD45 transcripts. Because the only commercially available antibody directed against hnRNPLL is not suit-

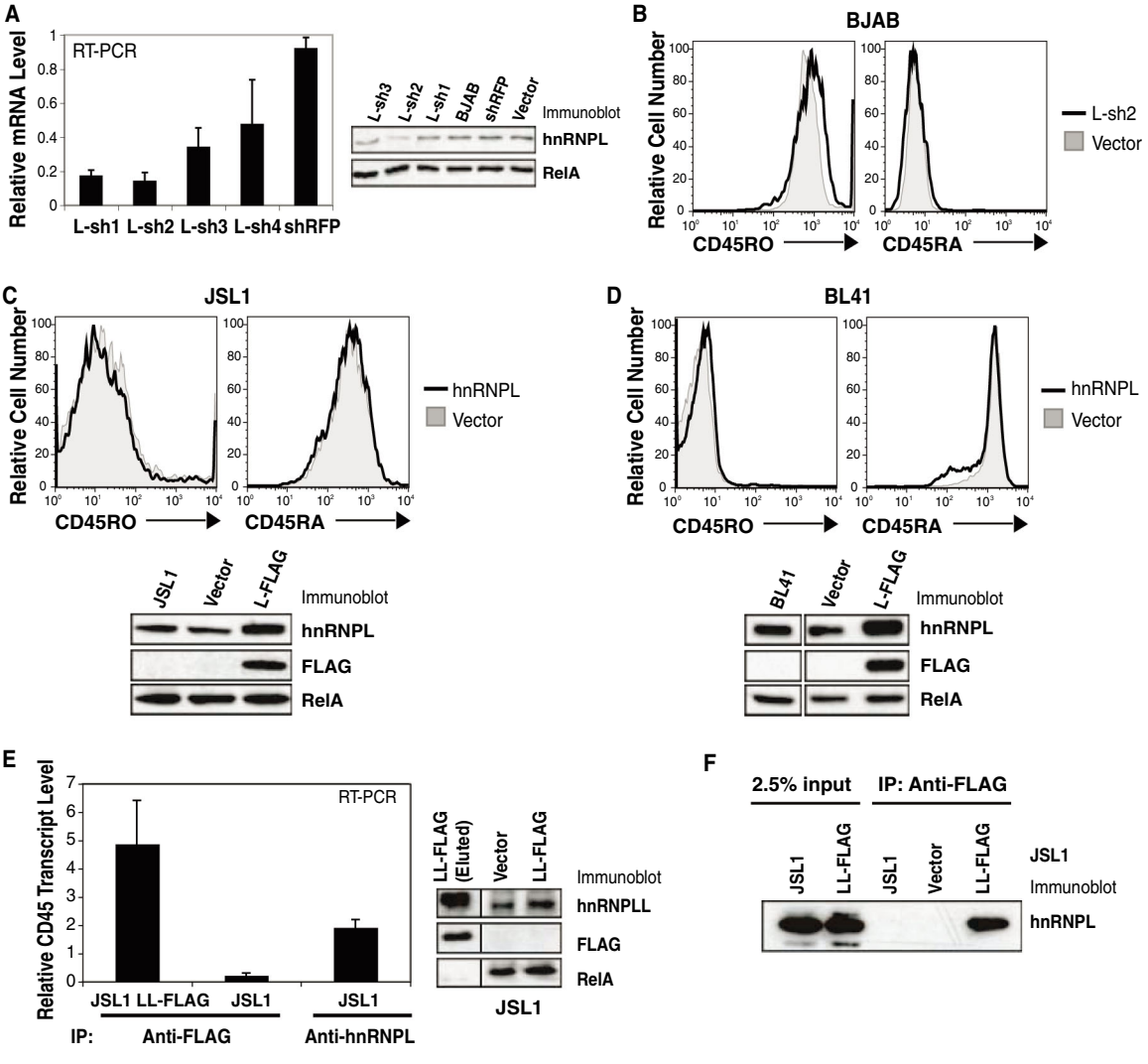

Fig. 3. Effect of hnRNPL on CD45 isoform expression. (**A**) Quantitative RT-PCR and immunoblot for hnRNPL in knockdown BJAB cells. (**B**) Cell-surface CD45 isoform expression was unaltered in L-sh2 BJAB cells. (**C**) JSL1 and (**D**) BL41 cells retrovirally transduced with FLAG-tagged hnRNPL (L-FLAG) were immunoblotted for hnRNPL and FLAG proteins. HnRNPL overexpression did not affect CD45 isoform expression. (**E**) FLAG-tagged hnRNPLL (LL-FLAG) or endogenous hnRNPL was immunoprecipitated from stably transduced or uninfected JSL1 cells with antibody to FLAG or antibody to hnRNPL (anti-L), respectively. Associated RNA was isolated, and quantitative RT-PCR was performed to detect CD45 transcripts. Immunoblot of LL-FLAG–transduced JSL1 cells indicated that hnRNPLL was not overexpressed relative to endogenous hnRNPLL. (**F**) Anti-FLAG immunoprecipitation from LL-FLAG–transduced JSL1 cells followed by immunoblotting for hnRNPL.

able for immunoprecipitation, FLAG-tagged hnRNPLL or empty vector were stably expressed in JSL1 cells. Cells overexpressing FLAG-hnRNPLL showed only a marginal increase in total hnRNPLL detected with an antibody to hnRNPLL (Fig. 3E, right). Moreover, FLAG-hnRNPLL could not be detected in lysates by immunoblotting with an antibody to FLAG, although it was detected upon loading high amounts of anti-FLAG immunoprecipitate (Fig. 3E and fig. S3C). Nevertheless, anti-FLAG immunoprecipitates from FLAG-hnRNPLL-expressing JSL1 cells showed enrichment of CD45 transcripts (exon 4 sequences) by a factor of 20 relative to vector-transduced cells (Fig. 3E). Based on CD45 transcript expression in 5% of the input fraction, we calculated that the FLAG-hnRNPLL immunoprecipitates bound ~0.25% of all CD45 transcripts in the lysates. By comparison, immunoprecipitates of endogenous hnRNPL from untransduced JSL1 cell lysates bound ~0.09% of all CD45 transcripts in the lysates (Fig. 3E) (*12*). We also found that endogenous hnRNPL robustly coimmunoprecipitated with FLAG-hnRNPLL (Fig. 3F), showing that the two proteins interact with each other and with CD45 transcripts.

Exon array analysis (*18*) was next used to test the possibility that hnRNPLL regulates a broader program of alternative splicing in activated T cells. A total of 132 genes, including CD45 (protein tyrosine phosphatase, receptor type C) itself (Fig. 4A), showed significant alternative exon usage ($P < 0.01$) in response to hnRNPLL knockdown, but not in response to shGFP infection (table S3). Of these, 36 genes showed significant alternative usage of corresponding exons in response to activation of cord blood cells (table S4), correlating with an increase in hnRNPLL expression by a factor of 5 in the activated cells. Expression of CD45 exons 4 and 6 was elevated in naïve cord blood and hnRNPLL-depleted peripheral T cells, relative to their expression in activated cord blood and peripheral T cells, respectively (Fig. 4A, left). Similarly, expression of CD44 exons 6 to 14, particularly exons 7 and 10, was increased in conditions lacking hnRNPLL (naïve or hnRNPLL-depleted cells) compared with activated cord blood and peripheral T cells (Fig. 4A, right) (*6*). Increased exon retention in response to hnRNPLL depletion was confirmed in peripheral T cells by RT-PCR for CD45 exon 4 and CD44 exon 10, as well as for STAT5A exon 5 (Fig. 4B). There is evidence for the existence of both latter transcripts (fig. S4B) (*19*). A complete analysis of alternative exon usage patterns and their potential functional consequences is being pursued.

Primary T cells lentivirally infected with LL-sh4 (shRNA directed against hnRNPLL) were consistently difficult to expand, in contrast to primary T cells infected with control shRNA directed against red fluorescent protein (RFP) (Fig. 4C). Moreover, these hnRNPLL-depleted T cells repeatedly showed reduced expression of CD25 compared with control shRFP-expressing cells (Fig. 4D). These data are consistent with our finding that hnRNPLL targets not only CD45 (Figs. 1 to 3 and Fig. 4A) but also STAT5A (Fig. 4B) and diverse other proteins involved in cell proliferation, activation, and cell death (tables S3 and S4).

Our data strongly suggest that hnRNPLL is a "master regulator" of alternative splicing in ac-

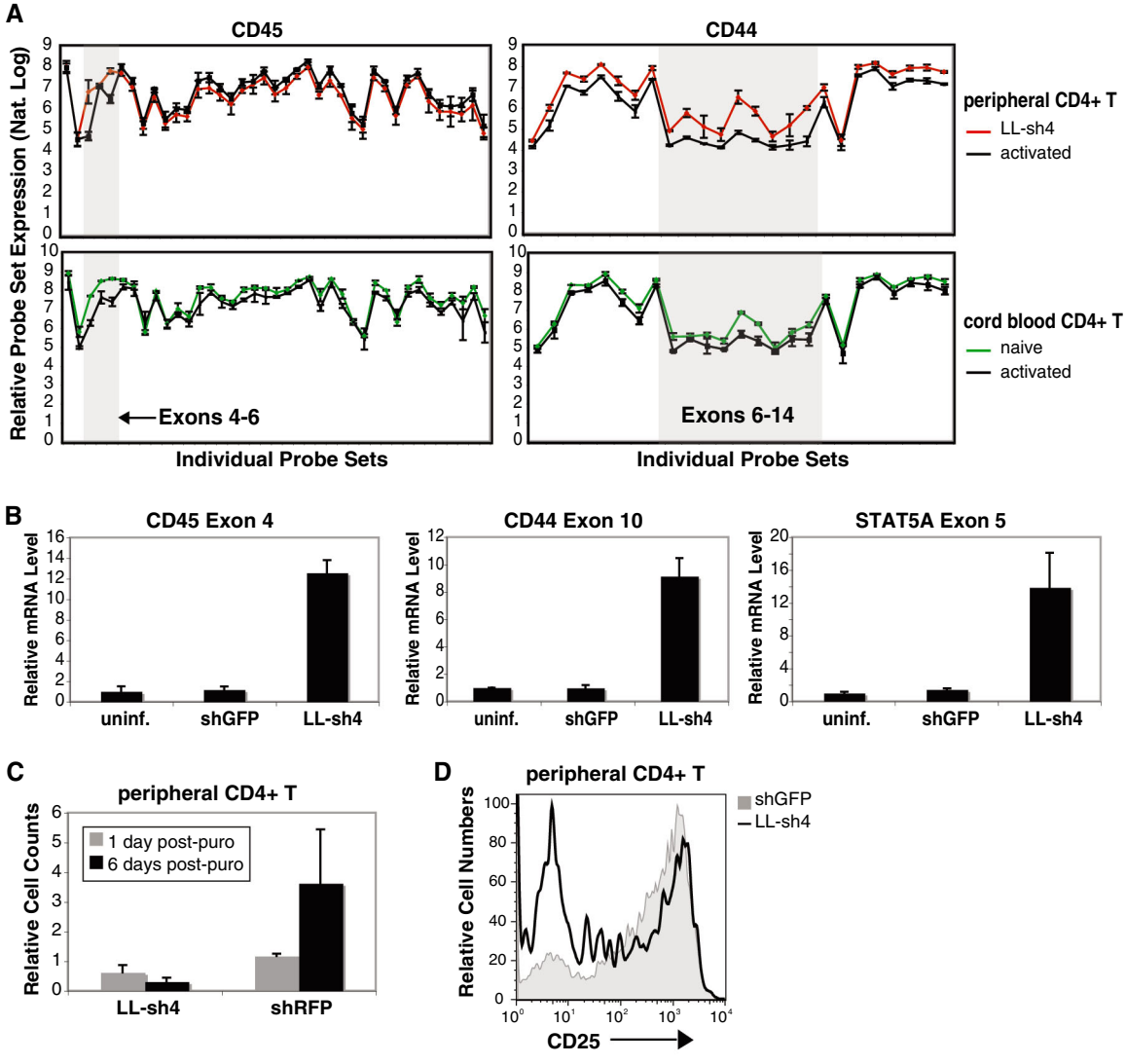

Fig. 4. HnRNPLL is a global regulator of alternative splicing in activated T cells. (**A**) Exon array analysis of RNA from activated peripheral $CD4^+$ T cells, LL-sh4–transduced peripheral $CD4^+$ T cells, naïve cord blood $CD4^+$ T cells, and activated cord blood $CD4^+$ T cells. As shown for CD45 and CD44 transcripts, low hnRNPLL expression (hnRNPLL knockdown or naïve cord blood) is associated with increased retention of select exons. (**B**) Quantitative RT-PCR for retained CD45, CD44, and STAT5A exons in hnRNPLL-depleted peripheral $CD4^+$ T cells. (**C**) HnRNPLL-depletion in peripheral $CD4^+$ T cells blocks proliferation. (**D**) Reduced CD25 expression in hnRNPLL-depleted peripheral $CD4^+$ T cells.

tivated T cells. HnRNPLL is induced upon T cell stimulation and as such is likely to correspond to the inducible, cycloheximide-sensitive factor postulated to promote the CD45RA > RO transition during T cell activation (*10*). Depletion of hnRNPLL causes an overall shift in patterns of alternative splicing, which by and large are in the opposite direction from those seen in activated T cells in which hnRNPLL expression is increased. Induction of hnRNPLL during the process of T cell activation and differentiation may represent a mechanism by which the cell can rapidly shift its transcriptome to favor proliferation and inhibit cell death.

There is increasing evidence that splicing and pre-mRNA processing involve multiprotein complexes in which individual components influence distinct aspects of transcript production (*20*, *21*). Several proteins, including hnRNPL, PSF (polypyrimidine tract binding protein–associated splicing factor), and hnRNPE2, have been shown to bind CD45 transcripts (*14*, *15*). However, none of these factors is induced upon T cell activation (*14*, *15*), and only PSF (splicing factor proline/glutamine-rich) was identified in our screen, albeit as a weak hit (table S2). Together with its associated factors, hnRNPL may influence diverse aspects of CD45 pre-mRNA processing, including basal splicing, mRNA stability, and export (*22*, *23*). After activation, hnRNPLL induction and recruitment to CD45 transcripts may then lead to the assembly of a high-affinity exon repression complex that mediates efficient CD45RO production as well as global changes in alternative splicing.

References and Notes

1. J. M. Johnson *et al.*, *Science* **302**, 2141 (2003).
2. B. Modrek, C. Lee, *Nat. Genet.* **30**, 13 (2002).
3. D. L. Black, *Annu. Rev. Biochem.* **72**, 291 (2003).
4. A. J. Matlin, F. Clark, C. W. Smith, *Nat. Rev. Mol. Cell Biol.* **6**, 386 (2005).
5. M. L. Hermiston, Z. Xu, A. Weiss, *Annu. Rev. Immunol.* **21**, 107 (2003).
6. K. W. Lynch, *Nat. Rev. Immunol.* **4**, 931 (2004).
7. R. J. Salmond, L. McNeill, N. Holmes, D. R. Alexander, *Int. Immunol.* **20**, 819 (2008).
8. N. Holmes, *Immunology* **117**, 145 (2006).
9. L. McNeill *et al.*, *Immunity* **27**, 425 (2007).
10. K. W. Lynch, A. Weiss, *Mol. Cell. Biol.* **20**, 70 (2000).
11. J. Moffat *et al.*, *Cell* **124**, 1283 (2006).
12. Materials and methods are available as supporting material on *Science* Online.
13. I. S. Trowbridge, M. L. Thomas, *Annu. Rev. Immunol.* **12**, 85 (1994).
14. C. R. Rothrock, A. E. House, K. W. Lynch, *EMBO J.* **24**, 2792 (2005).
15. A. A. Melton, J. Jackson, J. Wang, K. W. Lynch, *Mol. Cell. Biol.* **27**, 6972 (2007).
16. I. Shur, D. Ben-Avraham, D. Benayahu, *Gene* **334**, 113 (2004).
17. S. A. Tenenbaum, P. J. Lager, C. C. Carson, J. D. Keene, *Methods* **26**, 191 (2002).
18. M. J. Moore, P. A. Silver, *RNA* **14**, 197 (2008).
19. National Center for Biotechnology Information Database; www.ncbi.nlm.nih.gov/sites/entrez?db=gene
20. X. M. Ma, S. O. Yoon, C. J. Richardson, K. Julich, J. Blenis, *Cell* **133**, 303 (2008).
21. P. Valencia, A. P. Dias, R. Reed, *Proc. Natl. Acad. Sci. U.S.A.* **105**, 3386 (2008).
22. S. Guang, A. M. Felthauser, J. E. Mertz, *Mol. Cell. Biol.* **25**, 6303 (2005).
23. L. H. Hung *et al.*, *RNA* **14**, 284 (2008).

24. We thank A. Weiss for the JSL1 cell line, E. Kieff for BJAB and BL41 cells, B. North for the lentiviral expression plasmid, and the RNAi Consortium at the Broad Institute for providing the plasmids to produce the splicing factor library. We thank C. Moita for assistance in assembling the library and A. Astier and D. Hafler for aid in developing the protocol for infecting and silencing genes in primary human T cells. We thank K. Eger and D. Unutmaz for the naïve and activated cord blood samples. We thank J. Burke at Biotique for assistance with the array analysis. This work was supported by NIH grants CA42471, AI40127, and AI44432 to A.R., and U19 AI070352, R21 AI071060, and Defense Advanced Research Projects Agency grant W81XWH-04-C-0139 to N.H. S.O. is supported by postdoctoral training grant T32 HL066987 from the Joint Program in Transfusion Biology and Medicine, Children's Hospital, Boston.

Supporting Online Material

www.sciencemag.org/cgi/content/full/1157610/DC1
Materials and Methods
SOM Text
Figs. S1 to S4
Tables S1 to S4
References

11 March 2008; accepted 20 June 2008
Published online 10 July 2008;
10.1126/science.1157610
Include this information when citing this paper.

Pyogenic Bacterial Infections in Humans with MyD88 Deficiency

Horst von Bernuth,[1,2] Capucine Picard,[1,2,3] Zhongbo Jin,[4,5] Rungnapa Pankla,[4,6] Hui Xiao,[7] Cheng-Lung Ku,[1,2] Maya Chrabieh,[1,2] Imen Ben Mustapha,[1,2,8] Pegah Ghandil,[1,2] Yildiz Camcioglu,[9] Júlia Vasconcelos,[10] Nicolas Sirvent,[11] Margarida Guedes,[10] Artur Bonito Vitor,[12] María José Herrero-Mata,[13] Juan Ignacio Aróstegui,[14] Carlos Rodrigo,[15] Laia Alsina,[16] Estibaliz Ruiz-Ortiz,[13] Manel Juan,[14] Claudia Fortuny,[16] Jordi Yagüe,[14] Jordi Antón ,[16] Mariona Pascal,[14] Huey-Hsuan Chang,[17] Lucile Janniere,[1,2] Yoann Rose,[1,2] Ben-Zion Garty,[18] Helen Chapel,[19] Andrew Issekutz,[20] László Maródi,[21] Carlos Rodriguez-Gallego,[22] Jacques Banchereau,[4] Laurent Abel,[1,2] Xiaoxia Li,[7] Damien Chaussabel,[4] Anne Puel,[1,2] Jean-Laurent Casanova[1,2,23]*

MyD88 is a key downstream adapter for most Toll-like receptors (TLRs) and interleukin-1 receptors (IL-1Rs). MyD88 deficiency in mice leads to susceptibility to a broad range of pathogens in experimental settings of infection. We describe a distinct situation in a natural setting of human infection. Nine children with autosomal recessive MyD88 deficiency suffered from life-threatening, often recurrent pyogenic bacterial infections, including invasive pneumococcal disease. However, these patients were otherwise healthy, with normal resistance to other microbes. Their clinical status improved with age, but not due to any cellular leakiness in MyD88 deficiency. The MyD88-dependent TLRs and IL-1Rs are therefore essential for protective immunity to a small number of pyogenic bacteria, but redundant for host defense to most natural infections.

The search for human genetic etiologies of pediatric infectious diseases aims to decipher the molecular mechanism of disease and to reveal the function of immune genes *in natura* (*1*). The immunological investigation of children with invasive pneumococcal disease (IPD) led to the discovery of children lacking interleukin-1 receptor–associated kinase 4 (IRAK-4), which is selectively recruited to Toll-like receptors (TLRs) and interleukin-1 receptors (IL-1Rs) by MyD88 (*2*). The patients present with a life-threatening but narrow and transient predisposition to infection, apparently restricted to pyogenic bacterial diseases, particularly IPD, during the first 10 years of life (*3*). This clinical phenotype is surprising given the central role commonly attributed to both TLRs and IL-1Rs, and the high susceptibility of MyD88-deficient mice to experimental infections with at least 35 pathogens—19 bacteria, seven viruses, five parasites, and four fungi (*4*) (tables S1 to S3). However, IRAK-4–deficient mice have thus far been challenged with only a few pathogens (*5*). Fibro-

[1]Human Genetics of Infectious Diseases, INSERM U550, Paris, France. [2]Paris Descartes University, France. [3]Study Center of Primary Immunodeficiencies, Assistance Publique Hôpitaux de Paris, Necker Hospital, Paris, France. [4]Baylor Institute for Immunology Research, Dallas, TX 75204, USA. [5]Baylor University, Waco, TX 76798, USA. [6]Khon Kaen University, Thailand. [7]Cleveland Clinic Foundation, OH 44195, USA. [8]Pasteur Institute of Tunis, Tunisia. [9]Cerrahpasa Medical School, Istanbul University, Turkey. [10]General Hospital of Santo António, Porto, Portugal. [11]University Hospital Archet 2, Nice, France. [12]Hospital S.João, Porto, Portugal. [13]LIRAD–Banco de Sangre y Tejidos, Instituto de Investigación Germans Trias i Pujol, Badalona, Barcelona, Spain. [14]Immunology Department, Hospital Clinic, IDIBAPS, Barcelona, Spain. [15]Germans Trias i Pujol Hospital, Barcelona Autonomous University, Spain. [16]Sant Joan de Déu Hospital, Barcelona University, Spain. [17]Dendritic Cell Immunobiology, Institut Pasteur and INSERM U818, Paris, France. [18]Schneider Children's Medical Center, Petah Tiqva, Israel. [19]University of Oxford and Oxford Radcliffe Hospital, Oxford, UK. [20]Dalhousie University, Halifax, Nova Scotia, Canada. [21]Debrecen University, Hungary. [22]Gran Canaria Dr Negrin Hospital, Las Palmas de Gran Canaria, Spain. [23]Pediatric Hematology-Immunology Unit, Necker Hospital, Paris, France.

*To whom correspondence should be addressed. E-mail: jean-laurent.casanova@inserm.fr

blasts and individual leukocyte subsets from IRAK-4–deficient patients fail to respond to the TLR agonists tested, at least for the orthologs of the mouse MyD88-dependent target genes tested (*3*, *6*). The resistance of IRAK-4–deficient patients might thus be explained by IRAK-4–independent but MyD88-dependent TLR or IL-1R responses in other cell types and/or for other target genes.

We investigated nine children (P1 to P9) with invasive pyogenic bacterial diseases and without IRAK-4 deficiency, from five unrelated kindreds (supplementary note 1). Three children died between 1 and 11 months of age and six are now between 3 and 16 years old. A homozygous in-frame *MYD88* deletion was found in P1, P6, P8, and P9 (160del3, designated E52del), compound heterozygous missense mutations in P2 (278 T→C, L93P; 586 C→T, R196C), and a homozygous missense mutation in P3 and P4 (586 C→T, R196C) (Fig. 1, A and B, and fig. S1). The deletion and missense mutations were not found in 100 and 1728 healthy individuals, respectively. These mutations are nonconservative and affect residues conserved across species (Fig. 1C). Residues 195 to 197 are crucial for Toll/IL-1 receptor (TIR)/TIR interaction (*7*). The segregation of the *MYD88* genotype and of the clinical phenotype is consistent with an autosomal recessive trait (supplementary note 1, Fig. 1A, and figs. S2 to S5). The *MYD88* mRNA in fibroblasts from patients P1 to P4 (representing the three combinations of alleles) was of normal molecular weight and abundance (Fig. 1D and fig. S6). MyD88 protein was detected in SV40-transformed fibroblasts in trace amounts for P1, small amounts for P2, and normal amounts for P3 and P4, as shown by Western blotting (Fig. 1E). These data suggest that our patients have functional MyD88 deficiency, with low (P1 and P2, P5 to P9) or normal (P3 and P4) MyD88 protein levels.

The functional impact of the MyD88 mutations was then tested in cell lines derived from the patients. As in IRAK-4–deficient cells (*2*, *3*, *6*), IRAK-1 was not degraded in the patients' SV40-transformed fibroblasts up to 6 hours after stimulation with IL-1β (Fig. 2, A and D). Similarly, IRAK-1 was not degraded in the patients' Epstein-Barr virus–transformed B (EBV-B) cells up to 2 hours after stimulation with the TLR7/TLR8 agonist R-848 (fig. S7, A and B). Phosphorylation of the mitogen-activated protein kinases (MAPKs) p38 and c-Jun N-terminal kinase (JNK) and the DNA binding activity of nuclear factor κB (NF-κB) were impaired in the patients' SV40-transformed fibroblasts after stimulation with IL-1β (Fig. 2, B and C). Furthermore, the patients' EBV-B cells showed a complete lack of response to stimulation with R-848 for 24 hours, in terms of tumor necrosis factor–α (TNF-α) induction (fig. S7C). Similarly, the production of IL-6, IL-8, interferon-β (IFN-β), and IFN-λ was abolished after 24 hours of incubation of the patients' SV40-transformed fibroblasts with IL-1β, although these cells responded normally to TNF-α and poly(I:C), a TLR3-dependent agonist in human fibroblasts (*8*) (Fig. 2, E to H). Thus, two cell types derived from our patients carrying two mutant *MYD88* alleles, with normal (P3 and P4) or impaired (P1 and P2) MyD88 protein production, showed a selective failure to respond to the stimulation of two key IRAK-4–dependent signaling pathways (TLR7/8 and IL-1R). This uniform cellular phenotype suggests that each of the patients presents an autosomal recessive, functionally complete deficiency in MyD88.

Fibroblasts from a healthy control and from P1 and P2 (representing the three mutant alleles) and from an IRAK-4–deficient child were transiently transfected with expression vectors encoding wild-type (WT) MyD88 or IRAK-4. Cells from P1 and P2 regained IL-1β responsiveness after transfection with the WT *MYD88* gene only, as shown by the levels of IL-8 production (Fig. 2I). IRAK-4–deficient cells, used as a control, were complemented with WT *IRAK4* only (Fig. 2I). The human embryonic kidney (HEK) 293–

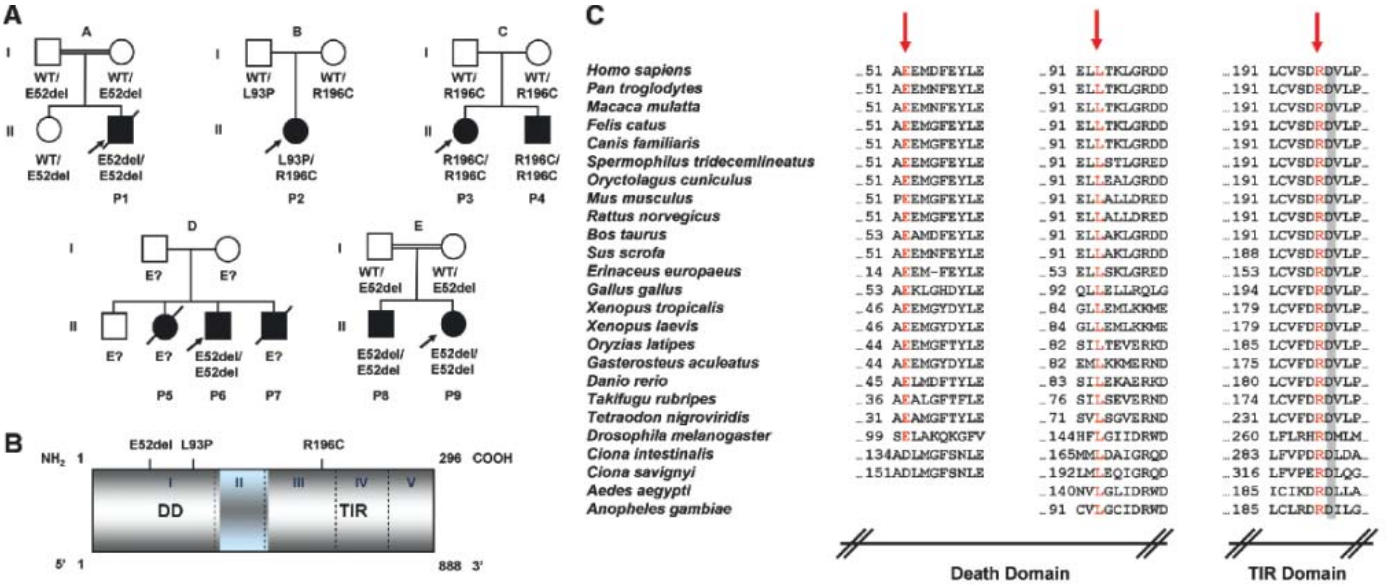

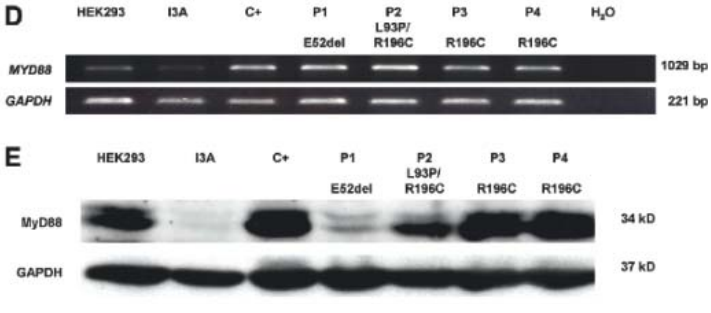

Fig. 1. (**A**) Kindreds and patients with *MYD88* mutations. (**B**) Positions of the MyD88 mutations in the death domain (DD) or the TIR domain of the protein. (**C**) Parts of the DD and TIR domain of MyD88 in humans and the corresponding regions in 24 other species. The residues mutated are indicated in red. Amino acid D197 (gray) is conserved in all species. (**D**) Full-length *MYD88* transcripts in SV40-transformed fibroblasts from a healthy control donor (C+), four MyD88-deficient patients (P1 to P4), the MyD88-deficient HEK293 cell line (I3A), and the parental MyD88-positive HEK293 cell line. (**E**) MyD88 protein expression in SV40-transformed fibroblasts from a healthy control (C+), four patients (P1 to P4), the I3A line, and the parental HEK293 cell line. The MyD88-specific antibody recognizes residues 279 to 296. Abbreviations for the amino acid residues are as follows: A, Ala; C, Cys; D, Asp; E, Glu; F, Phe; G, Gly; H, His; I, Ile; K, Lys; L, Leu; M, Met; N, Asn; P, Pro; Q, Gln; R, Arg; S, Ser; T, Thr; V, Val; W, Trp; and Y, Tyr.

derived MyD88-deficient I3A cell line (*9*) was then transiently transfected with WT, E52del, L93P, and R196C *MYD88* alleles. All of the *MYD88* alleles used for transfection were expressed, as shown by reverse transcription–polymerase chain reaction (RT-PCR) and Western blotting (Fig. 2J and fig. S8). I3A cells responded to IL-1β after transfection with the WT *MYD88* allele, but not after transfection with any of the three mutant *MYD88* alleles, as shown by IL-8 production levels (Fig. 2J). These analyses confirmed that all three *MYD88* mutant alleles were loss-of-function. Finally, immunoprecipitation and Western blotting experiments showed that the R196C mutation in the TIR domain prevents interaction with IL-1R, whereas the E52del and L93P mutations in the death domain (DD) prevent interaction with IRAK-4 (Fig. 2K). These results demonstrate that all nine patients had complete MyD88 deficiency, resulting from the inheritance of two loss-of-function *MYD88* alleles.

We then investigated the potential effect of MyD88 deficiency on blood TLR and IL-1R re-

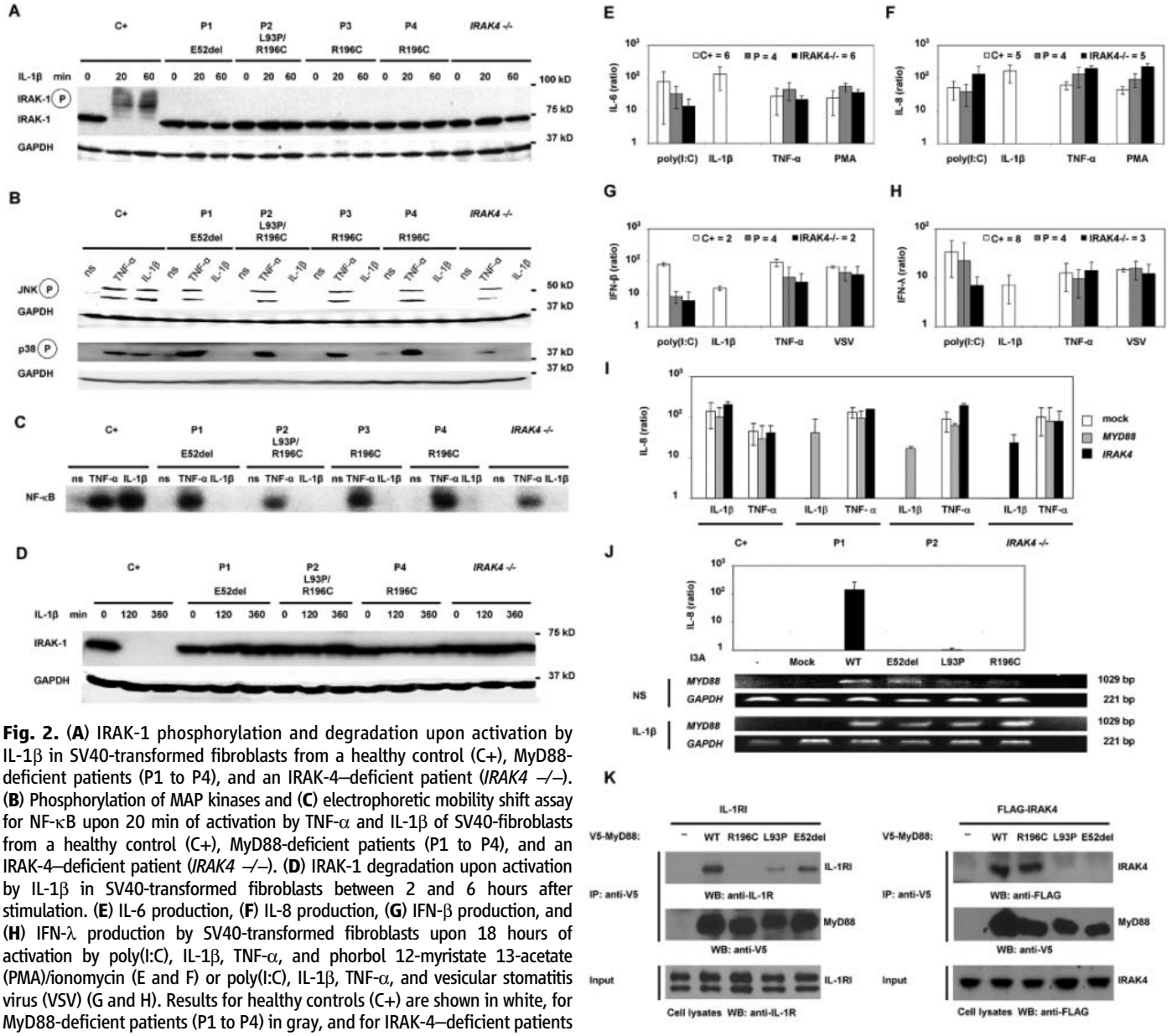

Fig. 2. (**A**) IRAK-1 phosphorylation and degradation upon activation by IL-1β in SV40-transformed fibroblasts from a healthy control (C+), MyD88-deficient patients (P1 to P4), and an IRAK-4–deficient patient (*IRAK4 –/–*). (**B**) Phosphorylation of MAP kinases and (**C**) electrophoretic mobility shift assay for NF-κB upon 20 min of activation by TNF-α and IL-1β of SV40-fibroblasts from a healthy control (C+), MyD88-deficient patients (P1 to P4), and an IRAK-4–deficient patient (*IRAK4 –/–*). (**D**) IRAK-1 degradation upon activation by IL-1β in SV40-transformed fibroblasts between 2 and 6 hours after stimulation. (**E**) IL-6 production, (**F**) IL-8 production, (**G**) IFN-β production, and (**H**) IFN-λ production by SV40-transformed fibroblasts upon 18 hours of activation by poly(I:C), IL-1β, TNF-α, and phorbol 12-myristate 13-acetate (PMA)/ionomycin (E and F) or poly(I:C), IL-1β, TNF-α, and vesicular stomatitis virus (VSV) (G and H). Results for healthy controls (C+) are shown in white, for MyD88-deficient patients (P1 to P4) in gray, and for IRAK-4–deficient patients (*IRAK4 –/–*) in black (numbers of individuals tested are indicated next to these boxes). Cytokine production is presented as the ratio of cytokine production by stimulated cells to that by nonstimulated cells. (**I**) IL-8 production upon activation of SV40-transformed fibroblasts from healthy donors (C+), MyD88-deficient patients (P1 and P2), and an IRAK-4–deficient patient (*IRAK4 –/–*) after transfection with the pUNO empty plasmid (white), wild-type pUNO-MyD88 (gray), and wild-type pcDNA3–IRAK-4 (black). Cells were also transfected with the pcDNA3 empty plasmid, giving results similar to those of the pUNO empty plasmid (not shown). (**J**) IL-8 production upon activation of I3A cells (MyD88-deficient HEK293 cells) without transfection and after transfection with pcDNA3.2 empty plasmid (mock), or pcDNA3.2 encoding V5-tagged wild-type *MYD88*, V5-tagged *MYD88-E52del*, V5-tagged *MYD88-L93P*, and V5-tagged *MYD88-R196C*. RT-PCR in nonactivated (NS) and activated I3A cells (IL-1β) served to check that the cells were correctly transfected with *MYD88*. Western blotting for the V5 tag was also done (fig. S8). (**K**) Coimmunoprecipitation in I3A cells, transfected with expression vectors encoding V5-tagged MyD88 and FLAG-tagged IRAK-4. Immunoprecipitation was carried out with V5- or FLAG-specific antibodies and Western blotting with V5-, FLAG-, or IL-1R–specific antibodies. Coimmunoprecipitation of IL-1R1 with the MyD88 mutants (left panel). MyD88-L93P and MyD88-E52del (in the DD) interact weakly with IL-1R1, whereas MyD88-R196C (in the TIR domain) cannot associate with IL-1R. Coimmunoprecipitation of IRAK-4 with MyD88 mutants (right panel). MyD88-L93P and MyD88-E52del cannot interact with IRAK-4, whereas MyD88-R196C still associates with IRAK-4.

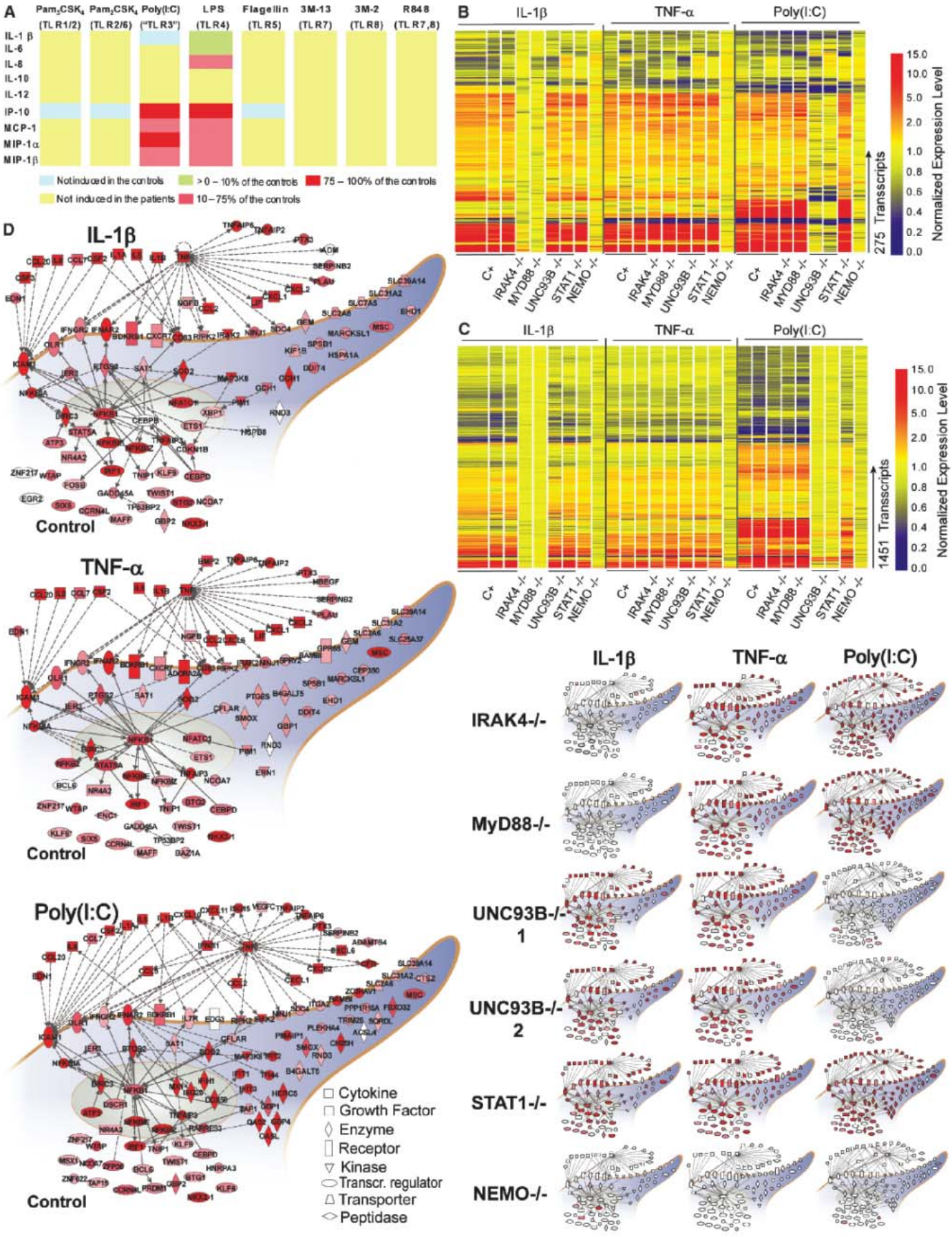
A
Pam3CSK4 (TLR1/2)
Pam3CSK4 (TLR2/6)
Poly(I:C) ("TLR3")
LPS (TLR4)
Flagellin (TLR5)
3M-13 (TLR7)
3M-2 (TLR8)
R848 (TLR7,8)
IL-1 β
IL-6
IL-8
IL-10
IL-12
IP-10
MCP-1
MIP-1α
MIP-1β
Not induced in the controls
> 0 – 10% of the controls
75 – 100% of the controls
Not induced in the patients
10 – 75% of the controls
B
IL-1β
TNF-α
Poly(I:C)
275 Transcripts
Normalized Expression Level
15.0
10.0
5.0
2.0
1.0
0.8
0.6
0.4
0.2
0.0
C+
IRAK4 -/-
MYD88 -/-
UNC93B -/-
STAT1 -/-
NEMO -/-
C
IL-1β
TNF-α
Poly(I:C)
1451 Transcripts
Normalized Expression Level
D
IL-1β
Control
TNF-α
Control
Poly(I:C)
Control
Cytokine
Growth Factor
Enzyme
Receptor
Kinase
Transcr. regulator
Transporter
Peptidase
IL-1β
TNF-α
Poly(I:C)
IRAK4-/-
MyD88-/-
UNC93B-/- 1
UNC93B-/- 2
STAT1-/-
NEMO-/-

Fig. 3. (**A**) Multiple cytokine secretion by whole-blood cells from three healthy donors and three MyD88-deficient patients (P2, P3, and P4), activated by incubation with various TLR agonists for 24 hours. Cytokine levels are presented as ratios of secretion by cells from MyD88-deficient patients to secretion by cells from the healthy control. (**B**) Transcriptional profiles of fibroblasts from healthy controls and patients stimulated with IL-1β, TNF-α, and poly(I:C) for 2 hours. Transcriptional signature of 275 genes differentially regulated upon stimulation with IL-1β, TNF-α, or poly(I:C) in at least two of three control fibroblast lines. Genes were arranged by hierarchical clustering and, for each donor, changes in expression with respect to the corresponding untreated conditions are represented on a heat map. Red indicates a relative increase in expression levels, blue indicates a relative decrease, and yellow indicates no change in expression level. Samples are grouped by stimulus and ordered by donor: controls (1 to 3), IRAK-4–deficient patient (*3*), MyD88-deficient patient, UNC-93B–deficient patients (1 and 2) (*11*), STAT1-deficient patient (*12*), and NEMO-deficient patient (*10*). (**C**) Transcriptional profiles of fibroblasts stimulated with IL-1β, TNF-α, and poly(IC) for 8 hours. Transcriptional signature of 1451 genes differentially regulated upon stimulation with IL-1β, TNF-α, or poly(IC) in at least two of three control fibroblast lines. (**D**) Functional pathways regulated in fibroblasts treated with IL-1β, TNF-α, or poly(IC) for 2 hours. Genes or gene products regulated by these factors are represented as nodes, and the biological relation between two nodes is represented as an edge (line). Solid and dashed lines indicate direct and indirect relations, respectively. All edges are supported by at least one reference from the literature. Nodes are arranged according to the cellular distribution of the corresponding gene products. Expression levels of individual genes are represented on a color scale on the main network: white denotes <1.5-fold difference from nonstimulated conditions; solid red denotes >5-fold difference from nonstimulated conditions. The main network indicates the average expression level for the three control cell lines. The scaled-down networks indicate the levels of expression obtained for cells derived from patients.

sponses. IL-6 production in peripheral blood mononuclear cells (PBMCs) after stimulation with agonists of TLR4, TLR7 and TLR8 (P1), and in whole blood after stimulation with agonists of IL-1R and TLR4 (P2, P3, and P4) was abolished (figs. S2 and S3). The shedding of CD62L by granulocytes normally seen in response to TLR1/2, TLR4, TLR7, and TLR8 stimulation was also impaired (figs. S4 and S5). Whole blood from P2, P3, and P4 was then stimulated with a broad range of TLR agonists, and cytokine secretion was measured by means of a multiplex cytometry-based system. Whole blood from MyD88-deficient patients showed no cytokine response to six of the eight TLR agonists tested, for any of the nine cytokines induced in controls by at least one TLR (Fig. 3A). After activation with poly(I:C), whole-blood cells from the patients displayed the induction of several cytokines to levels similar to those in healthy control cells, but no production of IL-6 and IL-8 was observed. After activation with lipopolysaccharide (LPS), whole-blood cells from the patients displayed normal induction of a smaller number of cytokines, including IP10. These data are similar to those previously reported for IRAK-4–deficient PBMCs (*3*, *6*). Thus, MyD88 deficiency generally abolishes cytokine responses to the TLR stimulation of blood cells, although most cytokines were produced after poly(I:C) treatment [possibly via receptors other than TLR3 (*8*)] and some were produced in response to LPS.

We investigated whether residual, MyD88-independent signaling occurred by evaluating the IL-1R pathway of MyD88-deficient patients in more detail, through the analysis of genome-wide transcriptional profiles (48,701 probes) in fibroblasts. In control fibroblasts, 275 transcripts were regulated by IL-1β, TNF-α, or poly(I:C) after 2 hours of culture and 1451 transcripts were regulated after 8 hours (tables S4 to S8). The prototypic signatures in cell lines derived from patients were as follows: NEMO-deficient cells (*10*) were unresponsive to all three stimuli, UNC-93B–deficient cells (*11*) did not respond to poly(I:C), and signal transducers and activators of transcription 1 (STAT1)–deficient cells (*12*) responded only weakly to poly(I:C) after 8 hours (Fig. 3, B and C). MyD88- and IRAK-4–deficient cells had indistinguishable phenotypes, as both were unresponsive to IL-1β at both time points. The signatures obtained in response to TNF-α and poly(I:C) [via TLR3 (*8*)] in these cells were similar to that of control fibroblasts (Fig. 3, B and C, and supplementary note 2). We then focused on the functional pathways regulated by IL-1β, TNF-α, and poly(I:C) in control fibroblasts and in fibroblasts derived from patients. Control fibroblasts treated with IL-1β responded by a rapid increase in production of inflammatory cytokines and chemokines (including TNF-α, IL-1β, IL-6, and IL-8) and cell surface receptors (including ICAM1, OLR1, IFN-γR2, and IFN-αR2) (Fig. 3D). Differences in the activation status of the IL-1β, TNF-α, and poly(I:C) functional networks among fibroblasts derived from patients clearly identified a complete, specific lack of response to IL-1β as a defining characteristic of IRAK-4 and MyD88 deficiencies (Fig. 3D).

We thus report nine children with inherited MyD88 deficiency. The immunological phenotype is similar to that of MyD88-deficient mice (tables S9 and S10) (*13*–*15*), but the infectious phenotype is different. Like MyD88-deficient mice, the patients are vulnerable to *Streptococcus pneumoniae* (*16*, *17*), *Staphylococcus aureus* (*18*, *19*), and *Pseudomonas aeruginosa* (*20*–*23*). However, the nine MyD88-deficient patients were normally resistant to most common bacteria, viruses, fungi, and parasites (supplementary note 1 and tables S10 and S11). By contrast, MyD88-deficient mice are vulnerable to almost all pathogens tested (at least 35 microbes, tables S1 to S3). Because MyD88- and IRAK-4–deficient patients have indistinguishable cellular phenotypes, the clinical phenotype of the 32 known IRAK-4–deficient patients may be taken into account when comparing mice and humans. The broad vulnerability of MyD88-deficient mice to experimental infections suggested that TLRs were the principal pathogen-associated molecular pattern receptors (*24*) or the principal microbial sensors (*25*) of innate immunity in vivo. The natural history of 41 patients with MyD88 or IRAK-4 deficiency suggests that the MyD88- and IRAK-4–dependent TLRs (and IL-1Rs) play a narrow, nonredundant role in protective immunity *in natura* (*1*, *26*). Although narrow, this role is vital early in life, because all affected children would probably have died before the advent of antibiotics. TIR signaling seems to be less important for survival later in life (supplementary note 1) (*3*). This may be due to the compensatory effect of adaptive immunity (*27*, *28*) and/or the maturation of TIR-independent innate immunity (*29*, *30*).

References and Notes

1. J. L. Casanova, L. Abel, *Science* **317**, 617 (2007).
2. C. Picard *et al.*, *Science* **299**, 2076 (2003).
3. C. L. Ku *et al.*, *J. Exp. Med.* **204**, 2407 (2007).
4. Supporting material is available on *Science* Online.
5. N. Suzuki *et al.*, *Nature* **416**, 750 (2002).
6. K. Yang *et al.*, *Immunity* **23**, 465 (2005).
7. C. Li, J. Zienkiewicz, J. Hawiger, *J. Biol. Chem.* **280**, 26152 (2005).
8. S. Y. Zhang *et al.*, *Science* **317**, 1522 (2007).
9. Z. Jiang, T. W. Mak, G. Sen, X. Li, *Proc. Natl. Acad. Sci. U.S.A.* **101**, 3533 (2004).
10. A. Smahi *et al.*, *Nature* **405**, 466 (2000).
11. A. Casrouge *et al.*, *Science* **314**, 308 (2006).
12. A. Chapgier *et al.*, *J. Immunol.* **176**, 5078 (2006).
13. O. Adachi *et al.*, *Immunity* **9**, 143 (1998).
14. T. Kawai, O. Adachi, T. Ogawa, K. Takeda, S. Akira, *Immunity* **11**, 115 (1999).
15. K. Hoebe *et al.*, *Nature* **424**, 743 (2003).
16. B. Albiger *et al.*, *Cell. Microbiol.* **7**, 1603 (2005).
17. A. Q. Khan, Q. Chen, Z. Q. Wu, J. C. Paton, C. M. Snapper, *Infect. Immun.* **73**, 298 (2005).
18. L. S. Miller *et al.*, *Immunity* **24**, 79 (2006).
19. O. Takeuchi, K. Hoshino, S. Akira, *J. Immunol.* **165**, 5392 (2000).
20. M. R. Power, Y. Peng, E. Maydanski, J. S. Marshall, T. J. Lin, *J. Biol. Chem.* **279**, 49315 (2004).
21. M. R. Power, J. S. Marshall, M. Yamamoto, S. Akira, T. J. Lin, *Clin. Exp. Immunol.* **146**, 323 (2006).
22. S. J. Skerrett, H. D. Liggitt, A. M. Hajjar, C. B. Wilson, *J. Immunol.* **172**, 3377 (2004).
23. S. J. Skerrett, C. B. Wilson, H. D. Liggitt, A. M. Hajjar, *Am. J. Physiol. Lung Cell. Mol. Physiol.* **292**, L312 (2007).
24. C. A. Janeway Jr., R. Medzhitov, *Annu. Rev. Immunol.* **20**, 197 (2002).
25. B. Beutler *et al.*, *Annu. Rev. Immunol.* **24**, 353 (2006).
26. L. Quintana-Murci, A. Alcais, L. Abel, J. L. Casanova, *Nat. Immunol.* **8**, 1165 (2007).
27. A. L. Gavin *et al.*, *Science* **314**, 1936 (2006).
28. A. Meyer-Bahlburg, S. Khim, D. J. Rawlings, *J. Exp. Med.* **204**, 3095 (2007).
29. M. S. Hirsch, B. Zisman, A. C. Allison, *J. Immunol.* **104**, 1160 (1970).
30. L. N. Pham, M. S. Dionne, M. Shirasu-Hiza, D. S. Schneider, *PLoS Pathog.* **3**, e26 (2007).

31. We thank the patients and their families, the members of the laboratory, and our collaborators A. Alcais,

C. Bidalled, M. Courat, M. N'Guyen, T. Leclerc, K. von Bernuth, E. von Bernuth, A. von Bernuth, J. von Bernuth, M. Gahr, F. de la Rocque, C. Levy, A. Lecuyer, M. Albert, F. Barrat, and R. Miller. This work was supported by grants from the INSERM, Agence Nationale de la Recherche, Institut des Maladies Rares, Programme Hospitalier de Recherche Clinique, Banque nationale de Paris Paribas Foundation, and the Dana Foundation (to J.-L.C.); grants from the NIH (U19 AIO57234-02) and the Dana Foundation (to D.C.); grants from the Hungarian Research Fund (to L.M.); and grants FIS/PI060241 (to J.Y.) and FIS/PI070329 (to M.J.) from Spain's Ministry of Health. H.v.B. was supported by the Deutsche Forschungsgemeinschaft, Legs Poix, and University San Rafaele Salute. J.-L.C. is an International Scholar of the Howard Hughes Medical Institute. The authors declare that they have no financial conflict of interest. The microarray data used in this study have been deposited in NCBI's Gene Expression Omnibus (GEO) with the accession number GSE 12124.

Supporting Online Material
www.sciencemag.org/cgi/content/full/321/5889/691/DC1
SOM Text
Figs. S1 to S8
Tables S1 to S11
References

26 March 2008; accepted 3 July 2008
10.1126/science.1158298

Censoring of Autoreactive B Cell Development by the Pre-B Cell Receptor

Rebecca A. Keenan,[1] Alessandra De Riva,[1] Björn Corleis,[1,2] Lucy Hepburn,[1] Steve Licence,[1] Thomas H. Winkler,[3] Inga-Lill Mårtensson[1]*

Antibody diversity occurs randomly as B cells recombine their immunoglobulin (Ig) heavy- and light-chain genes during development. This process inevitably generates reactivity against self structures, and several mechanisms prevent the development of autoreactive B cells. We report here a role for the pre-B cell receptor, composed of Ig heavy and surrogate light chains, in the negative selection of cells expressing Ig heavy chains with the potential to generate autoantibodies. Surrogate light-chain–deficient ($SLC^{-/-}$) mice harbored elevated levels of antinuclear antibodies (ANAs) in their serum and showed evidence of escape of pre-B cells expressing prototypic autoantibody heavy chains from negative selection, leading to mature autoantibody secreting $CD21^{-}CD23^{-}$ B cells in the periphery. Thus, the pre-B cell receptor appears to censor the development of certain autoantibody-secreting cells and may represent an important factor in multifactorial autoimmune diseases.

B lymphocytes express B cell receptors (BCRs), composed of Ig heavy chains (HCs) and light chains (LCs), on their surface. In order to respond to a vast number of different antigens, a diverse repertoire of such receptors is required and this is established by the somatic recombination of V, D, and J gene segments [V(D)J] (*1*). However, a consequence of this largely stochastic process is the generation of BCRs that have the potential to recognize self structures (*2*). Studies in transgenic mice have shown that several mechanisms eliminate immature B cells expressing autoreactive BCRs (*3*–*5*), which, by some estimates, constitute as much as half of the immature B cell population (*6*). Some of these are polyreactive, with others having specificity for nuclear antigens, such as DNA. Negative selection of autoreactive B cells is thus imperative for avoiding pathogenesis of autoimmune diseases, such as systemic lupus erythematosus (*7*).

V(D)J recombination takes place in a stepwise fashion, beginning at the HC locus and resulting in progenitor (pro-) and precursor (pre-) B cells expressing a pre-BCR (*8*). The pre-BCR is composed of HC and surrogate light chain (SLC); the latter is encoded by the invariant VpreB1/2 and λ5 genes (*9*). A process of quality control that acts on the pre-BCRs serves to positively select and expand pre-B cells that have undergone a successful V_H to DJ_H recombination [synthesizing μ heavy chains, the first isotype to be expressed (μHC)] (*10*–*12*). In mice lacking SLC ($SLC^{-/-}$), cells progress past the "pre-BCR" checkpoint and develop into immature and mature B cells, albeit in reduced numbers (*13*). Nevertheless, serum antibody levels are normal, and these mice respond to both T-cell–dependent and independent antigens.

In the course of analyzing serum from $SLC^{-/-}$ mice, IgG autoantibodies were detected (Fig. 1A), with levels of antinuclear antibodies (ANAs) (*14*) significantly higher in sera from $SLC^{-/-}$ than from control mice (Fig. 1B). These were predominantly of the IgG2b and IgG3 isotypes (fig. S1). In addition, IgG chromatin-specific antibodies were also detected in the same sera (Fig. 1C) as were IgG autoantibodies against single-stranded (ss) DNA (Fig. 1D). The levels of IgM antibodies to ssDNA and double-stranded DNA (dsDNA) and anticardiolipin antibodies were also significantly higher in $SLC^{-/-}$ mice (Fig. 1D).

Current models of negative selection of B cells suggest that several mechanisms operate in both primary and secondary lymphoid organs to ensure that autoreactive B cells are not allowed to differentiate into autoantibody-secreting plasma cells (*15*). The presence of autoantibodies in sera from $SLC^{-/-}$ mice was thus somewhat unexpected, because it indicates that some B cells had "escaped" negative selection and that, in turn, implied a potential role for the pre-BCR in censoring the development of autoreactive B cells. This would be unanticipated in light of the major role of the pre-BCR in positively selecting and expanding pre-B cells after successful V_H to DJ_H recombination.

To test whether a subpopulation of B cells in $SLC^{-/-}$ mice had indeed escaped negative selection, the composition of splenic B cells in $SLC^{-/-}$ mice was first analyzed. As expected, because of the substantial reduction in immature B cells in the bone marrow (BM) of $SLC^{-/-}$ mice (*13*), the absolute numbers of immature—determined by the surface expression of CD93—and mature ($CD93^{-}$) B cells ($B220^{+}IgM^{+}$) were lower in $SLC^{-/-}$ than in control mice (fig. S2). Among the mature B cells, the ratio of marginal zone (MZ) to follicular (FO) B cells was skewed toward the former in $SLC^{-/-}$ mice (Fig. 2A). As previously observed in λ5-deficient mice (*16*), $SLC^{-/-}$ animals contained a $CD93^{-}IgM^{low}CD21^{-}CD23^{-}$ B cell population (hereafter termed $CD21^{-}23^{-}$), that was measurably more prominent than such a population in control mice in the periphery (Fig. 2A), BM, and lymph nodes (fig. S2). As $CD21^{-}23^{-}$ cells were $CD43^{-}CD5^{-}Mac\text{-}1^{-}$, they were not typical B-1 B-lineage cells (fig. S2). The absolute number of $CD21^{-}23^{-}$ cells increased with age in both control and $SLC^{-/-}$ mice, but was consistently overrepresented in the latter. By the age of ~25 weeks, $CD21^{-}23^{-}$ B cells had reached control levels, as had MZ but not FO B cells (Fig. 2A). Thus, the composition of splenic B cells in $SLC^{-/-}$ mice was clearly different from that in control animals.

We next investigated the autoreactive potential of the mature B cell populations from $SLC^{-/-}$ mice. After activation of $CD21^{-}23^{-}$ and MZ B cells from both $SLC^{-/-}$ and control mice with lipopolysaccharide (LPS), only supernatants from $SLC^{-/-}$ $CD21^{-}23^{-}$ cells showed strong autoreactive staining (Fig. 2B). From this, we conclude that ANAs are secreted after in vitro stimulation of the $CD21^{-}23^{-}$ B cell population from $SLC^{-/-}$ mice.

In the antibody HC, the complementarity-determining regions (CDR1 to 3) contact antigen; CDR1 and 2 are encoded by the V_H and CDR3 by the V_H-D-J_H junction (Fig. 2C). The diversity of the CDR3 is further increased by N nucleotide additions and/or deletions, so that the diversity of the HC-CDR3 is sufficient for most antibody specificities (*17*). In contrast to conventional antibodies, the HC-CDR3 of ANAs frequently contains at least one basic amino acid, such as arginine (*18*), and in anti-DNA and anticardiolipin

[1]Laboratory of Lymphocyte Signalling and Development, The Babraham Institute, Cambridge CB22 3AT, UK. [2]Department of Molecular Immunology, Faculty for Biology, University Freiburg, Stübeweg 51, 79108 Freiburg, Germany. [3]Hematopoiesis Unit, Nikolaus-Fiebiger-Center, 91054 Erlangen, Germany.

*To whom correspondence should be addressed. E-mail: lill.martensson@bbsrc.ac.uk

antibodies, this arginine appears critical (*19*, *20*). Given the detection of ANAs in *SLC*$^{-/-}$ mice, it was possible that *SLC*$^{-/-}$ CD21^{-}23^{-} B cells express prototypic ANA HC-CDR3s.

We next analyzed the HC-CDR3s expressed by splenic B subpopulations for the presence of basic amino acid residues (tables S1 to S4), the distribution of which differed significantly (P = 0.03) between *SLC*$^{-/-}$ CD21^{-}23^{-} and the other B cell populations. The most prominent feature was the presence of two or more arginines (or one lysine plus one or more arginines) in *SLC*$^{-/-}$ CD21^{-}23^{-} B cells compared with the predominantly one arginine in control CD21^{-}23^{-} and MZ B cells of both genotypes (Table 1 and Fig. 2D). Overall in the HC-CDR3s, the proportions of arginines were much higher than that of lysine (Table 1). Thus, the HC-CDR3s expressed by *SLC*$^{-/-}$ CD21^{-}23^{-} B cells are typical of ANAs in that they contain a high proportion of basic amino acids.

In anti-DNA antibody HC-CDR3s, arginines are introduced by, for instance, N nucleotides or D-D fusions (*19*). In the HC-CDR3s from control CD21^{-}23^{-} and MZ B cells from both genotypes, the majority of arginines and lysines were encoded by 5′-N-nucleotides (table S1 to S4). However, in *SLC*$^{-/-}$ CD21^{-}23^{-} B cells, whereas one of the two arginines was often encoded by 5′-N-nucleotides, the second was preferentially encoded by the D gene segment. Arginines encoded by the D segment are indeed found in anti-DNA antibodies but, in order for a D segment to encode an arginine, it has to be translated in reading frame 3 (RF3), which is infrequently used; a strong preference has been observed for RF1 (*2*, *21*, *22*).

We determined that, in *SLC*$^{-/-}$ CD21^{-}23^{-} B cells, D segment RF usage of both RF2 and RF3 was increased compared with control CD21^{-}23^{-} B cells and MZ B cells from both genotypes, where RF1 was predominant (Table 1). Although RF3 does not necessarily have to result in an arginine (in RF3, 7 out of the 12 D gene segments can encode an arginine), in the *SLC*$^{-/-}$ CD21^{-}23^{-} B cells, all RF3 sequences did (tables S1 to S4). Thus, the presence of a subpopulation of B cells that, in *SLC*$^{-/-}$ mice, express prototypic anti-DNA antibodies offers a molecular basis for the presence of ANAs in serum from these animals and suggests that these B cells have escaped negative selection.

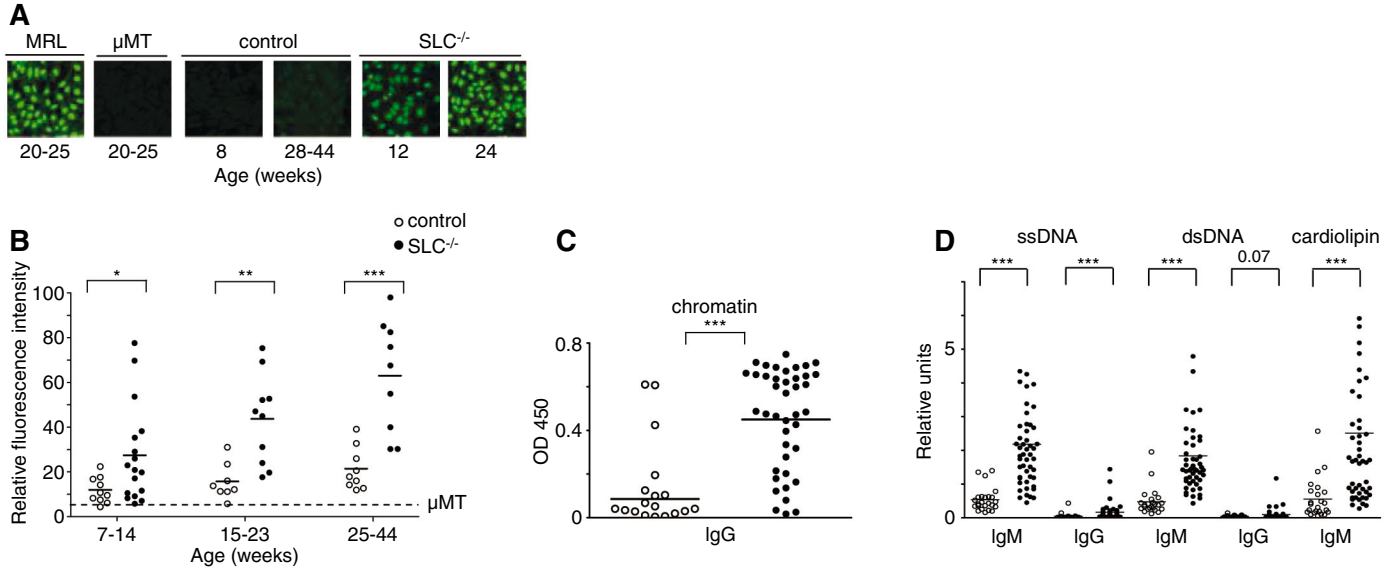

Fig. 1. ANAs in serum from *SLC*$^{-/-}$ mice. (**A**) Sera, diluted 1/40 (MRL mice, 1/100) from pools or individual (*SLC*$^{-/-}$) mice were incubated on HEp-2 slides (*14*) to detect IgG ANAs, visualized by confocal microscopy. (**B**) Relative fluorescence intensity of serum (1/40) IgG ANAs. Enzyme-linked immunosorbent assay (ELISA) to measure (**C**) IgG antibodies to chromatin, (**D**) IgM and IgG antibodies to ssDNA and dsDNA and phospholipids (cardiolipin). Genotypes are indicated. [(B) to (D)] n = 28 control and 38 to 42 *SLC*$^{-/-}$ mice. Horizontal line, the mean; dotted line, µMT (lacking antibodies). *P < 0.05; **P < 0.01; ***P < 0.001.

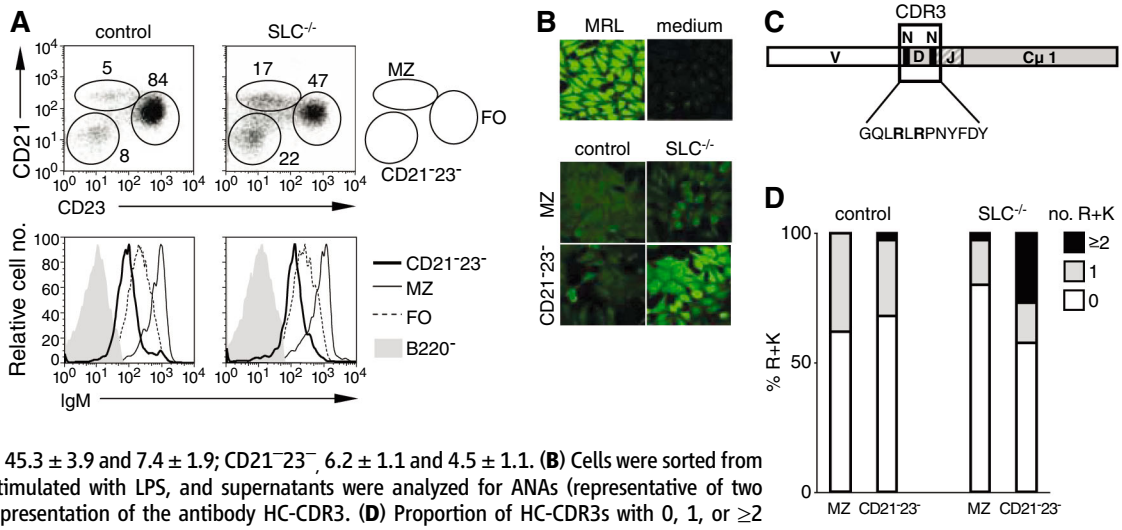

Fig. 2. *SLC*$^{-/-}$ CD21^{-}23^{-} mature B cells secrete autoantibodies following in vitro activation and express prototypic ANA HC-CDR3s. (**A**) Mature splenic B cells (CD93^{-}B220^{+}IgM^{+}) from indicated mice (~27 weeks) were analyzed by flow cytometry to determine (top) proportions of MZ, FO, and CD21^{-}23^{-} cells and (bottom) IgM levels on indicated populations (B220^{-} cells, negative control). B cell numbers (four to five mice per genotype), control and *SLC*$^{-/-}$ (×10^{6} ± SD): MZ, 2.4 ± 0.6 and 3.1 ± 0.9; FO, 45.3 ± 3.9 and 7.4 ± 1.9; CD21^{-}23^{-}, 6.2 ± 1.1 and 4.5 ± 1.1. (**B**) Cells were sorted from 9- to 11-week-old mice and stimulated with LPS, and supernatants were analyzed for ANAs (representative of two experiments). (**C**) Schematic representation of the antibody HC-CDR3. (**D**) Proportion of HC-CDR3s with 0, 1, or ≥2 arginines and lysines in cell populations and genotypes as indicated.

To investigate whether the pre-BCR is indeed involved in censoring the development of autoreactive B cells, we compared the HC-CDR3s expressed by pro- and pre-B cells (Fig. 3A), i.e., before and after the pre-BCR checkpoint (*23*). In control pro-B cells, the proportion with basic amino acids was significantly ($P = 0.045$) higher than in pre-B cells (tables S5 and S6), and those with two or more arginines decreased with developmental progression, as expected if they were undergoing selection (Table 1 and Fig. 3B). In $SLC^{-/-}$ mice, although the proportion of CDR3 with basic amino acids was high (tables S7 and S8), those with two or more decreased as cells progressed to the pre-B stage. As this may be due to expression of bona fide LCs and, therefore, BCR-mediated selection, we analyzed μHC-CDR3s expressed by pro- and pre-B cells lacking both SLC and LC ($SLC^{-/-}LC^{-/-}$) (*24*), as they are unable to express a BCR (tables S9 and S10). In these pre-B cells, the proportion of HC-CDR3s with basic amino acids was high and the distribution of arginines was similar to that in control pro-B cells, as would be expected if selection were abolished (Table 1 and Fig. 3B).

To assess whether RF3 played a role, RF usage was analyzed. In control pro-B cells RF3 was high and RF usage changed significantly ($P = 0.05$) as cells progressed to the pre-B stage (Table 1), with the majority of RF3s encoding an arginine. In $SLC^{-/-}$ and $SLC^{-/-}LC^{-/-}$ mice, RF usage was significantly ($P = 0.02$) different from that of control cells; in addition to the expected lack of RF2 selection, RF3 selection was abolished (Table 1). In $SLC^{-/-}LC^{-/-}$ pre-B cells, as in control pro-B and $SLC^{-/-}$ $CD21^{-}23^{-}$ B cells, most of the RF3s encoded an arginine.

These data support a role for the pre-BCR in preventing the development of cells expressing prototypic anti-DNA antibody HC-CDR3s. However, the mechanism was unclear. Because surface expression of μHC may be required for developmental progression, we compared the HC-CDR3s of those expressed in the presence and absence of SLC, after short-term expansion of cells in vitro; surface levels on freshly isolated pro-B cells are very low. The HCs expressed by both control and $SLC^{-/-}LC^{-/-}$ pro-B cells contained a high proportion of basic amino acid residues in the CDR3 (tables S11 and S12), but the distribution was significantly ($P = 0.02$) different, with a high proportion of two or more arginines only in $SLC^{-/-}LC^{-/-}$ pro-B cells (Table 1 and Fig. 3C). As the fraction of pro-B cells expressing surface versus intracellular μHCs appeared lower (Fig. 3D), it was possible that, in the presence of SLC, HCs with two or more arginines were retained intracellularly. However, this was not the case; intracellular HCs also lacked CDR3s with two or more arginines (Table 1 and Fig. 3C). Thus, in the presence of SLC, although freshly isolated pro-B cells express prototypic anti-DNA antibody HCs, after short-term expansion in vitro, they are no longer detectable, either on the surface or intracellularly, which suggests that pro-B cells expressing these undergo negative selection. By contrast, in the absence of SLC (and LC), pro-B cells readily express prototypic anti-DNA antibody HCs on their surface, which implies a cellular basis for the development of autoreactive B cells in $SLC^{-/-}$ mice.

On the basis of these data, we propose that the pre-BCR mediates a signal resulting in negative selection. Such a checkpoint may also exist in humans; pre-B cells from a patient with mutations

Table 1. Comparison of HC-CDR3 characteristics in various cell populations. The antibody HC-CDR3 was measured from the amino acid starting at the third residue following the conserved FWR3, YYC motif encoded in the V_H gene segment and ending at, but not including, the WGXGT motif in FWR4 encoded by the J_H gene segment (*30*). Indicated cell populations were sorted from either the spleen or bone marrow. The in vitro cultured pro-B cells were sorted as sμHC$^+$ and sμHC$^-$, referring to whether μHCs are expressed on the cell surface or intracellularly, respectively. The first row in each table part refers to number of HC-CDR3 sequences analyzed. R and/or K refers to the number of CDR3 sequences with arginine (R) and/or lysine (K) residues. Next row, the number of CDR3 sequences with either 1 R or 1 K residue is indicated. The next rows show the number of CDR3 sequences with ≥2 R residues or ≥2 R+K; there were no instances of ≥2 K residues. D segment reading frame (RF) usage in indicated cell population. D segment usage was only assigned if ≥5 nt were identical to the germ line D. RF has not been assigned to those without assigned D and those using D_{Q52}.

	Spleen				Bone marrow						In vitro cultured pro-B		
	Control		$SLC^{-/-}$		Control		$SLC^{-/-}$		$SLC^{-/-}LC^{-/-}$		Control		$SLC^{-/-}LC^{-/-}$
	MZ	21^-23^-	MZ	21^-23^-	Pro-B	Pre-B	Pro-B	Pre-B	Pro-B	Pre-B	sμHC$^-$	sμHC$^+$	sμHC$^+$
Sequences	45	38	35	41	31	23	32	32	22	32	37	45	40
R and/or K	17	12	7	17	16	6	13	14	7	17	16	18	16
1 R	14	8	6	6	6	4	8	12	4	10	15	16	7
1 K	3	3	0	0	1	0	0	1	0	0	1	1	0
≥2 R	0	1	1	10	9	2	1	1	2	7	0	1	7
≥2 R+K	0	0	0	1	0	0	4	0	1	0	0	0	2
RF 1:2:3	23:6:4	19:3:3	12:4:2	16:7:8	11:4:9	13:2:1	11:8:2	11:8:3	9:6:3	9:11:5	15:5:5	26:6:1	17:8:5

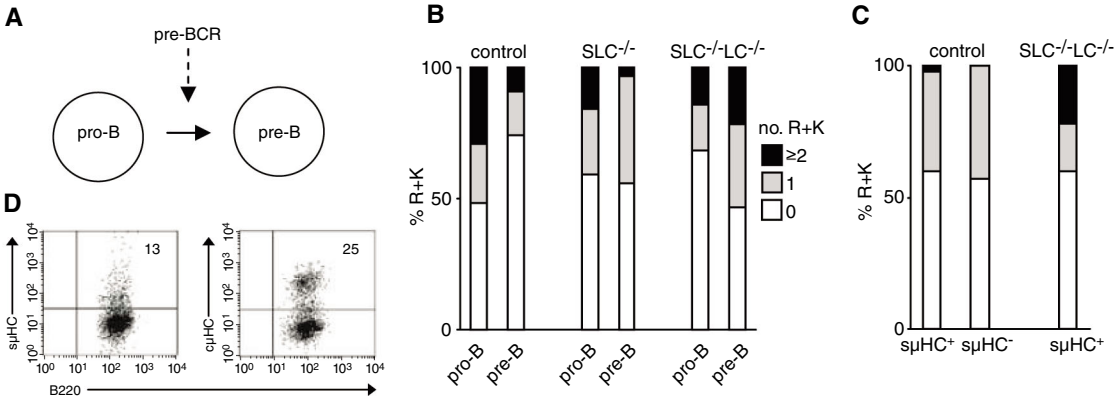

Fig. 3. A pre-B cell receptor–dependent checkpoint negatively selecting cells expressing prototypic ANA HC-CDR3s. (**A**) The pre-B cell receptor (pre-BCR) checkpoint. (**B**) Proportion of HC-CDR3s with 0, 1, or ≥2 arginines and lysines in cell populations and genotypes as indicated. (**C**) As in (B). (**D**) Flow cytometry to analyze surface (s) and intracellular (c) μHCs on pro-B cells from $SLC^{-/-}LC^{-/-}$ mice after short-term culture in vitro. Representative of two experiments and control pro-B cells. Cells (0.5×10^6) were plated, and 11.9 (control) and 9.5×10^6 ($SLC^{-/-}LC^{-/-}$) cells were harvested on day 6.

in λ5 express HC-CDR3s with an unusually high proportion of basic amino acids, although this particular λ5 mutant was associated with a block in B cell development and agammaglobulinemia (*25*, *26*) and, consequently, the possible development of autoreactive B cells was not open to investigation.

Self-tolerance at early stages of B cell development may be mediated by clonal deletion and/or receptor replacement. The latter (*27*, *28*), by analogy to receptor editing of the LC loci at later stages of B cell development, may result in expression of an innocuous receptor. An alternative to the self-tolerance explanation is that the autoreactivity conferred by a high proportion of basic amino acids in the HC-CDR3 is secondary or coincidental to structure and, for instance, toxic to the cell, although this would only be in the presence but not absence of SLC; they are readily expressed by $SLC^{-/-}LC^{-/-}$ pro-B cells.

Despite the presence of serum autoantibodies recognizing DNA, phospholipids, and chromatin, which are typical lupus antigens, we have, so far, not observed any pathology in $SLC^{-/-}$ mice. This is perhaps not surprising, however, as multiple checkpoints must be bypassed before overt autoimmune disease arises (*29*). Nevertheless, the pre-B cell receptor appears to censor the development of certain autoantibody-secreting cells and may represent an important factor in multifactorial autoimmune diseases.

References and Notes

1. S. Tonegawa, *Nature* **302**, 575 (1983).
2. K. Rajewsky, *Nature* **381**, 751 (1996).
3. D. Gay, T. Saunders, S. Camper, M. Weigert, *J. Exp. Med.* **177**, 999 (1993).
4. S. B. Hartley *et al.*, *Cell* **72**, 325 (1993).
5. S. L. Tiegs, D. M. Russell, D. Nemazee, *J. Exp. Med.* **177**, 1009 (1993).
6. H. Wardemann *et al.*, *Science* **301**, 1374 (2003).
7. B. L. Kotzin, *Cell* **85**, 303 (1996).
8. S. Pillai, D. Baltimore, *Nature* **329**, 172 (1987).
9. F. Melchers *et al.*, *Immunol. Today* **14**, 60 (1993).
10. P. D. Burrows *et al.*, *Semin. Immunol.* **14**, 343 (2002).
11. F. Melchers *et al.*, *Immunol. Rev.* **175**, 33 (2000).
12. C. Vettermann, K. Herrmann, H. M. Jack, *Semin. Immunol.* **18**, 44 (2006).
13. T. Shimizu, C. Mundt, S. Licence, F. Melchers, I. L. Martensson, *J. Immunol.* **168**, 6286 (2002).
14. Materials and methods are available as supporting material on *Science* Online.
15. M. J. Shlomchik, *Immunity* **28**, 18 (2008).
16. E. Harfst, J. Andersson, U. Grawunder, R. Ceredig, A. G. Rolink, *Immunol. Lett.* **101**, 173 (2005).
17. J. L. Xu, M. M. Davis, *Immunity* **13**, 37 (2000).
18. S. M. Barbas *et al.*, *Proc. Natl. Acad. Sci. U.S.A.* **92**, 2529 (1995).
19. M. Z. Radic, M. Weigert, *Annu. Rev. Immunol.* **12**, 487 (1994).
20. I. Giles *et al.*, *J. Immunol.* **177**, 1729 (2006).
21. M. Kaartinen, O. Makela, *Immunol. Today* **6**, 324 (1985).
22. Y. Ichihara, H. Hayashida, S. Miyazawa, Y. Kurosawa, *Eur. J. Immunol.* **19**, 1849 (1989).
23. I. L. Martensson, R. A. Keenan, S. Licence, *Curr. Opin. Immunol.* **19**, 137 (2007).
24. R. Keenan, thesis, Cambridge University (2006).
25. Y. Minegishi, M. E. Conley, *Immunity* **14**, 631 (2001).
26. Y. Minegishi *et al.*, *J. Exp. Med.* **187**, 71 (1998).
27. R. Kleinfield *et al.*, *Nature* **322**, 843 (1986).
28. M. Reth, P. Gehrmann, E. Petrac, P. Wiese, *Nature* **322**, 840 (1986).
29. C. C. Goodnow, *Cell* **130**, 25 (2007).
30. Single-letter abbreviations for the amino acid residues are as follows: A, Ala; C, Cys; D, Asp; E, Glu; F, Phe; G, Gly; H, His; I, Ile; K, Lys; L, Leu; M, Met; N, Asn; P, Pro; Q, Gln; R, Arg; S, Ser; T, Thr; V, Val; W, Trp; Y, Tyr; and X, any amino acid.

31. We thank G. Morgan for cell sorting, S. Walker and S. Andrews for support with microscopy and sequence analysis, and A. Segonds-Pichon for statistical analysis. Supported by the UK Biotechnology and Biological Sciences Research Council (BBSRC) and Medical Research Council (MRC) and the Deutsche Forschungsgemeinschaft (DFG) (FOR832 to T.H.W.).

Supporting Online Material

www.sciencemag.org/cgi/content/full/1157533/DC1
Materials and Methods
Figs. S1 and S2
Tables S1 to S13
References

10 March 2008; accepted 27 May 2008
Published online 19 June 2008;
10.1126/science.1157533
Include this information when citing this paper.

Generation of Pluripotent Stem Cells from Adult Mouse Liver and Stomach Cells

Takashi Aoi,[1,2] Kojiro Yae,[1] Masato Nakagawa,[1] Tomoko Ichisaka,[1,3] Keisuke Okita,[1] Kazutoshi Takahashi,[1] Tsutomu Chiba,[2] Shinya Yamanaka[1,3,4,5]*

Induced pluripotent stem (iPS) cells have been generated from mouse and human fibroblasts by the retroviral transduction of four transcription factors. However, the cell origins and molecular mechanisms of iPS cell induction remain elusive. This report describes the generation of iPS cells from adult mouse hepatocytes and gastric epithelial cells. These iPS cell clones appear to be equivalent to embryonic stem cells in gene expression and are competent to generate germline chimeras. Genetic lineage tracings show that liver-derived iPS cells are derived from albumin-expressing cells. No common retroviral integration sites are found among multiple clones. These data suggest that iPS cells are generated by direct reprogramming of lineage-committed somatic cells and that retroviral integration into specific sites is not required.

By retroviral transduction of four transcription factors, Oct 3/4, Sox2, Klf4, and c-Myc, adult mouse fibroblast cells have been reprogrammed to an undifferentiated state similar to that of embryonic stem (ES) cells (*1*, *2*), and these cells have been termed induced pluripotent (iPS) cells. Subsequently, human iPS cells were generated with use of two different sets of transcription factors (*3*, *4*). The generation of human iPS cells provides a method to produce patient-specific stem cells for study of the diseased state in culture (*3*–*5*). The mechanisms of iPS cell induction, however, are unknown. Low efficiency of iPS cell induction suggests that their origins may be of undifferentiated stem cells coexisting in fibroblast culture. In addition, retroviral integration into specific site(s) might be required for iPS cell induction (*6*).

In this study, we generated iPS cells from epithelial cells rather than fibroblasts. Primary hepatocytes and gastric epithelial cells (Fig. 1A) were isolated from mice in which β-geo [the fusion with β-galactocidase (β-gal) and the neomycin-resistant gene] was knocked into *Fbx15* (*7*), which is specifically expressed in ES cells and preimplantation embryos. Fbx15-selected iPS cells from fibroblasts [mouse embryonic fibroblast (MEF) or tail tip fibroblast (TTF)] were different from ES cells in gene expression, DNA methylation, and chimera formation (*2*).

Four transcription factors (Oct 3/4, Sox2, Klf4, and c-Myc) were introduced by retroviral vectors into hepatocytes or gastric epithelial cells. The efficiency of retroviral transduction was lower in epithelial cells (30 to 45%, fig. S1A) than in MEFs (>85%, fig. S1B). When MEFs were transduced with diluted retroviruses, of which transduction efficiency was ~30%, iPS cells could not be obtained (fig. S1B). Three days after epithelial cell transfection, the medium was changed to ES cell medium containing serum and G418. Two weeks later, multiple G418-resistant and ES cell–like colonies, characterized with large nuclei and scant cytoplasm, were observed from both hepatocytes and gastric epithelial cells, even with the low-efficiency retroviral transduction.

The G418-resistant colonies were expanded, and ~60% of them showed morphology indis-

[1]Department of Stem Cell Biology, Institute for Frontier Medical Sciences, Kyoto University, Kyoto 606-8507, Japan. [2]Department of Gastroenterology and Hepatology, Graduate School of Medicine, Kyoto University, Kyoto 606-8507, Japan. [3]Core Research in Embryonic Science and Technology (CREST), Japan Science and Technology Agency, Kawaguchi 332-0012, Japan. [4]Gladstone Institute of Cardiovascular Disease, San Francisco, CA 94158, USA. [5]Center for Induced Pluripotent Stem (iPS) Cell Research and Application, Institute for Integrated Cell-Material Sciences, Kyoto University, Kyoto 606-8507, Japan.

*To whom correspondence should be addressed. E-mail: yamanaka@frontier.kyoto-u.ac.jp

tinguishable from that of mouse ES cells (Fig. 1B). These cells were designated iPS-Hep (iPS-hepatic) and iPS-Stm (iPS-stomach). They also showed proliferation profiles similar to those of ES cells (fig. S2A). Reverse transcription polymerase chain reaction (RT-PCR) showed that iPS-Hep cells (Fig. 1C) and iPS-Stm cells (fig. S2B) expressed quantities of endogenous *Oct3/4* and *Sox2* comparable to those in ES cells. iPS-Hep and iPS-Stm cells also expressed ES cell marker genes, including *Nanog*, *ECAT1*, *Rex1*, *Cripto*, and *Gdf3*, at quantities comparable to those in ES cells. In contrast, Fbx15-selected iPS cells derived from TTF (iPS-TTF) showed lower expression of the ES cell marker genes (Fig. 1C). We tested two culture conditions during the generation of iPS-Hep cells and iPS-TTF cells: one containing epidermal growth factor (EGF) and hepatocyte growth factor (HGF) but no serum (Fig. 1C, medium A) and the other containing 10% serum but no EGF nor HGF (Fig. 1C, medium B). In both conditions, iPS-Hep cells showed higher expression of ES cell marker genes than did iPS-TTF cells. The promoter regions of *Oct3/4*, *Nanog*, and *Fbx15* are largely, albeit not completely, unmethylated in iPS-Hep and iPS-Stm cells (fig. S2C). This is

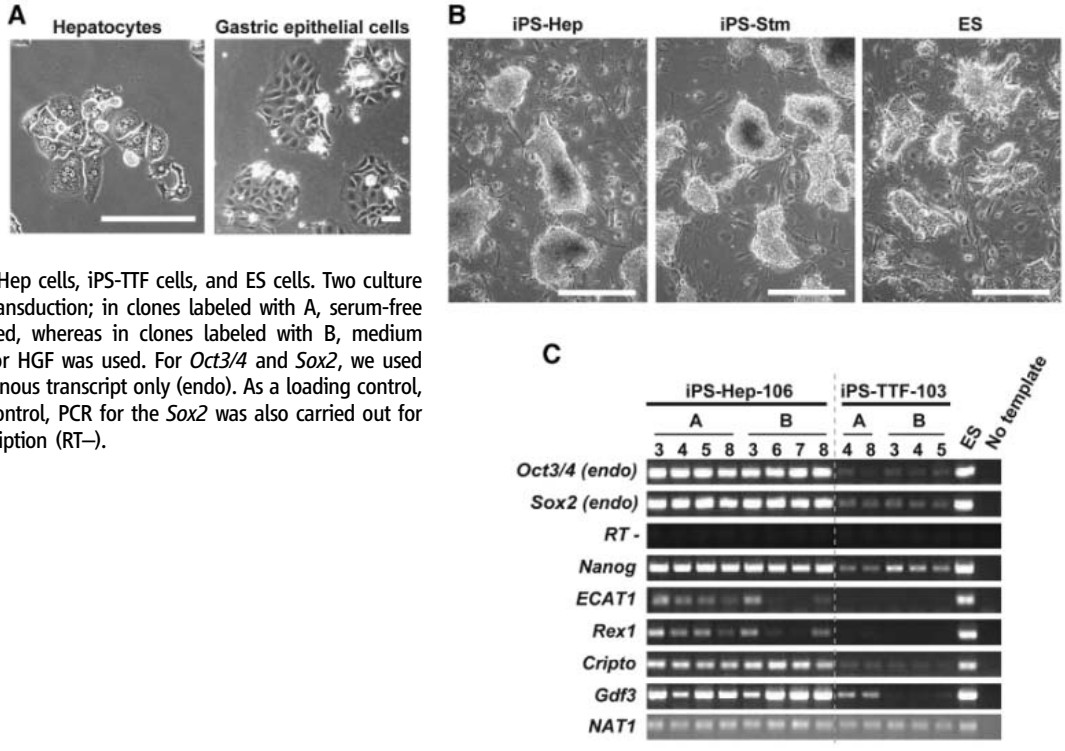

Fig. 1. Characterization of iPS cells from adult mouse hepatocytes and gastric epithelial cells. (**A**) Morphology of a primary culture of hepatocytes and gastric epithelial cells on gelatin-coated plates. Scale bars indicate 50 μm. (**B**) Morphology of iPS-Hep and iPS-Stm cells on STO feeder cells. Scale bars, 500 μm. (**C**) RT-PCR analyses of ES marker gene expression in iPS-Hep cells, iPS-TTF cells, and ES cells. Two culture media were used during retroviral transduction; in clones labeled with A, serum-free medium with EGF and HGF was used, whereas in clones labeled with B, medium containing 10% serum but no EGF or HGF was used. For *Oct3/4* and *Sox2*, we used primer sets that amplified the endogenous transcript only (endo). As a loading control, *NAT1* was used (*17*). As a negative control, PCR for the *Sox2* was also carried out for the templates without reverse transcription (RT–).

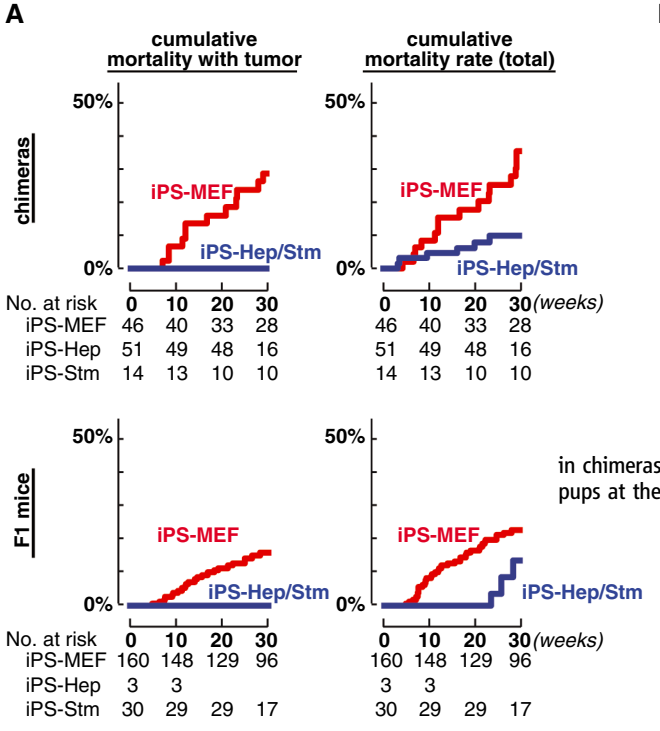

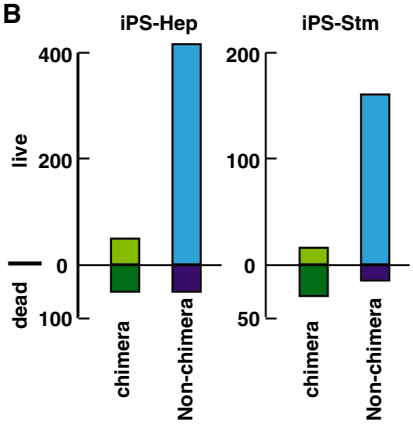

Fig. 2. Mice derived from of iPS-Hep/Stm cells. (**A**) Tumorigenicity and mortality of iPS cell–derived mice. The cumulative mortality related with tumor (left) and overall mortality (right) of the chimeric mice (top) or F1 mice (bottom) generated from iPS-MEF or from iPS-Hep/Stm are shown. "Death" includes the cases killed because of weakness. All the death cases were dissected to evaluate the cause of death. Shown at the bottom of each figure are the numbers of mice analyzed at each time point. (**B**) Higher incidence of perinatal death in chimeras derived from iPS-Hep and iPS-Stm cells. Shown are the numbers of live and dead pups at the day of birth.

also in contrast to iPS-TTF cells, which only showed partial demethylation (*2*). Thus, even with *Fbx15* selection, iPS-Hep and iPS-Stm cells are more similar to ES cells than they are to iPS-TTF cells.

We then tranplanted iPS-Hep and iPS-Stm cells (1×10^6 cells) subcutaneously into the hind flanks of nude mice (table S1). Four weeks after transplantation, all mice developed tumors containing various tissues of the three germ layers, including neural tissues, muscle, cartilage, and gutlike epithelial tissues (fig. S3). This demonstrated that the iPS-Hep and iPS-Stm cells are pluripotent.

These cells were also transplanted into blastocysts by microinjection (table S2). Eight iPS-Hep clones and six iPS-Stm clones, which were derived from Fbx15-reporter mice, were injected. We also injected five iPS-Hep clones that were generated with selection for *Nanog* expression. Most of these clones also contained a green fluorescent protein (GFP) transgene driven by the constitutively active CAG promoter (*8*). In addition, we injected one iPS-Hep clone, which we selected on the basis of morphology without selection makers (*9*–*11*). Among these, we obtained adult chimeric mice from 10 iPS-Hep clones and two iPS-Stm clones, as shown by mouse coat color (fig. S4A). The degree of chimerism was not determined in several mice (indicated as ND in table S2) because they died before evaluation or because iPS cells and host blastocysts resulted in the same coat color. From one iPS-Hep clone (derived from 21-week-old mouse) and two iPS-Stm clones (derived from 12-week-old mouse) that were selected for *Fbx15* expression, germline transmission was observed as judged from GFP expression and the presence of the transgenes (fig. S4B). Again, this is in contrast to the iPS-fibroblast (MEF or TTF) cells in that only *Nanog* selection but not *Fbx15* selection resulted in adult and germline chimeras (*2*).

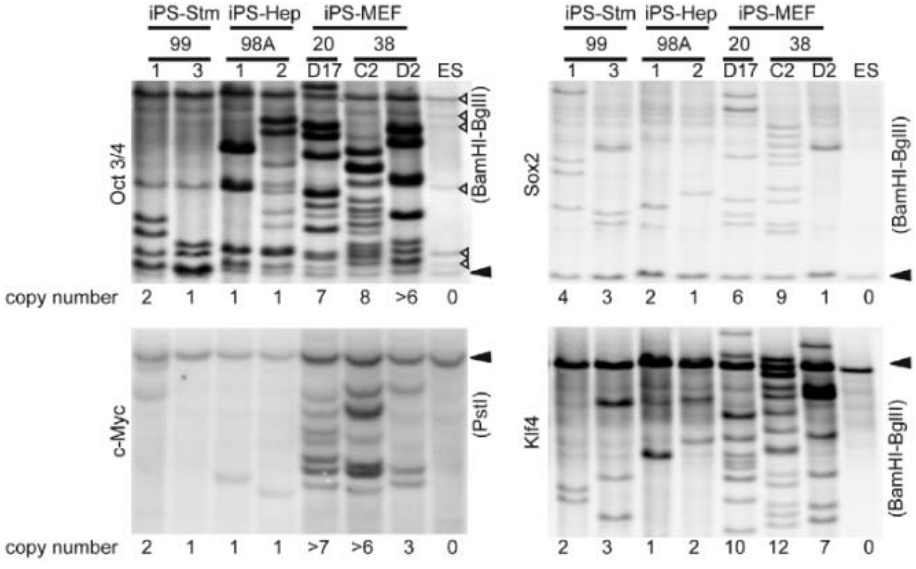

Fig. 3. Retroviral integration sites in iPS-Hep and iPS-Stm cells. Southern blot analyses of retroviral integration of Oct3/4, Sox, Klf4, and c-Myc in iPS-Hep and iPS-Stm clones. Genomic DNA isolated from iPS-Stm, iPS-Hep, or iPS-MEF, and wild-type ES cells were analyzed. The number of detected bands is shown at the bottom. Arrowheads indicate bands corresponding to the endogenous loci. Open arrowheads indicate bands corresponding to *Oct3/4* pseudogenes.

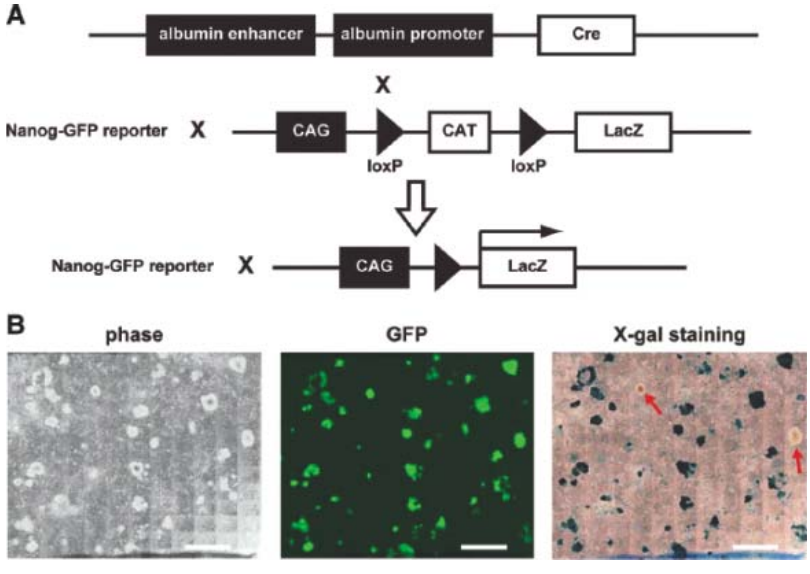

Fig. 4. iPS-Hep cells originated from albumin-expressing cells. (**A**) Strategy for cell fate tracing experiment. (**B**) Phase contrast, fluorescent, and X-gal staining photographs of iPS cell colonies derived from hepatocytes of the triple transgenic mouse. Red arrows indicate β-gal–negative colonies. Scale bars, 2 mm.

Tumorigenicity was then compared between mice derived from iPS-Hep cells, iPS-Stm cells, or iPS-MEF cells. Forty-six adult chimeras were obtained from 10 independent iPS-MEF clones out of 12 lines injected. Of these chimeras, about 30% of mouse chimeras developed tumors by the age of 30 weeks (Fig. 2A). In contrast, no tumor formation was observed from 65 adult chimeras derived from 12 iPS-Hep and iPS-Stm clones in this period. In addition, about 20% of the F1 mice derived from eight iPS-MEF clones developed tumors by the age of 30 weeks, whereas no tumor development has been observed in F1 mice from the iPS-Hep and iPS-Stm (iPS-Hep/Stm) cells (Fig. 2A). Some mice derived from iPS-Hep and iPS-Stm cells did die, especially after we relocated these mice to a conventional mouse facility, but we did not find tumors by necropsy (Fig. 2A).

There was, however, an incidence of perinatal death of chimeric mice derived from iPS-Hep and iPS-Stm cells that was higher than that of nonchimeras (Fig. 2B). Such higher perinatal mortality was not apparent with iPS-MEF cells. The dead mice appeared normal in gross appearance by necropsy, and the cause of death is not known. It is possible that some epigenetic abnormalities might be responsible for the perinatal death, as is believed to be the case in cloned animals (*12*). In contrast, we did not observe increased mortality in mice that survived the first day after birth (Fig. 2A).

Numbers of retroviral integration sites (RIS) were examined in iPS-Hep and iPS-Stm cells. Southern blot analyses detected one to four bands for each of the four retroviruses in each clone (Fig. 3). These are fewer than those in MEF-iPS cells, which showed 1 to 12 RIS for each retrovirus. In two iPS-Hep clones and two iPS-Stm clones, RIS were randomly distributed in multiple chromosomes, as determined with inverse PCR (fig. S5). The integrated genes did not show preferences either in their functional categories or in their intracellular localization (fig. S6). RIS mainly reside near the transcription initiation sites (figs. S7 to S11).

Our data show that iPS-Hep and iPS-Stm cells are different from iPS-fibroblasts in three properties. First, iPS-Hep and iPS-Stm cells contribute to adult chimeras even with the selection for *Fbx15*. Second, no increased tumorigenicity was observed in chimera mice derived from iPS-Hep and iPS-Stm cells evaluated up to 30 weeks. These two properties are similar to iPS-fibroblast cells that we recently generated without Myc retroviruses (*11*). This suggests that Myc plays a smaller role in the generation of iPS-Hep and iPS-Stm cells than its role in iPS-fibroblast cells. To test this possibility, we individually omitted each of the four factors to see the effect on the generation of iPS cells from hepatocytes. When we omitted Oct3/4, Sox2, or Klf4, no iPS cell colonies emerged (fig. S12A). By contrast, the omission of Myc decreased the colony numbers only 20 to 40% from those obtained by the four factors (fig. S12, A and B). This is in contrast to the generation of iPS-fibroblasts, in which the colony numbers decreased more than 90% upon the Myc omission (*11*), supporting the minor role of Myc in the generation of iPS cells from hepatocytes.

The third difference between iPS-Hep and iPS-Stm cells and iPS-fibroblasts is that the two former iPS have fewer RIS than did the latter. Retroviral expression levels of the four factors were higher in hepatocytes than in fibroblasts (fig. S13). This may explain, at least in part, the fewer RIS in iPS-Hep cells. In addition, it has been shown that ES cells have characteristics of the epithelium, such as tight intercellular contact and surface expression of E-cadherin (*13*). We confirmed that the expressions of E-cadherin and β-catenin in hepatocytes were higher than those in fibroblasts and equivalent to those in ES cells (fig. S13). This similarity may also contribute to the fewer RIS in iPS-Hep and iPS-Stm cells. Further studies are required to determine the precise molecular mechanisms underlying the substantial differences between iPS-Hep and iPS-Stm cells versus iPS-fibroblasts.

To examine the origin of iPS-Hep cells, we conducted a genetic lineage tracing experiment (Fig. 4A). The Nanog-reporter mice, in which GFP and the puromycin resistance gene was knocked into *Nanog* for selection of iPS cells, were first crossed with mice expressing a loxP-CAT-loxP-β-gal (where CAT is chloremphenicol acetyltransferase) cassette from the constitutively active promoter (*14*) and then crossed with mice expressing the Cre recombinase driven by the *albumin* promoter (*15*). In the triple transgenic mice, β-gal activity is turned on upon the activation of the *albumin* gene and continues even when *albumin* is turned off. Primary hepatocytes were isolated, and iPS cells were generated by the four factors. Fourteen days after the transfection, puromycin selection was initiated. By 30 days after the transfection, >100 GFP-positive colonies were obtained (Fig. 4B, left and center). Most of them were also positive for β-gal (Fig. 4B, right), indicating that iPS-Hep cells were derived from hepatocytes or other *albumin*-expressing cells but not from undifferentiated cells that do not express albumin. A few GFP-positive and β-gal–negative colonies were observed, which may have arisen from albumin-negative cells that coexist in primary hepatocyte cultures, or they may simply reflect incomplete excision by Cre.

This study demonstrates that the four transcription factors successfully reprogrammed somatic cells that had differentiated into a stage in which the *albumin* promoter is turned on. In addition, we showed that generation of iPS-Hep and iPS-Stm cells do not require retroviral integration into specific sites. This finding suggests that it might be possible to generate iPS cells with gene transfer methods free from an integration mechanism that may result in tumorigenicity after transplantation to patients (*16*).

Note added in proof: After publication of this manuscript online in *Science* Express, we became aware of the need for corrections, which are now published in the Letters section of this issue (see Corrections and Clarifications on page 641 and the revised SOM at www.sciencemag.org/cgi/content/full/1154884/DC2). In addition, after publication of the manuscript in *Science* Express, one chimera mouse derived from iPS-Hep cells developed an obvious tumor, and two other chimeras and one F1 mouse derived from iPS Hep/Stm cells showed areas of abnormal tissues that may represent tumors or be due to an inflammation response.

References and Notes

1. K. Okita, T. Ichisaka, S. Yamanaka, *Nature* **448**, 313 (2007).
2. K. Takahashi, S. Yamanaka, *Cell* **126**, 663 (2006).
3. K. Takahashi *et al.*, *Cell* **131**, 861 (2007).
4. J. Yu *et al.*, *Science* **318**, 1917 (2007); published online 19 November 2007 (10.1126/science.1151526).
5. I. H. Park *et al.*, *Nature* **451**, 141 (2008).
6. S. Yamanaka, *Cell Stem Cell* **1**, 39 (2007).
7. Y. Tokuzawa *et al.*, *Mol. Cell. Biol.* **23**, 2699 (2003).
8. H. Niwa, K. Yamamura, J. Miyazaki, *Gene* **108**, 193 (1991).
9. A. Meissner, M. Wernig, R. Jaenisch, *Nat. Biotechnol.* **25**, 1177 (2007).
10. R. Blelloch, M. Venere, J. Yen, M. Ramalho-Santos, *Cell Stem Cell* **1**, 245 (2007).
11. M. Nakagawa *et al.*, *Nat. Biotechnol.* **26**, 101 (2008).
12. X. Yang *et al.*, *Nat. Genet.* **39**, 295 (2007).
13. H. L. Spencer *et al.*, *Mol. Biol. Cell* **18**, 2838 (2007).
14. K. Sakai, J. Miyazaki, *Biochem. Biophys. Res. Commun.* **237**, 318 (1997).
15. C. Postic *et al.*, *J. Biol. Chem.* **274**, 305 (1999).
16. A. W. Nienhuis, C. E. Dunbar, B. P. Sorrentino, *Mol. Ther.* **13**, 1031 (2006).
17. S. Yamanaka, K. S. Poksay, K. S. Arnold, T. L. Innerarity, *Genes Dev.* **11**, 321 (1997).

18. We thank M. Koyanagi and K. Tanabe for scientific discussion; M. Narita, H. Miyachi, and S. Kitano for technical assistance; R. Kato and R. Iyama for administrative assistance; J. Miyazaki for CAG-CAT-Z mice; T. Kitamura for Plat-E cells and pMXs retroviral vectors; and R. Farese for RF8 ES cells. This study was supported in part by a grant from the Program for Promotion of Fundamental Studies in Health Sciences of National Institute of Biomedical Innovation, a grant from the Leading Project of Ministry of Education, Culture, Sports, Science, and Technology (MEXT), a grant from Uehara Memorial Foundation, and Grants-in-Aid for Scientific Research from Japan Society for the Promotion of Science (JSPS) and MEXT (to S.Y.). T. A. and K.O. are JSPS research fellows. K.Y. is an Inoue fellow.

Supporting Online Material

www.sciencemag.org/cgi/content/full/1154884/DC1
Materials and Methods
Figs. S1 to S13
Tables S1 and S2

7 January 2008; accepted 7 February 2008
Published online 14 February 2008;
10.1126/science.1154884
Include this information when citing this paper.

The Cell and Molecular Basis of Mechanical, Cold, and Inflammatory Pain

Bjarke Abrahamsen,[1] Jing Zhao,[1] Curtis O. Asante,[2] Cruz Miguel Cendan,[1] Steve Marsh,[2] Juan Pedro Martinez-Barbera,[3] Mohammed A. Nassar,[1] Anthony H. Dickenson,[2] John N. Wood[1]*

Peripheral pain pathways are activated by a range of stimuli. We used diphtheria toxin to kill all mouse postmitotic sensory neurons expressing the sodium channel $Na_v1.8$. Mice showed normal motor activity and low-threshold mechanical and acute noxious heat responses but did not respond to noxious mechanical pressure or cold. They also showed a loss of enhanced pain responses and spontaneous pain behavior upon treatment with inflammatory insults. In contrast, nerve injury led to heightened pain sensitivity to thermal and mechanical stimuli indistinguishable from that seen with normal littermates. Pain behavior correlates well with central input from sensory neurons measured electrophysiologically in vivo. These data demonstrate that $Na_v1.8$-expressing neurons are essential for mechanical, cold, and inflammatory pain but not for neuropathic pain or heat sensing.

Pain requires input from specialized peripheral sensory neurons, as the loss of these cells results in a pain-free phenotype (*1*–*3*). There is evidence that there are modality-specific sets of nociceptors hard-wired into the central nervous system. Heat and mechanical damage–evoked behavior show no genetic linkage, and these stimuli lead to different patterns

of c-*fos* expression in the dorsal horn of the spinal cord. Recordings from the thalamus show that neurons activated by peripheral application of heat are different from those that are activated by noxious pressure (*4*). However, electrophysiological analysis of skin-nerve preparations have revealed damage-sensing neurons that respond to heat and mechanical insults (*5*). In culture, many small-diameter sensory neurons respond to both mechanical stimuli and activation by capsaicin or thermal stimuli (*6*). On the basis of these in vitro studies, it has been assumed that most nociceptive neurons are polymodal.

Attempts to ascribe pain modalities and behavior to individual sensory neuron receptors have been problematic, probably because of the existence of multiple damage-sensing molecules. A good example is the capsaicin receptor TRPV1, which is activated by high temperatures but does not seem to be essential for acute heat sensing in vivo (*7*, *8*).

We used a genetic approach to identify neurons that convey essential information sufficient to activate central pathways and elicit a sensation of pain and a behavioral response in vivo (*9*). A thoroughly characterized $Na_v1.8$ knock-in Cre-expressing mouse that shows normal pain behavior was used to excise a floxed stop upstream of a globally expressed diphtheria toxin A (DTA)–subunit gene (*10*, *11*). By crossing heterozygous Cre mice with homozygous toxin-expressing floxed mice, equal numbers of control and experimental toxin-expressing (DTA) mice were generated (fig. S1). The DTA chain kills the $Na_v1.8$Cre-expressing neurons (*11*) and has no toxic effects when released into the extracellular space. The numbers of cells staining with antibodies to neurofilament N200 protein (a marker of A fiber associated sensory neurons) was slightly reduced in DTA mice (13%). Most nociceptive sensory neurons express peripherin (*12*), and the majority (>85%) of peripherin-positive neurons were killed (Fig. 1 and fig. S2). Counterstaining with isolectin-B4 and antibodies to calcitonin gene-related peptide (CGRP) (Fig. 1), showed that almost no detectable isolectin B4 (IB4)–positive neurons were retained, whereas ~12% of CGRP-positive neurons were spared. The remaining CGRP-positive neurons were heterogeneous, expressing substance P (36%) and TRPV1 (66%) (fig. S2). In the spinal cord, a lamina I–associated subset of CGRP-expressing terminals was present in the DTA mouse, but all the detectable IB4-positive neurons were absent (Fig. 1 and fig. S2).

We examined the behavior of the mice (*10*, *13*). Having shown that motor coordination was normal we examined acute pain thresholds for thermal and mechanical stimuli. Thermal threshold responses measured with a Hargreaves apparatus showed small altered threshold levels similar to those found in $Na_v1.7$ and $Na_v1.8$ knockouts (fig. S3), whereas behavior on a hot plate at a number of noxious temperatures (Fig. 2) showed no significant deficits between the DTA and control mice.

[1]Molecular Nociception Group, University College London (UCL), Gower Street, London, WC1E 6BT, UK. [2]Department of Pharmacology, UCL, Gower Street, London, WC1E 6BT, UK. [3]Neural Development Unit, UCL Institute of Child Health, 30 Guilford Street, London, WC1N 1EH, UK.

*To whom correspondence should be addressed. E-mail: j.wood@ucl.ac.uk

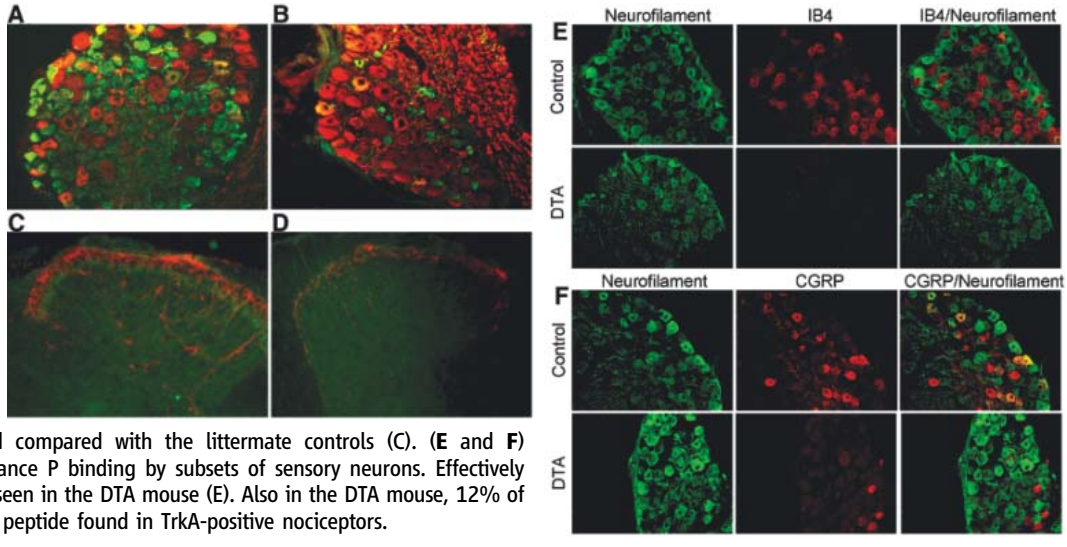

Fig. 1. Deletion of nociceptors using diphtheria toxin. (**A** and **B**) Cross section of L4 DRGs stained with anti-peripherin (green) and anti-neurofilament heavy chain antibodies (red). Peripherin-labeled neurons are reduced by >85% in the DTA mouse (B) compared with the littermate controls (A). (**C** and **D**) Central termination of sensory neurons. Cross section of the lumbar spinal cord stained with CGRP (red) and IB4 (green). In lamina I/II, some CGRP-positive terminals were identified in the DTA mouse (D), whereas all detectable IB4-positive terminals were deleted compared with the littermate controls (C). (**E** and **F**) Expression of CGRP, IB4, and substance P binding by subsets of sensory neurons. Effectively complete ablation of IB4 binding is seen in the DTA mouse (E). Also in the DTA mouse, 12% of control neurons express CGRP (F), a peptide found in TrkA-positive nociceptors.

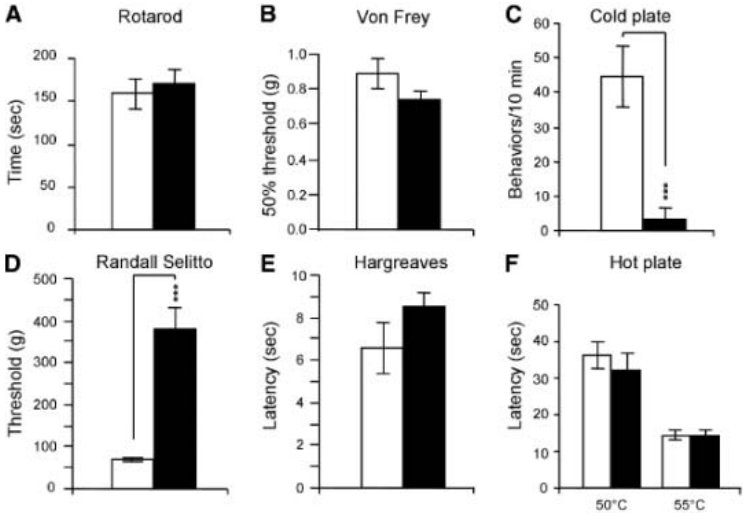

Fig. 2. Acute pain behavior in littermate controls (white bars) and DTA mice (black bars). (**A**) Motor function; time spent on the rotarod (littermate controls: $n = 9$ mice, 158 ± 4.55 s; DTA: $n = 14$, 171 ± 7.18 s). No difference was observed ($P > 0.01$). (**B**) Von Frey; mechanical thresholds were measured using von Frey filaments (littermate controls: $n = 13$; DTA: $n = 14$). No difference was observed ($P > 0.01$). (**C**) Cold behavior (littermate controls: $n = 7$, 44.43 ± 8.71 behaviors; DTA: $n = 7$, 3.57 ± 2.82 behaviors). An almost complete resistance to cold was observed (***$P < 0.005$). (**D**) Randall-Selitto apparatus (littermate controls: $n = 8$, 69.48 ± 5.00 g; DTA: $n = 13$, 381.67 ± 48.65 g). A strong resistance to noxious mechanical stimulation was observed in DTA mice (***$P < 0.0005$). (**E**) Hargreaves; noxious thermal stimulation (littermate controls: $n = 7$, 6.55 ± 1.21 s; DTA: $n = 6$, 8.48 ± 0.71 s). No difference was observed at the $P > 0.01$ level. (**F**) Hot plate; no differences were observed at either 50°C ($P > 0.01$) (littermate controls: $n = 7$, 31.93 ± 5.06 s; DTA: $n = 13$, 36.35 ± 3.66 s) or 55°C ($P > 0.01$) (littermate controls: $n = 15$, 14.26 ± 1.75 s; DTA: $n = 10$, 14.42 ± 1.43 s). In all panels, error bars indicate SE.

Thus, noxious heat perception is hardly affected by the loss of $Na_v1.8$-expressing neurons. Given the importance of CGRP in setting heat thresholds (*14*), the CGRP-expressing sensory neurons that remain in the DTA mice may be involved in heat sensing. In contrast to the normal levels of heat perception, there was no response to cold in the DTA mouse. $Na_v1.8$ has recently been shown to be the only voltage-gated sodium channel that remains functional in cold temperatures (*15*). Cooling behavior mediated mainly through activation of TRPM8 was normal, however (fig. S4). Responses to low-threshold mechanical stimuli applied with von Frey hairs were also normal in the DTA mice. In contrast, behavioral responses to noxious mechanosensation were absent in the DTA mouse (Fig. 2). Extracellular recording from wide dynamic range (WDR) neurons in the spinal cord deep laminae in response to short duration thermal and mechanical input showed deficits in punctuate noxious mechanical ($P > 0.05$) but not thermal coding consistent with the acute pain behavioral data (*16*) (Fig. 3).

We next examined inflammatory and neuropathic pain behavior in the DTA and littermate control mice (Fig. 4). There was an almost complete suppression of the second phase of the formalin response, which has been ascribed to activation of TRPA1 (*17*). The thermal hyperalgesia associated with Freund's complete adjuvant (FCA) injections was also lost. Foot-lifting after FCA injection [a measure of spontaneous pain (*18*)] was absent in the DTA mice. Nav1.8-expressing neurons thus play an essential role in thermal and mechanical hyperalgesia and spontaneous pain after an inflammatory insult such as FCA. Carageenan- and nerve growth factor–evoked hyperalgesia were also absent in the DTA mice (fig. S5).

The cells responsible for inflammatory thermal hyperalgesia are thus different from those that detect acute noxious heat. Nociceptors that are part of the $Na_v1.8$-expressing population may play a role in thermosensation only after becoming activated in inflammatory conditions and thus lowering pain thresholds. Inflammatory mediators are able to sensitize the $Na_v1.8$-expressing neurons lost in the DTA mice (*19*).

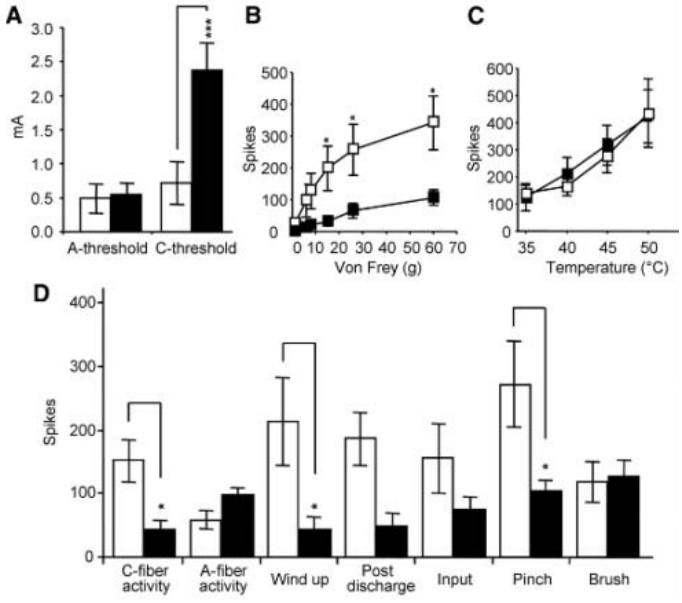

Fig. 3. In vivo electrophysiology of WDR neurons in DTA mice. (**A**) Increased C fiber firing thresholds of WDR neurons in DTA mice (black) ($n = 9$) and their littermate controls (white) ($n = 8$). (**B**) Evoked responses to von Frey filaments showed a mechanical deficit in DTA mice. (**C**) Evoked responses to thermal stimuli remained unchanged in DTA mice. (**D**) Responses to transcutaneous electrical stimulation of the receptive field. C fiber (but not A fiber) thresholds of activation, wind up, and post discharge were all significantly decreased in DTA mice (*16*). Evoked responses from noxious pinch were significantly decreased in DTA mice ($P > 0.05$); responses from non-noxious brush remained unchanged. Asterisks denote significant differences when compared with littermate controls ($P < 0.05$, Student's t test, unpaired). Error bars indicate SE.

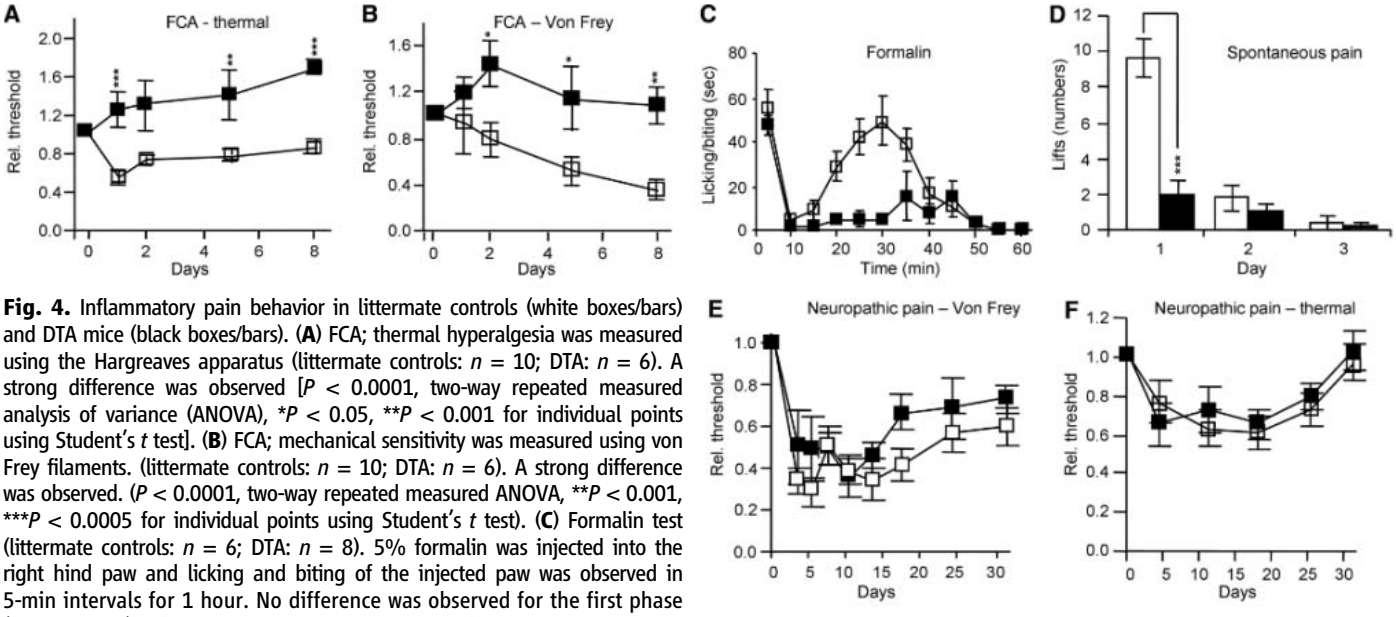

Fig. 4. Inflammatory pain behavior in littermate controls (white boxes/bars) and DTA mice (black boxes/bars). (**A**) FCA; thermal hyperalgesia was measured using the Hargreaves apparatus (littermate controls: $n = 10$; DTA: $n = 6$). A strong difference was observed [$P < 0.0001$, two-way repeated measured analysis of variance (ANOVA), $^*P < 0.05$, $^{**}P < 0.001$ for individual points using Student's t test]. (**B**) FCA; mechanical sensitivity was measured using von Frey filaments. (littermate controls: $n = 10$; DTA: $n = 6$). A strong difference was observed. ($P < 0.0001$, two-way repeated measured ANOVA, $^{**}P < 0.001$, $^{***}P < 0.0005$ for individual points using Student's t test). (**C**) Formalin test (littermate controls: $n = 6$; DTA: $n = 8$). 5% formalin was injected into the right hind paw and licking and biting of the injected paw was observed in 5-min intervals for 1 hour. No difference was observed for the first phase (0 to 10 min), whereas a strong resistance to inflammatory nociception was observed for the second phase (10 to 60 min) ($P < 0.0001$, two-way repeated measured ANOVA, $^{***}P < 0.001$ for individual points using Student's t test). (**D**) Spontaneous pain after injections of FCA (littermate controls: $n = 5$; DTA: $n = 8$). The mice were observed for 5 min on each of the days ($^{***}P < 0.0005$ for individual points using Student's t test). Neuropathic pain in littermate controls (white boxes) and DTA mice (black boxes). (**E**) Mechanical allodynia measured using von Frey filaments. No difference was observed (littermate controls: $n = 13$; DTA: $n = 8$) ($P > 0.05$, two-way repeated measured ANOVA). No difference was observed over the time course ($P > 0.05$, two-way repeated measured ANOVA). (**F**) Thermal hyperalgesia using the Hargreaves apparatus (littermate controls: $n = 13$; DTA: $n = 8$). No difference was observed over the time course ($P > 0.05$, two-way repeated measured ANOVA). Error bars indicate SE.

Input from $Na_v1.8$-expressing neurons may also sensitize second-order dorsal horn neurons. The release of brain-derived neurotrophic factor from Nav1.8-expressing sensory neurons has been shown to play an important role in inflammatory hyperalgesia through effects on *N*-methyl-D-aspartate receptors (*20*). Both mechanisms may contribute to thermal hyperalgesia.

We used calcium imaging to examine whether TRPV1-positive neurons were present in the DTA knockout mouse. Heat sensing is known to still occur in TRPV1 null mice (*7*). Only a small number (4.5% of control) of capsaicin-sensitive neurons were still present in the DTA mouse (fig. S6), and capsaicin-evoked pain behavior (*21*) was suppressed (fig. S4). Quantitative reverse transcription polymerase chain reaction also demonstrated a substantial loss of TrpV1 transcript (figs. S7 and S8). TRPV1 is known to be important for inflammatory responses to heat, however, and the substantial loss of TRPV1-expressing cells correlates well with the loss of heat hyperalgesia (*8*). Responses to cooling are mediated mainly through activation of TRPM8 (*22*). We found that the levels of TRPM8 mRNA as well as the responses to menthol were barely altered in the DTA mouse (figs. S4, S7, and S8). The loss of noxious mechanosensation in the absence of $Na_v1.8$-expressing neurons is consistent with earlier data. There is a division between responses to noxious or non-noxious mechanical stimuli that correlates with the presence of $Na_v1.8$-expressing neurons. $Na_v1.8$ knockout mice are completely insensitive to mechanically evoked pain (*13*), as are $Na_v1.7$ knockout mice (*10*). However, neither channel is a primary mechano-transducer because mechanically gated currents in sensory neurons are normal in $Na_v1.7$ and $Na_v1.8$ knockout mice (*10*).

Neuropathic pain is normal in the absence of $Na_v1.8$-expressing neurons. Although antisense oligonucleotides directed against $Na_v1.8$ have been claimed to reverse neuropathic pain, effects on other sodium channels cannot be ruled out (*23*). Neuromas show subtle alterations in excitability in the absence of $Na_v1.8$, and compounds with relative selectivity for $Na_v1.8$ have been shown to have some efficacy in neuropathic pain models (*24*), but it is clear that the principal conduit for many neuropathic pain conditions involves $Na_v1.8$-negative neurons.

We used microarrays to examine the altered repertoire of genes expressed in dorsal root ganglia (DRGs) from animals depleted of $Na_v1.8$-expressing neurons. These data are represented in fig. S9 and have been deposited in ArrayExpress. The loss of >96% of $Na_v1.8$ transcripts in DTA-mouse DRGs shows that the technique was effective. Both known nociceptor-specific transcripts (e.g., MrgA3, TRPA1, $Na_v1.9$, and P2X3) as well as many previously undescribed selectively expressed transcripts have been identified (fig. S9 and table S1).

In summary, acute heat and neuropathic pain do not require $Na_v1.8$-expressing neurons, but inflammatory, cold, and mechanical pain are absolutely dependent on these cells. The present study provides a repertoire of candidate molecules potentially involved in different aspects of somatosensation that can be examined experimentally through further tissue-specific ablation studies.

References and Notes

1. Y. Indo, *Hum. Mutat.* **18**, 462 (2001).
2. E. R. Perl, *Nat. Rev. Neurosci.* **8**, 71 (2007).
3. S. N. Lawson, *Exp. Physiol.* **87**, 239 (2002).
4. W. R. Lariviere *et al.*, *Pain* **97**, 75 (2002).
5. J. J. Lawson, S. L. McIlwrath, C. J. Woodbury, B. M. Davis, H. R. Koerber, *J. Pain* **9**, 298 (2008).
6. D. Julius, A. I. Basbaum, *Nature* **413**, 203 (2001).
7. C. J. Woodbury *et al.*, *J. Neurosci.* **24**, 6410 (2004).
8. M. J. Caterina, *Am. J. Physiol. Regul. Integr. Comp. Physiol.* **292**, R64 (2007).
9. Materials and methods are available as supporting material on *Science* Online.
10. M. A. Nassar *et al.*, *Proc. Natl. Acad. Sci. U.S.A.* **101**, 12706 (2004).
11. A. Ivanova *et al.*, *Genesis* **43**, 129 (2005).
12. M. E. Goldstein, S. B. House, H. Gainer, *J. Neurosci. Res.* **30**, 92 (1991).
13. A. N. Akopian *et al.*, *Nat. Neurosci.* **2**, 541 (1999).
14. J. S. Mogil *et al.*, *Proc. Natl. Acad. Sci. U.S.A.* **102**, 12938 (2005).
15. K. Zimmermann *et al.*, *Nature* **447**, 855 (2007).
16. E. A. Matthews, J. N. Wood, A. H. Dickenson, *Mol. Pain* **2**, 5 (2006).
17. C. R. McNamara *et al.*, *Proc. Natl. Acad. Sci. U.S.A.* **104**, 13525 (2007).
18. L. Djouhri, S. Koutsikou, X. Fang, S. McMullan, S. N. Lawson, *J. Neurosci.* **26**, 1281 (2006).
19. S. G. Khasar, M. S. Gold, J. D. Levine, *Neurosci. Lett.* **256**, 17 (1998).
20. J. Zhao *et al.*, *Mol. Cell. Neurosci.* **31**, 539 (2006).
21. F. Amaya *et al.*, *J. Neurosci.* **26**, 12852 (2006).
22. D. M. Bautista *et al.*, *Nature* **448**, 204 (2007).
23. J. Lai *et al.*, *Pain* **95**, 143 (2002).
24. J. Ekberg *et al.*, *Proc. Natl. Acad. Sci. U.S.A.* **103**, 17030 (2006).

25. We thank the Biotechnology and Biological Sciences Research Council, the Medical Research Council (UK), and the Wellcome Trust for supporting this work. We also thank the Institute of Child Health chimera production facility, which generated the DTA transgenic mouse line, and W. Huang for help and advice.

Supporting Online Material

www.sciencemag.org/cgi/content/full/321/5889/702/DC1
Materials and Methods
Figs. S1 to S9
Table S1
References

25 February 2008; accepted 27 June 2008
10.1126/science.1156916

"It would take a long time to put just one sample in front of the beam. If you can put the samples into a container and have a robot that can do that for you, you can speed it up and have less error."

hall is unlikely to work. "There are thousands of new technologies," adds Edwards. "Most will be doorstops in five years. But of all these many, many, many technologies, which are actually useful?"

The solution, he says, is to put these technologies through their paces in a controlled fashion. "That's what the field is doing," he says, "looking at the panoply of technologies, seeing which work, so you don't end up chasing your tail." Importantly, the community archives that knowledge in searchable public databases like TargetDB and PepcDB, which track not only what works, but also what doesn't.

Earlier this year members of the SGC (including Edwards) and 13 other structural genomics facilities around the world published their collective wisdom in a paper entitled "Protein production and purification" (*Nat Methods*, **5**:147-53, 2008). Andrzej Joachimiak, director of the **Midwest Center for Structural Genomics (MCSG),** calls the paper "a Maniatis manual for protein purification." Edwards, who was corresponding author, says the report represents "the final UN-negotiated solution," a probability-based consensus protocol for all protein jocks, not just structural biologists.

From Bad Media, a Breakthrough

The protocol contains such suggestions as developing multiple distinct constructs for each target; using ligation-independent cloning (commercialized as **Clontech's** In-Fusion 2.0 PCR Cloning kits); and the unified use of expression tags for easy purification with robots such as **GE Healthcare's** AKTA-express.

Another tip: try F. William Studier's autoinduction media (available from **EMD Biosciences** as Novagen Overnight Express.). "It is a technique everyone should be using," says Edwards.

Recombinant protein expression in bacteria is commonly controlled via the lactose control circuit. Place a *lac* operator in front of a gene of interest, and the gene will remain silent until you add the allolactose analog, IPTG. But IPTG must be added at just the right moment, and different cultures grow at different rates. "How do you get all the cultures growing at the same rate and at the same time to get optimal expression of these proteins in parallel?" asks Studier, of the **Brookhaven National Laboratory.**

In trying to solve that problem, Studier observed that some of his cultures induced on their own, without IPTG. He discovered that one of his media components was contaminated with trace lactose. Making use of this observation, Studier first designed a rich formulation in which cultures could grow to high optical density (OD) but never induce (noninducing medium). He then developed a precise blend of glucose, lactose, and glycerol in which the cells autoinduce upon hitting log phase. And they would do so while cranking out protein at higher levels than usual, because the cells can grow to much greater densities—up to OD 20, compared to OD 3 in Luria broth. "So all you have to do is grow 96 cultures in noninducing medium, then inoculate those into autoinducing medium, grow overnight, and collect induced cultures in the morning," he says.

Biophysical Considerations

It's not enough to express a protein; it also must be soluble, and properly folded. At the **Joint Center for Structural Genomics (JCSG)** researchers employ a battery of methods to ensure desirable biophysical properties are met, says director Ian Wilson. Size-exclusion chromatography indicates whether the protein is soluble or aggregating. SDS-PAGE reveals protein purity. And deuterium-exchange mass spectrometry highlights disordered regions that could cause trouble downstream. "You label for a few seconds with deuterium, quench at low pH, digest with protease, and look for which regions are disordered by how much it is exchanging with the deuterium in the solution," Wilson explains. "Only the disordered regions incorporate deuterium, because it is so fast."

Such data can be invaluable. Brian Kobilka of **Stanford University,** who solved the structure of the beta-2 adrenergic receptor, found (via separate methods) that a loop between transmembrane domains 5 and 6 was "floppy," inhibiting crystallization. His team overcame that via parallel approaches, one involving an antibody against the C-termini of these two helices, and the other, with Ray Stevens of the **Scripps Research Institute,** replacing that loop with a stable T4 lysozyme domain.

Others optimize structural work by tweaking protein length or surface chemistry. Researchers at the **European Molecular Biology Laboratory (EMBL)** outstation in Grenoble, France, site of the European Synchrotron Radiation Facility (ESRF), use a biotinylatable tag in their library construction and screening procedures to find soluble domains, says facility director Stephen Cusack.

Researchers at the MCSG, JCSG, and SGC improve crystal formation using reductive methylation and limited proteolysis. The former alters protein surface chemistry to allow different crystal packing and improve diffraction properties, while the latter removes disordered regions in situ. Both have been tested on large numbers of proteins, says Joachimiak—400 in the case of reductive methylation, yielding 30 structures that were otherwise unattainable.

Accelerating NMR

Structure determination by NMR has also benefited from 'omics efforts. HIFI-NMR, a "reduced dimensionality" approach developed at the PSI-2 **Center for Eukaryotic Structural Genomics (CESG),** reduces the time required to acquire spectral assignment data by a factor of 10, says principal investigator John Markley of the **University of Wisconsin, Madison.** Instead of blindly collecting data by standard methods, this approach leverages prior information at each step to get the job done in the most efficient manner.

Using NMR chemical shift data from the **Northeast Structural Genomics Consortium,** Yang Shen and Ad Bax from the **National Institutes of Health,** with Oliver Lange and David Baker at the **University of Washington,** validated a novel computational method (CS-ROSETTA) that predicts protein structure from chemical shift data. Their new approach thereby eliminates the need for both side-chain assignments and one of NMR's lengthiest steps, nuclear Overhauser effect experiments.

"There are algorithms available to predict chemical shifts from structure," says Markley. "[Bax] is using [CS-ROSETTA] to go the other way—from the chemical shifts you get a starting approximation of what the 3D conformation of the protein is." Then, using Baker's ROSETTA energetics algorithm, the software computes a likely final structure. In March, Bax and Baker applied CS-ROSETTA to 25 protein sequences; they estimated it can cut the structure-generation time by 50 percent.

Robotics

As with any 'omics enterprise, automation and robotics are integral to structural proteomics. HWI researchers have developed robotics

Featured Participants

Berkeley Center for Structural Biology
bcsb.als.lbl.gov

Brookhaven National Laboratory
www.bnl.gov

CellFree Sciences
www.cfsciences.com

Center for Eukaryotic Structural Genomics
www.uwstructuralgenomics.org

Center for High-Throughput Structural Biology
www.chtsb.org

Clontech
www.clontech.com

Columbia University
www.columbia.edu

EMBL
www.embl.org

EMD Biosciences
www.emdbiosciences.com

Fluidigm
www.fluidigm.com

GE Healthcare
www.gehealthcare.com

Hauptman-Woodward Medical Research Institute
www.hwi.buffalo.edu

Israel Structural Proteomics Center
www.weizmann.ac.il/ISPC

Joint Center for Structural Genomics
www.jcsg.org

Midwest Center for Structural Genomics
www.mcsg.anl.gov

National Institutes of Health
www.nih.gov

New York Consortium on Membrane Protein Structure
www.nycomps.org

New York SGX Research Center for Structural Genomics
www.nysgxrc.org

Northeast Structural Genomics Consortium
www.nesg.org

Oxford Protein Production Facility
www.oppf.ox.ac.uk

Rigaku
www.rigaku.com

Rutgers University
www.rutgers.edu

Scripps Research Institute
www.scripps.edu

Stanford University Research Institute
www.stanford.edu

Structural Genomics Consortium
www.thesgconline.orr

TTP LabTech
www.ttplabtech.com

University of Limerick
www.ul.ie

University of Washington
www.washington.edu

University of Wisconsin, Madison
www.wisc.edu

to automate crystallization trials. "We can do 1,536 conditions in about 20 minutes in a single plate," Malkowski says. "And then we image these samples every week for a month."

Such automation means researchers can do more with less, and more accurately. "When I was a postdoc, I would set up crystallization droplets of 20 to 30 μl. Now we use 200 to 500 nl," says Joachimiak.

Crystallization robots are available from **Rigaku** and **Fluidigm,** among others. Joachimiak uses **TTP LabTech's** mosquito. So does Joel Sussman, director of the **Israel Structural Proteomics Center** and coeditor of *Structural Proteomics and Its Impact on the Life Sciences* (World Scientific, 2008). In fact Sussman's lab is extensively automated, with robots for cloning, protein purification, and crystal visualization. At ESRF, where Sussman's team runs diffraction experiments, robots even mount their crystals into the beamline.

According to Paul Adams, head of the **Berkeley Center for Structural Biology,** automounting robots are especially useful for screening to see which crystals diffract best. Traditionally, "It would take a long time to put just one sample in front of the beam," he says. "If you can put the samples into a container and have a robot that can do that for you, you can speed it up and have less error."

Eukaryotic Troubles

Structural genomics centers have deposited over 6,600 structures in PDB. Yet challenges remain. Of 25,662 targets selected at the JCSG, 20,865 have been cloned, 20,546 expressed, 1,337 crystallized, and 686 solved—a 3.3 percent success rate. **The New York SGX Research Center for Structural Genomics** puts up comparable numbers: 486 structures from 8,849 selected targets (5.5 percent).

Eukaryotic proteins represent a particular challenge. For a variety of reasons, including posttranslational modifications, size, and domain structure, eukaryotic proteins are tougher nuts to crack than prokaryotic ones. As of June 1, 2008, the 10 PSI-2 centers have solved 1,716 protein structures, but just 197 of those are eukaryotic; the rest are either prokaryotic (1,500) or viral (19).

"Quite often proteins require glycosylation to be made properly," says Ray Owens, director of the **Oxford Protein Production Facility (OPPF),** Oxford, UK. "So you cannot make them in *E. coli*. They need to be made in eukaryotic cells, which will authentically glycosylate them." OPPF researchers use transient transfection of human embryonic kidney (HEK293) cells. Because most glycoproteins are secreted, purification is a snap: just collect the supernatant. The problem, Owens says, is "the chemical heterogeneity of the glycoproteins." To skirt that issue team members use inhibitors like kifunensine to freeze glycoprotein sugar chains in a more homogeneous form, and endoglycosidases to pare these glycans back.

CESG researchers use a cell-free eukaryotic wheat germ extract from **CellFree Sciences** for their protein expression. "We find that we get roughly twice the number of successful targets produced by wheat germ extract than with *E. coli*," says Markley. It is also faster, less expensive, and involves easier protein purification, because sufficient protein for a structure determination is isolated from milliliter reactions, rather than in liter quantities of cells.

Membrane Proteins

Membrane proteins also present unique structural challenges, says Scripps' Stevens. First, because the membrane represents such a small fraction of total cellular volume, they are present at relatively low levels. More important, the membrane itself is integral to their structure. "We have to solubilize them, which puts them in a very unstable state," he says.

Yet detergent interferes with the protein packing that is essential to crystallization. Stevens has developed or implemented several techniques to work with membrane proteins, including a high throughput "lipidic cubic phase" crystallization process first developed by Martin Caffrey of the **University of Limerick,** Ireland, that was key to solving the beta-2 adrenergic receptor structure.

Researchers at the **New York Consortium on Membrane Protein Structure (NYCOMPS),** a PSI-2 specialized center, have alternative methods, says director Wayne Hendrickson of **Columbia University.** "We have developed a pipeline process analogous to the kind that has been effective at large-scale centers for soluble proteins to produce membrane proteins and analyze them by crystallography and NMR," he says.

For instance, the consortium uses ultraviolet absorbance and light scattering to test which detergents work best and which proteins are in the proper oligomeric forms. More recently, they developed a generic antibody-based approach to extensively incorporate selenomethionine residues into protein complexes, key to solving X-ray diffraction "phase problems."

Using tools such as these, NYCOMPS researchers have produced over three thousand membrane proteins in the past year, resulting in five structures, with another seven or eight "in determination." "We are very much in early stages," Hendrickson says.

And despite the thousands of structures pouring out of high throughput labs around the world, so, it is safe to say, is structural proteomics in general.

Jeffrey Perkel is a freelance writer based in Pocatello, Idaho.

DOI: 10.1126/science.opms.p0800027

New Products

Millipore
For information 800-548-7853
www.millipore.com

Protein Detection System

The new SNAP i.d. protein detection system allows researchers to produce high-quality protein immunoblots 80 percent faster than with conventional immunodetection protocols. By shortening the time required for blocking, washing, and antibody incubations to 30 minutes, the SNAP i.d. system allows researchers to optimize their immunodetection conditions for high-quality results. The system is compatible with all membrane types and detection methods, such as chemiluminescence and fluorescence. Both sensitivity and specificity are equivalent to or higher than standard immunodetection. The system features a unique, vacuum-driven technology and built-in flow distributor to actively drive reagents through the membrane, ensuring even distribution. Three different sizes of blot holders accommodate up to three blots each, and two blot holders can be run in parallel. Thus researchers can process up to six blots in parallel.

Automated Hybridization Stations

The HS 4800 Pro and HS 400 Pro Hybridization Stations perform automated, reproducible microarray processing on single- and multisegment slides. The stations provide liquid agitation during hybridization, which increases sensitivity, stringency, and uniformity, and enables reduction of hybridization times. The stations minimize the risk of hybridization artifacts and interslide segment carry-over. They offer single-chamber, dual-chamber, and QuadChamber options that are easily interchangeable. A unique Active Bubble Suppression system avoids bubble artifacts. On-slide nitrogen drying avoids external drying steps and drying artifacts.

Tecan
For information +41-44-922-81-11
www.tecan.com

Protein Interaction Analysis

The Biacore T100 protein characterization software version 2 for the Biacore T100 label-free protein interaction analysis system enables calibration-free concentration analysis of proteins. The software makes it possible to measure protein concentration without using a standard. It also includes key functionality for protein characterization that reduces time spent on development of kinetic analysis assays through the single-cycle kinetics function. Single-cycle kinetics enables the analysis of molecular interactions that have previously been difficult to determine. In addition, the software significantly improves data evaluation so that multiple samples can be analyzed together with a few clicks. Determination of the target-binding drug fraction is important during the development of therapeutic proteins and provides an informative characterization profile in quality control of biotherapeutics.

GE Healthcare
For information 732-457-8149
www.biacore.com

Custom Peptide Synthesis

Activotec can supply high-quality, difficult-to-synthesize peptides at competitive prices. Synthetic peptides have a variety of uses, including structure-function analysis of sites within a protein, binding assays, receptor agonists/antagonists, and immunogens for the production of antisera. Using solid-phase and solution-phase chemistries as well as Fmoc and t-Boc methodologies, Activotec can produce peptides with difficult-to-synthesize sequences, cyclic peptides, hydrophobic peptides, very long-chain peptides, and nonnatural modifications. Using proprietary manual techniques and its own state-of-the-art automated synthesis equipment, Activotec can provide peptides in quantities ranging from milligrams to grams at all purity levels. Every peptide is delivered with individual mass spectroscopic and analytical high-performance liquid chromatography data.

Activotec
For information +44-1223-260008
wwww.activotec.com

Nickel Magnetic Beads

A powerful separation matrix, PureProteome Nickel Magnetic Beads allow fast, easy purification of polyhistidine-tagged recombinant proteins, a critical step in protein research. Millipore's patented process for magnetizing porous silica particles provides researchers with high-binding-capacity, high-affinity beads for efficient protein purification. These beads bind recombinant protein even in the presence of EDTA, a metal ion chelator. Compared with other magnetic beads, these beads offer higher purity while yielding comparable amounts of protein, according to the manufacturer.

Millipore
For information 800-548-7853
www.millipore.com

Antibody Purification Products

Two new products, affinity matrices for the purification of IgA and IgM, have been added to the CaptureSelect Antibody Toolbox. CaptureSelect Human IgA matrix contains an affinity ligand that binds to a unique domain that is present on all classes of human IgA, with no cross-reactivity with IgM or IgG. The CaptureSelect IgM affinity matrix contains an affinity ligand that is directed toward a unique domain present on both human and mouse IgM antibodies and is free of cross-reactivity with human or mouse IgA or IgM. The products in the CaptureSelect Antibody Toolbox streamline purification of antibodies by offering standardized protocols that enable researchers to follow a simple one-step process with no need for method testing or lengthy optimization steps.

BAC BV, the BioAffinity Company
For information +44-(0)-1260-296-506
www.captureselect.com

Electronically submit your new product description or product literature information! Go to **www.sciencemag.org/products/newproducts.dtl** for more information.

Newly offered instrumentation, apparatus, and laboratory materials of interest to researchers in all disciplines in academic, industrial, and governmental organizations are featured in this space. Emphasis is given to purpose, chief characteristics, and availabilty of products and materials. Endorsement by *Science* or AAAS of any products or materials mentioned is not implied. Additional information may be obtained from the manufacturer or supplier.